8-2018

Experimental and Analytical Techniques for Evaluating the Impact of Thermal Barrier Coatings on Low Temperature Combustion

Ryan O'Donnell
Clemson University, rodonne@g.clemson.edu

Experimental and Analytical Techniques for Evaluating the Impact of Thermal Barrier Coatings on Low Temperature Combustion

---

A Dissertation
Presented to
the Graduate School of
Clemson University

In Partial Fulfillment
of the Requirements for the Degree
Doctor of Philosophy
Automotive Engineering

---

by
Ryan O'Donnell
August 2018

Accepted by:
Dr. Zoran Filipi, Committee Chair
Dr. Mark Hoffman, Co-Chair
Dr. Richard Miller
Dr. Robert Prucka

Abstract

Homogeneous Charge Compression Ignition (HCCI), exhibits many fundamentally attractive thermodynamic characteristics. These traits, along with lean charge and low combustion temperatures, generally act to increase thermal efficiency relative to competing spark and/or compression ignition strategies. However, HCCI's extreme sensitivity to in-cylinder thermal conditions, place limits on practical implementation. Thus, at low temperatures, combustion remains incomplete limiting cycle efficiency while increasing emissions. In contrast, the introduction of thermal barrier coatings (TBCs) to in-cylinder surfaces has been shown to fundamentally alter gas-wall interactions. The work in this dissertation explores HCCI/TBC synergies. Both experimental and analytical pathways are explored, attempting to illuminate the impact(s) of coatings on engine heat transfer and combustion metrics. Efforts to correlate TBC thermophysical properties and surface phenomena with HCCI performance and emissions are also explored. Finally, methods are proposed to evaluate the TBC-gas interaction as it relates to thermal stratification of the in-cylinder charge.

The present work seeks to identify, and eventually quantify HCCI/TBC synergies. A specific research effort is developed, attempting to illuminate the impact(s) of TBCs on fundamental HCCI combustion metrics. Efforts to correlate TBC thermophysical properties and surface phenomena with HCCI performance and emissions are also proposed. Analysis is enabled through complimentary analytic and experimental pathways - which includes specialized solution methodology and experimental hardware. Combined, these tools enable a more complete qualitative assessment of thermal barrier coating's impact on engine performance and emissions metrics, heat loss at the wall, and ultimately thermal stratification of the in-cylinder temperature field.

Acknowledgments

The present document did not manifest in a vacuum. Rather, it represents the collaborative efforts of many individuals, all of which I wish to formally recognize.

To begin, the members of dissertation committee are due a sincere amount of gratitude. I would not be writing this document if it was not for the generosity of my advisor, Zoran Filipi. Had he not taken a 'leap of faith' in allowing a physics undergrad to study advanced engine concepts, I'd likely be counting electrons.

A great amount of thanks is also due to Mark Hoffman who brought with him considerable expertise in engine experimentation. He also brought the engine.

Rob Prucka taught much of the fundamental engine coursework at Clemson. Equally as important, he provided definitive proof that the demands of a young family can be satisfied despite the chaos of the Academic day-to-day.

Richard Miller taught two courses which had a tremendous impact on me intellectually and otherwise. Turbulence and Experimental Methods may well describe the bulk of my graduate existence.

Tommy Powell was my partner in crime(s against combustion) over the past 5+ years. Despite the relentless challenges which accompany building, operating, and maintaining an experimental platform, we remain standing. Weaker men would have faltered long ago... or started doing simulations. Thanks Tommy!

The tech and administrate staff have contributed so much to me personally and the automotive engineering program as a whole. I would like to specifically mention Gary, David, Frank, and Jeremy as the people responsible for keeping respective clearances in spec. Thanks guys.

My folks, Mark and Kathy, and my brother Greg deserve a special shout out. THANK YOU! If not for their encouragement and continued belief in my ability, I'm not certain I would have

continued on the long, windy road that lead to ICAR. Thank you for that, and thank you for the freedom to choice my own path - a truly wonderful gift.

Finally, I would like to recognize the countless contributions of my wife, Lindsey. If not for her unending support, love, and encouragement I would have long-ago dangled my hair into a spinning drive shaft. In all sincerity, none of this would be possible without her endless support. I love you Baby, Daddy's home!

This work is dedicated to my kiddos, Molly and Van. You are the best experiments I have known. I hope you too are afforded the chance to follow your intellectual curiosities wherever they may lead. The universe is filled with endless wonder, go get some.

> Those who have learned to walk on the threshold of the unknown worlds, by means of what are commonly termed par excellence the exact sciences, may then, with the fair white wings of imagination, hope to soar further into the unexplored amidst which we live.

-Ada Lovelace

> It's such a fine line between stupid and clever.

-David St. Hubbins

Table of Contents

List of Tables

List of Figures

Chapter 1

Thermal Barrier Coatings for HCCI

The internal combustion engine has been the prime instrument of power generation from the late 1800's through the present day [87]. Its reign as humankind's 'energy conversion device of choice' is projected to continue well into the 21^{st} Century [57]. Yet, despite a ubiquitous presence, many of the fundamental mechanism governing heat release and energy conversion within the engine environment remain poorly understood. Historically, engine researchers (including, but not limited to, combustion engineers, thermal-fluid scientists, chemical kinetitists, fluid dynamyists, etc.) have worked to systematically advance engine performance by fostering a more complete understanding of the underlying physics. Today, as a result of these efforts, researchers have more complete understanding combustion, mass, and energy transport processes. However, intellectual curiosity is hardly a solitary motivator. Research efforts have attempted to address many of the paramount 'real world' concerns regarding the impact on humankind and the environment, such as: fuel availability, energy conversion efficiency, and emission formation have also done their part to engendered progress in the developmental trajectory of contemporary engines [43]. Despite these efforts (and the associated advances), an incomplete understanding of the underlying 'science' remains. And so, the research continues.

This chapter will serve as an introduction to one of the more novel modes of internal combustion - Homogeneous Charge Compression Ignition (HCCI). This approach to internal combustion is

the exclusive focus of the experimental and analytical work presented in the proceeding document. As will be shown, HCCI is associated with a means of in-cylinder heat release distinctly separate from the more common spark-ignited flame-propagation and/or mixing-controlled compression-ignited schemes. Instead, this mode of combustion represents (somewhat) 'controlled auto-ignition' - where mixture composition, in-cylinder thermal conditions, and chemical kinetics determine the underlying fuel oxidation pathway.

Beyond the relative novelty of this combustion mode, beneficial thermodynamic characteristics of HCCI will also be discussed. These largely result from the HCCI engine's lean charge composition, high compression ratio, and 'low' in-cylinder temperatures during combustion. Ultimately, an argument will be offered to the reader, one which positions HCCI as a central player in the search for 'cleaner', more efficient, ICE-derived power generation.

In an effort to 'set the stage' for the work highlighted in later sections of this document, key research and development milestones will be reviewed. The purpose of this effort is twofold. First, the present work would not be possible if not for the many contributions of pioneering researchers. The shoulders of these proverbial 'giants' (big and small) provide the footing upon which the frontier of current understanding may be probed. With a little luck (and quite a bit more effort), the author hopes to shine his own light towards the previously unknown. Second, an effort will be made to construct a coherent historical narrative tracking the independent trajectories of low temperature combustion and thermal barrier coatings technologies within the engine environment. The crossroads of these pathways will be explored in later chapters.

1.1 Homogeneous Charge Compression Ignition - An Overview

Homogeneous Charge Compression Ignition (HCCI), when examined from a 1^{st} Principles perspective, exhibits many of the thermodynamic characteristics required for high efficiency, low emissions power generation. In this section, an overview of this mode of combustion will be provided - including a review of the underlying chemical kinetics, thermodynamic cycle attributes, and considerations relating to heat transfer and emissions formation. Specific focus is also given to in-cylinder thermal considerations - both those enabling low temperature combustion (LTC) processes and those limiting them. The section begins with an introduction to HCCI combustion in the context of the more familiar Spark Ignited (SI) and Compression Ignition (CI) combustion modes.

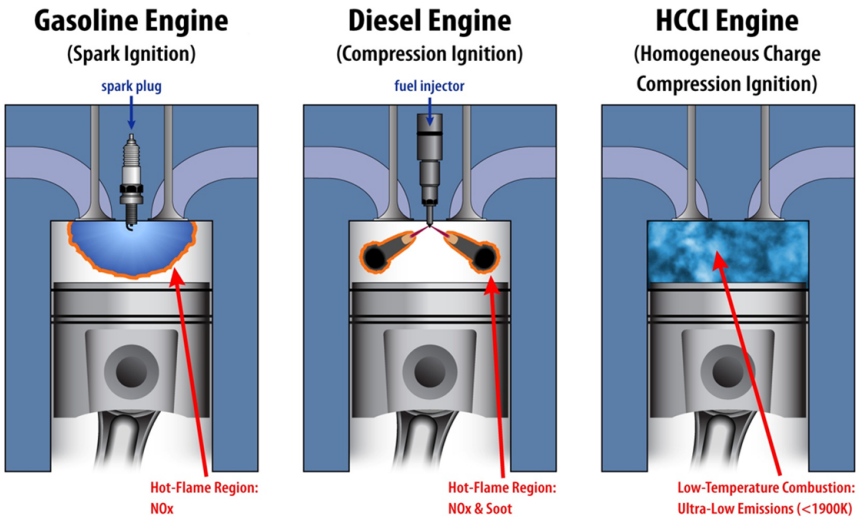

Figure 1.1: HCCI in the context of turbulent flame entertainment and mixing-controlled burning [**?**].

1.1.1 HCCI Autoignition in the context of Spark Ignited Turbulent Flame and Compression Ignited Diffusion Burning Combustion Modes

Considerable effort has been made to develop a more complete understanding of both spark-ignited, 'turbulent flame entrainment ('SI gasoline") and compression ignited mixing-controlled ('CI Diesel') processes. These more conventional modes of combustion account for the vast majority of ICE-derived power generation [**?**]. Thus, the relative familiarity of their operational characteristics provides a natural point of comparison to introduce Homogeneous Charge Compression Ignition.

As discussed in the preceeding section, HCCI is a relatively 'new' concept. First appearing in the literature in 1979, Onishi and colleaques [74] witnessed "abnormal combustion" when attempting to improve performance and emissions formation within a two-stroke gasoline-fueled SI engine. Using Schlieren-based optical diagnostics, the authors noted the following characteristic behavior,

> "...(HCCI) differs from conventional gasoline engine combustion in that combustion reactions occur spontaneously and at many points...".

This observation, subsequently confirmed by more recent efforts, positions HCCI distinctly seperate from the turbulent flame entrainment of spark-ignited gasoline combustion modes. and the mixing-controlled heat release associated with more conventional combustion concepts. Furthermore, the seeming 'spontaneity' of HCCI's many autoignition sites, has been shown to be closely correlated

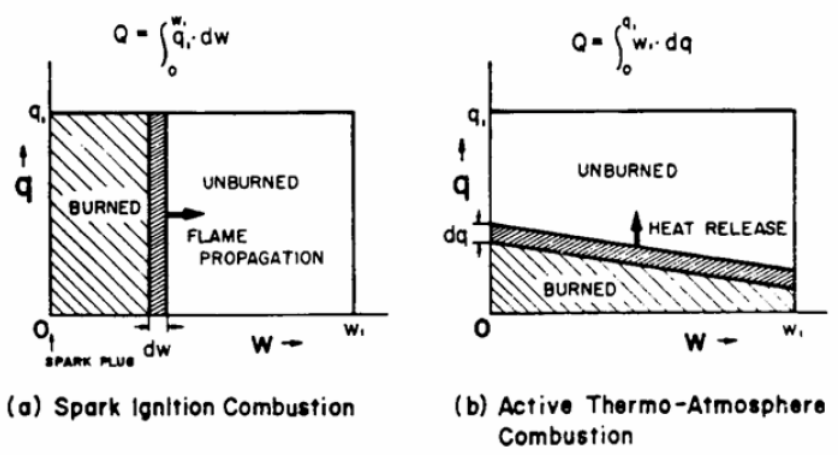

Figure 1.2: A fundamentally different mode of heat release, as reported by Onishi, et al. [74]

to the thermal stratification within the trapped charge [24]. This synergy will be developed in more complete detail in the follow sections.

As Onishi and his co-authors originally reported, the characteristics describing heat release during HCCI combustion is fundamentally distinct from that observed during turbulent flame entertainment [88] and/or diffusion burning. As would be discovered during later analysis, HCCI combustion is more aptly described as an 'cascading' autoignition [85, 83], totally reliant upon the thermal-fluid considerations governing the underlying chemical kinectics [1].

1.1.2 Flameless Combustion

Concurrent to Onishi's work at NiCE, Noguchi and colleagues at Toyota employed an optically-accessible, gasoline-fueled, two-stroke engine to further examine the physics underlying HCCI [70]. Like Nissan, Toyota's efforts confirmed multiple ignition locations while noting the absence of a coherent flame front. Spectroscopic measurements of intermediate species preceding combustion registered elevated levels of CH_2O, HO_2, and O radicals. Taken together, these observations help position chemical kinetics (rather than turbulent flame entrainment) as the primary mechanism driving HCCI combustion. These observations also provide an early experimental leak between HCCI and the problematic "knock" phenomenon associated with high temperature compression of the un-burned end gases. These observations also provide an early experimental link between HCCI combustion and the autoignition of high-temperature/high-pressure 'end gas' asso-

ciated with knocking.

From a practical standpoint, both Onishi and Noguchi reported dramatic decreases in cycle-to-cycle variability when operating their engines in HCCI mode. Cyclic variability for kinetically-driven modes of combustion such as HCCI are largely determined by in-cylinder thermal conditions.

1.1.3 From Two Strokes to Four

Homogeneous charge compression ignition was extended to four-stroke engine architecture by Najt and Foster at the University of Wisconsin [68]. Lacking the high temperature residual gas associated with the two-stroke scavenging process, the authors pre-heated incoming air to enable autoignition of the premixed charge. This charge-heating requirement foreshadows the targeted efforts of later researchers - including those at Lund University [46] and Sandia National Lab [24], [85]. This work, to be detailed further in subsequent sections, helped to further establish the connection between in-cylinder thermal condition and the HCCI combustion process. In an effort to better control the autoignition process, this pioneering work also included active manipulation of in-cylinder thermal conditions via charge heating/cooling and dilution.

1.1.4 Fundamental Thermodynamic Advantages of HCCI

Many of the underlying thermal-fluid and chemical mechanisms associated with HCCI result in quite 'favorable' thermodynamic cycle conditions [17, 16, 15, 23]. Identification of these mechanism, and evaluating their relative impact on cycle efficiency is critical given ongoing efforts to further optimism HCCI and other Low Temperature Combustion (LTC) strategies. This section will provide a systematic review of critical thermodynamic considerations relative to HCCI performance. Opportunities for further advancement, along with inherent trade-offs between parameters will be discussed.

As a foundational starting point, consider the follow expression describing thermodynamic cycle efficiency for the Otto cycle,

$$\eta_{f,i} = 1 - \frac{1}{r_c^{\gamma-1}} \tag{1.1}$$

The two variables of the right-hand side of Eq.1.1 capture geometric (compression ratio, r_c) and compositional parameters (ratio of specific heats, γ) unique to a particular engine archi-

tecture and combustion mode. The follow sections will develop the respective role for the high-compression/low-temperature environment inherent to HCCI.

1.1.4.1 Compression Ratio

Increasing compression ratio provides one of the more direct means for enhancing ICE thermal effeciency [43]. Non-compression ignition engines (including most conventional SI concepts) are typically knock-limited, in that compression is reduced to avoid unintentional autoignition of the end-gas (i.e., "knocking"). Fuel considerations must also be taken into account, with particular attention given to octane rating and other relevant reactivity metrics.

A series of cycle-efficiency curves are provided across a representative range of compression ratio in Fig.1.3. Assuming a fixed mixture composition and uniform thermal conditions (i.e., constant gamma), thermal efficiency steadily increases as compression ratio is elevated. As mentioned, geometric compression is typically limited by knock constraints in more conventional SI engines. However, practical knock limits also exist for CI combustion modes including HCCI. The volumetric clearance required by engine components including injectors, spark-plugs, and valves is not negligible. In the case of HCCI, a balance exists between obtaining sufficient compression heating (to help facilitate autoignition), and clearance for necessary engine hardware.

By its very name, HCCI is a compression ignition concept. Autoignition of the lean mixture requires high geometric compression, which in turn further elevates cycle efficiency relative to the SI combustion mode.

1.1.4.2 Gamma Considerations

The lower combustion temperatures which accompany homogeneous lean burn concepts (such as HCCI) contributes to a number of favorable efficiency benefits [43]. For a fixed mixture composition, the ratio of specific heats generally increases as charge temperature is decreased. In a practical sense this enables 'cooler' (higher γ) mixtures to extract more work from a given heat release. This gamma-efficiency link is shown explicitly in Fig.1.3.

Charge composition also has a an impact on gamma. In the case of HCCI, (lean mixtures with significant EGR dilution), gamma values are further elevated relative to stoichiometric combustion modes [43]. This reality further enhances cycle efficiency.

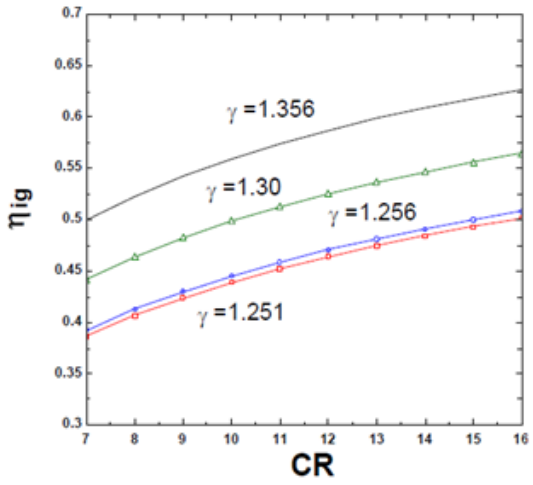

Figure 1.3: The impact of γ and compression ratio on cycle efficiency [28].

1.1.4.3 Low Temperatures, Low Heat Transfer

Reduced heat loss remains an additional benefit of HCCI. The lower peak combustion temperatures associated with HCCI's lean burn strategy decreases heat loss to the wall [19]. Preserving more heat in-cylinder helps reduce one of the primary loss mechanism, increasing cycle efficiency.

1.1.4.4 More 'Instantaneous-Like' Combustion

The time-scales required to complete 'real' combustion processes are non-negligible. That's to say, charge mass does not burn instantly. Thus, when compared to idealized thermodynamic cycles (i.e., 'constant-volume' combustion), real engine processes exhibit losses as the combustion process extends to either side of top dead center.

Accordingly, a more rapid burn (such as that realized during HCCI combustion) helps to counteract these time-based losses. However, considerations including excessive pressure-rise and audible engine 'ringing' place practical limitations on the acceptable range of burn duration.

1.1.4.5 Emission Considerations

In addition to favorable thermodynamic attributes, HCCI also exhibits 'trace' levels of engine-out emissions relative to spark-ignited gasoline and compression-ignited diesel combustion modes. Homogeneous charge mixture avoids the particulate formation associated with rich mixtures.

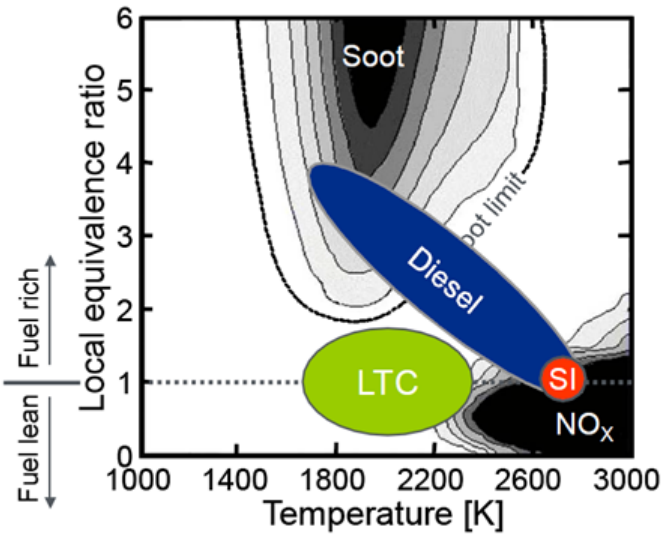

Figure 1.4: Combustion modes and the $NO_X - Soot$ "Trade Off". Homgeneous mixture preparation and low in-cylinder temperatures help postion HCCI in the emissions "sweet spot" [52]

.

In addition, HCCI's lean air-to-fuel ratio ensures lower peak combustion temperatures, avoiding the threshold required for NO_X formation.

This emissions 'Sweet Spot' is conceptualized by [52] in Fig.1.4.

1.1.5 HCCI:Implementation Challenges and Combustion Inefficiency

The efficiency and emissions benefits outlined in the preceding section ensure that HCCI has a 'place at the table' when considering future combustion concepts. However, significant challenges remain, particularly with respect to practical implementation. The vast majority of these challenges are attributed to two key characteristics of the HCCI Engine: limited operational range and non-optimal combustion efficiency. As will be established in later chapters, in-cylinder temperatures are a key 'driver' for both of these metrics.

1.1.5.1 Operational Limitations and Relative Efficiency Gains - A Vehicle Level Perspective

To better demonstrate the operational limits of a gasoline-fueled HCCI engine, vehicle-level performance is evaluated. This analysis considers a 'multi-mode' engine scenario, where the load and

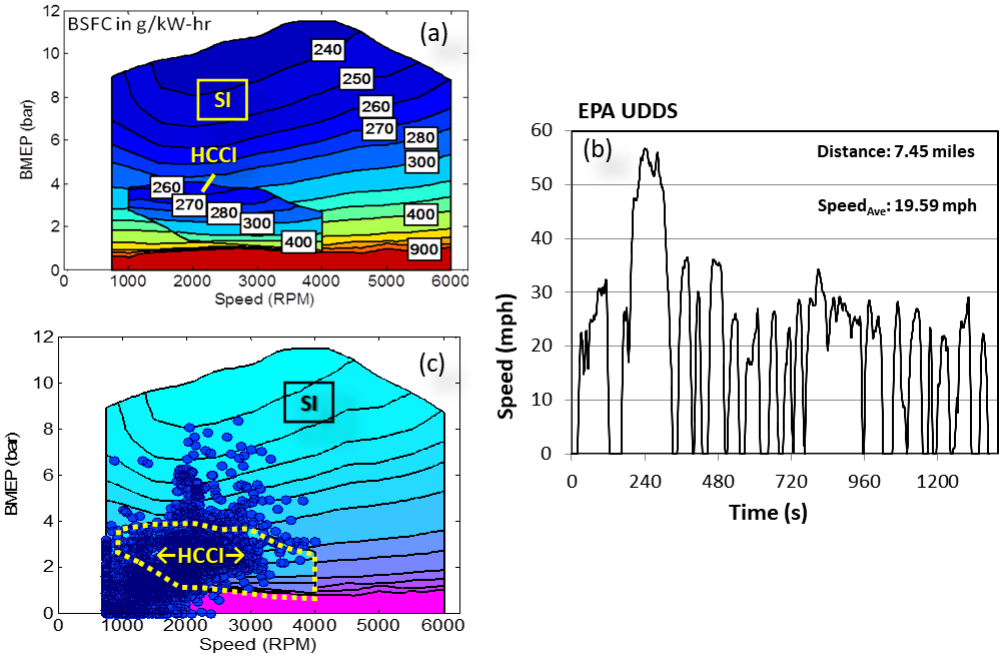

Figure 1.5: Investigation of a multimode engine concept (SI/HCCI) evaluated over an urban drive cycle [60]. Although limited, the HCCI operational range exhibits significant efficiency gains.

speed points from a given drive cycle (EPA UDDS, see Fig.1.5b) populate the corresponding engine map (Fig.1.5c). In light of the discussions of the preceding section, note the considerable efficiency gains in the 'shared operational zone' shown in the brake-specific-fuel-consumption plot(BSFC) of Fig.1.5a. This plot captures the vehicle-level manifestation of the fundamental thermodynamic benefits discussed in Sec.1.1.4. Furthermore, a 'traditional' SI engine operates with considerable throttle restriction over the shared load/speed range. The pumping losses which accompany the SI engine in this operational regime are completely absent in the HCCI engine - a consequence of this engine platform's unthrottled operation.

A final comment regarding Fig.1.5. Despite HCCI's limited operational range, a considerable number of the 'UDDS' speed/load coordinates fall into the HCCI zone. Further extension of the low-load/low-speed operational boundary toward 'idle-like' conditions would net even greater efficiency gains. (In a practical sense, an expanded operational range would also lessen the control burden associated with mode-switching within a multi-mode engine). The work contained within this documentation largely explores the thermal conditions necessary to extend HCCI's low-load operational range.

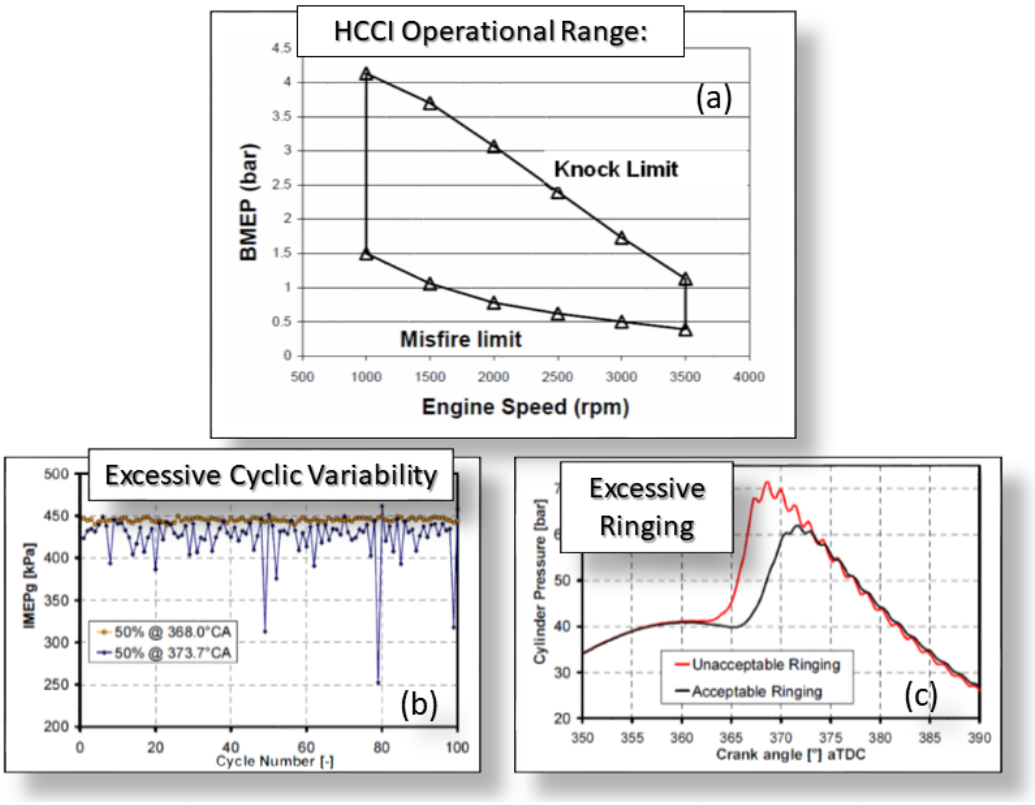

Figure 1.6: A coser look at mechisms limiting HCCI's operation. A representative operational zone is provided in (a) [47]. Subplots (b) and (c) examine engine behavior associated with the respective low-load/high-load operational boundaries [84]. As discussed in the main text, charge temperature underlies behavior at both extremes.

1.1.5.2 A Closer Look at Engine Performance at the Operational Limits of HCCI

To better understand the physical mechanism(s) which define the operational limits of HCCI (recall Fig.1.5a), a closer look at engine-level attributes are warranted. Here, cylinder pressure histories and cycle statistics will be examined. In-cylinder thermal conditions will be discussed as the primary mechanism defining both the high-load (ringing intensity) and low-load (misfire limit) operational boundary.

Figure 1.6 provides a more fundamental perspective on the operational limitations of HCCI. The familiar HCCI range is again plotted relative to engine load/speed in Fig1.6a. The behavior which defines low-load operation is shown in Fig.1.6. Here, indicated mean effective pressure (IMEP) is plotted for 100 consecutive cycles. Two cases are considered, one where combustion phasing (as determined by the %50 burn location, i.e., MFB_{50}) is positioned at $8^{o}aTDC$ and another where

MFB_{50} is positioned at 13^oaTDC. Phasing of the combustion event is determined by the intake air temperature - a clear demonstration of HCCI's sensitivity to thermal conditions.

First considering the case where combustion exhibits a more optimal phasing (8^oaTDC), cycle-to-cycle variation in IMEP is minimal. This trend is indicative of robust engine operation, and conceptually occupies the 'inner-most' region of the regimes shown in Fig.'s1.5 and 1.6. In contrast, as the intake temperature is decreased, and combustion is phased away from a more optimal timing, significant variation in cycle-to-cycle performance is demonstrated. At the engine-level, this manifests as extremely 'rough' operation, and is the result of incomplete oxidation (or total misfire in extreme cases) of the trapped charge. Emission would likely exhibit evidence of incomplete oxidation reactions (unburned-hydrocarbons, carbon monoxide, etc.) - all of which are undesirable regardless of engine platform or combustion mode. As mentioned, temperature is the primary distinction between the stable/misfiring combustion regimes. This connection, and its implications, will be developed in much greater detail, in the following sections. For now, we will consider excessive cyclic variation in IMEP as defining the lower operation bound in Figs.1.5a and 1.6a.

Shifting focus to Figure 1.6c, we examine the behavior of cylinder pressure over combustion-relevant crank angles. Again, two seperate cases are considered - where intake temperature determines the relative phasing. As temperature of the trapped charge increases, the ignition delay of the charge decreases. (Recall, HCCI is a combustion mode which relies entirely on the thermo-kinectic mechanisms underlying the autoignition event. Combustion, is almost entirely determined by in-cylinder pressure/temperature histories.) Thus, for higher temperatures, the phasing of HCCI combustion is advanced and the burn duration is decreased. This behavior manifests at the engine level as high frequency 'ringing' within the pressure trace - see the red-colored profile in Fig.1.6c. Mild ringing is often described in-terms of undesirable acoustic characteristic - i.e., "Why does my gasoline engine sound like a diesel?" - while excessive ringing can transition into knocking and case severe mechanical damage to engine components within the combustion chamber. Thus, metrics such as 'ringing intensity' define the upper bound of the HCCI operational range. Again, this limiting behavior is directly influenced by the thermal history of the in-cylinder content.

Finally, in an effort to further establish charge temperature as a primary influence on both cyclic variability and ringing intensity, the reader is directed to Fig.1.7. The 50% burn location is again manipulated by altering the intake temperature - where higher temperatures result in advanced

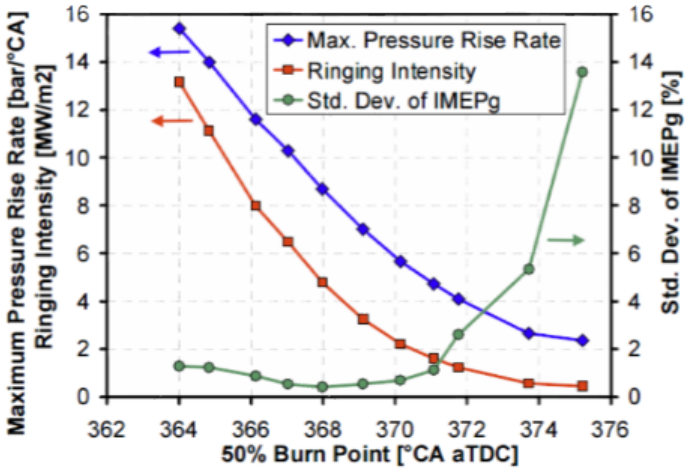

Figure 1.7: Too hot, too cold... Charge temperature largely determines the operational characteristcis of the HCCI engine. Adapted from [84].

phasing and lower temperatures retard combustion. As temperature increases, phasing advances toward TDC (i.e., 360^o) increasing both ringing intensity and pressure rise rate (left axis). Likewise, cooler temperatures retard combustion, eventually leading to excessive cycle-to-cycle variability (right axis), decreased combustion efficiency, and increased hydrocarbon and CO emissions.

1.2 Heat Transfer at the Gas-Wall Boundary and its Effect on HCCI

Flow fields and temperatures in the cylinder critically depend on the features of the intake process. However, after the valves close, thermal conditions at the gas-wall interface influence much of the transport and mixing phenomena associated with in-cylinder processes. The dynamic evolution and structural behavior of the velocity and thermal boundary layers in the vicinity of exposed combustion chamber surfaces are quite complex and remain poorly understood [2, 11, 33, 32, 93, 50]. As will be shown, a process involving heat loss at the wall and turbulent entrainment of resulting 'cool' structures into the bulk gas has a dramatic impact on the thermal composition of the interior charge. As a result, this in-homogeneity, or "stratification" of in-cylinder contents has an immediate impact on autoignition, cycle efficiencies, and emission formation.

As will be shown, thermal stratification of in-cylinder contents is largely determined by the

turbulent transport of 'cool' wall-derived structures into interior region(s) of the trapped mass. Yet, popular treatment of engine transport processes commonly rely on physical assumptions directly opposed to such complex near-wall phenomena [14, 63, 69, 82].

This section will highlight insight and analysis from previous efforts which more accurately characterize in-cylinder heat loss and transport processes. Efforts to better understand the physical processes at the gas-wall interface remain the focus of this section. Particular attention will be given to insight and observations relevant to the HCCI environment.

1.2.1 Turbulent Transport and the Thermal Stratification of Trapped Mass

The turbulent entrainment of 'cool' wall-derived structures is the primary physical mechanism responsible for the thermal stratification of in-cylinder contents. The link between the resulting temperature non-uniformity and the 'cascade' of autoignition events which characterize HCCI was recognized in the pioneering work of [84]. A conceptual model detailing the interplay between localized charge temperature and autoignition sites is provided in Fig.1.8.

Figure 1.8 shows a non-uniform temperature field, where spatial variation in temperature contributes to localized 'hot' and 'cold' zones. A 'critical ignition temperature' is defined relative to the generalized field. (This theoretical threshold represents the thermal condition(s) at which autoignition reactions commence). As the the piston moves toward top-dead-center (over the time interval $t = 0$ to $t = 1$), the temperature of the trapped charge elevates in response to compression heating. During compression, localized 'hot zones' exceed the aforementioned ignition temperature and autoignite, releasing heat. The final sequence of temperature traces in Fig.1.8 corresponds to $t = 2$. (Note: This time is not explicitly labeled in the figure). Here, compression heating continues to elevate charge temperature, while locations in the vicinity of ignition sights from the previous time-step experience additional increase in the localized temperature. This process continues over the duration of the burn.

The degree to which spatial irregularities exist in the temperature field largely characterize the HCCI combustion process. Simply put, given a single-valued temperature field (and a homogeneous mixture composition), the entire charge would ignite at once - resulting in excessive ringing intensity and pressure-rise-rates. In reality, thermal stratification within the cylinder results in a

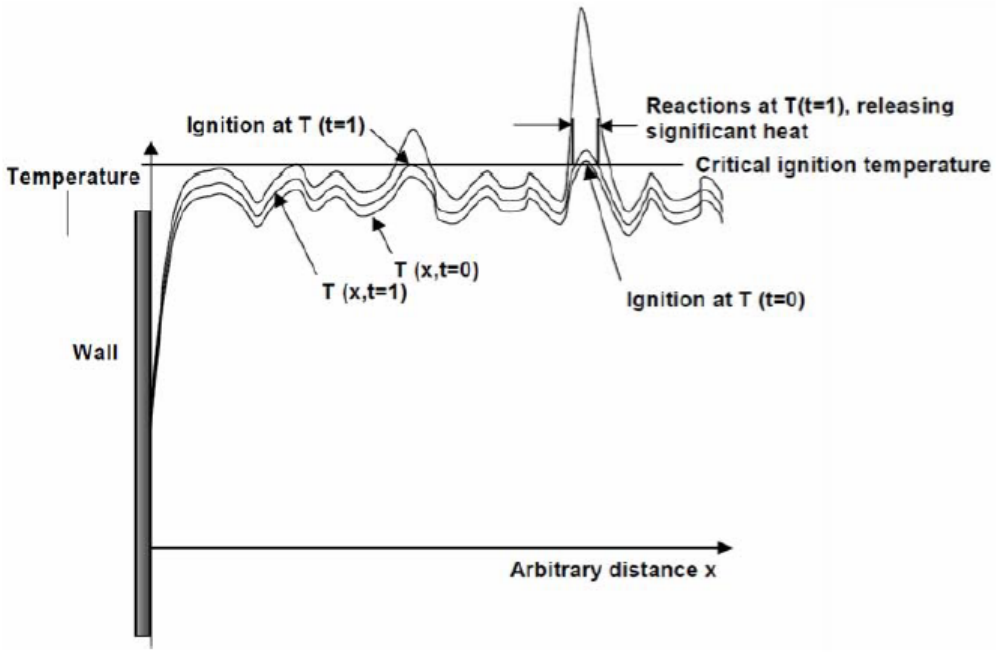

Figure 1.8: Early conceptual model of the HCCI combustion process [74]. A non-uniform temperature field [46]

.

'cascade' of localized autoignition sites, helping to 'smooth' heat release rates while limiting ringing intensity to moderate levels. Furthermore, excessively cool temperature zones, which fail to reach the 'Critical Ignition Temperature', will not ignite. This is analogous to a localized misfire, and contributes to increased amounts UBHC and CO in the exhaust and decreased combustion efficiency. Beyond emissions and efficiency considerations, in-cylinder thermal stratification ultimately determines the phasing, duration, and stability of the combustion event.

Moving away from the conceptual treatment of in-cylinder temperatures, a sequence of images from an optically accessible engine is considered in Fig.1.9. Here, planar laser induced florescence (PLIF) is used to visualize the evolution of in-cylinder temperatures during closed-cycle operation (compression and ignition). It should be noted that images in Fig.1.9 correspond to a non-reacting motored cycle, where nitrogen is compressed and re-expanded in the absence of chemical reactivity. As a consequence, the evolution of in-cylinder temperature is solely determined by geometric compression and heat loss at the wall.

A more nuanced inspection of Fig.1.9 offers dramatic insight into the complex nature of the heat loss and transport processes. To begin, a fresh charge (of non-reactive N_2) is inducted during

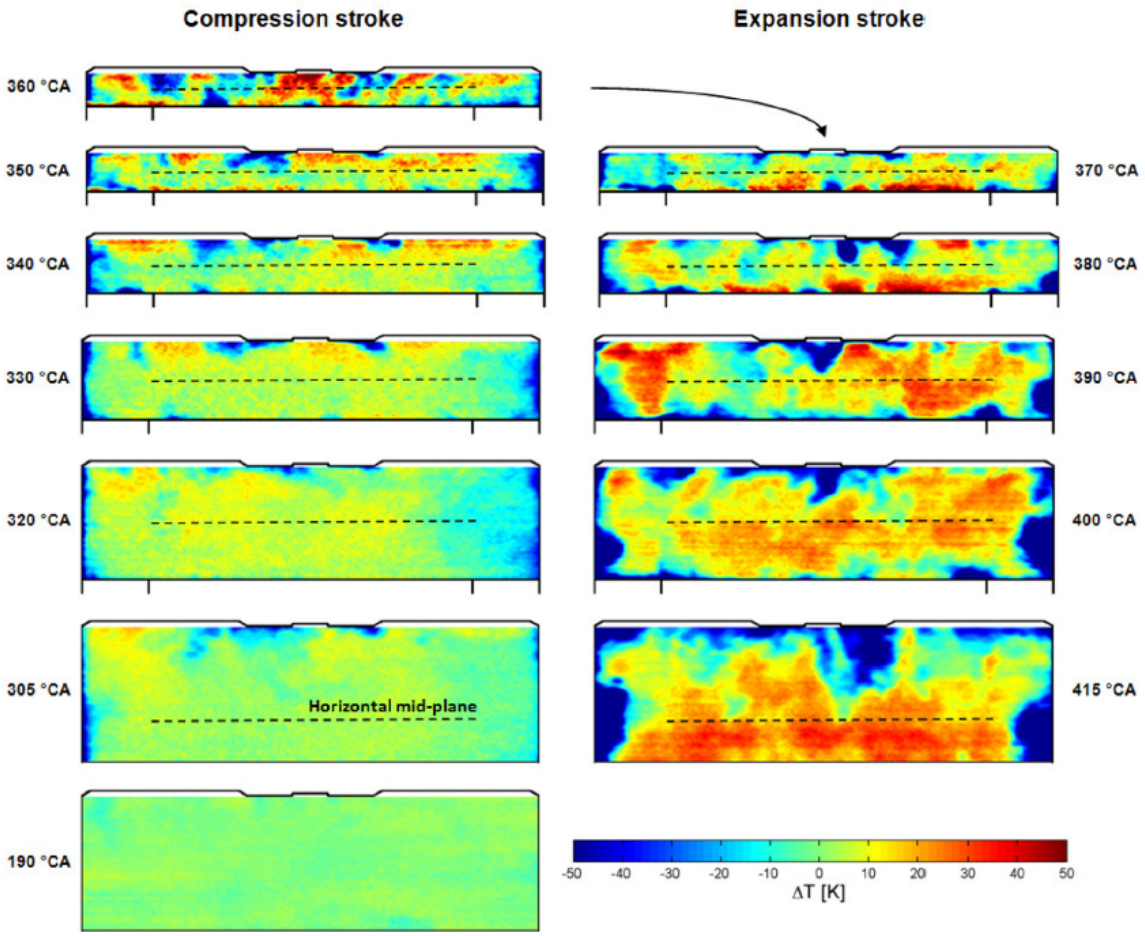

Figure 1.9: CAD-resolved PLIF images capturing the turbulent entrainment of 'cool' wall-derived eddies within the hotter interior region of the trapped charge [24].

the intake process. As shown in the first image of the PLIF sequence, the temperature at the onset of compression is quite uniform (see legend at lower-right for normalized temperature range). As the piston compresses the charge towards TDC, 'cool' zones begin to emerge in the regions closest to the combustion chamber surfaces - the result of heat exchange between 'cool' exposed surfaces and the hotter compressed gas. (Note: Thermal conditions at the gas-wall interface largely determine the extend to which heat is exchanged (i.e., 'lost') in the near-wall region. Elevated surface temperatures would limit heat flow relative to cooler wall temperatures. As a result, increased wall temperatures can be employed to preserve more heat in-cylinder, elevating over-all charge temperatures. This effort represent a primary focus of the work contained within this dissertation.)

Continuing anlysis of Fig.1.9, the coherent 'cool' structures begin to separate from the near-wall regions in response to adverse pressure gradients and turbulent flow dynamics [50]. This entrainment process, combined with decreasing in-cylinder volume, results in significant non-uniformity of the temperature field over the crank angles in the vicinity of 360^o. After TDC the piston motion reverses, resulting in flow reversal which further separates 'cool' zones from the near-wall region.

In general, the complex reality of the physical transport and heat transfer processes captured in Fig.1.9 result in a high degree of 'natural' thermal stratification. As discussed in the preceding sections, the localized characteristics of the temperature field are of critical importance to gasoline compression ignition concepts such as HCCI. Insufficient thermal 'availability' within the coolest eddies prevents such zones from satisfying the thermal conditions required for autoignition. As a consequence, it is the zones with the lowest in-cylinder temperatures which contribute to unburned hydrocarbons, decreased combustion efficiency, and increase exhaust components associated with incomplete fuel oxidation (CO). In the extreme, these cool zones can increase cycle-to-cycle variability beyond acceptable limits due to unstable combustion and/or misfire.

Together, the insight from the conceptual treatment presented in Fig.1.8 and the experimental analysis of Fig.1.9 make clear the importance of thermal conditions at the gas-wall interface. It is the exchange of heat at this interface, combined with the turbulent flow field, which determines the evolution of the flow field during the compression and expansion processes. It is not an unreasonable leap in imagination to consider the manipulation of wall temperature as a means to influence the in-cylinder temperature distribution.

1.3 Manipulating In-cylinder Wall Temperature

This sections serves as part historical overview and part path forward. To begin, key results from previous efforts to manipulate engine heat transfer are reviewed. These efforts include the use of thermal barrier coatings and monolithic ceramic inserts to impact heat loss at the wall. Highlisghts, and 'lessons learned' from this work will help conceptualize a modified path forward, where pitfalls of previous efforts are avoided and benefits maximized.

1.3.1 Thermal Barriers and Surface Temperatures

Research efforts examining the impact of thermal barriers and monolithic ceramic inserts on internal combustion engines have been primarily focused on gasoline (SI) and diesel (CI) applications [73, 13, 5, 30, 53, 49, 42, 39, 96, 6, 54, 5, 27, 92, 29]. In addition, the coatings employed by these studies are generally classified as 'thick' - typically on the order of 500-1000μm [53]. Given the timescales defined by engine speeds, combustion events, and heat transfer configurations, such 'thick' coatings tend to increase the engine's effective heat capacity and thermal inertia. As will be discussed in detail, the aforementioned increase in heat storage has a profound impact on in-cylinder thermal-fluid conditions at the gas-wall interface.

An extreme, and from today's perspective physically questionable, objective of some early efforts was the realization of the "Adiabatic Engine". Efforts in pursuit of this idea attempted to minimize (if not entirely eliminate) heat loss to coolant. Two main camps emerged, each focusing on dramatically different targets. Researchers in the first camp were targeting 1^{st} Law 'thermodynamic enhancements' - where heat retained in-cylinder would manifest as additional work at the piston. Alternatively, (and perhaps more justified), the efforts of the second camp focused on reducing the burden placed upon cooling systems within heavy-duty diesel platforms. In general, knock considerations limited experimental analysis to conventional compression ignition concepts (i.e., Diesel).

Figure 1.10 demonstrates representative outcomes of the aforementioned developmental targets. Both groups pursued adiabatic engine architectures through application of thick thermal barrier coatings in conjunction with complete monolithic inserts. Isuzu effort's focused on passenger car implimentation [73], while Cummins focused on heavy duty applications [13]. Detailed analysis of these efforts can be found in the referenced literature, a concise overview of the main outcomes is

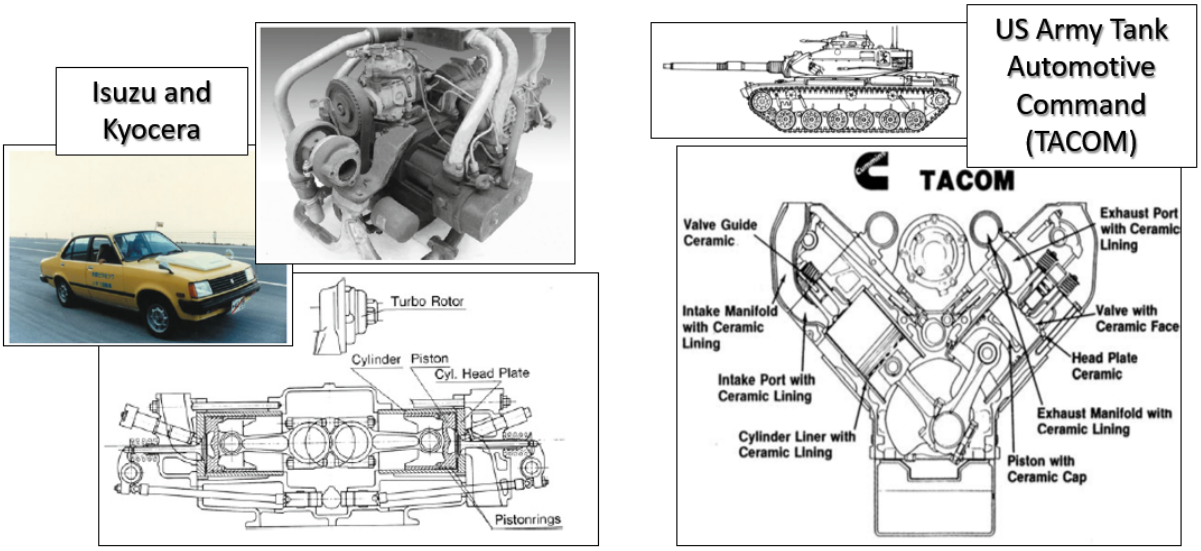

Figure 1.10: Early attempts to realize an adiabatic engine included indpendent efforts by Isuzu and Cummins. [73, 13]

provided below.

In general, the specific coating materials utilized in the above studies elevated surface temperatures over the entire cycle. Any work gains (due to decreased heat loss) where quickly erased by charge heating effects, where elevated open-cycle temperatures heat incoming charge, decreasing charge density (ρ_{Charge}) and volumetric efficiency (η_{Vol}).

The higher temperatures of the (unintentionally) 'pre-heated' charge negatively impact key thermophysical properties - most notably the ratio of specific heats (γ). (recall, this parameter has an immediate effect on cycle efficiency - see Eq.1.1.) Elevated charge temperature in the oxygen rich diesel environment also supports increased NO_x production, placing a greater burden on aftertreatment systems.

Finally, reduced heat loss did not lead to increased work at the piston. Rather, it simply increased the temperatures of the combustion products, with the heat eventually escaping the cylinder as increased enthalpy within the exhaust gas. The increased enthalpy at the end of the expansion stroke (i.e., elevated T_{Exh}) requires additional "downstream" efforts to re-capture energy in a 'usable' form. This necessitates increased system complexity in the form of turbocharging, turbo-compounding, waste heat recovery, bottoming cycles, etc.

1.3.2 Conceptual Development of an 'Ideal' TBC

Given the insight of prior experimental efforts investigating the effect of insulating ceramic coatings, it is clear that a different approach is needed, one aimed specifically at reducing heat loss when it matters the most, rather application of "brute force" insulation. This leads to the logical question of how an idealized TBC should perform within the engine environment? In a qualitative sense, this thought experiment may well result in the conceptualization of a 'dynamic' coating, one which enables coating surface temperatures to closely track the bulk gas temperature over the engine cycle. In this way, the temperature differential driving heat transfer at the gas-wall interface is minimized and expansion work is increased. This type of dynamic surface temperature swing would minimize heat loss during compression and expansion while also avoiding charge heating during the intake process. This conceptual exploration has recently been explored for spark-ignited gasoline engine application in [30].

This analysis may be extended to explore the thermophysical/morphological characteristics necessary to achieve a dynamic coating surface temperature. In general, 'thin' coatings utilizing low conductivity materials can be expected to avoid heat retention (and the associated charge heating) while increasing the peak magnitude of the dynamic surface temperature profile, i.e. temperature 'swing', thus reducing the temperature differential. Furthermore, surface characteristics such as roughness and/or exposed porosity should also be expected to influence both flow dynamics and heat exchange.

In short, material selection is likely to have a profound influence on coating performance. Therefore, thorough development of an 'ideal' TBC must include fundamental exploration of coating morphology and thermophysical properties, enabling correlation between these attributes, observed surface temperature response, and ultimately engine performance and efficiencies.

1.4 Thin Coatings and Surface Temperature "Swing"

Prior attempts to actively manage in-cylinder surface temperatures have included the use of relatively 'thin' ceramic layers. These efforts typically make use of TBCs on the order of hundreds, rather than thousands of microns [5] [56]. The influence of material selection (relative to thermophysical properties), and the related impact on thermal conditions at the surface was explored. These authors also provide some of the earliest experimental evidence of the surface temperature

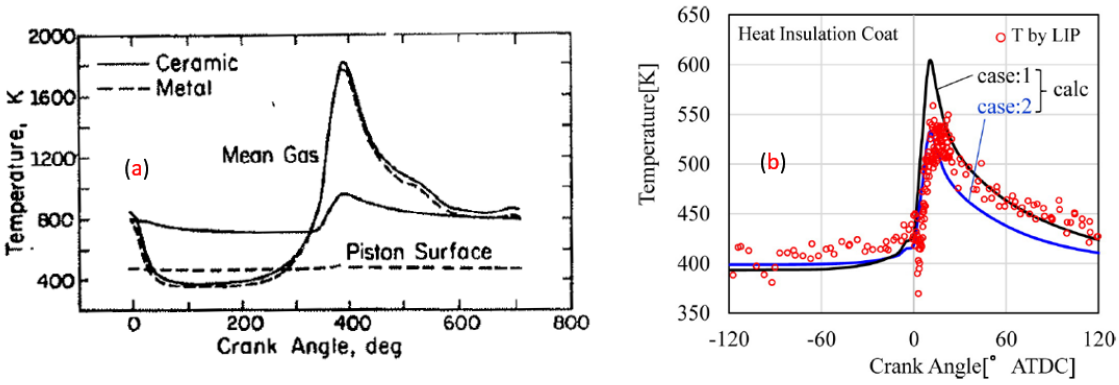

Figure 1.11: Comparison of TBC surface temperature Profiles. [5, 30]

'swing' concept, as highlighted in Fig. 1.11.

Despite efficient power generation and low emission production, HCCI's wide-spread implementation is restricted by its limited operational range. These limits are largely determined by fundamental thermal-fluid processes and their associated impact on the chemical-kinetics driving autoignition - with excessive pressure rise rates defining the high-load threshold and insufficient thermal availability establishing the ignitability limit.

This section will motivate fundamental questions pertaining to optimal TBC 'performance' while identifying potential synergies between TBC's and HCCI. Finally, in an attempt to better understand the physical mechanisms governing the in-cylinder environment, a thorough examination of the underlying physics pertaining to energy and mass transfer will be proposed.

1.4.1 Potential Synergies between TBCs and HCCI

The critical inquiry of the preceding section may be extended to examine potential synergies between TBC application and HCCI performance. Simply put, the deliberate (selective) manipulation of combustion chamber surface temperature (via TBCs) is likely to have a significant impact on HCCI combustion, emission formation, and over-all engine cycle performance. One could reasonably expect the previously described surface temperature swing to preserve more thermal energy in-cylinder during compression/combustion/expansion. Given the sensitivity of HCCI autoignition to closed-cycle thermal conditions [85, 83], any influence on charge temperature is likely to impact the combustion event. Specific metrics such as combustion phasing and burn duration can be

monitored to help quantify impacts of TBC on HCCI. Furthermore, retention of thermal energy in-cylinder may well facilitate more robust combustion (as determined by exhaust species concentrations, UBHC, etc.), resulting in increased combustion efficiency. Over-all thermal efficiency will also be increased if losses associated with heat transfer close to TDC are reduced. In all, there may be multiple pathways which together enhance fuel conversion efficiency, and this increases the impetus for investigating TBCs optimized specifically for HCCI engine.

Chapter 2

A Conceptual Exploration of Thermal Barrier Coating Design Space

This section will development a conceptual framework for exploration of the TBC design space. Efforts seek to identify those thermophysical properties and spatial attributes with the largest influence on transient surface temperature behavior. In this way, key parameters will be identified relative to desired TBC behavior under engine-like conditions. Insight garnered from this process will ultimately inform material selection and other critical design parameters during the experimental work presented in subsequent chapters. To begin, behavioral characteristics of an idealized temperature 'swing' profile will be developed.

2.1 Definition of the Temperature Swing Hypothesis

A discussed in the preceding section, surface temperature plays a significant role in the engine heat transfer process. The reader is reminded of the PLIF sequence reported in [24], where heat loss (driven by the gas/wall temperature differential) directly contributes to stratification of the in-cylinder temperature field.

It follows, that a targeted increase in surface temperature over the closed portion of the

engine cycle would reduce the aforementioned temperature differential, ultimately limiting heat loss. Reducing heat loss close to TDC has the highest value, because it will directly lead to increased expansion work, and consequently higher thermal efficiency. In the context of HCCI, reduced heat loss enhances both thermal efficiency and combustion efficiency. Again, recall the discussion(s) of the introductory chapter, where excessively 'cool' zones are shown to impede (or prevent) the complete oxidation of the in-cylinder charge.

Thus, removing the reality of any 'hard' physical constraints, the sequence displayed in Fig2.2 will develop a characteristic framework which describes an idealized TBC surface temperature profile. To further distinguish any 'new' thinking from the ideas of past efforts, profiles representing representative metal and 'thick TBC' profiles will be reviewed.

To begin, Fig.2.2a provides a characteristic temperature trace for the bulk combustion gas and surface temperature profiles. Individual strokes of the engine cycle are also identified. In general, the greatest difference between bulk gas and surface temperature occurs during the closed portion of the cycle, when heat released during combustion (combined with compression heating) rapidly elevate the charge temperature. For conventional engine configurations (i.e., engine platforms with metal surfaces), the combustion-induced surface temperature transient is minimal relative to the peak gas temperature. Thus, the large temperature differential (i.e., ΔT) contributes to increased heat loss. Furthermore, during gas exchange - and the intake process specifically - the charge temperature returns to values approximating on the order of those associated with the metal surface. This is of practical importance, as elevated surface temperature during intake contribute to charge heating, decreasing power density and volumetric efficiency [13].

Figure 2.2b captures the qualitative behavior of a 'thick' thermal barrier coating. This approach approximates the coating material associated with historical attempts to manipulate thermal conditions at the gas-wall boundary, including efforts to realize 'adiabatic' engines [73, 13]. The coating temperature profile is elevated over the duration of the cycle. This is primarily due to the coating insulating properties and the increased 'thermal mass' associated with the relatively thick coatings and monolithic inserts inherent to the traditional adiabatic approach. As a result, the temperature differential during closed-cycle operation is greatly reduced relative to the metal engine configuration. However, the 'thick' TBC material fails to shed heat over the engine time-scale. This results in engine temperatures which remain elevated over the crank angles spanning gas exchange. As discussed above, these elevated surface temperatures heat incoming air, decrease charge density,

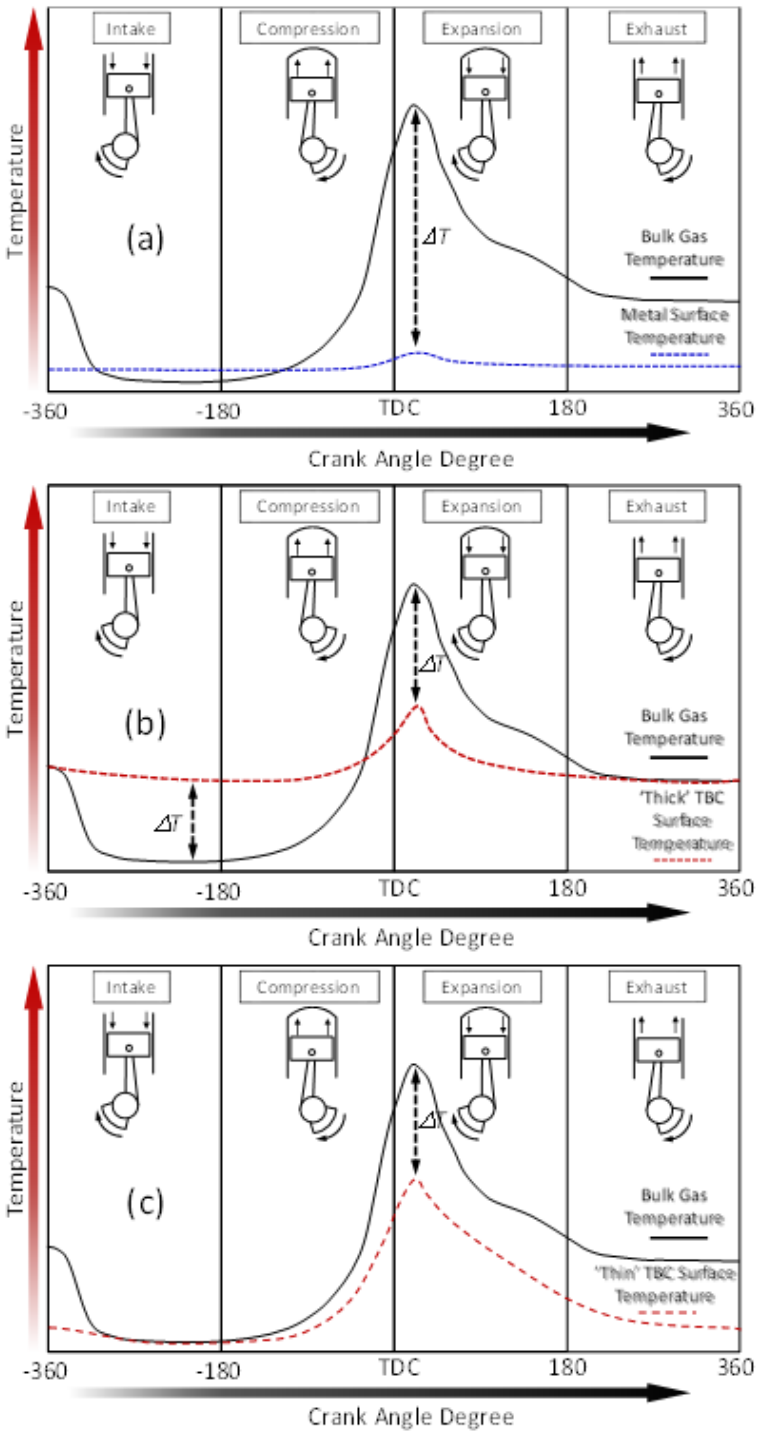

Figure 2.1: Conceptual exploration of various engine configurations. The temperature profiles in (a) represent a metal engine configuration, (b) a 'thick/monolithic' coating configuration, and (c) a 'thin' TBC layer which enables the desired temperature 'swing' behavior.

and negatively impact volumetric efficiency. Most of teh heat retained in the cylinder escapes with during teh exhaust process.

Finally, a the most favorable characteristics of Fig.'s2.2a- 2.2b are incorporated into Fig.2.2v. Here the behavior of a thin, low-conductivity TBC is conceptualized. The limited thermal mass ('thin') and low volumetric heat capacity of the hypothetical coating enable the TBC layer to respond quickly to surface heating/cooling events. In this way, the minimal thickness, reduced conductivity, and limited heat capacity of the swing coating enable surface temperatures to rise quickly during combustion, while also enabling temperatures to return to acceptable levels during the intake process. The ability to 'mimic' bulk gas temperature over the engine cycle allows the engine greatly reduce the gas/wall temperature differential (i.e., ΔT) during combustion, while avoiding the charge heating penalties accompanying increased surface temperatures.

In the context of HCCI, reduced closed-cycle heat loss will facilitate more complete combustion of the in-cylinder contents (helping to address the combustion inefficiency associated with this combustion mode). Recall the role of surface temperature relative to gas-wall heat exchange and the subsequent impact on thermal stratification outlined in the introductory chapter.

A more systematic exploration of parameters, with particular regard to the aforementioned temperature swing behavior is explored in detail in the following section.

2.2 Modeling the Heat Transfer System

To better understand the physical mechanism(s) controlling thermal conditions at the TBC surface, a simplified model of thermophysical system is introduced. In particular, a reduced-dimension (1D) finite difference model is introduced in Fig.2.2.

The simplified heat transfer arrangement detailed in Fig.2.2 is formalized mathematically using the following equation group:

$$\frac{\partial}{\partial x}(k\frac{\partial T}{\partial x}) = \rho c\frac{\partial T}{\partial t}; 0 < x < L \tag{2.1}$$

$$T(x,0) = T_o(x) \tag{2.2}$$

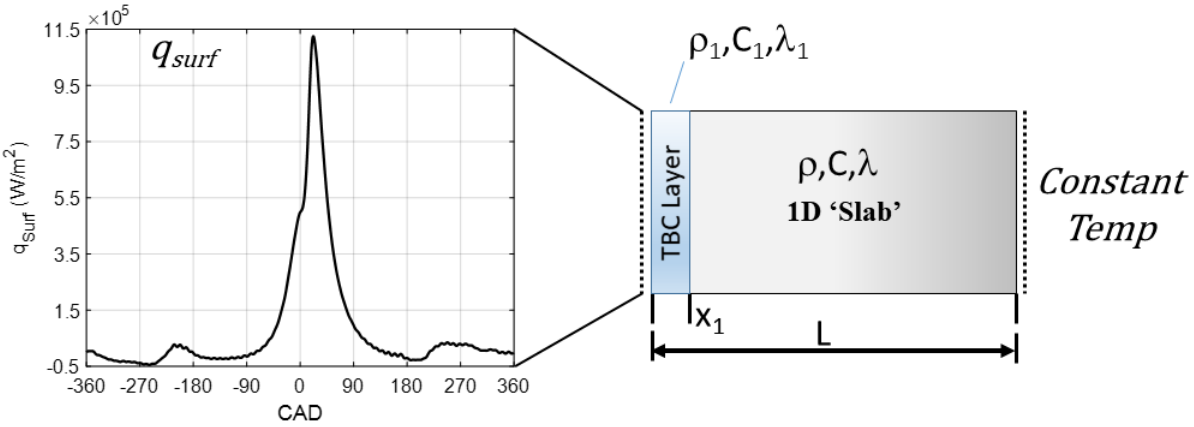

Figure 2.2: A schematic representation of the finite difference model. One-dimensional planar geometry is assumed, where material properties of the underlying substrate are representative of 304 stainless steel alloy (i.e., $\rho, C, and \lambda$) with a total length of 4mm. The surface TBC layer represents the main degree of freedom, where parameters including: layer thickness (x_1), volumetric heat capacity $|rhoC_p$, and thermal conductivity are (λ) can be explored as independent inputs.

$$-k\frac{\partial T}{\partial x} = q_{Surf,Exp} \tag{2.3}$$

$$T(L,t) = T_o \tag{2.4}$$

Equation 2.1 describes the governing heat diffusion model given the reduced dimensionality of the system of interest. A generalized initial temperature distribution (to be discussion later) is referenced in Eq.5.3. Front and backside boundary conditions are defined by Eq.'s5.4 and 5.5, respectively.

Some comments regarding the specific form of the frontside boundary condition (shown in Fig.2.2 and referenced in Eq.5.4) are warranted. To ensure engine-relevant results, an experimentally-derived surface heat flux profile is used as the front-side boundary condition. The measured profile is derived from high-fidelity in-cylinder temperature measurements, and represents surface heat flux under robust operational conditions.

The back-side boundary condition corresponds to a fixed temperature T_o, and also references an experimentally derived condition.

In the following analysis, the governing heat diffusion equation (i.e., Eq.2.1) is discretized

and solved numerically. Full details of this effort, including detailed treatment of the numerical solver are handled in subsequent chapters.

For now, the system is initialized using a uniform temperature (T_o), and the periodic frontside boundary condition is applied at $t = 1$. The cycle simulation repeats until a quasi-steady-state temperature distribution is realized - typically requiring 500 total cycles simulation. Results are recorded for the specific parametric group (i.e., engine speed, TBC thickness, volumetric heat capacity, and thermal conductivity), and the process begins again using slightly different parametric values. The aforementioned thermophysical parameters are varied systematically across physically-relevant values and the results are collected below.

2.3 Detailed Analysis of Modeling Outcomes

In general, the conceptual exploration of the thermophysical 'parameter space' is motivated by two considerations: i)evaluation of the temperature 'swing' concept (i.e., 'Is it feasible?'), and ii) guidance towards selection of optimal coating parameters. With these goals in mind, results of the aforementioned modeling efforts will be evaluated in teh following section.

The first collection of simulated surface temperature profiles are plotted in Fig.2.3. This initial results are limited to the 1200rpm operational point.

Analysis begins with Fig.2.3a. As an initial assessment of coating behavior (over a range of TBC-relevant parameters), the surface temperature profiles under engine relevant conditions begin to exhibit 'swing-like' behavior. This is quite encouraging, and warrants a few targeted comments. First, a clear trend emerges relative to volumetric heat capacity - coatings with lower ρC_P values achieve higher magnitude temperature swing. This includes higher peak temperatures over combuston-relevant crank angles and 'cooler' minimal temperatures during gas exchange. In the framework of the conceptual model, this remains an important feature as the gas-to-wall temperature differential decreases during combustion/expansion while elevated surface temperatures return to 'metal-like' values during gas exchange. Total peak-to-peak swing magnitude is on the order of 50^oC for the given parameters (1200rpm, $150\mu m$, and 1W/mK). It should be noted that the prescribed conductivity value for these cases approximates many commonplace TBC formulations [51, 48, 12], including the Yittria Stabilzed Zirconia (YSZ) material detailed in later chapters.

Shifting focus to Fig.2.3b, parametric values within the design space remain fixed with the

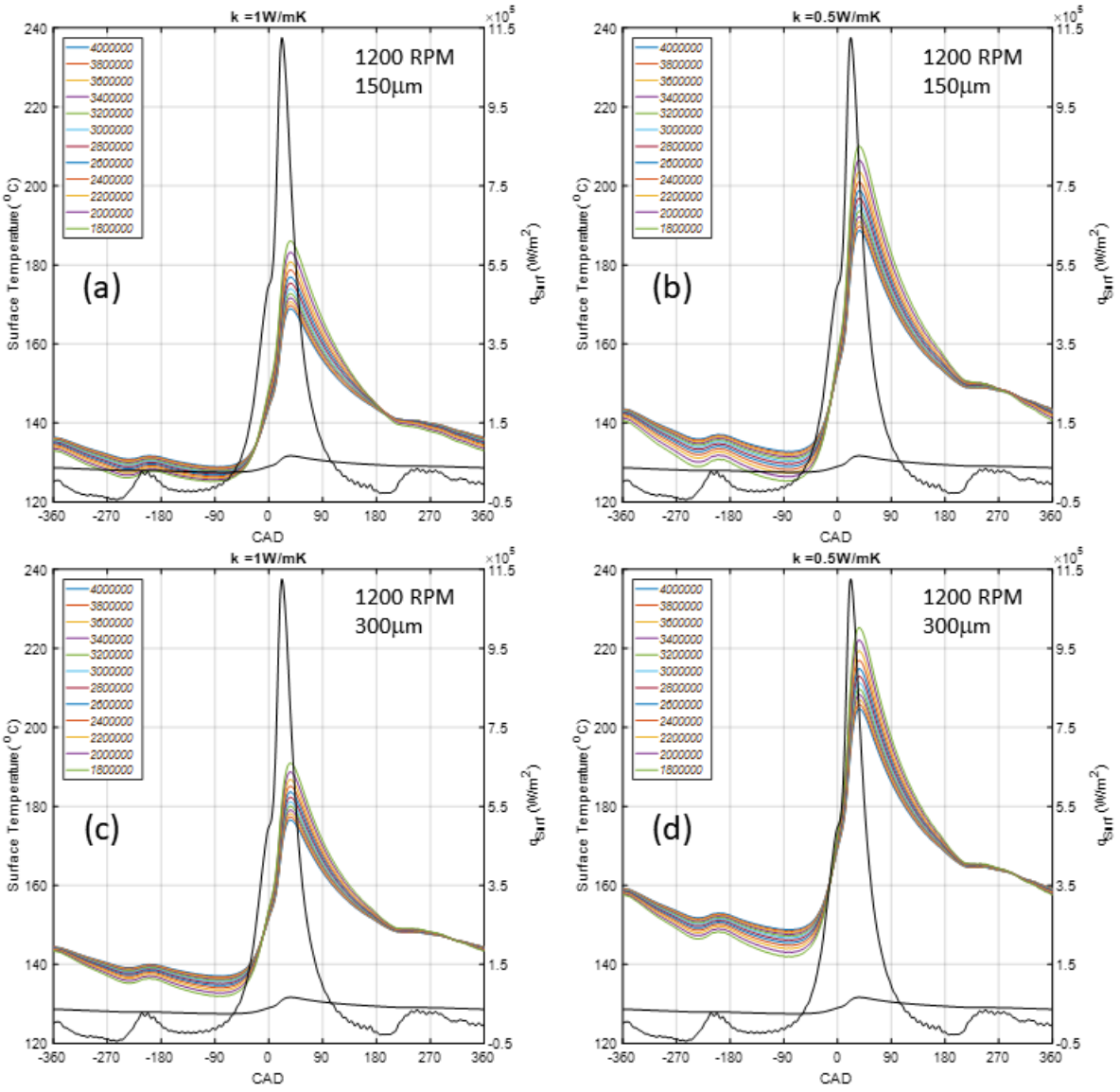

Figure 2.3: At 1200rpm, 12 separate coatings are considered - each having a unique volumetric heat capacity (ρC_p in (J/K)). The individual ρC_p values are provided in the upper right quadrant. The corresponding metal surface temperate (measured) is shown in black, with the associated heat flux trace plotted on the right-hand axis. Engine speed and coating thickness are noted in the upper right quadrant.

notable exception of thermal conductivity. In this sequence, conductivity is reduced by half to a values of $.5W/mK$. This low value is consistent with 'ultra-low conductivity' materials, including the gadolinium zirconate material explored in detail in later chapters [65, 61, 94]. As a consequence of the reduced conductivity, the magnitude of peak-to-peak temperature swing increases to values approximately equal to 70^oC. Despite absolute increases in surface temperature around TDC, these low-k coatings still manage to rapidly shed heat during the intake process, ultimately reaching temperatures which are consistent with the values reported for the metal engine configuration.

Next, a similar sequence of coating surface temperature profiles are considered in Fig.2.3c. In this case, all parameters remain the same with the exception of coating thickness, which is doubled to 300 μm. This 'physical' addition of coating material introduces more heat storage (as a result of increased coating mass). As a result, the additional heat storage elevates mean temperatures over the engine-relevant timescale (1200rpm). On one hand, this bulk shift helps to further reduce the wall-to-gas temperature differential during late-expansion/combustion - which by extension should help reduce heat loss. However, open-cycle temperatures remain elevated relative to the metal engine result. This would likely result in charge heating - reducing both power density and volumetric efficiency. In other words, for the particular parametric values defined in Fig.2.3c, Surface temperature profiles begin to exhibit traits similar to those realized during the aforementioned adiabatic coating efforts. This limiting behavior provides an important 'check' on desired coating thickness.

In the final sequence ('d') of Fig.2.3, thermal conductivity is again halved to $.5W/mK$. Coating thickness remains 300 μm, and the familiar range of volumetric heat capacities are considered. As shown, the modeled TBC surface temperature profiles exhibit an additional bulk shift in temperature over relative to the traces captured in Fig.2.3c.

Given the considerations detailed above, the peak-to-peak temperature span is not explicitly quantified for this case. (In qualitative terms, the decreased thermal conductivity again exceeds the ranges reported for the comparable 1W/mK case.) That said, the considerable increase in open-cycle temperatures relative to the baseline metal performance representative a considerable likelihood of charge heating. Thus, heat loss gains associated with elevated closed-cycle temperatures would likely be 'counteracted' by decreased volumetric efficiency and charge density. These results provide further indication of the limits (relative to coating thickness) at which the conceptualized TBC material fails to realize the swing concept outlined at the onset.

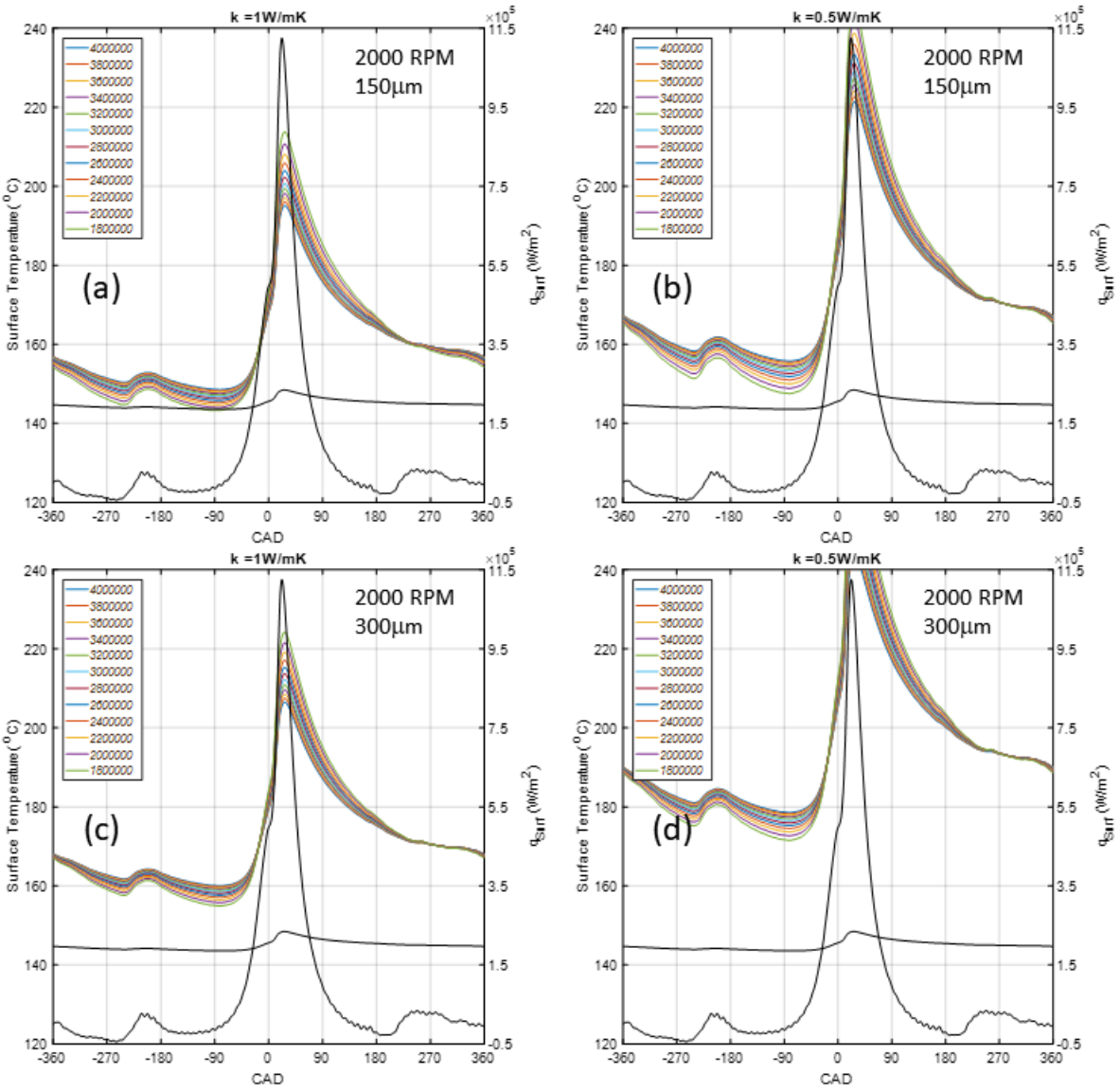

Figure 2.4: Similar to the results of Fig.2.3, 12 separate coatings are considered at 2000rpm for 12 unique volumetric heat capacity (ρC_p in J/K). The individual ρC_p values (J/K) are again provided in the upper right quadrant. The corresponding metal surface temperate (measured) is shown in black, with the associated heat flux trace plotted on the right-hand axis. Engine speed and coating thickness are noted in the upper right quadrant.

To better explore the impact of timescale, the parametric sequences reported in Fig.'s2.3a - 2.3d are re-evaluated for an engine speed corresponding to 2000rpm. These results are reported in Fig.2.4. Coating thickness, thermal conductivity, and volumetric heat capacity are again limited to the ranges explored for the 1200rpm case.

A brief note: To ensure a more direct comparison, the maximum temperature for all plots in this sequence is limited to 240^{o}C. As a result, the extreme case(s) reported in Fig.2.4d are clipped below their respective maximum values.

Qualitative observations (similar to those detailed in Fig.2.3) can be made for the series of temperature profiles reported in the aforementioned figures. That's to say: i) decreased volumetric heat capacity again results in higher max temperatures and lower min temperatures, ii) decreased thermal conductivity increases the peak-to-peak temperature span given fixed parameters, and iii) additional coating mass (associated with increased coating thickness) raises the average surface temperature over the cycle - elevating surface temperatures above those reported for the metal engine.

The most obvious manifestation of the decreased timescale (resulting from increased engine speed) is the case-wide increase in cycle average temperature. It is important to note that the engine temperature profiles - which result from direct measurement of in-cylinder conditions - also experience the aforementioned increase in cycle-average temperatures. This level of agreement between modeled and measured temperature behavior further strengthens the outcomes associated with the 'conceptual model'.

In this light, even cases associated with the 'thin' coating configuration - i.e., $150\mu m$ - demonstrate a marked increase in cycle average temperature. As expected, the thicker coating configurations ($300\mu m$) further amplify average temperature values, while also increasing the relative disparity between open-cycle metal and TBC temperatures. Taken together, these attributes help establish the upper limits of TBC-appropriate time-scales (i.e., engine speed) - and by extension further stress the importance of minimizing thermal mass.

2.4 Concluding Remarks

Employing a reduced dimensional model to explore the relevant TBC 'design space', a number of critical outcomes have been identified. These include the relative impact (and importance) of

key TBC parameters including: thickness, heat capacity, and thermal conductivity. Furthermore, the influence of engine speed (relative to absolute heat transfer timescale) is also considered. The modeling outcomes suggest a coating selection which minimizes conductivity, volumetric heat capacity, and thickness. Further parametric optimization may aid in extending the range of time-scales (and thus, rpm) over which a particular coating formulation exhibits favorable behavior relative to metal engine configurations.

2.4.1 Foreshadowing the Path Forward

Insight from the modeling outcomes listed above remain limited in their ability to 'fully' quantify heat loss and the subsequent impact on such engine performance metrics including: cycle work, efficiencies, heat loss, and emissions. As a result, a full-scale experimental effort is planned in which thermal conditions at the gas-wall interface will be probed directly. This research effort will require an expanded experimental array, where in-cylinder temperature measurements are acquired at multiple locations within the combustion chamber (including piston). This experimental effort will enable construction of a 'globally representative' heat transfer profile - helping to further correlate TBC thermophysical properties with key cycle metrics. Furthermore, specialized analytic tools will be modified and/or developed to enable similar quantification of TBC surface heat flux and temperature profiles using the available instrumentation array. This requires re-construction of TBC surface temperature profiles using sub-TBC temperatures. Detailed development of these experimental and analytic tool-sets are the subject of subsequent chapters.

Chapter 3

Overview of Experimental Apparatus and Procedures

The analysis of later chapters relies heavily on experimental data. These include measurements from both in situ and ex situ platforms. As such, critical details regarding the instrumentation and functionality of relevant experimental environments are the central focus of the current chapter.

3.1 Engine Platform and Critical Subsystems

This section will overview the hardware, instrumentation, and support systems within the Advanced Combustion Test Cell at Clemson University's International Center for Automotive Research. Particular focus will be given to the test cell enclosure, AC dynomometer (Baldor Motors, 100 HP Rating), engine platform, signal conditioning hardware, and data acquisition systems.

3.1.1 Test Engine

In situ data is derived from a single cylinder, gasoline-fueled, low temperature combustion research engine see Fig3.1. The engine is operated in Homogeneous Charge Compression Ignition mode and is fully instrumented to monitor engine performance and emissions while ensuring constant operational conditions. A concise overview of engine subsystems is included below.

It should also be noted that the engine platform (and major subsystems) are further housed

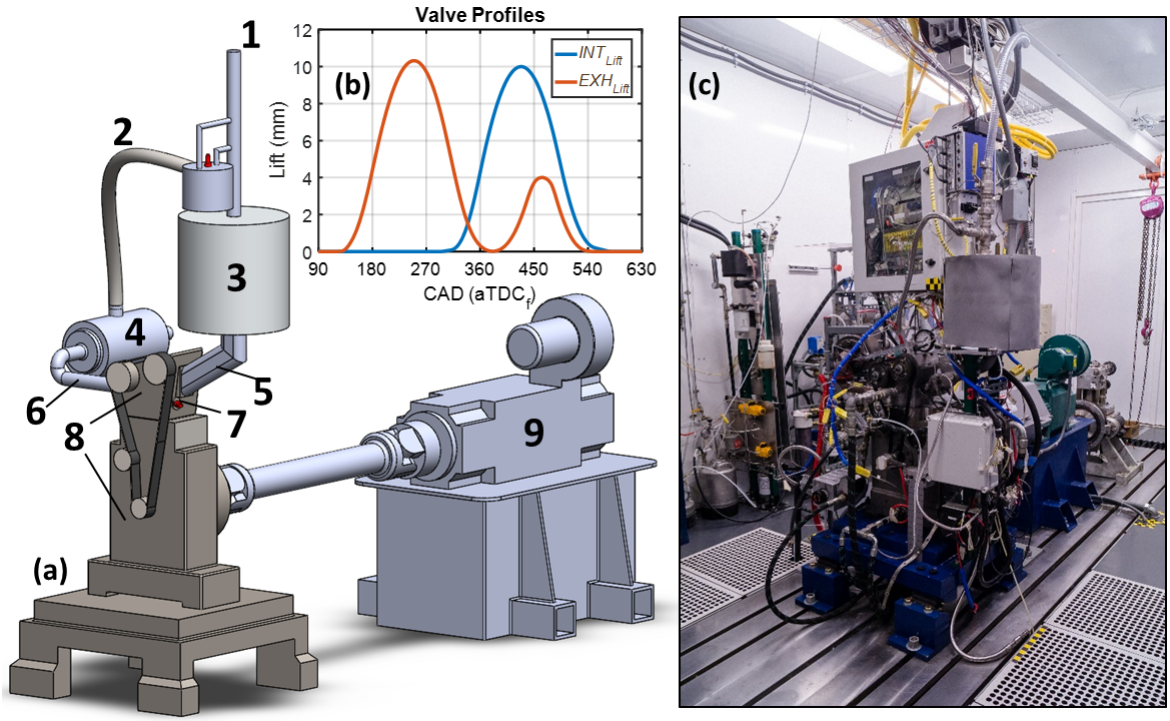

Figure 3.1: Details of Engine/Dyno arrangement. A schematic overview is provided in (a). Major components have been labeled to help facilitate the discussion within the main body of the text. The lift profiles for intake (blue) and exhaust (red) camshafts are plotted in (b). The fully-instrumented engine/dyno arrangement is shown in (c).

within a fully enclosed test-cell, with adequate cross-flow ventilation, exhaust gas extraction, and fire suppression capability - shown in Fig.3.1c.

A detailed schematic of critical engine systems is provided in Fig.3.1a. Individual components includes: (1) Fresh air inlet. Air service utilizes the building's compressed air circuit. A critical orifice system upstream of the inlet position controls the intake-side pressure. (Note: The operational points considered in this dissertation remain 'un-boosted', with inlet pressures fixed at 1 atm.) (2) A 'cooled' Exhaust Gas Recycle (EGR) circuit is available. When operational, external EGR is mixed with the incoming air upstream of the heater. (3) The intake-side plenum has an internal volume 20 times greater than the engine's displaced volume. This cavity preheats incoming air while ensuring uniform boundary conditions at the intake valve. Gaseous EGR is sampled at this location. (4) The exhaust-side plenum dampens pressure oscillations downstream of the exhaust runner. A gaseous exhaust sample is drawn from this volume. (5) The intake runner connects the heated plenum to the intake port in the cylinder head. Intake temperature is monitored (and con-

Table 3.1: Engine Deatails

Research Engine	Single Cylinder, 4 Valve
Bore/Stroke	86.0 mm/94.6 mm
Displacement	0.5459 L
Connecting Rod	152.2 mm
Piston Pin Offset	0.8 mm
Compression Ratio	12.5:1
IVO/IVC	$346^oaTDC_f/128^obTDC_f$
Main EVO/EVC	$130^oaTDC_f/352^obTDC_f$
2^{nd} EVO/EVC	$326^oaTDC_f/189^obTDC_f$
Injector Type	70^o Spray Angle w/20^o Offset

trolled) from this location. (6) The exhaust runner directs flow exiting the combustion chamber into the primary exhaust pathway. Exhaust gas temperature is monitored at this location. (7) A side-mounted injector delivers fuel directly into the cylinder. Early injection timing ($SOI = 333^obTDC_f$) ensures adequate mixing of the air/fuel charge. Injector rail pressure is fixed at 1500psi. (8) The main engine body. An aluminum 'pentroof' style head, with dual-overhead cams and 4 valves sits on-top of a cast iron crankcase. The head was furnished by General Motors Research and Development, and shares critical geometry with production I-Line 4-cyclinder engines from the early 2000's. A Ricardo 'Hydra' crankcase provide the bottom-end hardware. Full geometric details of the engine are shown in Table 3.1, while cam lift profiles are plotted in Fig.3.1b. (9) Engine power is absorbed by an AC dynamoter (manufactured by Balco Corporation). The dyno can also provide power to engine during motoring. Dyno electrical service is routed through an external cabinet and controlled remotely.

3.1.2 Engine Subsystems and Instrumentation

Additional details pertaining to critical engine components and subsystems are discussed. Specialized instrumentation enabling high-fidelity measurement of in-cylinder surface temperatures will also be discussed.

Fuel Delivery and Metering

A Bosch HDEV1 Fuel Injector ($\approx 1500psi$ line pressure) (PN 103079297, B 438173512/17, 15cc/s rated) delivers fuel in-cylinder. The nozzle yields solid cone geometry, and has been optimized

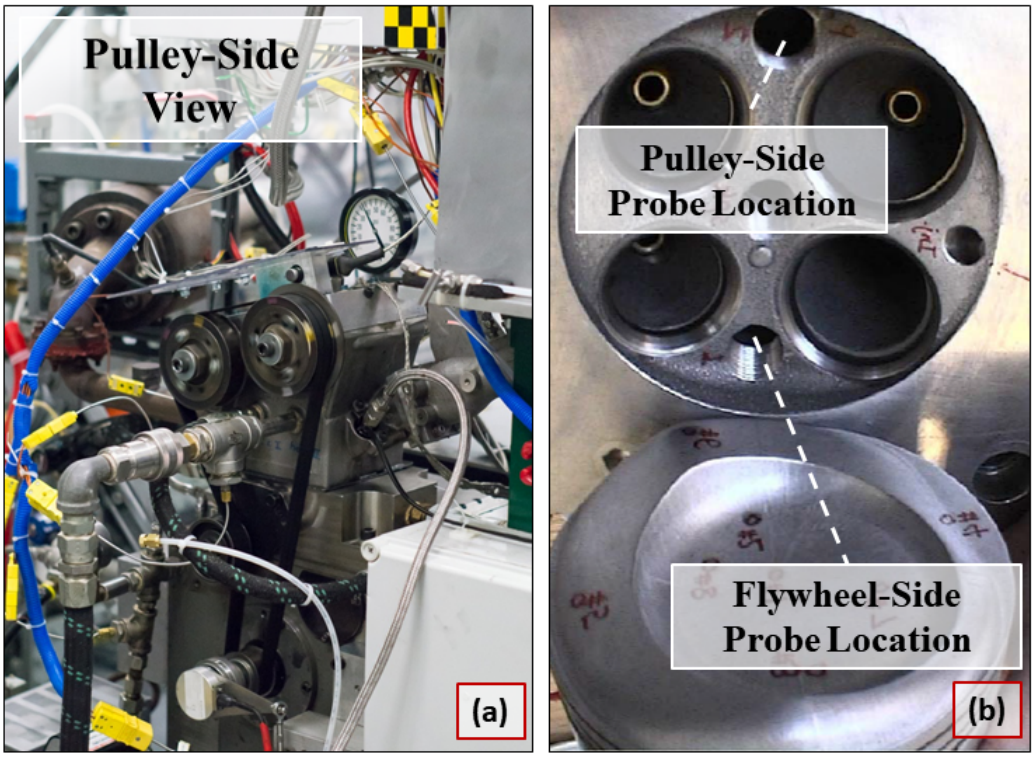

Figure 3.2: A pulley-side view of the fully-instrumented engine, firing in HCCI mode at 2000rpm (a). A detailed view of the pent-roof combustion chamber is also included (b). Note the location of the side-mounted injector. The two access points for the fast-response heat flux probes are also shown. These locations flank the centrally mounted spark-plug. Note: Intake and exhaust valves have been removed.

Table 3.2: Fuel Specifications

Fuel Prod. No.	Gage 91 RON Test Fuel (40665-55F)
Research Octane Number (RON)	90.8
Motor Octane Number (MON)	83.0
Octane Rating (R+M)/2	86.9
Octane Sensitivity (R-M)	7.8
C/H Ratio (Wt/Wt)	5.606
H/C Ratio (Mole/Mole)	2.126
Heat of Combustion (MJ/kg)	43.3

for targeting within the GM cylinder head. As mentioned, start-of-injection occurs at 333 CAD before top dead center firing (bTDCFiring), ensuring homogeneity of the air/fuel mixture. The injector nozzle geometry supports a 70^o Cone, with a 20^o axial offset.

Fuel is pressured using an external hydraulic accumulator - pressurized to 1500psi. This removes the parasitic burden inherent engine-driven fuel pressurization. Fuel flow-rate is metered using a volumetric flow device from Max Machinery, Inc. (Flow Meter: 213-611-000,29-300-000). Instrument calibration is guaranteed for flow rates between 1.8 and 1750 cc/min. A mass flow-rate is calculated using the fuel density provided from the supplier (to be detailed below).

A research grade gasoline is sourced from Gage Products Co ('91 RON Test Fuel', Packaged Product 40665-55F). The manufacturer provided specs are detailed in Table 3.2

Air Management

As mentioned in the overview provided in Sec.3.1.1, a critical orifice system regulates pressure of the air supply. Air flow is metered using a Fox Mass Flow meter (Model FT2-20PSSSTE1DDBO). This instrument is hard-mounted upstream of the main plenum inlet using a straight pipe section, with fixed diameter. The ensures spatially uniformity in the flow field at the measurement location.

3.1.2.1 Exhaust AFR and Gaseous Emission

A Bosch wideband lambda sensor (LSU49) monitors air-fuel-ratio immediately downstream of the exhaust port. This device is capable of monitoring a wide range of compositional conditions ($0.65 \leq \lambda < \infty$). Complete instrument details including accuracy as a function of measured lambda are available here [?].

The LSU49 sensor is supported by an Etas AWS2-E 'Lambda Module' [?]. This device is programmable, and accepts specific input related to fuel properties. This helps further ensure accuracy of the reported lambda measurement.

Emission components and EGR percentage are sampled and analyzed using a Horiba 'MEXA-7100D EGR' system. This system consists of integrated sensors responsible for: (i)Total Hydrocarbon Measurements (THC) using Hydrogen Flame Ion Detection (FID), (ii) NO/NOx measurements via chemiluminescence detection, and (iii) CO/CO2 concentrations using Non-Disbursive Infrared (NDIR). Full operational details (including required feed gases) and respective accuracy are available in [].

3.1.2.2 Engine Control Unit

Engine control is commanded using a Bosch Electronic Control Unit (B 261 204 883). Set-point control is achieved using custom-design graphic user interface (GM R&D), operated remotely from the dyno-cell control room. Spark, injection timing and dwell are controlled through this interface.

3.1.2.3 Cylinder and Manifold Pressure Transducers

in-cylinder pressure is measured using a Kistler 6125a pressure transducer [21]. This device is high-temperature-rated piezo-electric pressure sensor. The device is capable of measuring pressures fro 0-300 bar with a reported thermal shock error of $\leq 0.3 \pm bar$. The instrument utulizes a flame shield to further assuage thermal shock, and is mounted flush with the surface of the firedeck.

Intake pressure is measured using a Kistler's 4007B series pressure sensor covers measuring ranges of 0 to 5 bar, (0 to 20 bar absolute), from 40^oC to 200^oC. This instrument also uses a piezoresistive measuring element. The sensing element relies on an implanted resistive bridge to minimizes hysteresis and repeatability errors. The sensor is mounted in the intak erunner upstream of the intake ports.

Exhaust pressure is measured using a Kistler 4045A. This sensor utulizes a thin steel diaphram to tansfor pressure (via silicone load cell) to piezo-resistive sensor connected in a Wheatstone bridge. Pressure distirbance unbalance the Wheatstone device, producing a proportional output signal. The sensor is paired with a cooled switching adapter (Type 7533B) to help ensure longevity given elevated exhaust-side temperatures. Thermal sensitivity is reported at $\leq 1\%$.

3.1.2.4 Fuel Match/Phase Match Operational Procedure

Given fixed operational set points (including fuel mass, AFR, T_{Intake}, etc.) TBC's have been shown to advance combustion phasing relative to their metal engine counterpart [80]. Variability in combustion phasing should be minimized in order to isolate the strictly 'thermal' impact(s) of TBCs on engine performance and heat transfer. The authors have developed a "Fuel Match, Phase Match" (FMPM) operational procedure with this goal in mind. A brief overview follows.

Beginning with the metal engine configuration, fueling is adjusted to enable 'robust' HCCI operation. Cycle-to-cycle variation, as measured by COV_{IMEP}, remains below 3%. Ringing Intensity (RI) is also limited to 5 MW/m^2. Fueling rates satisfying these conditions are established at each RPM, and become the set-points for subsequent evaluation.

With fueling established, the temperature of the air mass entering the metal engine is adjusted until combustion phasing is positioned at 7 CAD aTDC, (i.e., $CA50 = 7^o$ aTDC). Five hundred consecutive cycles are recorded under the aforementioned operational conditions generating a 'baseline' metal engine dataset for each RPM of interest.

With metal engine data acquisition complete, the engine is 'rebuilt' to include (at minimum) a TBC-treated piston and probe. To counteract the resultant phase-advance of the TBC configured engine, the intake air temperature is again adjusted to re-position CA50 at 7^o aTDC. It should be noted that all other operational set points remain fixed ensuring similar operational parameters relative to the baseline metal engine case. A sample of corresponding results, as seen in phase-averaged cylinder pressure data and heat release data, is included in Figure ??.

A final note regarding FMPM operation: While the above mentioned procedure is designed to elucidate the thermal influence of TBCs upon relevant combustion/heat transfer metrics, the authors recognize that secondary impacts likely exist. For example, the use of external EGR to retard combustion phasing within the TBC treated engine may impact the over-all composition of the in-cylinder charge. If compositional variations between metal and TBC engine configurations exist, they may well influence the chemical-kinetics underlying HCCI autoignition. Even if total EGR percentage remains constant during FMPM evaluation, the external EGR utilized by the TBC-treated engine enters the combustion chamber at a much lower temperature than the internal EGR associated with the rebreathe event. This would likely effect the bulk gas temperature during closed-cycle CAD, impacting heat transfer and by extension autoignition. Given the potential for

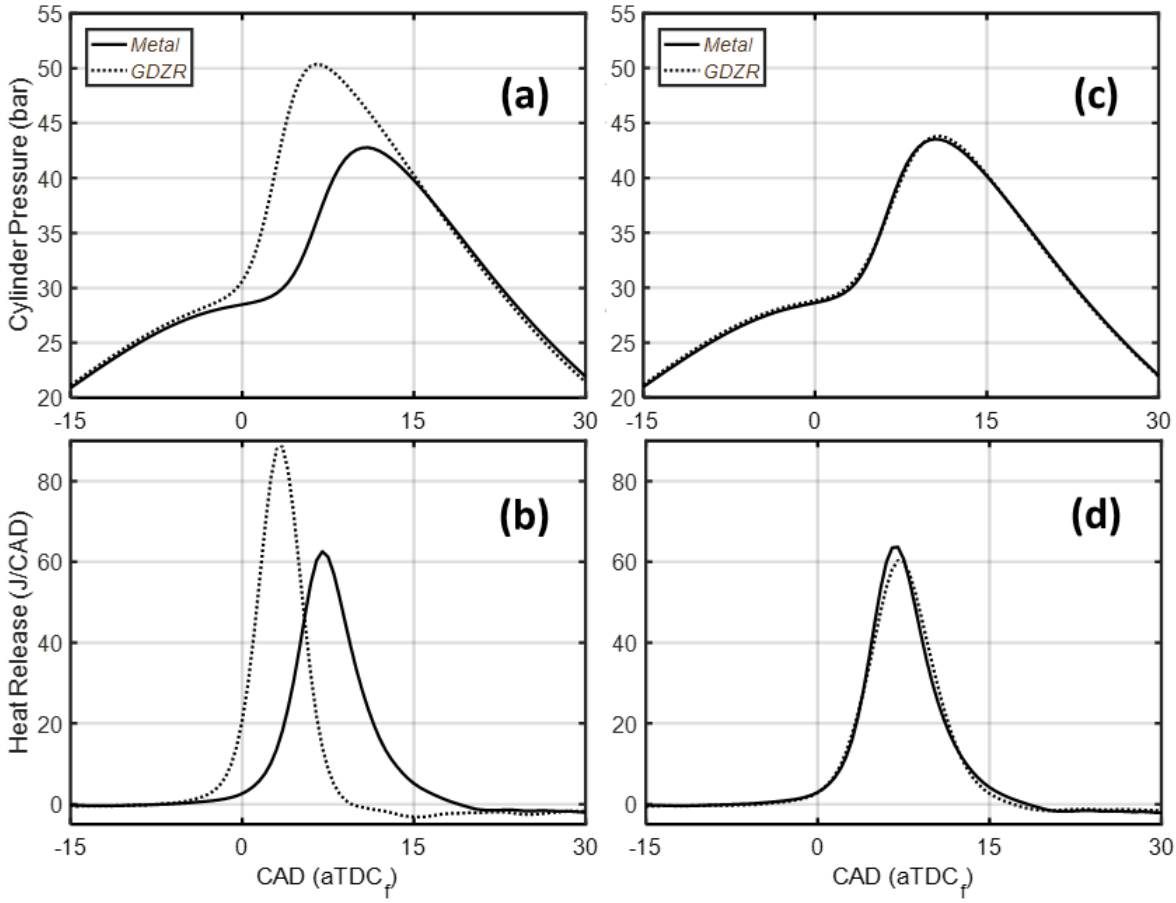

Figure 3.3: An example of "Fuel Match" (a,b) and "Fuel Match/Phase Match" (c,d) operation. Here the TBC treated engine (GDZR) is 're-phased' to better reflect combustion within the metal engine. Raw pressure traces and the associated heat release rate are shown. Intake temperature is shared in (a,b). In contrast, intake temperature of the GDZR-treated engine is lowered in (c,d) until the GDZR treated engin euntil phasing is re-established at $7^o aTDC_f$.

such secondary effects of the current Fuel-Match/Phase-Match operating procedure, the authors continue to evaluate best practices relative to the goals stated at the onset of this section.

3.1.3 Fast Response Heat Flux Probes

A major focus of the work presented in this dissertation is the measurement and characterization of engine heat transfer. This analysis requires high fidelity measurement of in-cylinder surface temperatures. The work presented in later chapters will utilize measurements from fast-response thermocouples. These probes are sourced from two separate suppliers. Their operational principle remains the same, however the respective design and supporting architecture are slightly different. Characteristics attributes of each probe type are presented below.

A custom fabricated fast-response heat flux probe manufactured by the Medtherm Corporation [22] is shown in Fig.3.4a. These probes are J-type tri-axial thermocouples with independent front and backside junctions. Each junction is formed using a separate pair of leads (i.e., no common junction) - resulting in four independent wires. The dimensional offset between measurement junctions is used in conjunction with known material properties to calculate heat flux at the probe's surface. The Medtherm probe variant utilizes a vapor deposited front-side junction. This construction method limits the 'thermal mass' of the measurement junction, enabling a sensor time-constant on the order of $1x10^{-6}$ sec. Shielded J-type wire extend from the probe's body to the data acquisitions 'break-out' panel, at which point the voltage transitions to shielded copper leds. The temperature of this reference junction is monitored independent of the instrument's primary signal to ensure accurate voltage-to-temperature conversion.

In general, this probe type is quite robust and has been utilized by a number of authors in the literature [19, 37, 71]. Of particular consequence is the material used for construction of the probe body. As demonstrated in the preceding chapter, given a fixed-magnitude, periodic heat flux, lower conductivity materials result in higher surface temperatures. To better establish a baseline case, it is worth remembering that the Medtherm construction uses a 1010 low carbon steel.

As an alternative to the Medtherm probe, a secondary design from IR Telemetrics is also considered - see Fig.3.4b. Here again, two measurement junctions are separated by a known distance to enable calculation of the surface heat flux. However, this probe style forms its front-side measurement junction by laser-welding a thin section of platinum wire between the J-type leads. It should be noted that the negative lead is shared between front and backside junctions. Furthermore, the

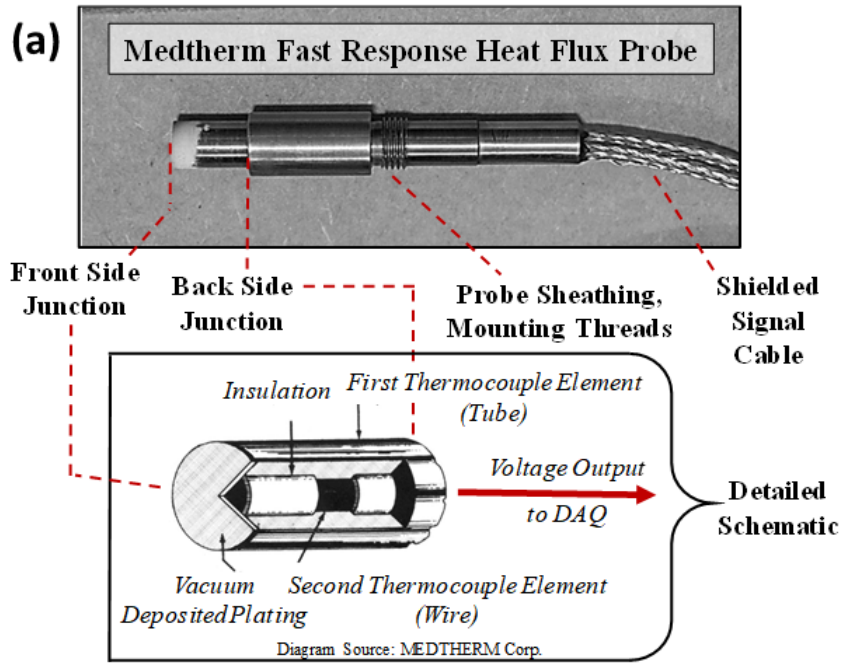

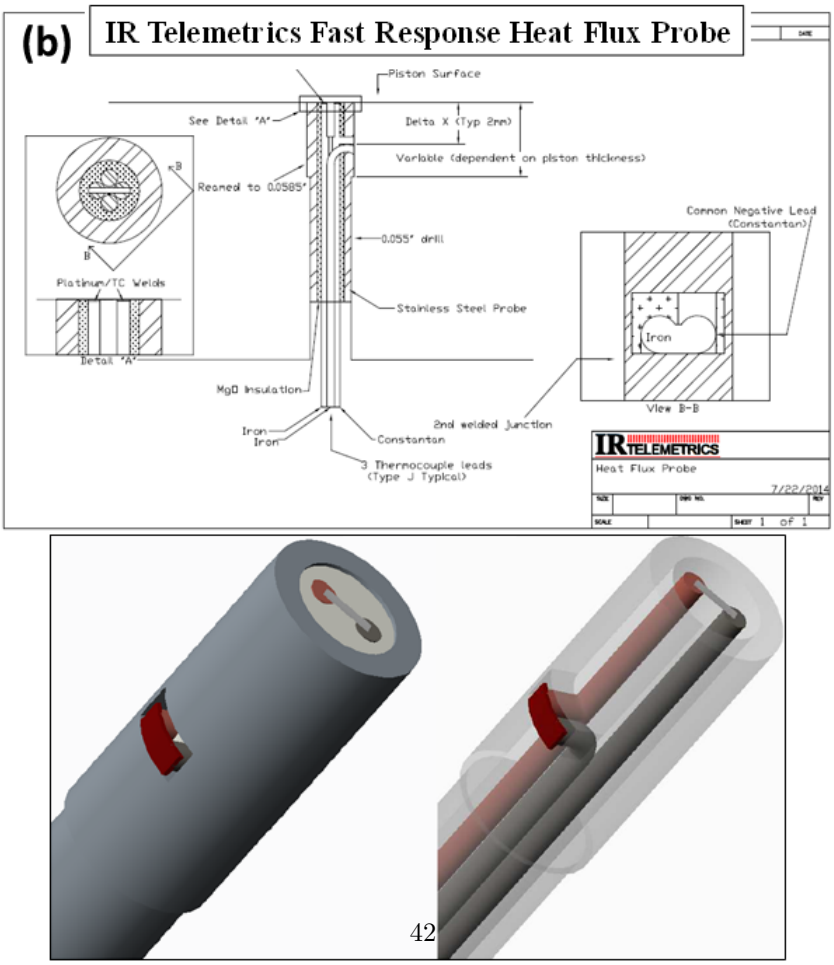

Figure 3.4: Fast response heat flux probes. The MedTherm design (a), and the IR Telemtrics Variant (b).

backside junction is offset from the central axis, and is formed on the outer radial surface of the probe body. This geometric offset requires certain assumptions pertaining to the effective dimensionality of the heat transfer pathway, namely that heat flow remains 1D between measurement surfaces.

Finally, the IR probe body is machined from 304 SS alloy - a material considerably less conductive than the Medtherm's mild steel body. As a consequence, the IR probe generally exhibits a higher magnitude temperature response (under similar engine speed/load conditions). This characteristic feature is quit beneficial, as signal-to-noise considerations are paramount, particularly for TBC-treated probes.

It should be noted that both probe types mimic the external dimensions of the 6125a Kistler pressure transducer. This enables a convenient standardization of machining requirements. The common geometry also ensures that both probe types remain compatible with the head-based mounting locations highlighted in Fig.3.2b.

3.1.4 Telemetry Linkage System

A major focus of this dissertation is the characterization of heat transfer within a variety of engine configurations. In an experimental setting, this typically requires 'real time' measurement of surface temperature. As discussed in Sec.3.1.3, current efforts utilize a number of fast-response thermocouple designs. However, in the standard experimental configuration described in Sec.3.1.1, in-cylinder surface temperatures are limited to locations within the cylinder head.

To better resolve global temperature and heat flux trends, it becomes necessary to expand the temperature array beyond the fixed head locations. To achieve this goal, a telemetry linakge system (specifically designed for this engine platform [36]) is employed.

The Medtherm-style probes are installed at eight separate locations in the piston. (Individual locations are identified in Fig.3.5a, these are formalized in later chapters). The instrumentation array provides covers both the bowl and squish regions of the piston. The primary challenge associated with the piston-based measurements, involves the physical routing of signals through reciprocating components. As such, the linkage assembly is aptly described as 'high-risk/high-reward', and ultimately offers the opportunity to more fully characterize surface boundary conditions at the gas-wall interface.

Two separate instrumented-piston configurations are considered in the current work. The first build, shown in Fig.3.5a, utilizes an uncoated (i.e., metal) piston. The second variant applies

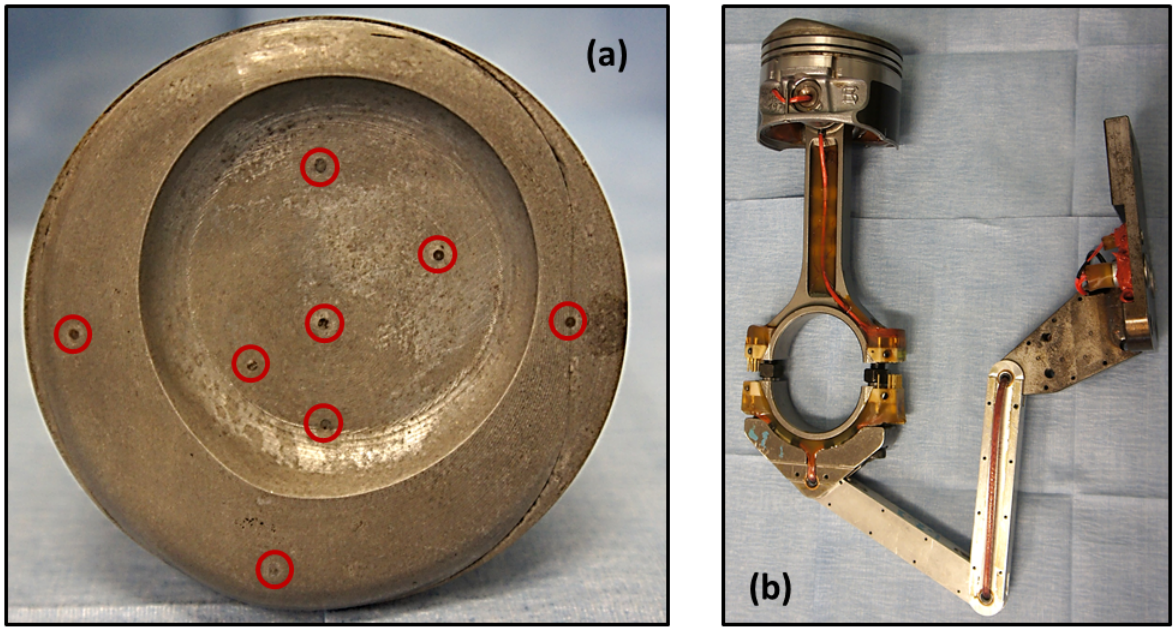

Figure 3.5: A close-up view of the instrumented piston (a), with measurement surfaces circled in red. An external mock-up of the piston-conrod assembly (b), prior to final fabrication and installation.

a low-conductivity TBC layer to the surface of the piston. As will be discussed in upcoming chapters, the TBC-coated probe locations measures sub-coated temperature response, and thus require additional post-processing to characterize the surface conditions.

In general, the telemetry linkage represent a significant eperimental investment. A single 'build' can take upward sof two weeks, with teh most robust variants lasting 20 hours. However, as will be fully-developed in subsequent chapters, the measurements enabled by this device help to more completely characterize the impact of TBC's on engine heat transfer, combustion, metrics, and emissions.

3.2 Ex situ Radiation Chamber

A custom fabricated Radiation Chamber subjects the aforementioned temperature probe to HCCI-like heat flux pulses on the order of 0.25-1.0 MW/m^2. The duration of each pulse is likewise comparable to the HCCI combustion event at typical engine operational speeds. Unlike the turbulent and reacting flow encountered in-cylinder, the ex situ environment is both quiescent and inert. The absence of spatial variability ensures shared boundary conditions at each probe location

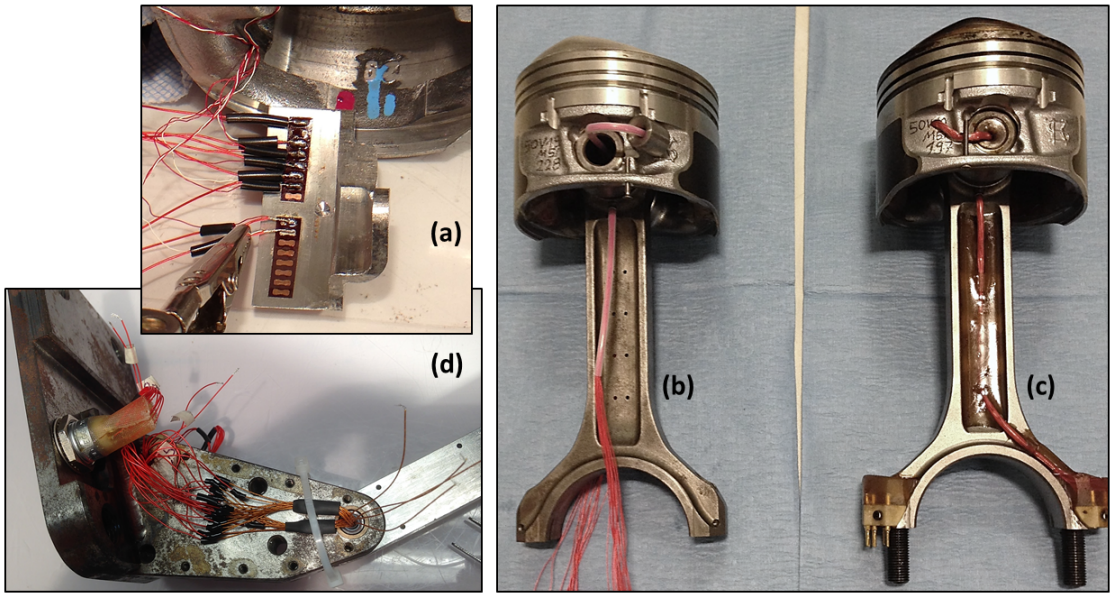

Figure 3.6: Key milestones of the piston/linkage build. Splicing thermocouple leads at the isothermal plate (a). Routing of main signal harness through the wrist-pin, and down the con-rod (b). Completed piston build, with potting of wire harness and soldering of individual wires at break-out pins. Splicing of main harness at lower end of telemetry linkage (d). The millivolt signals are intercepted at the Amphenol connectors, amplified, and feed to the high speed data acquisition system.

enabling comparison between surface-based (i.e., 'direct') and subsurface-based (i.e., 'inverse') heat transfer calculations. Note: this methods are developed in later chapters.

Detailed discussions of this apparatus and its capabilities are available from [44]. A simplified operational schematic of the device is detailed in Fig3.7.

A final note regarding radiative heat transfer. As can be expected, radiative characteristics vary between non-coated (i.e., metal) and TBC-treated probes. To counteract this discrepancy, a thin layer of aerosol-based graphite is applied to both surfaces ensuring equal absorptivity/emissivity at the surface of interest.

3.3 Thermal Barrier Coatings

The analysis of later chapters will consider three separate coating formulations. To establish a common reference, measurements from a metal engine (i.e., 'non-TBC' configuration) establish baseline results. The characteristics of individual coatings will be developed in detail below. Before focus shifts to material considerations, two common application techniques are reviewed.

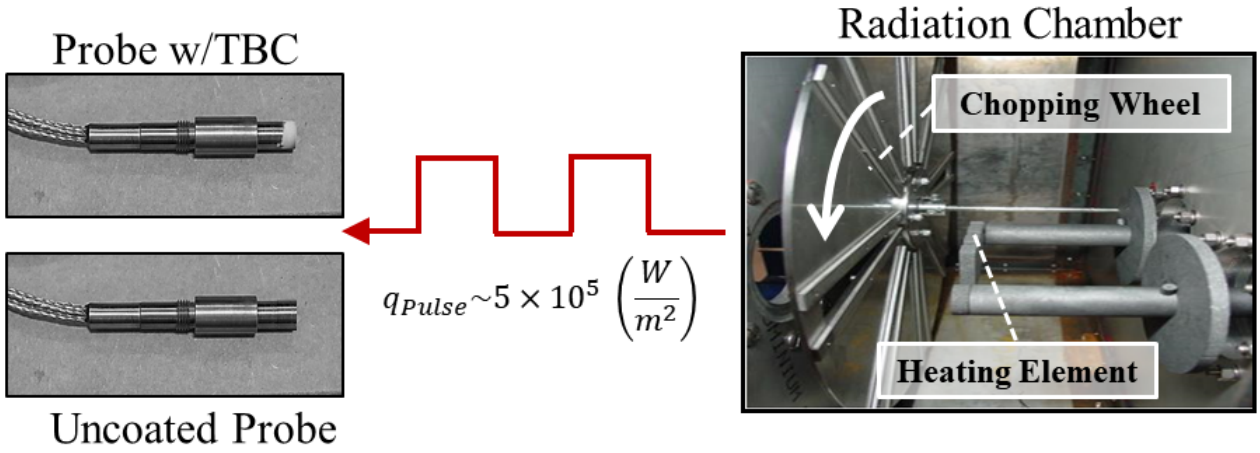

Figure 3.7: Operational Schematic of the Ex Situ Radiation Chamber. An electrically powered resistive heating element generates a constant radiative heat flux of $.5MW/m2$. A rotating 'chopping wheel' periodically interrupts the 'line-of-sight' between heat source and incident temperature probes providing a dynamic heating event similar in magnitude and duration to HCCI combustion, while avoiding the turbulent reactivity of the in-cylinder environment

Three main coating formulations are included in this work. The first coating represent a common TBC formulation (yyitria stabilized zirconia), and is applied using an 'air plasma spray process'. In general, this application process yields results in a spatially uniform, dense material layer. To enable more complete coating structure, a solution precursor spray technique is also available. In this method, wet chemistry is used in-place of dry powder. The SPPS technique ensures tighter control over individual coating layers while also enabling complex morphological structures. A more compete overview of these processes are available in [51]and [48].

In general, each generation of coating material seeks to elevate closed-cycle surface temperatures by systematically reducing thermal conductivity and heat capacity. Coating applications is limited to the piston surface - sparsity which is primarily driven by the . A review of key characteristics, including relevant thermophysical properties, is provided for each of the thermal barrier coatings.

Yittria Stabilized Zirconia - Dense

A yittria stabilized zirconia TBC (YSZ) is applied to the piston using an air plasma spray (APS)deposition process. Figure **??**a provides a representative image of a TBC-coated piston prior to installion within the engine. In general, the APS application method yields a robust coating

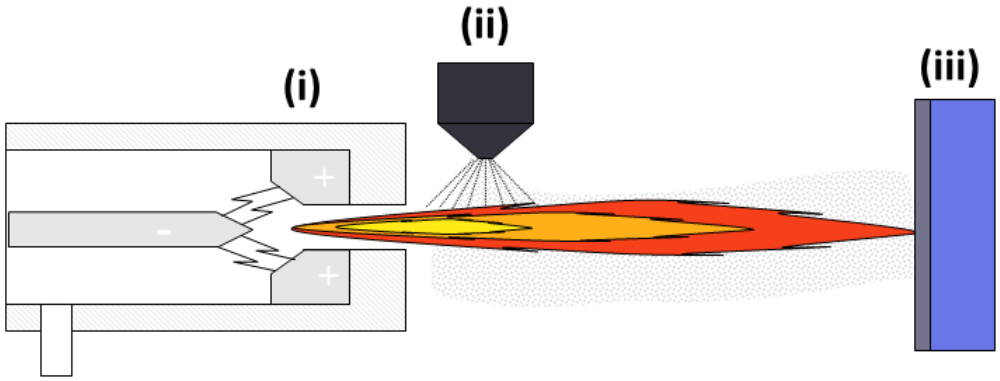

Figure 3.8: A schematic of the plasma spray deposition process. A plasma gun (i) focuses it's output on the material substrate (iii). Raw thermal barrier material is introduced at (ii). Conventional spray application (APS) use a dry powder at (ii). Alternatively, a solution precursor (SPPS) can also be used, where wet chemistry enables additional complexity in the TBC layer. Figure adapted from [51].

layer, while minimizing the porosity fraction [51]. Estimates for thermal conductivity and diffusivity for this TBC are $1.1\frac{W}{mK}$ and $0.83x10^{-6}\frac{m^2}{s}$, respectively. These values remain consistent with those reported in the literature [12].

Yittria Stabilized Zirconia - Structured Porosity

In an effort to further enhace the the 'effective' thermophysical characteristics of the YSZ material, structured porosity can be introduced into the main TBC layer. Creation of such microstructures requires advanced application techniques. The present work utulizes a Solution Precursor Plasma Spray Process (SPPS). As shown in Fig. **??**b, multiple layers are applied to the substrate material - resulting in porous microstructures, or "inter-pass boundaries". As such, this TBC formulation is labeled 'YSZ_{SP}' (i.e., "YSZ w/Structured Porosity"). In essesnce, discountinuities at the interface between adjecent layers result in non-neglidgible contact resistence, further reducing the conducvity ($1.0\frac{W}{mK}$) and diffusivity ($0.67x10^{-6}\frac{m^2}{s}$) of the YSZ material [51] [48].

Gadolinium Zirconate

As an alternative to increased morphological complexity, a seperate low-porosity (i.e., 'dense') TBC material is also considered. This material, Gadolinioum Zirconate (GDZR), has inherently lower conductivity ($0.65\frac{W}{mK}$) and diffusivity ($0.50x10^{-6}\frac{m^2}{s}$) than the YSZ-based coatings described above. Additional information, including can be found in [65] [61] [94].

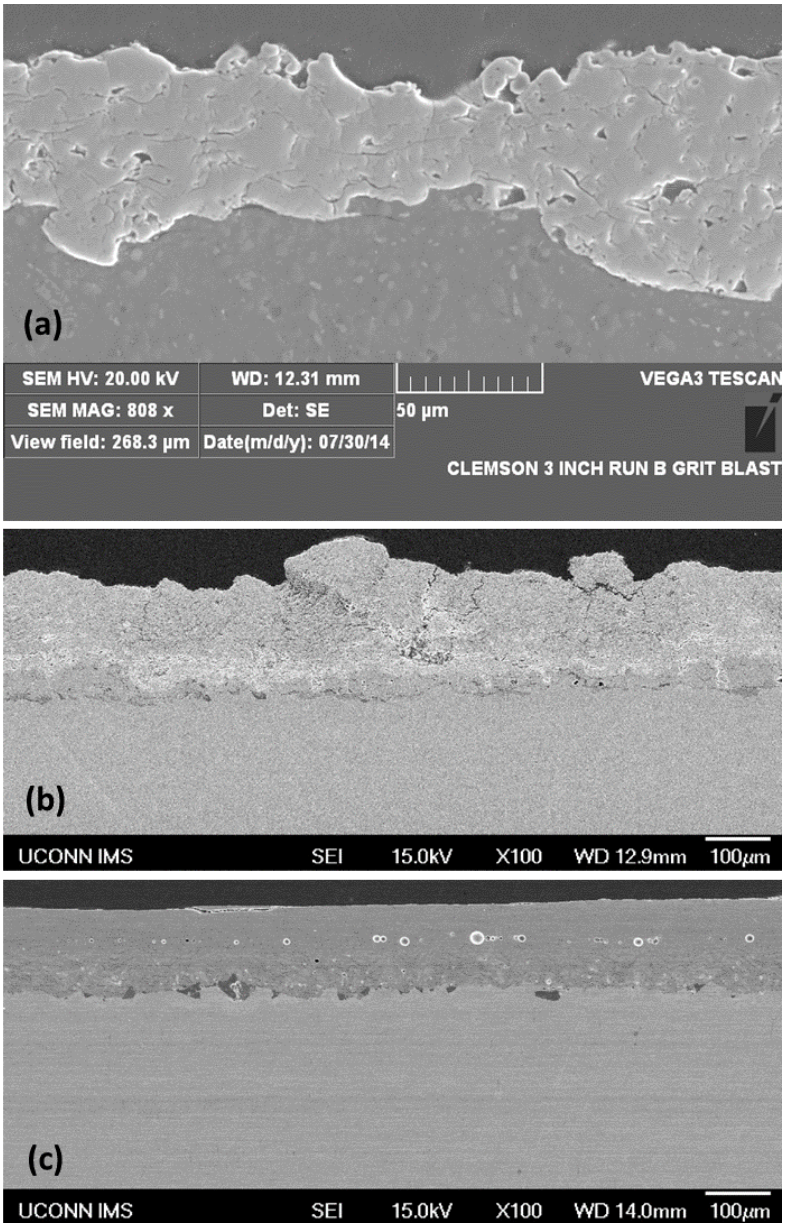

Figure 3.9: Cross-sectional profiles of the various TBC materials. The APS-applied yittria stabilized zirconia is shown in (a), note the dense main coaying layer. Scale for this image is 50 μm, all other images shown at 100 μm. Subfigure (b) shows an SPPS application of the YSZ material - note the structured porosity in the main coating layer. Final the dense GDZR material is shown in (c).

Chapter 4

Inverse Heat Conduction and the Sequential Function Specification Method

This chapter will motivate, develop, and validate the analytic tools required in the proceeding chapters. As will be shown, quantification of temperature and heat flow at the gas-wall interface is a major focus of this dissertation. A number of pre-established techniques (well-established in the literature [41]) are available to calculate surface heat flux using measurements of in-cylinder surface temperatures. However, the application of a thermal barrier material to in situ instrumentation prevents the direct measurement of the aforementioned surface temperature profiles. Instead, 'sub-TBC' temperature response is recorded for the TBC engine configuration. From a qualitative point-of-view, the TBC-treated probe's signal is both attenuated and phasing-lagged relative to the surface temperature measurement - a result of the 'diffusive' nature of heat flow. From a practical standpoint, these subsurface *subsurface* measurements no longer provide a direct evaluation of the 'boundary condition' (i.e., surface temperature) required to evaluate the governing heat diffusion equation. As a consequence, this heat transfer configuration is commonly labeled an 'Inverse Heat Conduction Problem' (IHCP). Such problems are 'ill-posed', and require specialized solution methodology to address the challenges inherent to this heat transfer configuration. The solution will allow "closing the loop", i.e., correlating the TBC's thermal properties with its impact on combustion

and efficiency, via the estimation of surface temperature and heat flux profiles.

This chapter begins with a review of the mathematics necessary to model heat flow in the TBC-temperature probe system. A particularly flexible IHCP solution methodology will be reviewed and ultimately modified to address the time-lag between surface heat/cooling events and subsurface temperature response. This modified solution methodology is validated in an ex situ experiment first, and eventually extended to in-cylinder temperature measurements.

4.1 Some Requisite Background

Thorough analysis of engine combustion and performance relies upon the accurate characterization of energy flow, including heat transfer. Experimentalists within the engine research community commonly employ fast response thermocouples with sub-Crank Angle Degree (CAD) resolution [18, 4] to measure combustion chamber surface temperatures within a firing engine [36, 64]. These temperature profiles provide the boundary conditions necessary to solve the associated heat transfer configuration(s) typically heat diffusion problems of varying geometric complexity. A variety of pre-established analytical and numerical techniques are available to calculate the surface heat flux associated with recorded surface temperature traces [41].

Related analyses of mass and energy transfer, including the study of turbulent, wall-bounded, reciprocating flows [25, 26], utilize similar high-resolution/high-fidelity temperature measurements which enable the calculation of surface heat flux. These empirically derived results are then used to evaluate analytically solutions to the equations governing mass and energy exchange.

In contrast to direct surface measurements, some engine operating conditions and/or configurations restrict the placement of in-cylinder temperature sensors. Examples include: (1) the formation of Combustion Chamber Deposits (CCD) during engine operation and [35] (2) the application of Thermal Barrier Coatings (TBC) to exposed combustion chamber surfaces. Under such conditions, the temperature profiles measured by embedded sensors no longer represent surface temperature information. Rather, these measurements reflect sub-surface temperature variations. As a consequence, the boundary conditions governing heat transfer cannot be measured directly. The resulting mathematical configuration is commonly described as the Inverse Heat Conduction Problem (IHCP), and cannot be solved using the conventional analytic/numeric techniques associated with 'direct' heat conduction problems.

In this section, an established solution to the IHCP known as the Sequential Function Specification Method (SFSM) [9] is modified to solve heat transfer within TBC treated engine components and temperature probes. This process utilizes sub-TBC temperature measurements to estimate the functional form of TBC surface heat flux and temperature traces. An ex situ radiation chamber, which generates heat flux pulses of known magnitude, is used to validate the SFSM technique. The algorithm is then extended to calculate TBC surface heat flux in situ using sub-surface temperature measurements from a firing Homogeneous Charge Compression Ignition (HCCI) engine.

4.1.1 The Inverse Heat Conduction Problem

The IHCP found particular significance with the proliferation of the aerospace and nuclear industries during the 1960s. The heat transfer problems encountered in these fields often involve surface boundary conditions of extreme magnitude that prohibit the direct measurement of temperature profiles (e.g., surfaces of orbital satellites upon atmospheric re-entry, and core surfaces of active nuclear reactors). Thus, practical monitoring of many transient thermal processes was limited to subsurface temperature measurements. As a result, much of the pioneering IHCP solution methodology dates from this period [9, 8], including the SFSM.

Inverse problems also been encountered in engine research... talk about Orgun's "Lead-Corrector"...

4.1.2 Conceptual and Mathematical Description of the IHCP

Figure 4.1 provides a conceptual IHCP representation for a simplified geometric configuration (one-dimensional, planar). A plane of known thermophysical properties (ρ, C_p, k) and finite dimension L is subject to prescribed boundary conditions ($BC_0 at x = 0 and BC_2 at x = L$). Boundary condition 1 (i.e., $BC1$) is unknown due to the inability to conduct direct surface measurements, while boundsry condition 2 (i.e., $BC2$) is assumed known. A temperature sensor located at x_1 (such that $0 < x_1 < L$) records subsurface temperature. As shown in Fig.4.1, this configuration can be subdivided at the sensor location x_1 to further illustrate the Inverse versus Direct regions.

Assuming one-dimensional heat conduction in planar geometry, the parabolic heat diffusion equation, in conjunction with the appropriate boundary and initial conditions, provides the math-

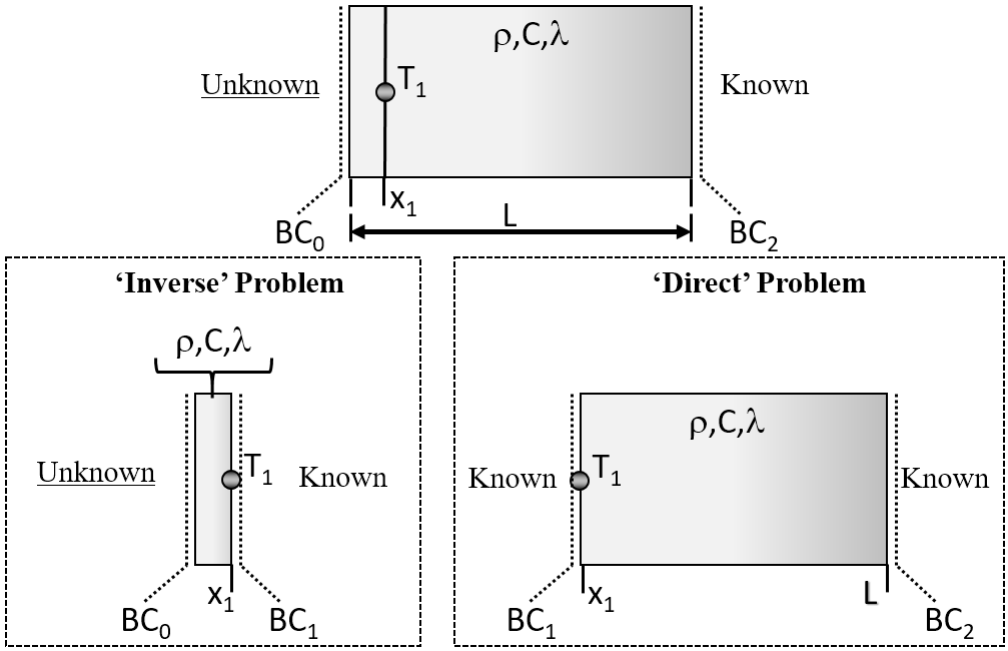

Figure 4.1: A simplified one-dimensional thermophysical system with known back-side boundary condition and interior temperature measurement locations. Subdivision further highlights the inverse and direct regions

ematical framework for the IHCP. As will be shown in detail, the SFSM assumes a prescribed heat flux at $x = 0$. Equation group 4.1-4.4 describes the inverse regime:

$$\frac{\partial}{\partial x}(k\frac{\partial T}{\partial x}) = \rho c\frac{\partial T}{\partial t} \tag{4.1}$$

$$T(x,0) = T_o(x) \tag{4.2}$$

$$T(x_k,t) \tag{4.3}$$

$$-k\frac{\partial T(x_{Surf},t)}{\partial x} \tag{4.4}$$

While equation group 4.5-4.10 describes the direct problem:

$$\frac{\partial}{\partial x}(k\frac{\partial T}{\partial x}) = \rho c\frac{\partial T}{\partial t} \tag{4.5}$$

$$T(x,0) = T_o(x) \tag{4.6}$$

$$T(x_k,t) \tag{4.7}$$

$$T(L,t) \tag{4.8}$$

$$-k\frac{\partial T(L,t)}{\partial x} \tag{4.9}$$

$$-k\frac{\partial T(L,t)}{\partial x} = h[T_\infty - T(L,t)] \tag{4.10}$$

For the purpose of the SFSM, (and the IHCP in general), the boundary condition at $x = L$ can take any form, (i.e., Temperature, Heat Flux, Mixed-Convection), as described by equations 2.4.1 - 2.4.3. The experimental data processed in the later portion of this paper will use a measured temperature at the $x = L$ boundary. As mentioned, Equation Group 2 describes a direct, parabolic, one-dimensional conduction problem. Thus, the appropriate analytic and/or numeric solution methodology [67, 77, 78] may be chosen to match the boundary conditions and linearity specific to the problem. In contrast, if the surface boundary condition (assumed to be a prescribed heat flux) is unknown, the mathematical description of the parabolic diffusive system (Equation Group 1) is rendered incomplete. As a result, the inverse problem is ill-posed [89] and cannot be solved using the techniques commonly employed by the direct problem.

It should be noted that considerable work has been invested in inverse problem solution methodology [7, 76]. (Inverse heat transfer analysis utilizing engine derived temperature measurements commonly employ iterative solvers [38]. However, even with favorable initial conditions, such solvers may become computational expensive when applied to large datasets with high temporal resolution.) It is not within the scope of this paper to review the breadth of existing inverse methods. Instead, the particularly flexible SFSM will be used exclusively to solve the IHCP as described in

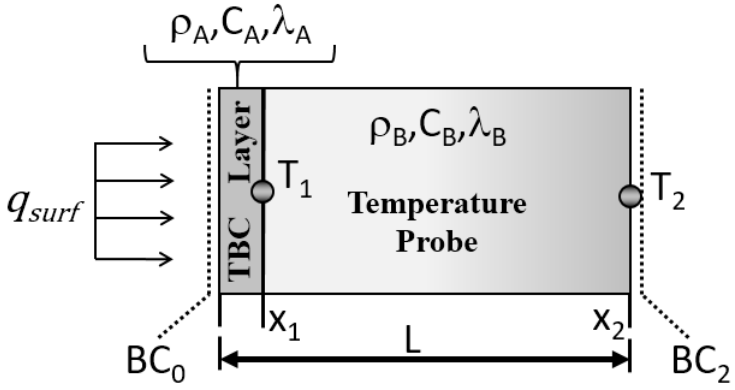

Figure 4.2: One-dimensional representation of experimental system. A fast response heat flux probe measures temperature at two independent locations one subsurface (T_1) and one at the backside boundary (T_2). The TBC layer applied to the surface of the probe creates a composite system. Inverse techniques will enable estimation of the (unknown) surface heat flux via subsurface temperature information.

the following section. The solution for typical engine 'in-cylinder' conditions has not been published before.

4.1.3 The Sequential Function Specification Method

The mechanics of the SFSM algorithm, as developed by Beck [7], will be highlighted below. Figure 2 provides a detailed representation of the system of interest i.e., a ceramic covered temperature sensor. This composite 'planar-slab' model is utilized exclusively throughout this chapter and extended to the analysis of the proceeding sections. For simplicity, only two layers will be shown during the derivation/validation efforts. However, when required, the results developed below can readily extended to include multiple TBC layer configurations.

The TBC/Temperature sensor arrangement from 4.2 will be treated as a single system, governed by the transient heat conduction equation group:

$$\frac{\partial}{\partial x}(k\frac{\partial T}{\partial x}) = \rho c\frac{\partial T}{\partial t} \tag{4.11}$$

$$T(x, t_o) = T_{M-1}(x) \tag{4.12}$$

$$T(L,t) = T_2 \tag{4.13}$$

$$-k\frac{\partial T(x_{Surf},t)}{\partial x} = \mathbf{q_M} \tag{4.14}$$

Where (for a discretized system) M represent the current time-step, $T_{M-1}(x)$ is the initial condition (or more generally, the temperature field solution at time t_{M-1}), $T2$ represents the backside temperature boundary condition measured by the fast response thermocouple at $x = L$, and q_M is the yet-to-be-estimated surface heat flux for time step M. The thermal systems sensitivity to a step change in surface heat flux (i.e., $q(x = 0)$) plays a significant role in the SFSM [7]. Accordingly, this metric is described as the Sensitivity Coefficient X, and is defined at each sensor location k and time step i such that:

$$X_{k,i} = \frac{\partial T(x_k, t_{M+i-1}, \mathbf{q_M})}{\partial \mathbf{q_M}} \tag{4.15}$$

Where X_k,i is governed by the following equation set:

$$\frac{\partial}{\partial x}(k\frac{\partial X}{\partial x}) = \rho c\frac{\partial X}{\partial t} \tag{4.16}$$

$$X(x,t_o) = 0 \tag{4.17}$$

$$-k\frac{\partial X(x,t)}{\partial x}\bigg|_{x=0} = 0 \tag{4.18}$$

$$-k\frac{\partial X(x,t)}{\partial x}\bigg|_{x=L} = 0 \tag{4.19}$$

More complete interpretation and analysis of the sensitivity coefficient can be found in [7]. However, it should be noted that the similarities between Equation Groups (3) and (5) allow for the use of the same (or slightly modified) solution methodology. (For example, a finite difference solver developed to numerically integrate equation group ref may also be used to solve equation group ref). Solution algorithms taking advantage of this similarity can gain significant computational savings

[7].

If allowed, an exact analytic solution to the partial differential equations describing the transient heat flow may be used to integrate the temperature and sensitivity fields. However, due to the particular boundary conditions and composite nature of the system of interest (4.2), a discretized approximation (finite-difference) is used to evaluate equation groups ref and ref. It should also be noted that the discretized approximation to the governing system can easily be modified to accommodate temperature-dependent thermal-physical properties [90] and imperfect thermal contact at the material interface [77] further extending the flexibility of the SFSM.

With the appropriate temporal/spatial temperature field modeled, an initial surface heat flux estimate, $q*$, is prescribed as the boundary condition at surface $x = 0$. The resultant system of equations is tridiagonal and the numerically integrated is completed via the Thomas Algorithm [81] over the current time step, M, plus r future time steps.

The use of future time steps is a critical component of Becks SFSM. It provides a means of 'regularizing' the solution methodology, stabilizing the algorithm, and minimizing the impact of measurement error and/or noise [41]. It does, however, rely upon the temporary (and potentially incorrect) assumption that the heat flux remains constant over all r future time steps. Thus, the use of excessively large future time steps may mask high-frequency components of the estimated surface heat flux. Large r values also impact phasing of the estimated heat flux event, [90]. A more complete discuss of regularization (including the use of future time) is developed in the next section.

The temperature $T(x_k, t_M)$ predicted by the finite difference model at the sensor location x_k for the current time-step t_M is then compared to the recorded temperature, $Y(x_k, t_M)$ at the same spatial/temporal conditions. The difference between the modeled and measured values is then expressed as a sum of squares, and is commonly defined as the 'Objective Function', S:

$$S = \sum_{i=1}^{r} [Y(x_k, t_{M+i-1}) - T(x_k, t_{M+i-1}, \mathbf{q}_M)]^2 \tag{4.20}$$

This difference function is minimized at each time step by differentiating S with respect to the estimated heat flux q_M, and setting the resultant equation equal to zero:

$$0 = \frac{\partial S}{\partial \mathbf{q}_M} = -2 \sum_{i=1}^{r} [Y(x_k, t_{M+i-1}) - T(x_k, t_{M+i-1}, \mathbf{q}_M)][\frac{\partial T(x_k, t_{M+i-1}, \mathbf{q_M})}{\partial \mathbf{q}_M}] \tag{4.21}$$

It should be noted that Eq. ref may be re-written in-terms of the 'Sensitivity Coefficient', X_k, i, from Eq. ref: such that:

$$0 = \frac{\partial S}{\partial \mathbf{q}_M} = -2\sum_{i=1}^{r}[Y(x_k, t_{M+i-1}) - T(x_k, t_{M+i-1}, \mathbf{q}_M][X_{k,i}] \tag{4.22}$$

Since heat flux is assumed constant and continuous over r future time steps, the modeled temperature $T(x, t, q_M)$ may be represented as a Taylor Series Expansion about the initial heat flux estimate, $q*$. Neglecting higher-order terms, T may be re-expressed as:

(4.23)

And, using Eq. ref:

$$T(x_k, t_{M+i-1}, \mathbf{q}_M) = T(x_k, t_{M+i-1}, q^*) + (\mathbf{q}_M - q^*)X_{k,i} \tag{4.24}$$

This expression is used in conjunction with Eq. ref to solve for q_M:

$$\mathbf{q}_M = q^* + \frac{\sum_{i=1}^{r}[Y(x_k, t_{M+i-1}) - T(x_k, t_{M+i-1}, \mathbf{q}_M][X_{k,i}]}{\sum_{i=1}^{r}(X_{k,j})^2} \tag{4.25}$$

To further simplify this result, a 'Gain Coefficient' may be defined where:

$$K_{k,i} = \frac{X_{k,i}}{\sum_{i=1}^{r}(X_{k,j})^2} \tag{4.26}$$

This allows Eq. ref to be re-expressed concisely:

$$\mathbf{q}_M = q^* + \sum_{i=1}^{r}[Y(x_k, t_{M+i-1}) - T(x_k, t_{M+i-1}, \mathbf{q}_M][K_{k,i}] \tag{4.27}$$

This final expression hints at the elegance of Beck's procedure the estimated surface heat flux for time step M can be expressed as an initial guess $q*$, modified by a correction term. Furthermore, the correction term represents a summation of magnified differences (i.e. 'errors') between measured temperature (Y) and modeled temperature (T) across r future time-steps. Larger differences result in larger correction terms. The relatively straightforward structure of this important result lends itself to efficient adaptation within algorithm-based IHCP solvers. The solution procedure is extended to time-step $M+1$, with the surface heat flux estimate from the previous time-step

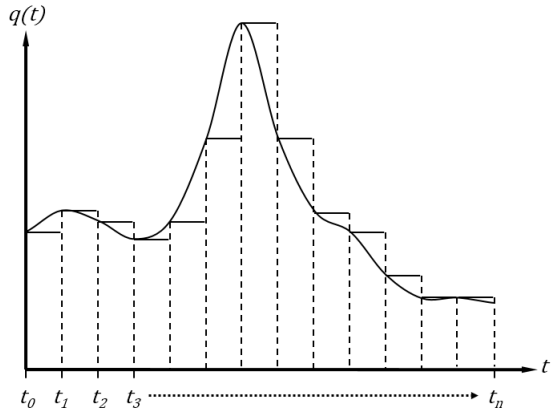

Figure 4.3: Piece-wise estimate of a continuous function. Note: The estimate assumes a constant value of q between times steps. Also, the step width $(t_{n-1} - t_n)$ has been deliberately exaggerated. In general, a much finer time step is achieved, resulting in more accurate approximations of the continuous function $q(t)$.

(i.e., q_M) taking the place of $q*$. The correction term is again calculated and applied to $q*$, after which the estimation procedure advances to the next time step. This process continues over $N - r$ time steps where N represents the total number of samples in Y. Once complete, a 'piece-wise' approximation of the functional form of the surface heat flux is obtained.

The 'non-iterative' nature of the SFSM further enhances computational efficiency. Unlike convergence-based solution procedures, the Sequential Function Specification Method applies a single correction term, as determine by Eq. ref, to the heat flux estimate $q*$ at each time step. This provides 'exact' closure on the measured temperature value within the accuracy retained by the truncated Taylor Series of Eq. ref For an idealized case, where all thermal-physical properties, spatial dimensions, and temperature measurements are known to infinite precision, the exact matching scheme results in an exact solution. However, under the inevitable influence of noise, measurement uncertainty/error, etc., this exact matching criterion contaminates the solution with these imperfections. In other words, when the objective function S is minimized, the modeled temperature T approaches Y regardless of the measured temperature's integrity/accuracy. As mentioned, the inclusion of future time-steps within the solution methodology helps to counteract the influence of measurement uncertainty. However, further regularization is often necessary to more effectively counteract the influence of data noise and/or error.

4.1.4 Regularization and Future Time Steps

Unlike convergence based solution procedures [38], the sequential function specification method applies a single correction term, as determined by Eq. 4.27, to the heat flux estimate q^* at each time step. This provides "exact" closure on the measured temperature value within the accuracy retained by the truncated Taylor series (Eq. 4.23). Simply stated, the objective function S (which describes the 'error' between modeled and measured temperatures) is minimized regardless of the integrity of the measured signal. In reality, the experimentally derived measurement array Y is subject to noise, error, and uncertainty. As a consequence, inverse solution methodology is inherently subject to the various 'impurities' associated with inexact instrumentation and noisy experimental data.

Within the SFSM, the solution methodology is particularly sensitive to signal contaminants during the minimization of the Objective Function (Eq.'s 4.21 and 4.22). From a qualitative standpoint, it is helpful to remember that surface heating (or cooling) events have a diminishing influence on the temperature profile at interior spatial locations. Simply put, a heat flux applied to the surface has less impact (in terms of the magnitude of the associated temperature response) at locations near the 'backside' dimension (i.e., the positions nearing $x = L$ in Fig. 4.2).

In some key aspects, this surface-to-interior signal attenuation represents a key challenge of inverse problems. Simply, the 'solution direction' is reversed when evaluating the IHCP, i.e. interior measurements are used to extract surface heat flux and temperature profiles. Accordingly, signal error present at the interior (sub-surface) sensor location is amplified (rather than attenuated) as the solution methodology marches toward the surface. As a result, seemingly 'subtle' temperature noise/error at the sensor location can overwhelm the SFSM solution estimate at the surface.

To combat the SFSM's extreme sensitivity to noise/measurement-error, various forms of regularization have been proposed, including methods attributed to Tikhonov and Arsenin [89], Alifanov [3], and Bell and Wardlaw [10], among others [7].

In keeping with the sequential nature of the SFSM, a sequential regularization technique is considered as formulated by Beck, et.al, in [7]. This scheme adds multiple 'regularization terms' of increasing order to the Objective Function, S. These terms effectively 'relax' the exact matching constraint between observed and modeled temperatures required during the error minimization process outlined in Eq.'s 4.21 and 4.22. For clarity, the modified objective function S_{Reg} with 0^{th}

through 2^{nd} order regularization terms is shown below.

$$S_{Reg} = \sum_{i=1}^{r}[Y_{M+i-1} - T_{M+i-1}]^2 + \beta W_0 \sum_{i=1}^{r} {q_i}^2 + \beta W_1 \sum_{i=1}^{r-1} q_{i+1} - {q_i}^2 + \beta W_2 \sum_{i=1}^{r-2} q_{i+2} - q_{i+1} + {q_i}^2 \tag{4.28}$$

W_0, W_1, and W_2 are binary coefficients (meaning their values are limited to 0 or 1), and are used to modify the objective function when selecting the desired order of regularization. The parameter β is a fixed multiplier preceding the regularization terms and is used to help determine the overall gain of the regularization. This coefficient is often defined in-terms of the statistical characteristics inherent to the temperature measurements. Commonly, temperature measurement variance at the sensor location is normalized by the magnitude of the heat flux estimate at each time step. Accordingly, this statistically-driven metric may be expressed as:

$$\beta = \left(\frac{\sigma_i}{q_i})\right)^2 \tag{4.29}$$

(Here, σ_i and q_i represent the variance in temperature measurement and the magnitude of surface heat flux estimated at sensor location i). The first term in of equation ref reflects the standard objective function described in Eq. ref. The second through fourth terms introduce regularization. For clarity, these terms may be interpreted as discretized approximations of the heat flux magnitude, its 1st order time rate of change, and its 2nd order time rate of change evaluated over the interval [tn, tn+r]. In other words, the summations involved in the second through fourth terms of Eq. ref may be interpreted as discrete approximations of their continuous analogs, i.e.

$$\beta W_0 \sum_{i=1}^{r} {q_i}^2 \sim \beta W_0 {q_i}^2 \tag{4.30}$$

$$\beta W_1 \sum_{i=1}^{r-1} q_{i+1} - {q_i}^2 \sim \beta W_1 \int_{t_n}^{t_{n+r}} \left(\frac{dq}{dt}\right)^2 dt \tag{4.31}$$

$$\beta W_2 \sum_{i=1}^{r-2} q_{i+2} - q_{i+1} + {q_i}^2 \sim \beta W_2 \int_{t_n}^{t_{n+r}} \left(\frac{d^2q}{dt^2}\right)^2 dt \tag{4.32}$$

As such, the 0th-order term (4.30) impacts the magnitude of the estimated heat flux, the

1st-order term (4.31) addresses the time rate of change in estimated heat flux, while the 2nd-order term (4.32) influences higher-order variations within the surface heat flux estimate.

The use of 'future time' is, in of itself, a method of regularization. That is to say, the surface heat flux estimate becomes less sensitive to signal contaminants as it is (artificially) held constant beyond the current time step t_M. However, increasing r indefinitely is not without consequence, and as such, a few words regarding the impact of "future time" inclusion is warranted. As mentioned in the preceding section, the use of future time steps within the framework of the SFSM requires the temporary (and potentially incorrect) assumption that surface heat flux remains constant over $t_M \rightarrow t_{M+r}$ time interval. As a result, excessively large r values may mask high-frequency components within the estimated surface heat flux. They may also distort phasing of the solution [90]. Methodological adaptations developed to avoid this type of over-regularization will be developed in the proceeding section. It should be noted that the SFSM calculations presented in this dissertation are limited to $r = 3$ future time steps.

Regularization of ill-posed problems is itself an active area of research. Many appraoches have been explored, with certain techniques taylored to specific applications, etc. A more complete discussion of Regularization can be found in the literature, inluding references [7], [76], [3], and [89].

4.1.5 A Few Words Regarding Uncertainty

This section will overview uncertainty estimation within the framework of the Sequential Function Specification Method. A concise overview of is provided below.

As an alternative to the 'Gain Form' of Beck's SFSM (i.e., 4.27), an equivalent expression may be constructed using 'Filter Coefficients'. Expressing the initial temperature as T_o, the 'Filter Form' of the SFSM is written as follows:

$$\mathbf{q}_M = \sum_{i=1}^{M+r-1} \frac{\delta q_{M+r-i}}{\delta Y_r}(Y_i - T_o) \tag{4.33}$$

(Note: For now the validity of this expression will be taken 'for granted. A more complete derivation of this expression may be found in [7], for now we will proceed using the outcome of the cited work, avoiding a more rigorous treatment.)

The differential term $frac\delta q_{M+r-i}\delta Y_r$ describes a 'Filter Coefficient'. In general, this approach to the IHCP utilizes the superposition principle, and as such, is restricted to linear (in

temperature) heat diffusion systems. Using Eq. 4.33, the solution of the governing equation is decomposed into an arbitrary number of temperature components $(Y_1, Y_2, Y_3, Y_4, \cdots, Y_j)$ each with an associated heat flux. The total surface heat flux at time t_M is then represented by the sum of individual heat flux components spanning the interval $t_o \rightarrow t_{M+r}$, where r again represents the number of future time steps. In addition to linearity, a few statistical assumptions are also necessary to employ the 'Filter Coefficient' approach. These include: (i) random/additive temperature measurements, (ii) zero mean measurement errors, which remain (iii) uncorrelated.

To provide a representative example of this alternative SFSM approach, we will decompose the surface heat flux (via the superposition assumption) into $j = 4$ components. Further generalizing for the case where $r = 3$, we can write:

$$\frac{\delta q_M}{\delta Y_j} = 0, \text{ for } j > M + r - 1 \tag{4.34}$$

This initial relation simply ensures that no contributions are made from times beyond the specified 'future time' window, (i.e., $j > M + r - 1$). For all other times ($j \leq M + r - 1$) we can expand the filter coefficient of Eq. 4.33 as follows:

$$\frac{\delta q_M}{\delta Y_j} = \begin{array}{l} \frac{\delta q_1}{\delta Y_3} = \frac{\delta q_2}{\delta Y_4} = \cdots = \frac{\delta q_M}{\delta Y_{M+r-1}} \\ \frac{\delta q_2}{\delta Y_3} = \frac{\delta q_3}{\delta Y_4} = \cdots = \frac{\delta q_M}{\delta Y_{M+r-2}} \end{array} \tag{4.35}$$

Keeping in mind that we seek to express uncertainty of the SFSM's heat flux estimate, i.e., q_M, as a function of the variance in measured subsurface temperatures, we again rely on the more thorough development of Beck et al. [7], and present the follow relation:

$$var(\mathbf{q}_M) = \sigma^2 \sum_{i=1}^{M+r-1} (\frac{\delta q_{M+r-i}}{\delta Y_r})^2 \tag{4.36}$$

In the above expression, σ represents the standard deviation of temperature over the time interval of interest. Although the SFSM procedures outlined in Eq.'s 4.27 and 4.33 utilize a 'phase averaged' temperature profile (discussed below), individual cycles statistics are used to calculate the σ^2 term in Eq. 4.36.

A few cursory comments regarding signal conditioning are warranted. For the analysis contained within this dissertation, temperature profiles from both ex situ (i.e., 'Radiation Chamber') and in situ (i.e., 'Engine') environments are recorded over many hundreds of consecutive cycles -

400 and 500, respectively. Given the quasi-steady state operation of both experimental platforms, individual cycle temperature measurements are phase-averaged to produce a representative, and substantially 'cleaned' temperature profile. In general, the averaging process attenuates non-coherent ("Gaussian") noise present in both of the aforementioned experimental environments - producing temperature profiles with dramatically enhanced signal-to-noise ratio. A more comprehensive discussion of pre-processing efforts is developed in the proceeding chapter. For now, the reader is reminded that the "ill-posedness" of the IHCP renders any solution methodology extremely sensitivity to noise contamination and measurement error.

4.2 Modified SFSM with Direct Measurement of Diffusive Time Scale

This section modifies the SFSM via inclusion of a diffusive time scale. Efforts are made to quantify the time-lag between a specific surface temperature 'event' and its subsequent response at subsurface temperature probe. A review of parabolic heat diffusion is provided, followed by suggested methodology for estimation and eventual measurement of the surface-to-sensor time lag.

4.2.1 Defining the Experimental and Diffusive Time Scales

Thus far, the heat diffusion models considered are parabolic in nature [45] - (see Eq.'s 4.1, 4.5, and 4.16). An inherent characteristic of parabolic systems is the instantaneous transfer of 'information' throughout the entire domain of interest. For the heat diffusion and sensitivity problems described by the aforementioned equation sets, this implies that a change in surface heat flux will immediately impact the temperature (or sensitivity) throughout the entirety of the spatial domain. In other words, a change in heat flux at the surface will instantaneously impact all subsurface temperatures. This behavior is clearly not physical, and is strictly an artifact of the parabolic mathematical form of the governing equations.

For direct conduction problems, the parabolic heat diffusion equation generally avoids complications associated with this non-relativistic behavior. In contrast, when solving the parabolic form of the IHCP, it is important to properly account for the time-lag between a surface heat flux event and its detection at subsurface locations. (This is particularly true when the time-scales

associated with data acquisition and surface-to-senor diffusion become large.) As will be shown, the inverse heat transfer problem and the solution methodology associated with the SFSM may be further enhanced through use of multiple time regimes.

In this work, the experimental time-step δt is largely determined by the fidelity of the temperature sensor and the sampling frequency of the corresponding data acquisition system. In general, a sampling frequency atleast twice as large as the transient behavior of interest is required to avoid aliasing during analogue-to-digital conversion. (See Ref. [75] for more complete signal processing details). Higher sampling frequency also enables more targeted filtering during post-processing.

In order to characterizes the surface-to-sensor measurement lag within the IHCP, it is first necessary to establish a time scale which characterizes the interval between data points:

$$\Delta t = t_M - t_{M-1} \tag{4.37}$$

The interval Δt defines the "experimental" time-step, and is typically determined by sampling frequency and operational speed (i.e., RPM).

In addition to experimental time, it is necessary to quantify the "diffusive time scale" which defines the characteristic time lag between surface heating/cooling events and subsequent detection at the sensor location. Two distinct methods to quantify this interval are considered. The first, developed below, utilizes dimensional analysis. Simple manipulation system's thermal physical properties and relevant physical dimension(s) yields the follow expression:

$$t_\alpha = \frac{x_{Sensor}^2}{\alpha} \tag{4.38}$$

In this expression α, on the right-hand side of the equation, is the effective thermal diffusivity of the system (in m^2/s or compatible units) while x_{Sensor} is the location of the temperature sensor relative to the surface (in m). As a result, t_α has units of time and, as discussed, defines a characteristic time-scale for surface 'information' (in the form of temperature variation) to reach the sensor. In the absence of direct measurement, this material-property based method offers an 'order-of-magnitude' approximation of the time lag due to finite thermal wave speed.

It should be noted that any error in the sensor position relative to the surface, (a metric driven by the TBC thickness in the current study), will directly impact the accuracy of the dif-

fusive time scale. Likewise, errors associated with the specified thermal diffusivity, α, will further undermine the integrity of t_α.

In addition to a 'stand-alone' parameter, thermal diffusivity may be expressed as the ratio of thermal conductivity k to volumetric heat capacity ρC_p such that:

$$\alpha = \frac{k}{\rho C_p} \tag{4.39}$$

Using the above relation, an expression equivalent to the diffusive time introduced in 4.40 may be written:

$$t_\alpha = \frac{\rho C_p x_{Sensor}^2}{k} \tag{4.40}$$

Again, any error in the k and/or ρC_p parameters will directly impact the diffusive time-scale estimate.

A few closing remarks regarding the parameter-based estimate outlined above. In general, this 'order-of-magnitude' assessment is most applicable to thermal systems experiencing a step-change in heat flux at the surface boundary. For periodic boundary conditions, such as those experienced in the engine environment, the diffusive time scale becomes a function of the 'driving' frequency of the combined heating/cooling even(s). As will be shown in the next chapter (by drawing upon an 'exact' solutions to heat diffusion equation), the diffusive time-scale can be modified to better reflect the periodicity of the heating event in both radiation chamber and engine environments.

4.2.2 Normalized Diffusive Time in the Context of Parabolic Heat Diffusion

To better assess the impact of the diffusion-driven lag on IHCP solution methodology, it is helpful to normalize t_{alpha} by the experimental time step. This simply re-expresses the diffusive time-scale (originally reported in seconds) as an equivalent number of dimensionless time-steps. This process is formalized in the following transform:

$$\tau_N = \frac{t_\alpha}{\Delta t} \tag{4.41}$$

To simplify analysis, τ_N should be expressed in whole number intervals - i.e., Eq. 4.41as is

rounded to the nearest integer value.

Normalization of the diffusive time-step effectively distinguishes between systems with 'instantaneous-like' thermal wave speed (where the coarseness of the measurement interval masks the time-lag of the finite wave speed) and those where multiple time-intervals are required for surface transients to 'register' at subsurface locations. These regions, and their implications, are formalized below.

4.2.2.1 'Effective Parabolic' Regime

For cases where $\tau_N 1$, the transmission of surface information to the sensor location may be considered instantaneous. Simply put, the full spectral frequency of the 'continuous' system's transient event(s), (in our case analog voltage generated at subsurface thermocouples), can not be fully resolved. Under these conditions, the diffusive time lag is masked by the coarseness of the experimental time-step. This scenario appears to be the case in many of the 'traditional' inverse heat transfer configures explored during the time of Beck's pioneering work [7]. These early efforts were focused primarily on developing/exploring the conceptual framework required to tackle the demands unique to inverse heat transfer. Furthermore, data from experimental IHCP configurations of this time was often limited by the fidelity of the available hardware of the period (data acquisition systems, analog-to-digital converters, etc.) Course data arrays were also necessary to satisfy the computational bandwidth of the day - particularly when thermophysical complexity required numerical solutions to the equations governing heat transfer, sensitivity coefficients, and the SFSM estimation.

As a result, systems with relatively 'moderate' transient components and sparsely-sampled temperature fields could be adequately treated within a purely parabolic mathematical framework.

4.2.2.2 'Effective Hyperbolic' Regime

In contrast to the $\tau_N 1$ region, the surface-to-sensor time lag cannot be ignored when high fidelity (i.e., 'finely' sampled) temperature measurements are available. In this case, where $\Delta t < t_\alpha$ and $\tau_N > 1$, the surface temperature transient will not immediately 'register' at the subsurface sensor location. Instead, a 'record' of this transient will only arrive at the subsurface sensor once t_α seconds have elapsed. In this way, the subsurface temperature response will temporally lag the surface temperature transient throughout the measurement sequence.

Under these conditions, the SFSM algorithm presented in Eq. 4.27 can not adequately

resolve the surface transient. Under this scenario, closure between the measured temperature (i.e., Y) and the modeled temperature (i..e, T) becomes difficult, often leading to solver instability.

Recall, at each time step m the SFSM attempts to minimize the $(Y(m) - T(m))$ interval by modifying the surface heat flux estimate q_M. If the temperature field at the sensor location lags the surface heat flux transient, as is the case for $\tau_N > 1$, the surface heat flux and subsurface temperature difference are temporally 'disjointed', and it remains physically unreasonable to expect closure. However, the SFSM algorithm is unaware of this physical 'disconnect' - and continues to inflate the magnitude of q_M in an effort to banish the error between modeled and measured temperatures. As one may anticipate, when τ_N becomes sufficiently large, the surface heat flux estimate will inflate exponentially towards infinity in a desperate effort to influence the temperature response.

A common approach to combating SFSM-based solver instability involves increasing the number of future time-steps, r. As mentioned previously, an excessively large increase in the number of future time steps tends to 'smooth' the surface heat flux estimate. One can think of increasing r as inflating the mathematical 'stiffness' of the solver - helping to reduce sensitivity to noise/error, but also limiting the solver's ability to respond rapidly to changes in subsurface temperature. Thus, if the relative difference between the diffusive and computational time steps necessitates an excessively large number of future time steps for stability, the SFSM (as described by 4.27) may be unable to resolve the highest frequency components of the function of interest, is any.

4.2.3 Inclusion of Diffusive Time Steps in SFSM

As an alternative to excessive future time steps, it is possible to modify Becks form of the SFSM to recognize both computational and diffusive time scales. This possiblity has been regonized before - see [55] for an alternative approach.

A simplified methodology is developed below. For the work considered in this dissertation, the normalized diffusive time step τ_N can temporally 'offset' the surface heat flux transients from subsurface temperature variations in a manner that is consistent with physical reasoning. That's to say, we can use the order-of-magnitude analysis of 4.40 (or more accurate measurements discussed in the next section) to account for the hyperbolic behavior of the $\tau_N > 1$ regime while maintaining a parabolic diffusion model. Simply stated, we are altering the estimation algorithm of Eq. 4.27 without modify the mathematics used to model the thermal system.

In practice, this modification is achieved by direct substitution of the diffusive time step into Eq. 4.27:

$$\mathbf{q}_M = q^* + \sum_{i=\tau_N+1}^{\tau_N+r} [Y(x_k, t_{M+i-1}) - T(x_k, t_{M+i-1}, \mathbf{q}_M][K_{k,i}] \tag{4.42}$$

From a qualitative point-of-view, the modification outlined above 're-aligns' the surface heat flux transient with it's response at the sensor location. This is achieved by imposing a finite time offset (i.e., t_N) between heat flux transients applied to the front-side boundary and their subsequent detection at the sensor.

Furthermore, solver instability due to the temporal misalignment discussed in 4.2.2.2 is greatly reduced, and large numbers of future time steps are no longer needed to regularize the SFSM algorithm.

It is worthwhile to note that the general 'form' of Beck's procedure remains unchanged. Again, because the governing equations are the same parabolic equation sets shown in Eq.'s 4.11-4.14 and 4.16-4.19, the mathematical arguments leading to 4.27 and 4.42 still hold. From a practical point of view, this enable the same set of solution methodology (i.e., 'exact analytic', 'numerical', etc.) as those permitted by Beck's original estimation routine.

4.2.3.1 Direct Measurement of Diffusive Time Scale

Utilizing the ex-situ experimental apparatus discussed in the preceding chapter, two probes are simultaneously subjected to the same heat square flux pulse. One sensor remains uncoated and, as a result, provides direct measurement of the surface temperature. The second probe has a low conductivity TBC applied to it's surface measurement junction. As a result, the temperature response of the TBC probe represents the sub-TBC temperature field. As outlined in the description of the experimental setup, the fidelity of the sensor and the high frequency sampling-rate enabled by the DAQ hardware provide microsecond-resolved temperature profiles at each probe location an example of which can be seen in Fig. 4.4.

The radiation chamber is operated under quasi steady-state conditions (i.e., fixed rotational speed, constant power delivery to heating element, etc.) and 400 consecutive cycles are recorded at each probe location. These individual cycles are phase-averaged, and any remaining coherent noise is treated with an appropriate filter. (Note: Specifics of the phase-averaging and signal processing

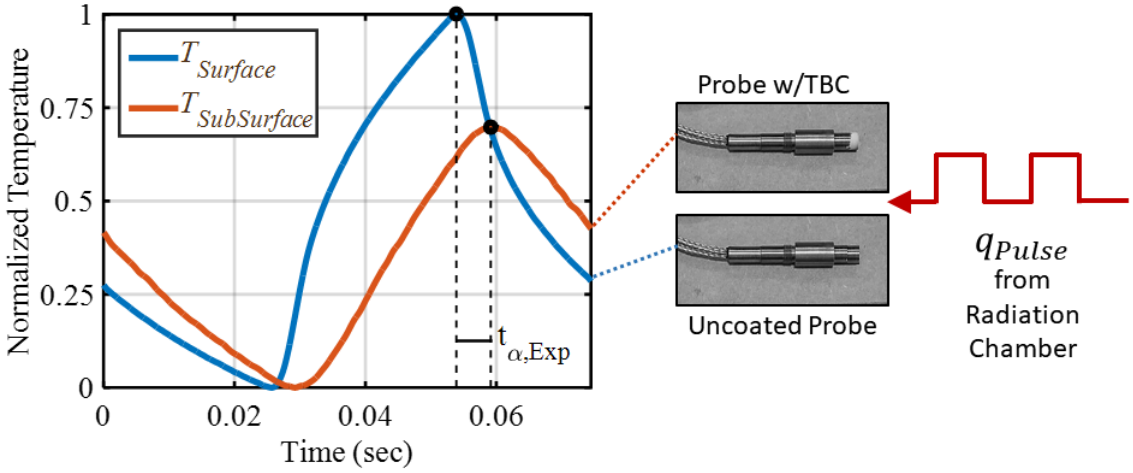

Figure 4.4: Ex situ temperature response for uncoated and TBC-treated probes. The delay associated with the peak temperature value of the TBC trace is directly attributable to the diffusive time delay t_α. (Note: To enable a more direct comparison, both temperature profiles have been normalized by the maximum surface temperature.)

routines will be explored in complete detail in the next chapter. For now, the reader is asked to accept that the data processing decisions outlined above are 'reasonable'.)

As a result of the pre-processing/filter efforts and the quasi-steady chamber operation, the phase-average traces shown in Fig 4.4 exhibit excellent signal-to-noise characteristics and remain representative of actual cycle dynamics. Furthermore, the maximum temperature value recorded at each probe location can be identified directly. In this way, the difference in arrival time between respective maxima represents the diffusive-time lag for the chambers specific operating conditions.

This procedure is formalized below:

$$t_{\alpha,Exp} = t_{max,Surface} - t_{max,SubSurface} \tag{4.43}$$

And, re-expressing as non-dimensionalized diffusive time-steps:

$$\tau_{N,Exp} = \frac{t_{\alpha,Exp}}{\Delta t} \tag{4.44}$$

Again, $\tau_{N,Exp}$ is expressed as a whole number by rounding the result of 4.44 to its nearest integer value.

(Note: The experimental t_α shown in Fig. 4.4 is a function of the frequency of the surface

heat flux event in the chamber. As a result, diffusive time-scales measured in the chamber environment will not translate directly to engine measurements. In practice, the chamber-derived t_α must be scaled to match the engine's operational parameters, including: rotational speed, number of 'heating events' per rotation, etc.)

In general, the empirically-derived diffusion time interval defined above (4.44) offers key advantages relative to parameter based estimates (4.41). Most obvious is the absence of the uncertainty/error which often accompanies ill-defined thermophysical properties. This inaccuracy is essentially bypassed by the direct measurement method.

Furthermore, even in the hypothetical extreme, when 'ideal' conditions are present and thermophysical/spatial parameters are known to infinite precision, the influence of secondary heat transfer parameters (e.g. thermal contact resistance at each layer, porosity fraction, etc.) may only be known to gross approximations. Experimental evaluation of the τ_α term inherently accounts for all resistances within the heat transfer pathway. Ultimately this enables a more 'physical' description of the diffusive time.

4.2.4 Ex Situ Modified SFSM Results

The theoretical background and methodological adaptations of the preceding sections are used to write an SFSM-based IHCP solver. Specifically, this algorithm minimizes the objective function described by Eq. 4.20 using the modified SFSM (i.e., Eq. 4.42).

The ex situ randation chamber is used to evaluate the quality of the SFSM-derived heat flux. Specifically, the spatial uniform surface boundary condition (q_{Surf}) is applied simultaneously to both 'untreated' (i.e., metal) and 'TBC-treated' probes. An Air Plasma Sprayed (APS) Yittria Stabilized Zirconia (YSZ) thermal barrier is used exclusively during the validation effort. The coating layer is $100\mu m$ thick with minimal porosity fraction. A nickel-based bondcoat layer ($50\mu m$) is applied between the probe's metal surface and the main TBC to ensure adequate stress relief.

As discussed previously, raw temperature data is recorded over several hundred cycles, at which point the individual cycles are phase-averaged, digitally filtered, and smoothed to enhance signal quality. The results of this effort for the TBC-treated probe are shown in figure 4.5.

Direct surface measurements from the metal probe undergo similar pre-processing treatment. The resulting phase-averaged data is used in conjunction with Fourier decomposition processing techniques [18, 37] to calculate the surface heat flux. This 'direct' analytic analysis of surface

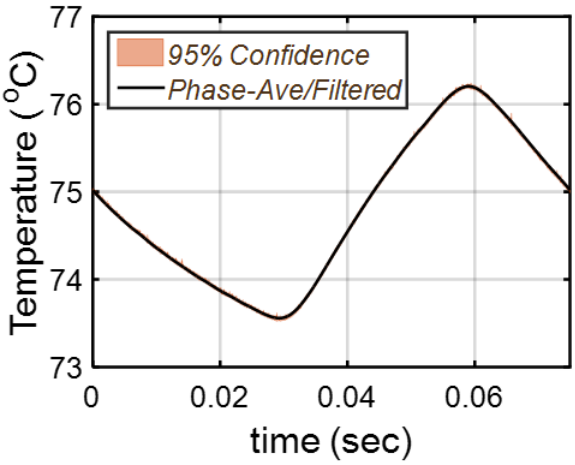

Figure 4.5: Phase-averaged and filtered sub-TBC temperature trace from the radiation chamber. The 95% confidence region is only slightly larger than line thickness.

heat flux assumes a 1D conduction pathway (as does the SFSM), and provides a well-established benchmark with which judge the outcome of the inverse analysis.

Results for inverse and direct methods are displayed in Fig. 4.6.

Minimization of the objective function effectively 'closes' the difference between measured (Y) and modeled (T) temperature traces. This is demonstrated by the overlapping profiles in Fig. 4.6 (a). As a result, TBC surface heat flux estimates from the modified SFSM correlate quite well with the direct calculations of surface heat flux as can be seen in Fig. 4.6 (b). Moreover, the phasing and magnitude of the inverse heat flux solution is consistent with the metal probe results, and thus the solution of the corresponding direct problem.

Of particular significance is the ability of the TBCs surface temperature to dramatically 'swing' in response to the heating and cooling events see Fig. 4.6 (c). This is primarily due to the low thermal conductivity, limited heat capacity, and relative 'thinness' of the YSZ layer. Importantly, this initial experimental analysis, reinforcing the exaggerated dynamic profile of the "low conductivity/low heat capacity" coating material conceptualized in the modeling work of the preceding chapters. The impact of elevated surface temperatures on combustion and cycle performance metrics will be explored in detail in a later chapter. For now, the reader is asked to consider the agreement between the direct and inverse heat flux calculations.

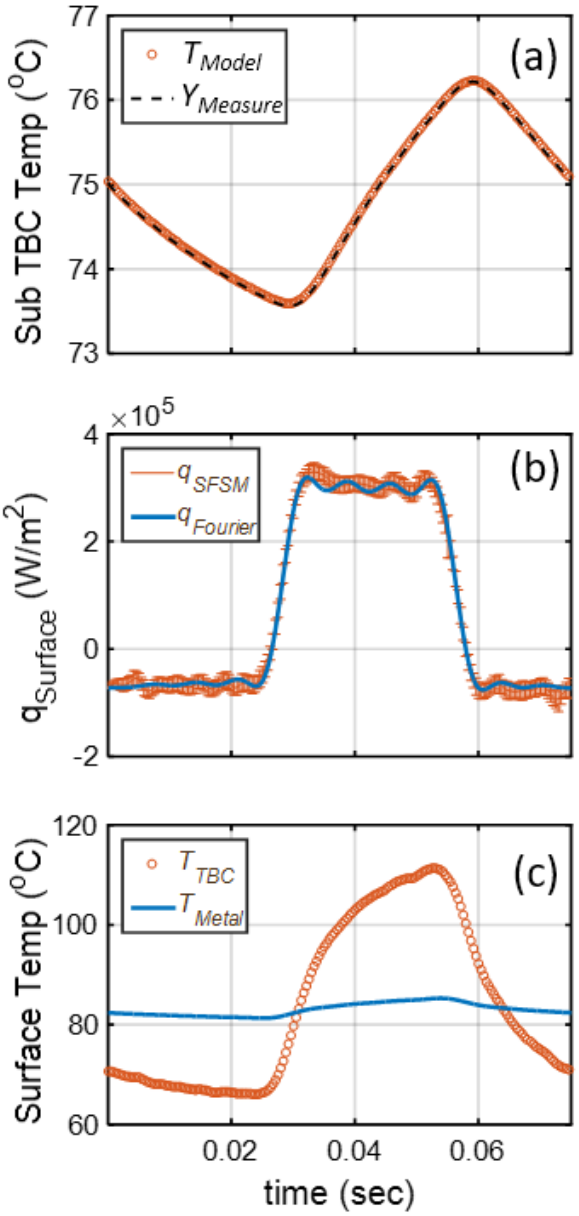

Figure 4.6: Successful minimization of the objective function S (as defined by Eq. ref) yields similar measured and modeled temperature profiles at the sensor location: (a) "direct" and "inverse" solutions to the surface heat flux, (b) the SFSM estimate is bounded by its uncertainty and the associated surface temperature profiles are also provided (c). Notice the dramatic increase in temperature swing magnitude for the TBC surfacethis is a direct consequence of the order of magnitude decrease in thermal conductivity of the coated probe versus its metal counterpart. Layer 'thickness' and the volumetric heat capacity (i.e., ρC_p) also impact the magnitude of the surface temperature profile.

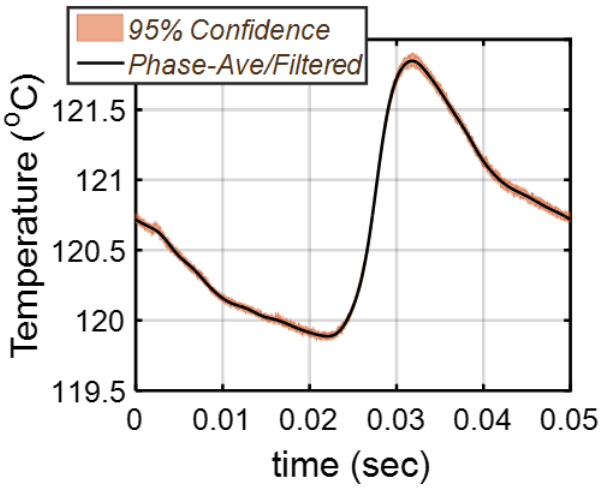

Figure 4.7: Phase-averaged and filtered sub-TBC temperature trace from the experimental engine during fired operation at 1200 RPM. The 95% confidence region is slightly larger than that found in the radiation chamber - the likely result of increased noise contamination and cyclic variability.

4.2.5 Application of Modified SFSM to In Situ Engine Measurements

With the SFSM algorithm validated ex situ, the IHCP solver is extended to derive surface temperature and heat flux profiles within the firing HCCI engine detailed in previous. The same fast response heat flux probes used in the radiation chamber are mounted within the cylinder head of the research engine. Plasma-sprayed YSZ is again selected as the primary TBC material. The engine is operated in multiple configurations (i) 'uninsulated' where uncoated heat flux probes are paired with an uncoated aluminum piston, and (ii) 'insulated', where a TBC-coated probe is paired with a similarly coated piston.

An overview of the pre-processed, sub-TBC, data trace is provided in Fig 4.7. As expected, the phase-averaging/filtering process yields a high-quality, 'averaged' temperature trace which is input to the SFSM-based solver. Close inspection reveals a slightly expanded confidence region relative to the chamber's pre-processed trace. This largely results from the increased noise in the engine environment, i.e., contaminants from both mechanical and electrical sources. As will be outlined in detail in the next chapter, considerable effort is invested in the pre-processing of the engine-derived temperature measurements. The modified SFSM algorithm remains sensitive to excess noise levels, and targeted pre-process can have a dramatic impact on solver outcome.

Unlike the uniform heat source produced by the radiation chamber, engine heat flow is

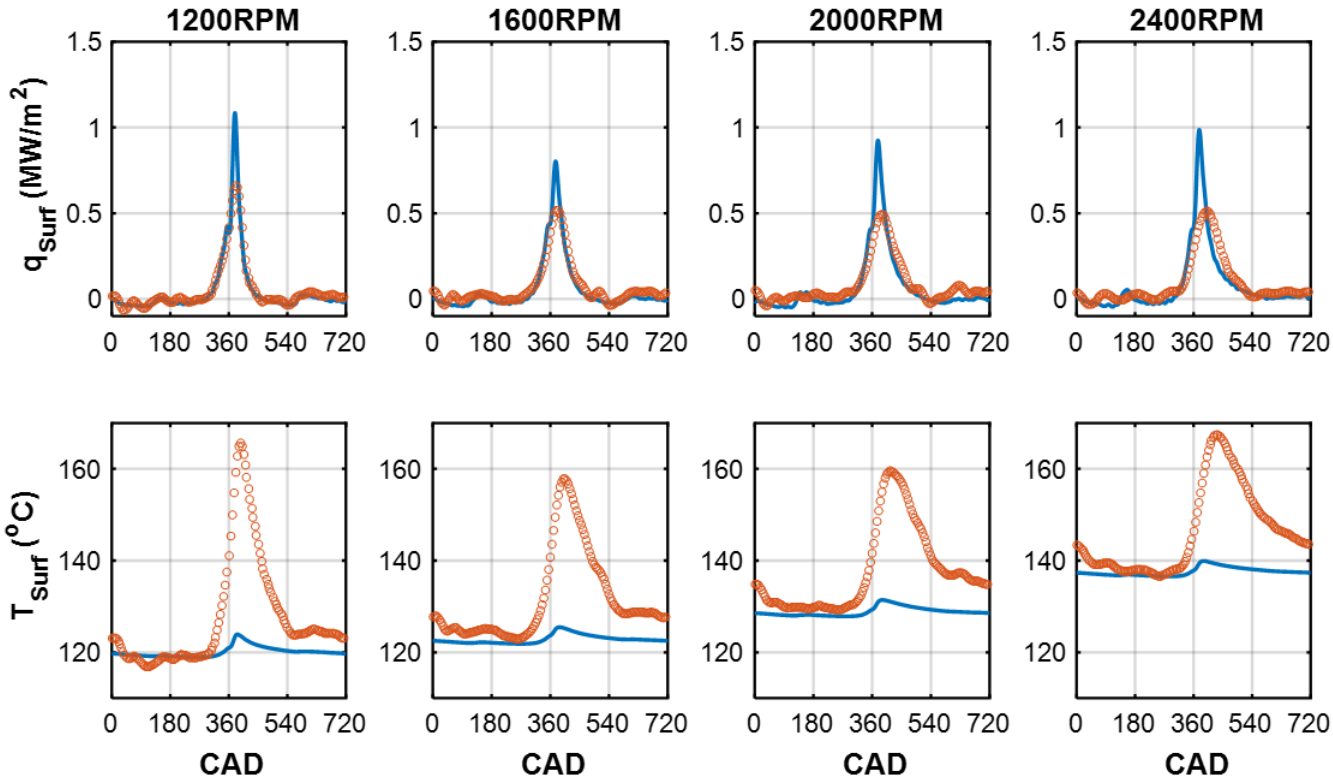

Figure 4.8: 'Direct' and 'inverse' estimates of the surface heatflux for 1200 RPM ($11.7mg/cycleoffuel$), 1600 RPM ($10.5mg/cycleoffuel$), 2000 ($10.3mg/cycleoffuel$), and 2000 ($10.5mg/cycleoffuel$). The associated surface temperature profiles are also provided. The magnitude of the temperature swing at the TBC surface is significantly increased relative to the metal (i.e., uncoated) probe's profile.

both temporally and spatially variant a result of turbulent and reactive gas dynamics. To ensure consistent evaluation between engine configurations, temperature measurements are taken from the same probe location (i.e., "pulley-side"). Operational set-points (AFR, intake temperature/pressure, etc.) are matched for each of the engine configurations to further ensure consistency.

Figure 4.8 summarizes in situ results across multiple engine speeds. Closure terms demonstrate effective minimization of the Objective Function by the modified solver. The general phasing and over-all fidelity of the heat flux event (particularly over CADs spanning compression and combustion) remains consistent between the two engine configurations.

The dynamic characteristic in situ is qualitatively similar to that witness in the radiation chamber. Specifically, the TBC layer exhibits a much exaggerated surface temperature 'swing' during compression and combustion heating (see Fig. (c)). The achieved temperature swing is relatively

sharp, as desired. Surface temperature increases at a high rate towards the end of compression and right after the start of combustion, and it declines back to values typical of the metal surface by the start of the next intake event. The amplitude is highest at 1200rpm. It decreases somewhat at higher speeds as teh swing stretches due to time scale effects.

The SFSM does appear to become more susceptible to signal contaminants throughout the intake and exhaust processes (i.e., 'open-cycle'). As surface temperatures drop during gas exchange, the relative strength of the mechanical noise (including valve actuation) increases degrading the signal-to-noise ratio. As a result, open-cycle temperature measurements generally exhibit higher statistical deviation from mean values. (Beyond it's immediate impact on signal fidelity, this also increases the magnitude of the uncertainty bounds for the q_{Surf} estimate over this range. Thus, the systematic quantification of heat transfer of later chapters will focus on crank angles spanning late compression into the early expansion where signal fidelity is high and uncertainty remains low.)

A few closing remarks with respect to TBCs impact on engine heat transfer, emissions, and efficiency. Given the dominance of convection within the engine environment, any differences in the thermal conditions at the gas-wall boundary (including elevated surface temperatures) will have a dramatic impact on heat transfer. The TBC layer effectively decreases the differential between combustion chamber surface temperature and that of the bulk gas during late-compression and combustion. (Recall the conceptual plot presented at the onset of the modeling work). This helps 'preserve' heat in-cylinder, which has been shown to have an immediate impact on engine performance, emissions, and efficiencies - particularly in the context of low temperature combustion [79]. The analysis enabled by the modified SFSM algorithm helps to elucidate the influence of TBCs on HCCI, enabling quantification of key metrics including surface temperature and heat transfer. This work forms the a major component of the following chapters.

Chapter 5

Error Sources and Limitations of the Inverse Solver: A Closer Look

Development and modification of inverse solution methodology was formalized in the preceding chapter. This section will serve to identify and evaluate the primary source(s) of error and signal degradation (i.e., 'signal loss') related to the SFSM estimates. To better evaluate the integrity of the inverse-derived results, the current section will consider the following three areas: (i) Impacts relating to the discretization of the equations governing the temperature field (i.e., 1-D Finite difference model), (ii) limitation associated with combined effect of low conductivity materials and subsurface temperature measurements, and (iii) signal routing and instrumentation failure(s) specific to the telemetry linkage.

5.1 Validation of Finite Difference Model: A comparison of Exact vs. Discretized Solutions

At the heart of the inverse solver is a discretized version of the governing heat diffusion system treated at length in earlier chapters. A particularly flexible discretization method (commonly know as the "Combined Method" [78]) takes the following form:

$$\frac{T_i^{n+1} - T_i^n}{\Delta t} = \alpha[\theta \frac{T_{i-1}^{n+1} - 2T_i^{n+1} + T_{i+1}^{n+1}}{(\Delta x^2)} + (1-\theta)\frac{T_{i-1}^{n} - 2T_i^{n} + T_{i+1}^{n}}{(\Delta x^2)}] \tag{5.1}$$

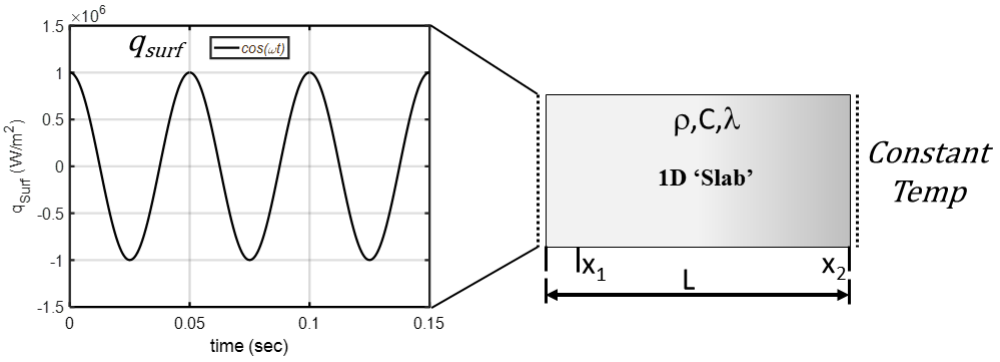

Figure 5.1: A representative schematic of the simplified heat transfer system. To enable an exact solution, a sine function is selected as a representative frontside boundary condition. A constant temperature is applied at the backside boundary, and the slab itself is made of a single, uniform material.

where i references the location (i.e., "node") within the temperature field T at time n. In addition, α represents thermal diffusivity ($\frac{m^2}{s}$), Δx the spatial step in meters (i.e., node spacing or "mesh" resolution), and Δt the time-step in (sec). The coeffecient θ spans teh interval $0 \leq \theta \leq 1$. For cases where $\theta = 0$ 5.1 reduces to a 'simple explicit' form of the difference equation. Likewise, $\theta = 1$ yields the 'simple implicit' variant. A more complete overview of this method can be found in [78]. For now, the reader is asked to consider the case where $\theta = frac12$. This value of θ transforms 5.1 into the "Crank-Nicholson" form of the discretized diffusion equation. Evaluation of the leading truncation error term reveals 2^{nd}-order accuracy in both space and time.

In general, the algorthim for the resulting finite difference equation follows the approach first outlined by Crank-Nicholson method. [45]

5.1.1 Periodic Heating: An Exact Solution Using Green's Functions

To assess the performance of the finite difference model it is helpful to compare its numerical solution against an exact solution (when available) to the governing equations. Typically, exact solutions are limited to relatively simple systems/boundary conditions - which generally limits their application to 'idealized' problems. Despite this lack of range, it's possible to capture the essential dynamics of more complex heat transfer configurations by studying exact solutions of (near) analogous systems when available. This is the approach employed herein.

The TBC treated probe and/or piston is more accurately modeled as a composite slab -

that's to say, multiple layers (with varying thermophysical properties) occupy the space between front and backside boundaries. (See Fig. 4.2 for reference). To simplify analysis, and enable analytical techniques, we will temporarily consider a 'unislab' configuration - a single material system with uniform material properties. Next, we must select a simplified boundary condition which still captures the dynamical 'essence' of those found in both the radiation chamber and engine environments. That's to say, a periodic boundary conditions with peak amplitude of $1\ fracMWm^2$. By exploiting the mathematical symmetry of the cosine function, we can approximate the periodicity of both in situ/ex situ boundary conditions while avoiding the functional complexity (and, in the case of the engine, considerable cycle-to-cycle variability) of both experimental regimes.

The mathematics of the governing system are formalized below:

$$\frac{\partial}{\partial x}(k\frac{\partial T}{\partial x}) = \rho c\frac{\partial T}{\partial t}; 0 < x < L \tag{5.2}$$

$$T(x,0) = T_o(x) \tag{5.3}$$

$$-k\frac{\partial T}{\partial x} = q_o\cos(\omega t) \tag{5.4}$$

$$T(L,t) = T_o \tag{5.5}$$

Note: In an effort to remain consistent with the modeling framework of preceeding chapters, a fixed temperature is applied at the backside boundary. Additionally, the initial temperature profile ($T(x,0)$) is spatial uniform, and set equal to T_o.

In an effort to remove dimensional constraints, temperature, time, position, and rotational frequency may be re-express as:

$$\tilde{T} = \frac{T(x,t) - T_o}{q_o L/k} \tag{5.6}$$

$$\tilde{x} = \frac{x}{L} \tag{5.7}$$

$$\tilde{t} = \frac{\alpha t}{L^2} \tag{5.8}$$

$$\tilde{\omega} = \frac{\omega L^2}{\alpha} \tag{5.9}$$

Substitution of these non-dimensional term into Eq.'s 5.2 - 5.5 yields:

$$\frac{\partial^2 \tilde{T}}{\partial \tilde{x}^2} = \frac{\partial \tilde{T}}{\partial \tilde{t}}; 0 < \tilde{x} < 1 \tag{5.10}$$

$$\tilde{T}(\tilde{x}, 0) = 0 \tag{5.11}$$

$$-\frac{\partial \tilde{T}}{\partial \tilde{x}} = \cos(\tilde{\omega}\tilde{t}) \tag{5.12}$$

$$\tilde{T}(1, \tilde{t}) = 0 \tag{5.13}$$

The simplicity of this non-dimensionalized set of equations enables an exact solution in the form of Green's Functions [20]. Specifically, a "co-time", series solution may be expressed as a function of non-dimensional space, time, and periodicity where:

$$\tilde{T}(\tilde{x}, \tilde{t}, \tilde{\omega}) = 2 \sum_{m=1}^{\infty} \frac{\cos(\beta_m \tilde{x})}{\beta_m^4 + \tilde{\omega}^2} [\beta_m^2 \cos(\tilde{\omega}\tilde{t}) + \tilde{\omega} \sin(\tilde{\omega}\tilde{t})] - 2 \sum_{m=1}^{\infty} \frac{\cos(\beta_m \tilde{x})}{\beta_m^4 + \tilde{\omega}^2} [\beta_m^2 \exp(-\beta_m^2 \tilde{t})] \tag{5.14}$$

where,

$$\beta_m = \pi(m - \frac{1}{2}) \tag{5.15}$$

The 'counting variable' m represents the individual terms of the , and as the summation implies runs from 1 to inf.

A brief comment regarding the summation terms on the right-hand-side of 5.14. The first series represents the 'steady periodic' component of the temperature solution, that's to say the component of the over-all temperature field which remains once 'start-up' transients (at early times)

fade away. In contrast, the second term encodes the aformentioned 'decaying transient' component of the temperature response. It should be noted that the 'steady periodic' term, as expressed in 5.14, is slow to converge - in other words, it requires rather large values of m. To ease analysis of the "co-time" series, a non-series term may be substituted [20] as follows:

$$2\sum_{m=1}^{\infty}\frac{\cos(\beta_m\tilde{x})}{\beta_m^4+\tilde{\omega}^2}[\beta_m^2\cos(\tilde{\omega}\tilde{t})+\tilde{\omega}\sin(\tilde{\omega}\tilde{t})] \Longrightarrow Real[\frac{e^{\sigma\tilde{x}}-e^{-\sigma(2-\tilde{x})}}{\sigma(1+e^{-2\sigma})}e^{i\tilde{\omega}\tilde{t}}] \tag{5.16}$$

where,

$$\sigma=(1+i)\sqrt{\frac{\tilde{\omega}}{2}} \tag{5.17}$$

The real part of the complex expression in 5.16 is substituted into **??**, enabling more efficient analysis. In practice the remaining terms associated with the early-time transient is generally truncated by tracking the magnitude of the exponential operation . As one might expect, early times require a slightly longer series ($m_{t_{early}} \approx 100$) to capture the influence of the start-up transient, while later times (as the "quasi" steady-state condition is approached) reduce the burden on the series component ($m_{t_{late}} \approx 25$).

For a more in-depth treatment of Green's Functions, including the solution methodology outlined above, the interested reader should reference the following source material [20]. In an effort to establish the efficacy of the discretized thermal model (and the associated numerical approach) of the present analysis, the Green's Functions will enable a qualitative comparison between solution methodology.

5.1.1.1 Evaluation of Discretized Grid Size and Time Step

The solution methodology outlined above will enable evaluation of numerical results over a range of rotational speeds and mesh sizes. In general, this analysis attempts to create engine-relevant time scales by varying the periodicity of the applied sine wave. However, before comparing the analytic and numeric methods, a brief note regarding rotational speeds is warranted.

Within the context of this dissertation, engine operation and analysis is limited to three specific rotational speeds: 1200rpm, 1600rpm, and 2000rpm. Given the 4-stroke cycle sequence of the HCCI test engine, fired events (i.e., combustion at TDC_f) require two complete crank rotations. This effectively 'halves' the periodicity of the 'heated' portion of the cycle relative to engine speed.

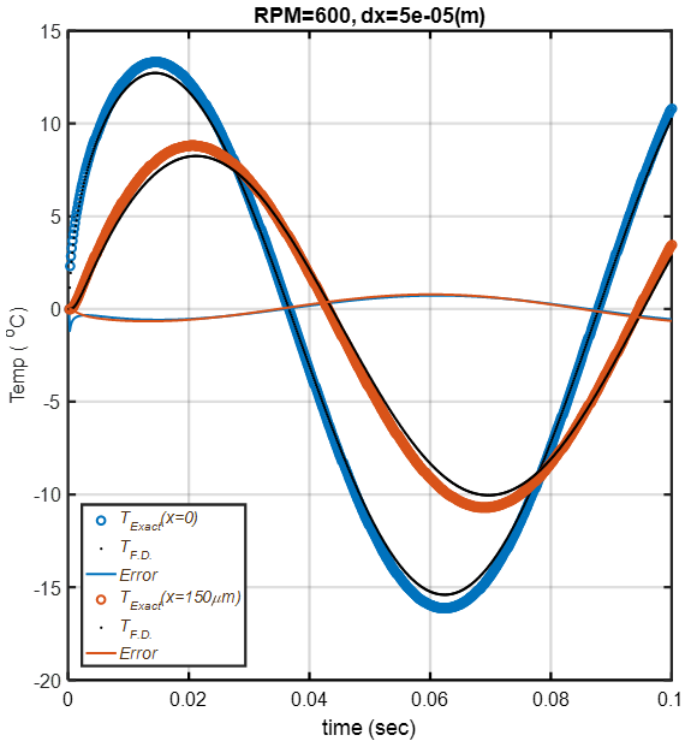

Figure 5.2: A comparison between the exact temperature field, and the results of the finite difference model - 600rpm, $dx = 5 \cdot 10^{-5}$m.

Thus, when a four-stroke engine spins at 1200rpm (20Hz), the periodicity of fired events mimics a 10Hz event.

In contrast to the 4-stroke engine cycle, the sine wave associated with the front-side boundary condition (i.e., the applied heat flux described in Eq. 5.5) produces a heating event with each rotation. Thus, to ensure an engine relevant time-scale, the govern system will be evaluated for rotational speeds which are a factor of two slower than the corresponding engine speeds. These results are presented (graphically) below, and examine the slowest (1200rpm) and fastest (2000rpm) engine speeds. A concise discussion of outcomes follows.

Figures 5.3 - 5.4 summarize the results of the grid study for the 1200rpm 'engine-equivalent' case. The ultimate goal of this bench-marking analysis is twofold. First, equivalence between the numerical solution to the governing system of equations and its analytic counterpart must be established. Second, and not unrelated, the grid spacing which yields mesh independent results must also be determined. It is only after both conditions are satisfied that numeric results can be treated

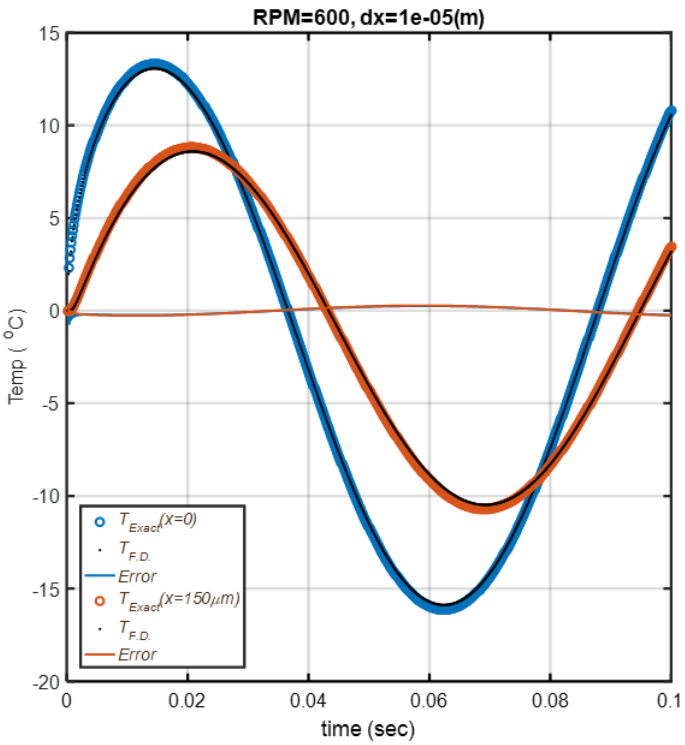

Figure 5.3: A comparison between the exact temperature field, and the results of the finite difference model - 600rpm, $dx = 1 \cdot 10^{-5}$m.

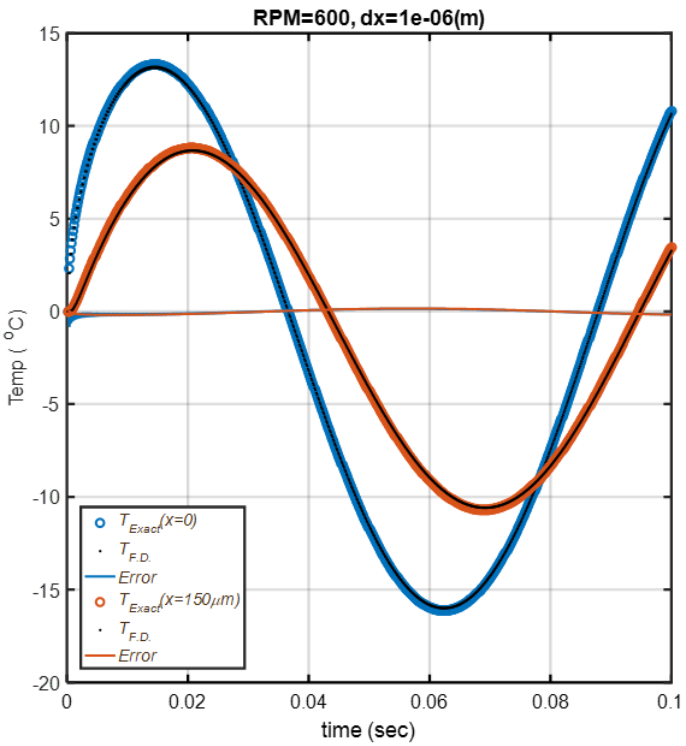

Figure 5.4: A comparison between the exact temperature field, and the results of the finite difference model - 600rpm, $dx = 1 \cdot 10^{-6}$m.

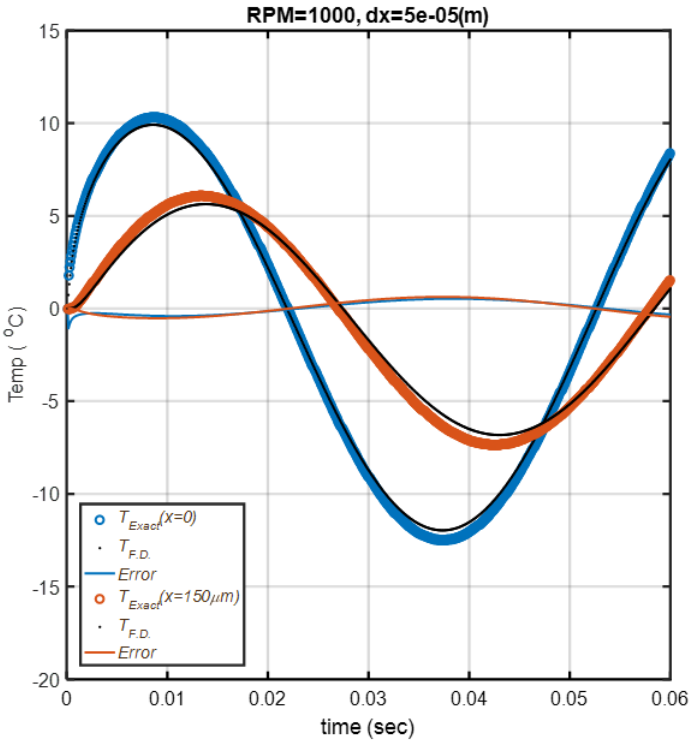

Figure 5.5: A comparison between the exact temperature field, and the results of the finite difference model - 1000rpm, $dx = 5 \cdot 10^{-5}$m.

as 'equivalent' to exact solutions within the fidelity of the current measurements and experimental setup.

Figure 5.2 plots results for a relatively 'coarse' grid interval ($dx = 5 \cdot 10^{-5}$m). In addition, Fig. 5.3 provides an intermediary grid spacing ($dx = 1 \cdot 10^{-5}$m), while Fig. 5.4 plots results for the finest grid interval($dx = 1 \cdot 10^{-6}$m).

A similar sequence of results is included for the 2000rpm 'engine-equivalent' case - Figures 5.6 - 5.7. In both sequences, temperature profiles for both surface and subsurface locations are provided. It should be noted that the subsurface location (at $150\mu m$ depth) was selected to approximate the desired TBC thickness. Recall, the TBC-treated temperature probes record temperature at depths roughly equivalent to this interval. The error between analytic (Green's Function approach) and numeric (Crank Nicholson) are also provided in.

In general, the error between solution methodologies moves toward a minimum as grid size approaches the lower bound ($dx = 1 \cdot 10^{-6}$m). Within the context of experimental data, the error

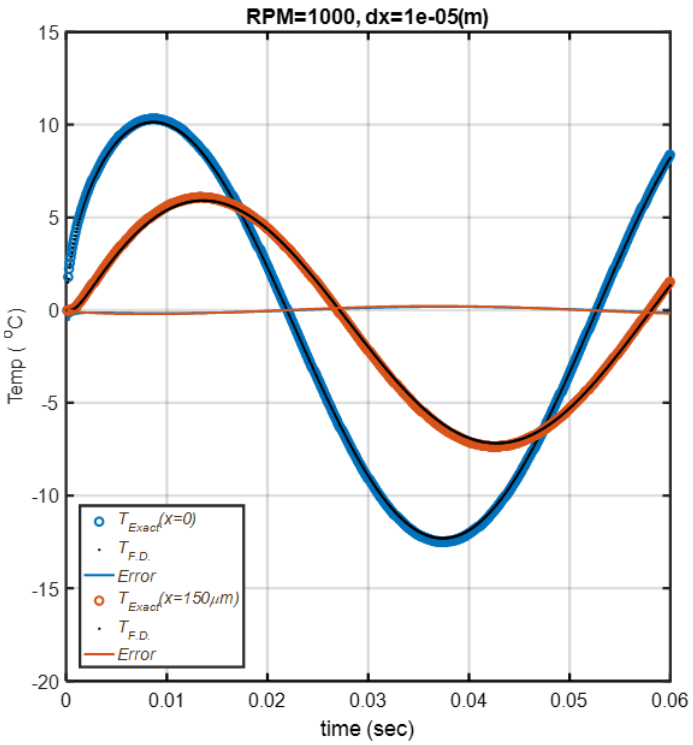

Figure 5.6: A comparison between the exact temperature field, and the results of the finite difference model - 1000rpm, $dx = 1 \cdot 10^{-5}$m.

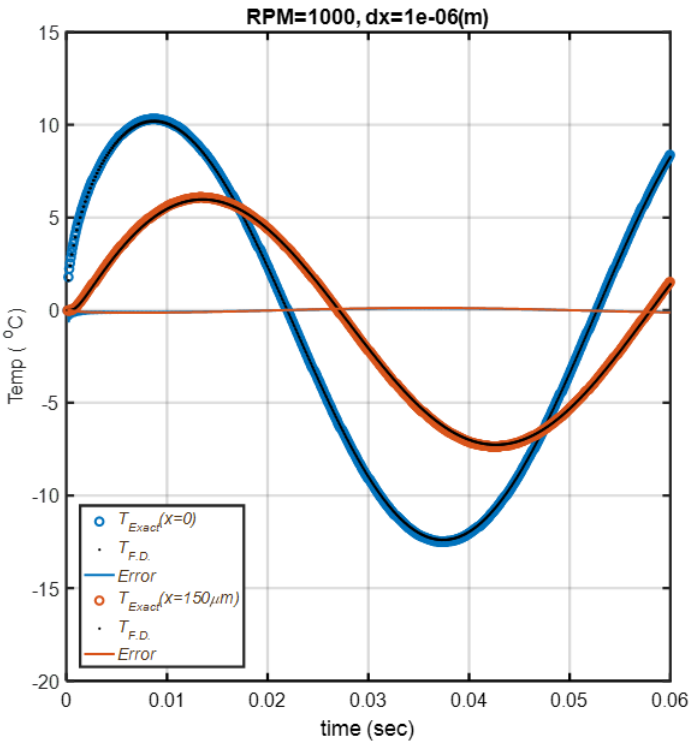

Figure 5.7: A comparison between the exact temperature field, and the results of the finite difference model - 1000rpm, $dx = 1 \cdot 10^{-6}$m.

reported for the finest mesh is well below the expected uncertainty of the J-type thermocouples used in both in/ex situ environments - (typically $+/-2^oC$ or 2%, whichever is larger). Thus, the numeric results may be treated as indeed equivalent to the exact solution with respect to the fidelity of the associated experimental measurements.

As mentioned at the onset, this bench-marking should establish the appropriate mesh requirement while also verifying the accuracy of the numeric approximation. Upon review of the $dx = 1 \cdot 10^{-6}$m results, these conditions are satisfied for each of the rotational speeds. As such, analysis within this dissertation is performed in accordance with the aforementioned grid spacing, and will be treated as equivalent to exact solution methodology.

5.2 Periodic Surface Heating and Subsurface 'Information' Loss

The exact solution discussed at length in the preceding section is also useful for evaluating the propagation of specific frequency components given a composite boundary condition waveform. Of particular interest are the interior locations corresponding to sub-surface temperature sensors positions within the experimental environment.

Signal lag and attenuation is an inherent characteristic of the governing equations describing heat flow as it diffuses away from the surface source term. In general, change in the surface boundary condition (heat flux, in this case) will induce change in the temperature field throughout the domain of interest. However, the magnitude of the dynamic temperature response decreases at locations further removed from the surface - again, as a result of the diffusive nature of the governing equation. This reality has a significant impact on the 'recoverability limits' of inverse methods which reconstruct surface trends using subsurface measurements. To gain a better 'feel' for the extent to which such considerations impact the current analysis, a composite signal of three distinct frequency bands will be considered. Furthermore, the propagation of the composite surface heating term is evaluated for two distinct substrate materials - one metal and one ceramic.

In order to construct a a periodic heating term with multiple frequency components, superposition of individual dine waves is pursued. As a consequence, linearity of the thermal system is required. This implies that the relevant thermophysical parameters such as thermal conductivity and heat capacity do not change as the temperature field responses to the transient dynamics of

the surface heating event. Such a pre-condition remains entirely compatible with the treatment of thermophysical properties throughout the present work. That's to say, key parameters are held constant over the temperature ranges considered in this dissertation.

The present section seeks to quantify the available frequency content at sub-surface locations corresponding to sensor positions. For the purposes of this work, frequency content is in fact analagous with information. That's to say, transient heating (as defined by surface heating/cooling processes) 'disturbs' the temperature field at frequencies corresponding to physical processes. In the engine environment, the principle frequency driving temperature transients is that of the combustion event - which is determined by the rotational speed. This is particularly true given steady-state operation. Additional frequencies generated by excessive 'ringing' (i.e., 'engine knock') may also be present. In a physical sense, the composite temperature transient results in a temperature time-series (i.e., profile) at the sensor location. In the metal engine, this sensor records surface temperatures. The TBC-treated engine records subsurface temperatures. Thus, given the diffusive nature of heat conduction it is important to identify and evaluate the frequency spectrum which can (and cannot) be resolved at the sensor locations. Ultimately, this information will help determine the limitation of the inverse methodology utilized in the present study.

5.2.1 Quantify Information Loss via Superposition

In this section an effort is made to quantify the frequency content at surface and subsurface locations which results when multiple sine waves (of varyingperiodicity) are applied to the surface of the model introduces in Fig. 5.1. Two distinct material are considered, and differences in the resulting temperature fields are quantified.

To begin, the temperature field resulting from the application of a multi-component surface heat flux 'waveform' is considered. The waveform itself is constructed by superimposing three separate sine waves, each oscillating at distinct frequencies (1200rpm or 20rot/s, 12,000rpm or 200 rot/s, and 120,000rpm or 2000 rot/s). It should be noted that 1200rpm is the most 'engine-relevant' frequency in the above series. However, to better identify the impact of sensor placement on information loss, an expanded frequency range is required.

The waveform which results after superposition of individual sine waves is shown in Fig. 5.8 - with subplot (a) showing individual waves and subplot (b) showing the combined waveform. The power spectral density is also provided in Fig. 5.8c. The primary frequencies of the individual sine

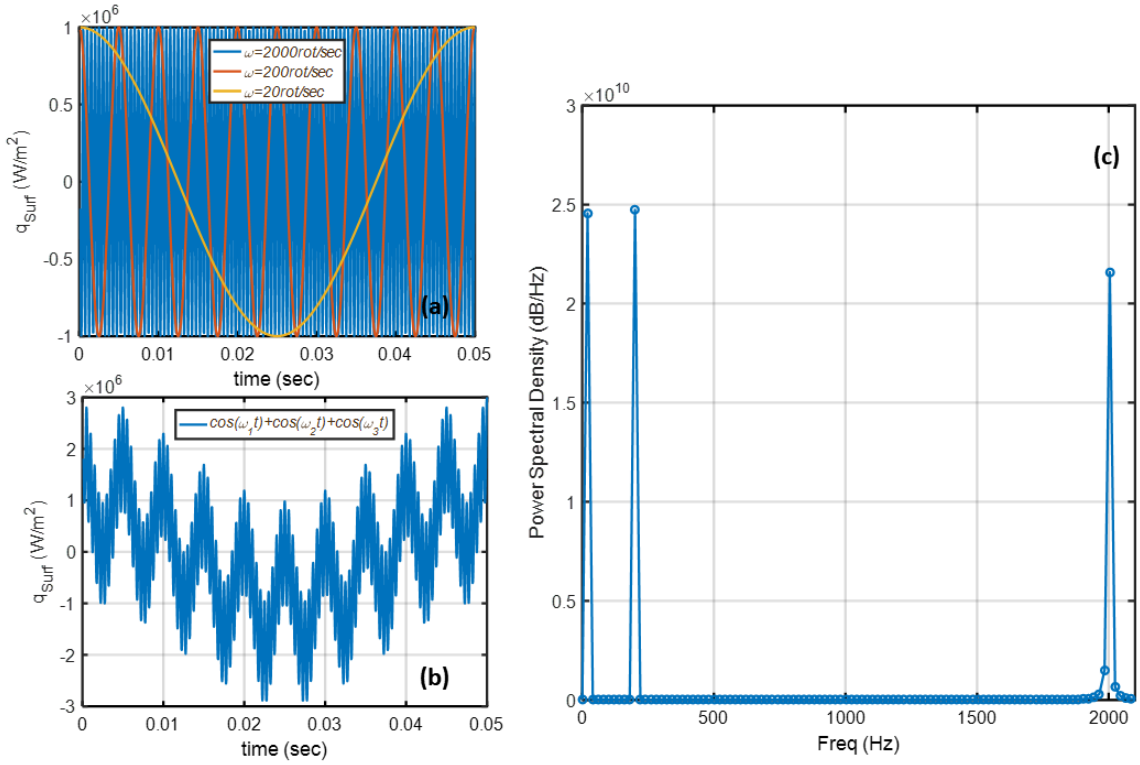

Figure 5.8: A superposition of three distinct sine waves, with frequencies spanning three-orders of magnitude. Figure (a) plots individual waves, while (b) display the associated super-position. Spectral density of the combined waveform is shown in (c).

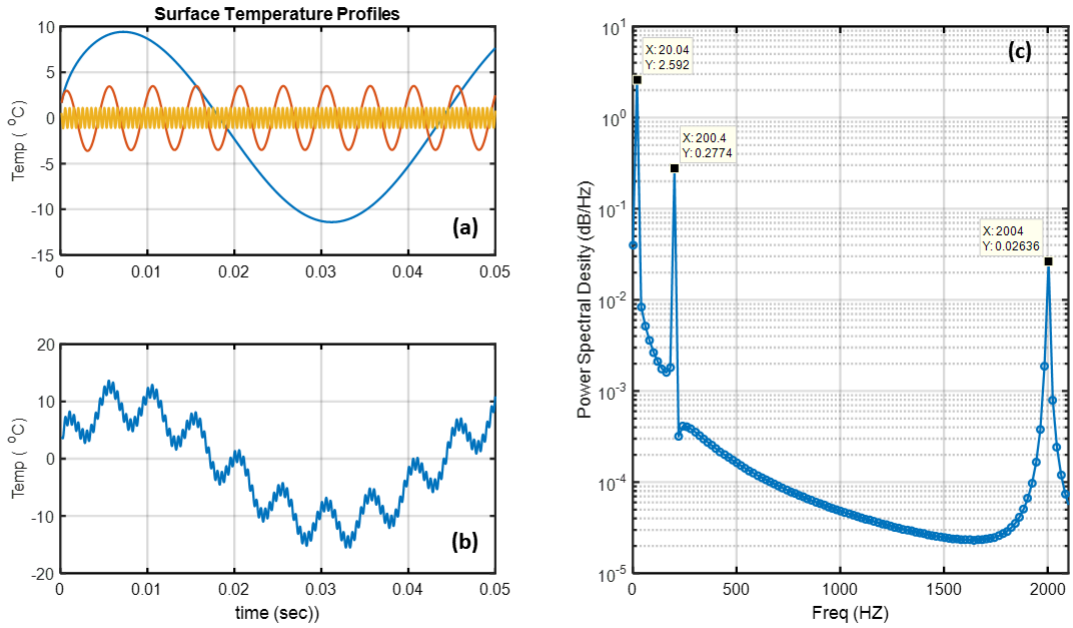

Figure 5.9: The solution to the temperature field is evaluated at the metal surface. Figure (a) plots the individual solution components, while (b) display the associated super-position. Spectral density of the combined waveform is shown in (c).

waves correspond to the spectral density 'spikes' Notice the similar magnitudes.

Applying the composite boundary condition to the thermal system outlined in Fig. 5.1, and assigning thermophysical properties congruent with the stainless steel body of the IR Telemetrics probe, results in the surface profiles displayed in Fig. 5.9a-c. The corresponding subsurface profiles are displayed in Fig. 5.11a-c.

Inspection of the surface temperature response shown in Fig. 5.9a-b reveals dynamic behavior which is physically consistent with the relative time-scale(s) of the individual sine waves. That's to say that the temperature swing associated with the highest frequency component exhibits the smallest peak-to-peak span. After all, this waveform results in smallest heating/cooling time (in an absolute sense) relative to the other sine waves. Likewise, the sine wave with the lowest oscillatory frequency yields the highest peak-to-peak temperature swing. This behavior translates directly to the spectral density peaks shown in Fig. 5.9c. Simply, surface signal strength (and by extension 'information') is remains amplified towards the lower end of the frequency band.

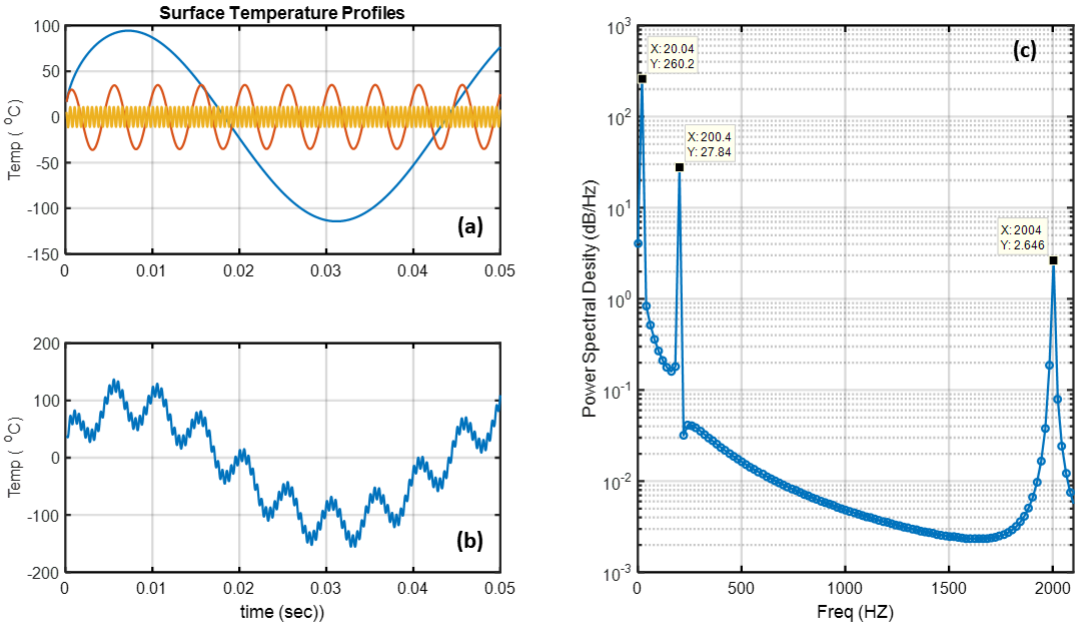

Figure 5.10: The solution to the temperature field is evaluated at the gadolinium zirconate surface. Figure (a) plots the individual solution components, while (b) display the associated super-position. Spectral density of the combined waveform is shown in (c).

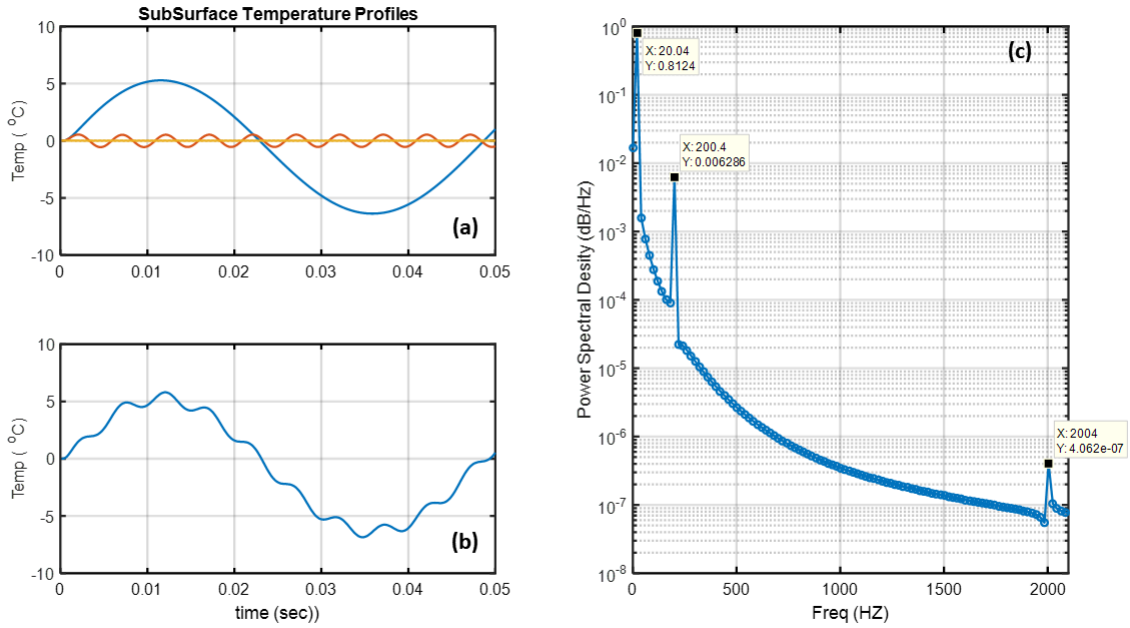

Figure 5.11: The solution to the temperature field is evaluated $150\mu m$ below the metal surface. Figure (a) plots the individual solution components, while (b) display the associated super-position. Spectral density of the combined waveform is shown in (c).

A similar series of plots is shown for a thermal system which has been assigned properties equivalent to the gadolinium zirconate material. These results, compiled in Fig. 5.10a-c, show similar behavior to the corresponding metal trends. It should be noted that the over-all magnitude of the peak-to-peak surface temperature swing is elevated for the gdzr case. This observation remains entirely consistent with the temperature swing concept developed at the onset of this dissertation. Furthermore, when evaluating the composite waveform of in Fig. 5.10b, the contributions from the individual sine waves are readily identifiable in the composite waveform.

We now consider the analysis at the center of this current section. Specifically, we consider the temperature field $150\mu m$ below the surface of the respective materials. For the metal case, results are shown in Fig, 5.11a-c. Here the diffusive nature of governing system begins to manifest. The composite waveform has 'lost' the majority of the frequency content associated with the 2000 rot/s sine wave. Qualitatively, this is apparent in the superposed signal of 5.11b. To gain a more quantitative assessment, one should consider the power spectral density reported in 5.11c. Here, the

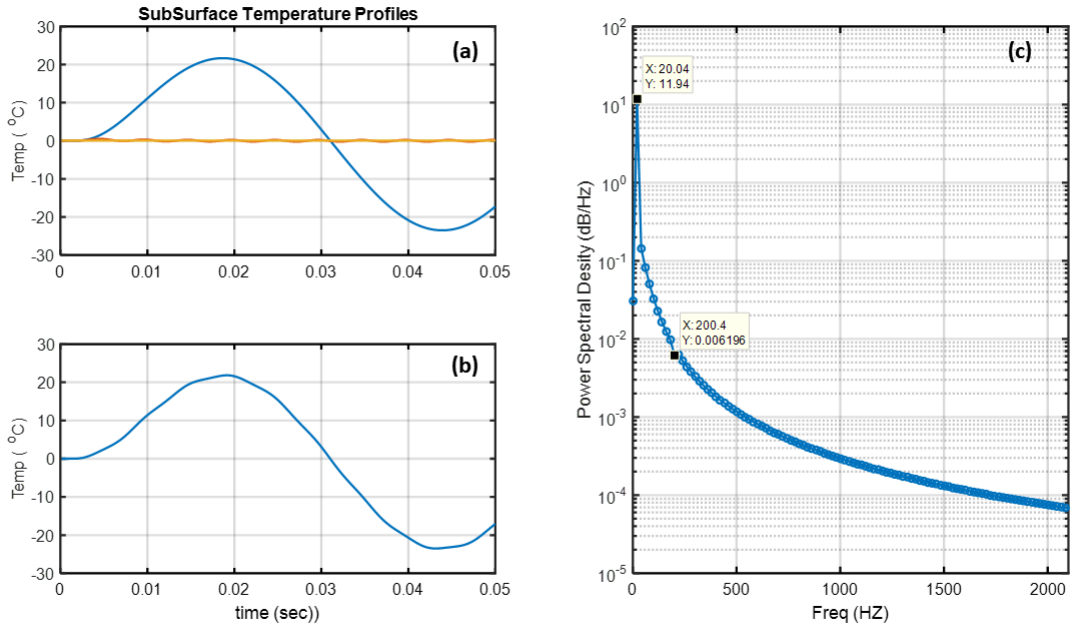

Figure 5.12: The solution to the temperature field is evaluated $150\mu m$ below the gadolinium zironate surface. Figure (a) plots the individual solution components, while (b) display the associated superposition. Spectral density of the combined waveform is shown in (c).

relative power between lowest-to-highest frequency waveforms spans nearly 6.5 orders of magnitude. In comparison, the spectral peaks accompanying the metal surface PSD were within two orders of magnitude of eachother. Clearly information associated with the highest frequency component of the over-all transient are 'lost' prior to arrival at the subsurface sensor location.

Finally, the subsurface results for the GDZR treated probe are considered. As shown in Fig. 5.12a-c, the width of the 'surviving' frequency band continues to diminish, with only the lowest frequency component registering at the subsurface. The qualitative response of the subsurface waveform is clearly dominated by the 20rot/s sine wave. A 'trace' amount of energy remains at the 200 rot/s location, while energy from the 2000 rot/s sine wave is undetectable at the sensor location. Only the 20 rot/s wave transfers energy (and thus, usable 'information') $150\mu m$ below the gdzr material's surface.

5.2.2 Concluding Remarks

Signal attenuation is an inherent feature of any diffusive system. As such, the current heat transfer configuration is subject to information 'loss' at subsurface sensor locations. By utilizing the exact solution developed in Sec. 5, a composite waveform spanning three orders of magnitude was utilized as the front side boundary condition. This approach enabled the 'recoverability limits' of inverse methods to be quantified relative to the available frequency content at the sensor location. in general, the assessment demonstrated that engine-relevant frequencies are still present at the sensor location for both metal and gdzr configurations. However, upper range spectral content was not present at the probe depth. This may have implications for higher frequency components of the surface temperature and/or heat flux profiles. This being said, the primary component of engine heat events (i.e., combustion) disturbs the temperature field at the sensor location - and thus inverse methods remain applicable.

Chapter 6

Quantifying the Impact of Thermal Barrier Coatings on Heat Transfer

This chapter serves as the 'meeting ground' for the various models, techniques, and analytic processes discussed in the preceding chapters. Together, this combined 'toolset' will enable quantitative assessment of heat transfer at the cylinder. The thermal composition of the interior charge will also be assessed. Accordingly, two major thrusts will be pursued.

First, the inverse solver developed in the preceding chapter, along with direct measurements from the metal engine, will be used to quantify in situ surface temperatures and heat flux. Analysis will consider key cycle metrics, (including instantaneous work-rate, combustion efficiency, etc.), in an effort to better understand the mechanism(s) underlying performance and efficiency gains. The data presented in this section will compare metal engine results against those of the gadolinium zirconate treated engine.

The efforts of the current analysis will ultimately support the analysis of subsequent chapters, where a novel post-processing technique will combine the results of $1^{st} Law$ Heat Release Analysis with predicted ignition-delay time using an HCCI-relevant autoignition correlation. In essence, this method assigns charge mass (from the Mass Fraction Burned profile) to hypothetical temperature 'zones' (modeled within the A.I. correlation) to enable a probabilistic description of the in-cylinder charge temperature distribution. This technique quantifies the degree to which in-cylinder contents are 'Thermally Stratified'. This section will compare metal engine results against three

separate coating formulations.

6.1 Global Heat Transfer

The evaluation of cylinder-wide (i.e., 'global') heat transfer is a combined effort, relying on the complete array of analytic and experimental methods highlighted in the preceding chapters. Instrumentation is expanded to include the telemetry linkage system. the apparatus will provide a vastly expanded measurement array, where temperature measurements from multiple in-cylinder locations inform a global heat transfer evaluation. Similar instrumentation arrays are explored for both metal and gadolinium zirconate engine configurations - enabling direct comparison of surface temperatures and heat flux profiles. As a consequence, the following analysis will utilize both 'direct' and 'inverse' approaches to evaluate the associated heat transfer configurations.

To begin, this section will summarize relevant experimental considerations - reviewing the expanded instrumentation array and establishing common measurement locations for each of the engine configuration. A detailed overview of the requisite processing/calculation methodology is also provided. This effort is intended to make clear the 'analytic pathway' from raw temperature measurements to global heat loss numbers. The realities of experimental noise and sub-optimal instrument integrity (i.e., sensor degradation) will also be discussed. Clear disclosure of these details (and the associated impact on signal fidelity, etc.) will help contextualize quantitative conclusions relative to the integrity of the underlying raw measurements.

To help facilitate this analysis, a detailed 'walk through' of relevant processing methodology is included for the '1200 Fuel Match' engine operational point. This effort will review signal quality and processing specifics at each of the shared (spatial) measurement locations. Finally, results from individual locations will be used to construct a representative Global Heat Flux Trace. Different averaging strategies will discussed, and their outcomes evaluated.

Following the thorough presentation of the preceding section, comprehensive point-by-point analysis described above is streamlined. Instead, results and discussion are limited to the Global profiles. This approach enables more efficient analysis across the complete engine operational range.

To further strengthen the temperature-based observations, a detailed analysis of instantaneous cycle-work (both rate-based and cumulative) is also provided. Accordingly, a crank-angle resolved work-rate (i.e., dP/dV) is constructed for each of the operational cases listed above. This

analysis offers an independent (pressure-based) perspective on cycle gains (i.e., efficiency mechanism). This final effort ties critical TBC parameters to heat transfer trends and cycle performance metrics - helping to reveal the full dimensional impact of the coating formulation.

6.1.1 A Review of Instrumentation

The telemetry linkage apparatus represents the major experimental component of the present work. Although this device greatly expands the measurement array, successful integration into the the existing data acquisition stream (and sufficient operational longevity) represent *the* major experimental challenge of this work. A number of the specific challenges where highlighted in detail in the last chapter.

As a consequence of the high-risk/high-reward characteristic of the expanded experimental array, a limited number of measurement locations remain operational for the duration of metal/GDZR engine experiments. To ensure a 'even-handed' comparison between the engine results, analysis is limited measurement locations which remained operational for both engine configurations. These 'shared' locations are detailed in Fig.6.1.

The in-cylinder measurement array also includes the head mounted probes shown earlier in teh experimental setup. This expands surface coverage to non-reciprocating engine components. Head locations utilize the 'IR-Telemetrics' style probe. (Recall, pistons are instrumented with 'Medtherm' probes.) As a consequence, the head-derived temperature information exhibits higher over-all signal quality, and remains less susceptible to the mechanical failure modes associated with the reciprocating linkage assembly. Individual signal quality and the associated processing sequence are reviewed in detail below.

6.1.2 Derivation of Global Heat Flux from In-Cylinder Temperature Measurements

This section provides an in-depth look at the signal-fidelity characteristics, processing outcomes, and heat transfer results for each of the 'shared' probe locations identified in Fig. 6.1. 'Localized' heat flux is calculated using 'direct' (metal engine) and 'inverse' (TBC engine) techniques. These results are transformed into rate-based expressions, and integrated over combustion-relevant crank-angles to evaluate cumulative heat 'loss' between the respective engine configurations.

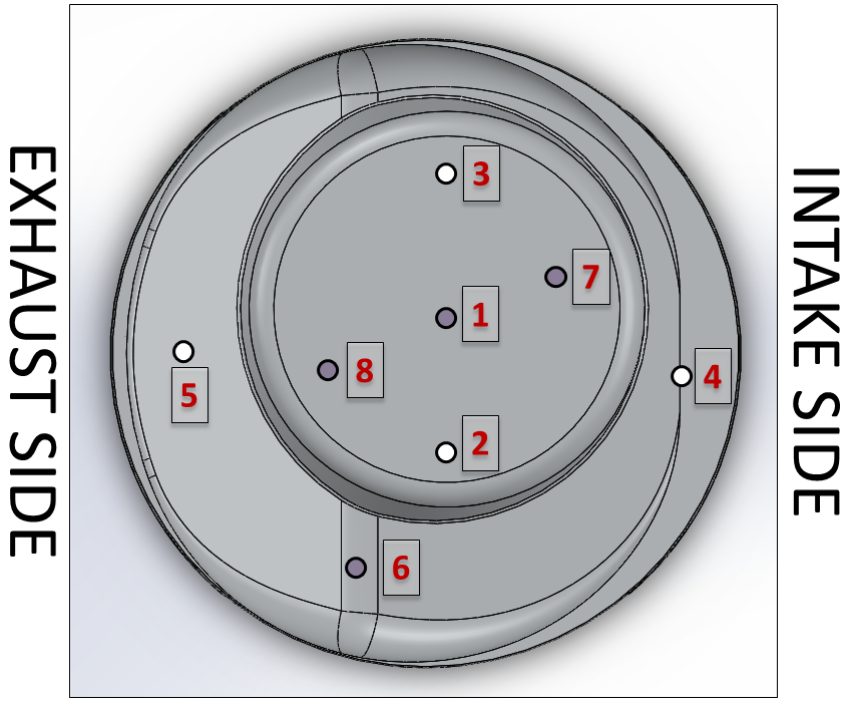

Figure 6.1: A review of piston thermocouple locations. Those remaining operational for *both* metal and GDZR engine experiments are highlighted in purple. The bowl region remains well 'sampled' (probes 1,7,8), while the squish region is limited to a single probe (6). Two head-mounted probes are also available for analysis.

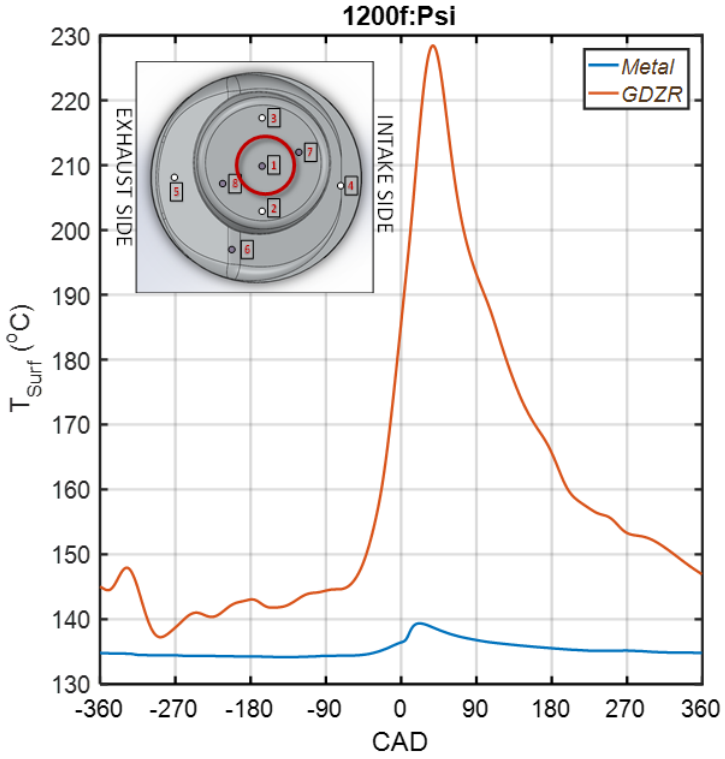

Figure 6.2: Measured ('direct') and estimated ('inverse') surface temperatures for the metal and gadolinium zirconate engine configurations. Operational conditions: $1200RPM, \dot{fuel} = 11.6\frac{mg}{cycle}$

To enable more compact analysis, 'local' results are spatially averaged to construct a single 'global' profile. The averaging processes has the added benefit of further attenuating non-coherent noise.

In an effort to provide a more complete overview of the processing routine (while disclosing the implication of individual decisions), full details are provided for the '1200RPM Fuel Match' point (i.e., '1200f'). This detailed review is followed by a summary of heat transfer outcomes for the remaining operational points - where focus shifts to the spatially-averaged data.

Piston Location: 'Psi'

Analysis of the '1200f' point begins with a comparison of surface temperature profiles at the Psi location. A convention introduced here, and followed throughout the analysis, is the identification of sensor location in the upper left quadrant of Fig. 6.2.

Metal and GDZR surface temperature profiles are compared at the Psi location. As a

consequence of inherently low thermal conductivity, the SFSM results clearly show GDZR's dramatic surface temperature 'swing' in-response to the incident combustion heat. Peak values occur shortly after TDC_f, and largely 'recover' to metal-like levels during the gas exchange process.

A few remarks regarding 'open-cycle' temperature values are warranted. As discussed at length in the preceding chapter, signal-to-noise is least favorable during open-cycle crank angles. This is largely driven by decreased signal amplitude in the (almost complete) absence of significant heating/cooling events. As a consequence, SFSM-derived results generally exhibit their lowest level of fidelity during this time - and in extreme cases may prove unreliable.

A notable exception involves impingement of fuel spray atop the piston surface during the DI event. Certain probe locations on the piston surface interact directly with the fuel spray during this period. (Recall, injection begins at $333^o bTDC_f$). The impinging fuel demands a considerable amount of heat as it transitions from liquid film to vapor. As a consequence, this phase transition generates a measurable negative heat flux at the sensor location - which ultimately manifest as a downward temperature spike. This detail, barely visible in the current figure (i.e., Fig.), becomes noticeably pronounced at other piston locations and/or operational points.

The results of the SFSM sequence, again for the Psi location are shown in Fig. 6.3. Solver convergence is demonstrated in (a), with measured and modeled sub-TBC profiles 'falling' on top of each-other. This agreement is further established in the 'measured-vs.-modeled' difference profiles plotted in (b). Finally, the resulting surface heat flux is plotted against the metal engine profile. Initial inspection shows both smaller peak heat flux and evidence of fuel interaction in the vicinity of the Psi location.

The crank-angle resolved heat flux profile shown in Fig. 6.3c is converted into a rate-based metric using the exposed in-cylinder surface area. Note: Piston and firedeck surface area is estimated using their representative CAD (i.e., 'computer added design') models within SolidWorks. This values remain constant across the engine cycle. In contrast, the exposed surface area of the cylinder liner varies with crank angle. This values are calculated using the following sequence [43].

First the distance between crank axis and wrist pin offset is determined using the following expression:

$$s(\theta) = a\cos\theta + \left(l^2 - a^2\sin^2\theta\right)^{\frac{1}{2}} \tag{6.1}$$

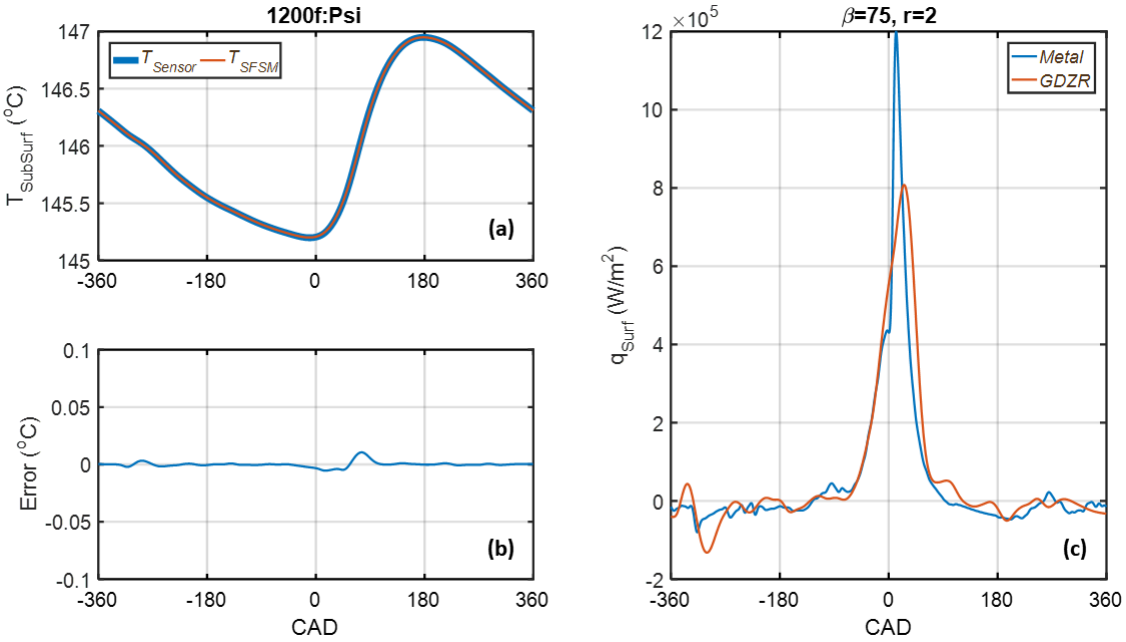

Figure 6.3: Summary of SFSM results, where: (a)Display's solver convergence at the node corresponding to the recorded subsurface temperature. (b)Displays difference (i.e., 'Error') between measured and modeled temps in (a). Lastly, (c) shows measured $q_{Surf,Metal}$ ('direct') and estimated $q_{Surf,GDZR}$ ('inverse').

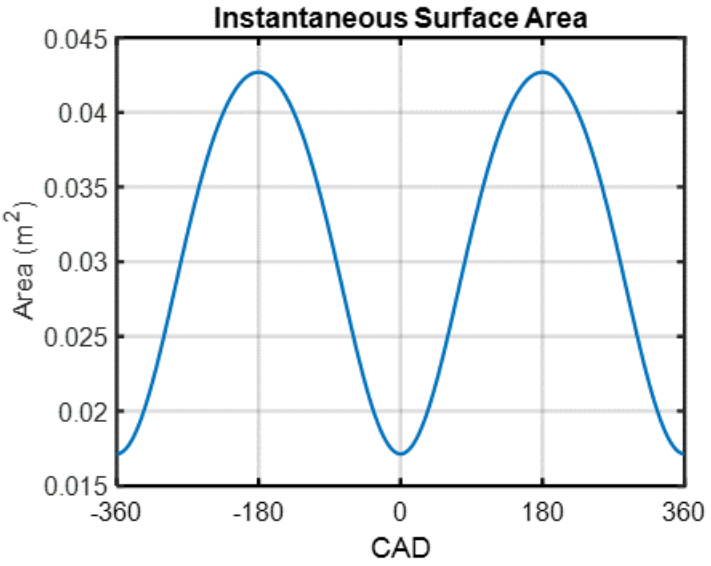

Figure 6.4: Crank-angle resolved (i.e., 'Instantaneous') surface area for two crank rotations - one complete engine cycle. Note: $Piston_{Area} = 6998.4e^{-6}(m^2)$ and $Head_{Area} = 101.37e^{-4}(m^2)$. Exposed liner area (i.e., 'A_{Liner}') varies with crank position, and can be calculated using geometric parameters outlined in an earlier section.

This allows a crank-angle resolved volume array to be calculated such that:

$$V(\theta) = V_c + \left(\frac{\pi}{4} \cdot B^2 \left(L + a - s(\theta)\right)\right) \tag{6.2}$$

Given the cylindrical geometry of the liner, the displaced cylinder volume may be re-expressed as an instantaneous liner surface area where,

$$A_{Liner}(\theta) = \frac{4}{B} \left(V(\theta) - V_c\right) \tag{6.3}$$

With the result of Eq.6.3 the total surface area at each crank angle may be re-expressed as:

$$A_{Total} = A_{Head} + A_{Piston} + A_{Liner} \tag{6.4}$$

The results of this effort, reflecting the engine geometry outlined in an earlier section are shown in Fig. 6.4

The instantaneous surface area values are used in conjunction with the heat flux profiles reported in Fig. 6.5a to calculate the representative 'heat flow rate' shown in Fig. 6.5b (left axis). The qualitative characteristic of these profiles largely matches that of the heat flux trace. However, a few notable deviations exist - particularly over closed-cycle crank angle degrees.

For example, in-cylinder surface area is greatest when the piston approaches TDC - see Fig 6.4. These 'elevated' scalar values are essentially used as a multiplier when converting from W/m^2 (i.e., instantaneous heat flux) to J/CAD (i.e., heat flow rate). Thus, features of the heat flux trace in the vicinity of the TDC locations are 'exaggerated' by the increased magnitude of the area scalar. In the case of the SFSM-derived profile, this is particularly unfortunate as the signal quality is lowest over this portion of the cycle. (As discussed, open-cycle temperature traces have degraded signal-to-noise in the absence of 'significant' heating/cooling events). This reality will limit analysis of cumulative heat loss to crank angles spanning late-compression and combustion.

A final comparison between metal and GDZR-treated engine variants involves the evaluation of 'combustion-relevant' heat loss. This metric will be limited to the crank angles immediately surround TDC_{firing}, and will include the -90 to 90 interval. The heat loss rate of Fig.6.5b is numerically integrated to better evaluate total heat loss over this interval. The outcome of this evaluation is shown in Fig.6.5c.

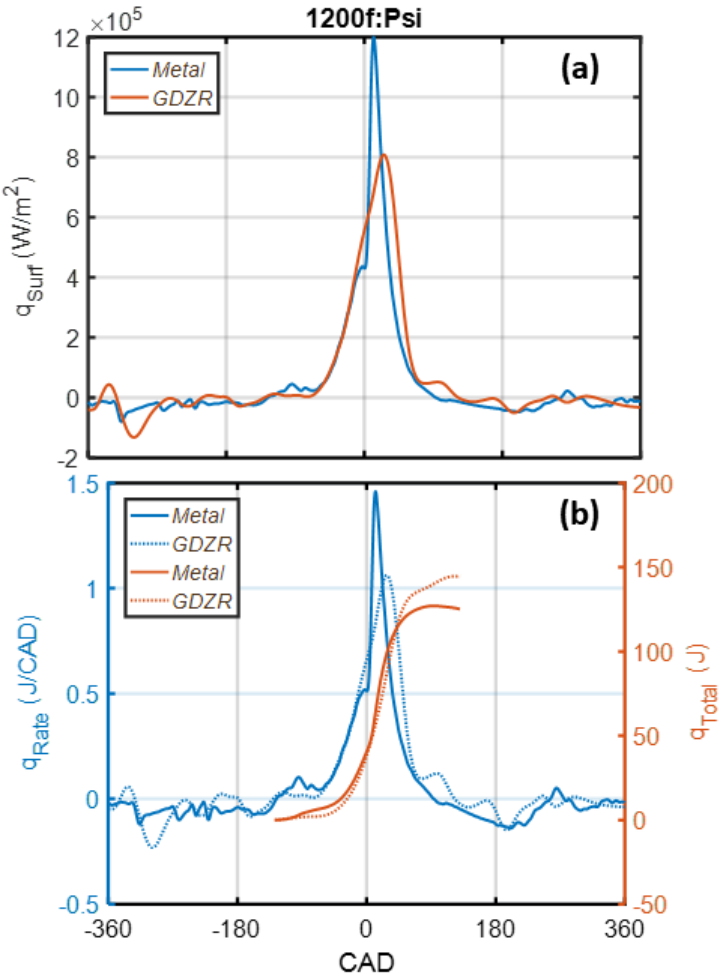

Figure 6.5: The instantaneous q_{Surf} profiles from 6.3 are re-plotted in (a). Instantaneous surface area is used to calculated the corresponding 'heat flow rate' ($\frac{J}{cad}$). This rate is then integrated over 'closed-cycle' crank angles to evaluate total heat loss at the wall (J) (b).

The trends reported in the cumulative heat flux trace are somewhat counter-intuitive. That's to say, the total heat loss reported for the metal engine configuration is less than the values reported for GDZR-treated engine. This result is in direct opposition to the advanced combustion phasing, decreased burn duration, and increased combustion efficiency reported for TBC engine configurations [80]. In short, the cumulative heat loss observation at this probe location is rather suspect.

Closer inspection of the heat loss profile reported in Fig.6.5 may help identify the source of this discrepancy. First, the phasing of the peak heat flux (and corresponding heat loss rate) in the GDZR engine are phased later than the peak value measured in the metal engine. This is most likely the result of the pre-processing efforts performed during SFSM analysis. Slight 're-shaping' of the sub-TBC temperature trace (due to excessive smoothing of signal noise, for example) could substantially alter the character and phasing of the surface heat flux estimate. Furthermore, the 'oscillatory' behavior of SFSM-derived heat flux trace during the $90CAD - 180CAD$ interval is most certainly not physical. Again, noise within the sub-TBC trace is the likely culprit. However, the net effect of this feature is the further elevation of the cumulative heat loss within the GDZR-treated engine to values beyond those reported for the metal engine.

In an effort to counteract the influence of noise-driven error at individual probe locations, spatially-averaged heat flux and heat loss profiles are constructed. However, the remaining shared probe locations will be examined before the 'averaged' results are considered.

Piston Location: 'Psvi'

Next, the piston surface probe at the 'Psvi' location is considered. This probe represent the only shared location in the piston squish zone. A similar processing sequence is pursued, beginning with a comparison of surface temperature profiles for each of the engine configurations.

Similar to the trends shown for the 'Psi' location, the GDZR-treated piston exhibits a dramatic increase in surface temperature over late-compression and combustion processes - see Fig.6.6. A major qualitative distinction accompanying the data from this probe location is the relative 'cleanliness' of the signal. In contrast the trace results at the 'Psi' probe, measurements at this spatial location contain inherently less noise.

Again, agreement between the measured sub-TBC temperature and the modeled trace are excellent - as shown in Fig.6.7a - Fig.6.7b. A comparison between metal and GDZR surface heat flux profiles are also shown (Fig.6.7c.). As anticipated, open-cycle heat flux is similar between engine

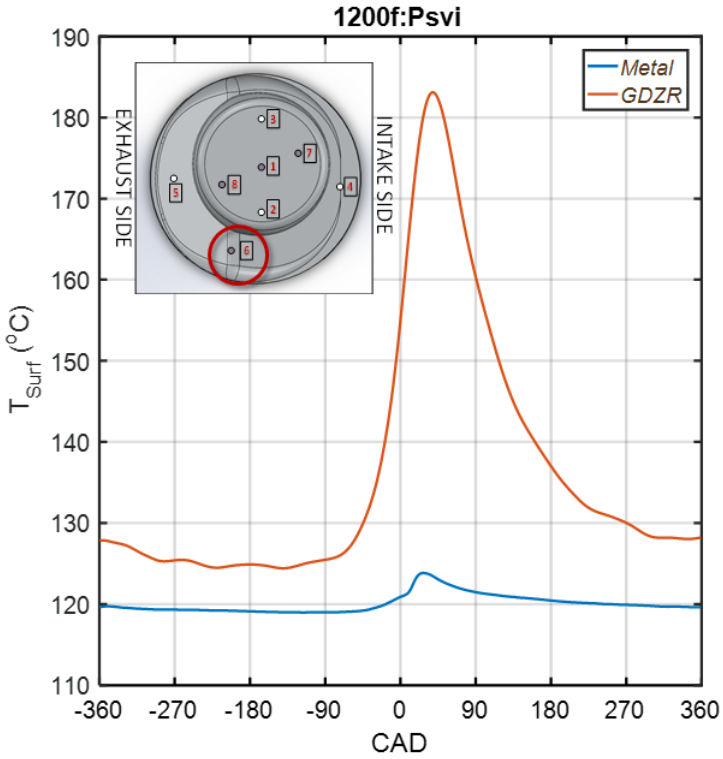

Figure 6.6: Measured ('direct') and estimated ('inverse') surface temperatures for the metal and gadolinium zirconate engine configurations. Operational conditions: $1200RPM, \dot{fuel} = 11.6\frac{mg}{cycle}$

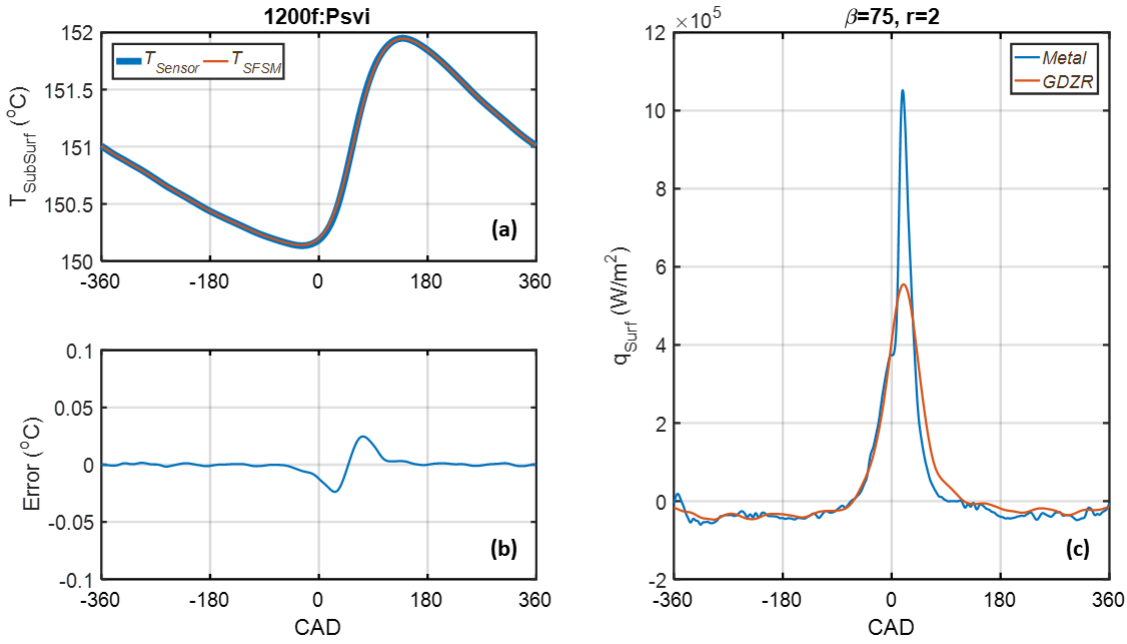

Figure 6.7: Summary of SFSM results, where: (a)Display's solver convergence at the node corresponding to the recorded subsurface temperature. (b)Displays difference (i.e., 'Error') between measured and modeled temps in (a). Lastly, (c) shows measured $q_{Surf,Metal}$ ('direct') and estimated $q_{Surf,GDZR}$ ('inverse').

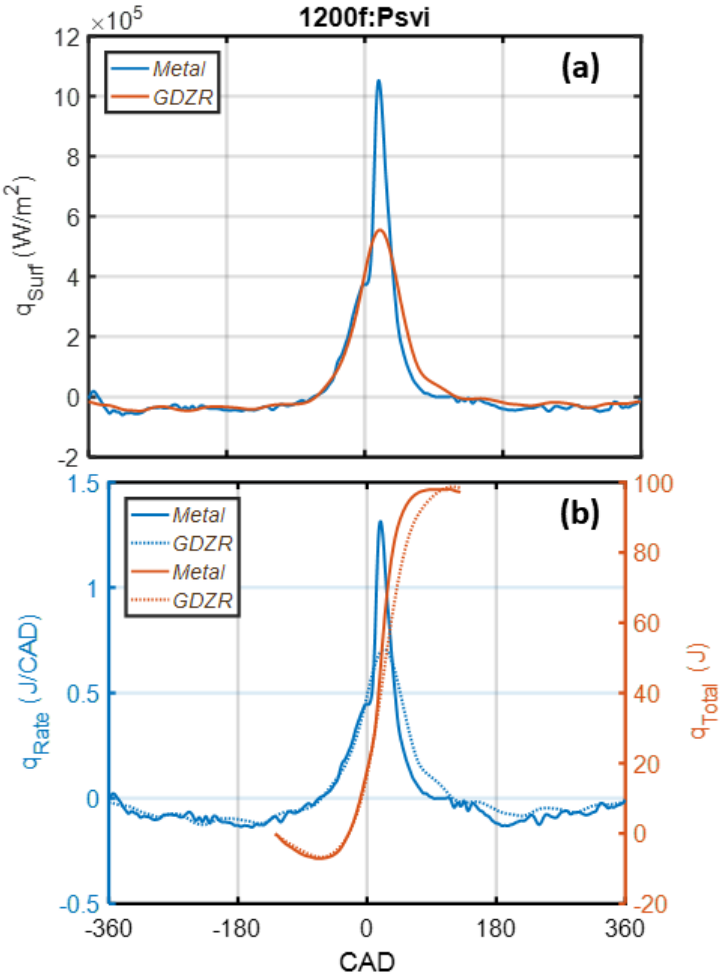

Figure 6.8: The instantaneous q_{Surf} profiles from 6.3 are replotted in (a). Instantaneous surface area is used to calculated the corresponding 'heat flow rate' ($\frac{J}{cad}$). This rate is then integrated over 'closed-cycle' crank angles to evaluate total heat loss at the wall (J) (b).

types, with the largest relative differences occurring over the crank angles spanning TDC.

The instantaneous heat flux profiles of Fig.6.7c and Fig.6.8a are again re-expressed as heat loss rates in Fig.6.8b (left axis). Note the substantial agreement between engine types over open-cycle crank-angles. This is largely driven by the superior signal quality at the 'Psvi' location. This enhanced signal condition is most likely the combined result of better probe health (i.e., 'intact' measurement junctions) and more optimal pre-processing of the sub-TBC temperature trace.

Evaluation of total heat loss over the -90 to 90 interval is again shown in the final sequence of Fig.6.8. Unlike the results reported for the 'Psi' location, a more physically-consistent trend is

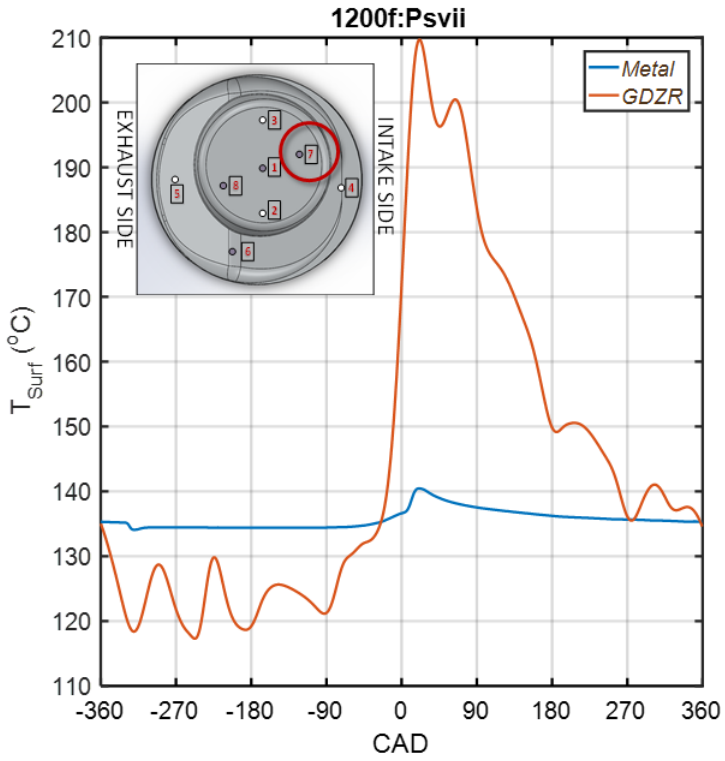

Figure 6.9: Measured ('direct') and estimated ('inverse') surface temperatures for the metal and gadolinium zirconate engine configurations. Operational conditions: $1200 RPM, \dot{fuel} = 11.6 \frac{mg}{cycle}$

shown in Fig6.8c. A slight reduction in cumulative heat loss is displayed for the GDZR engine, particularly over the crank angles corresponding to the peak surface temperature values reported in Fig.6.6. Interesting to note is the 'convergence' of total heat loss at the conclusion of the evaluation interval (i.e., $90^o aTDC_f$). This result is consistent with the trends reported for a separate coating material by citeo2017inverse.

Piston Location: 'Psvii'

Analysis now considers the 'PSvii' probe. Data recorded at this location stands in distinct contrast to the temperature measurements detailed at the 'Psi' and 'Psvi' locations. Although the 'Psvii' measurement junction remains functional, signal fidelity is significantly compromised - the likely result of increased noise susceptibility of a physically degraded measurement junction.

The poor signal quality of the subsurface temperature measurement is amplified in the SFSM surface temperature estimate shown in Fig.6.9. Although the general qualitative characteristic

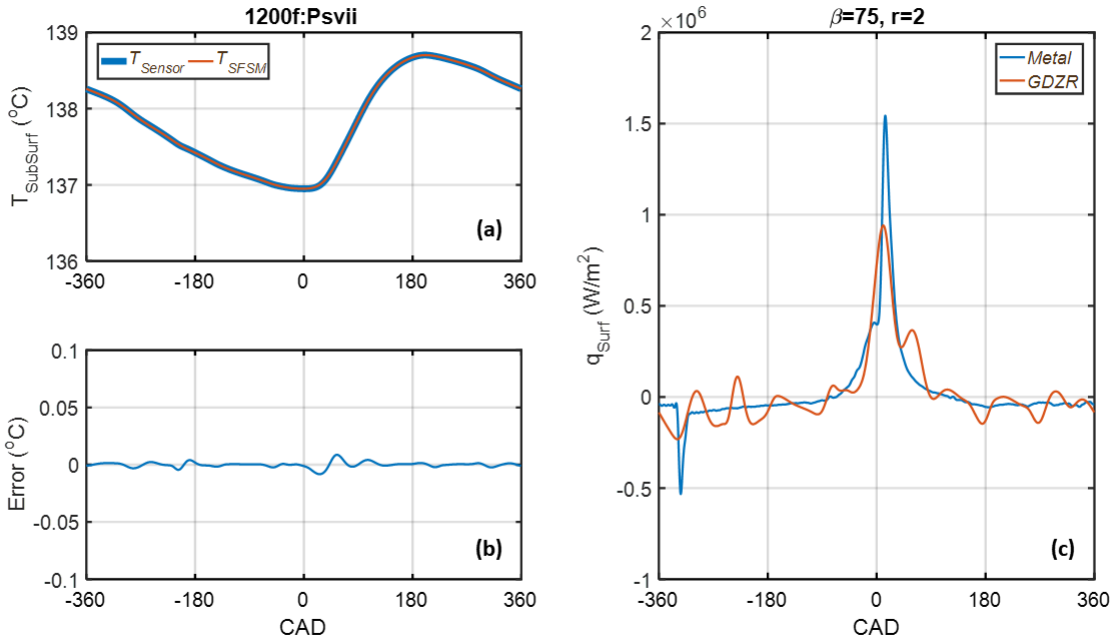

Figure 6.10: Summary of SFSM results, where: (a)Display's solver convergence at the node corresponding to the recorded subsurface temperature. (b)Displays difference (i.e., 'Error') between measured and modeled temps in (a). Lastly, (c) shows measured $q_{Surf,Metal}$ ('direct') and estimated $q_{Surf,GDZR}$ ('inverse').

of the SFSM-derived surface temperature profile remains consistent with the previously discussed results, a substantial noise train extends throughout the cycle. However, it is interesting to note the substantial dip in GDZR surface temperature during intake and early compression relative to the metal engine trace. It should be noted that both the metal and TBC-treated engine configurations are subject to fuel impingement at this location. A slightly negative 'dip' (≈2 degrees) in surface temperature is clearly shown in the metal piston data. Thus, it remains a reasonable expectation that the GDZR material should experience a similar 'cooling' event, when the impinging (liquid) fuel spray contacts the TBC surface. Furthermore, the low thermal inertia of the GDZR material enables the material to respond quickly to surface heating *and* cooling transients. Thus, in a manner similar to the rapid temperature swing observed during compression/combustion heating, the GDZR surface temperature will likewise trend downward during impingement events. This behavior remains consistent with the idealized coating behavior conceptualized at the onset.

In general, convergence of the inverse solver remains excellent at this probe location. That

said, 'hints' of subsurface noise can be seen in rapidly fluctuating component of the profiles shown in Fig.6.10a. The high frequencies associated with the noise-driven fluctuations extend beyond the solver's capability. This behavior further manifests in the error reported in Fig.6.10b, where large noise-driven transients elevate the localized error magnitude. Despite the noise contaminants, and the associated error, the general qualitative characteristics of the temperature swing remain intact. Furthermore, peak surface heat flux estimates remain below those measured in the metal engine - see Fig.6.10c. Taken together, these attributes offer further verification of the GDZR material as a favorable TBC formulation.

Finally, heat loss is evaluated for the 'Psvii' location. The familiar 'heat-flow-rate' to 'cumulative heat loss' calculation pathway is pursued to quantify the combustion-relevant heat flow. Consistent with the results of the preceding sections, pervasive noise contamination continues to degrades the fidelity of the SFSM-derived estimates. The severity of the noise at this location renders the final analysis questionable. In a practical sense, the fluctuating (wave-like) noise component of the continuous heat transfer rate shown in Fig.6.11b severely limits meaningful analysis of this profile. (Recall, when converting heat flux to heat flow rate, an instantaneous surface area scalar is applied at each time-step. The scalar values are greatest over open-cycle crank angle - which unfortunately coincide with the most 'exaggerated component of the noise train.) However, some signal stability is regained when integrating the the signal over the $-90 to 90$ CAD interval. Limiting analysis to the qualitative characteristic of this profile, reduction in over-all heat loss is again demonstrated over crank angles spanning the combustion event.

Piston Location: 'Psviii'

Attention now shifts to the final shared piston location, 'Psviii', shown in the upper right-hand quadrant of Fig.6.12. This locations captures the temperature response in the bowl, towards the exhaust side of the piston. The estimated surface temperature profile again exhibits the desired temperature swing profile, rising quickly in response to the combustion event, while shedding heat over the open portion of the cycle. It should noted that open cycles temperatures remains slightly elevated with respect to the metal surface profile. This may be the result of slight variability in the coating thickness (additional material would increase the effective heat capacity). The incomplete treatment of raw thermocouple voltage (error in reference temp, etc) is also a potential error source. Regardless of the source for this minor offset - physical or otherwise - the respective engine

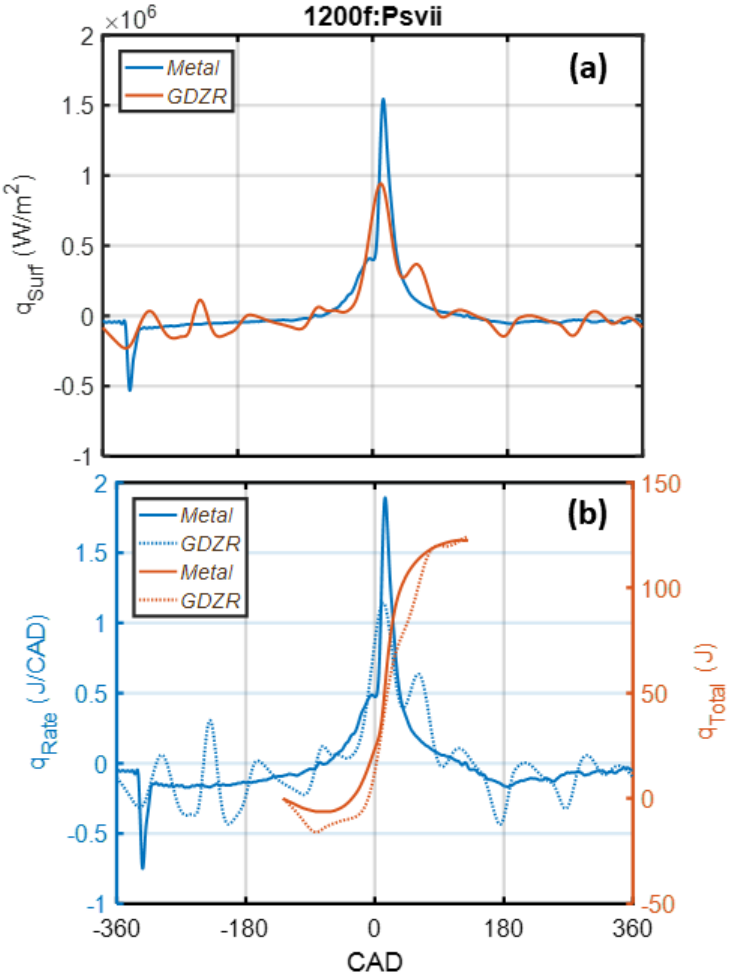

Figure 6.11: The instantaneous q_{Surf} profiles from 6.3 are replotted in (a). Instantaneous surface area is used to calculated the corresponding 'heat flow rate' ($\frac{J}{cad}$). This rate is then integrated over 'closed-cycle' crank angles to evaluate total heat loss at the wall (J) (b).

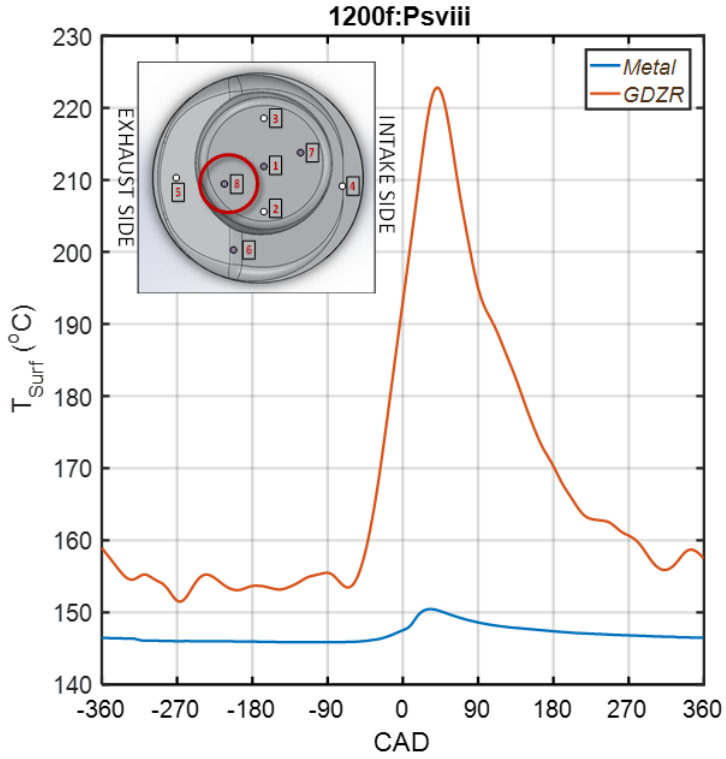

Figure 6.12: Measured ('direct') and estimated ('inverse') surface temperatures for the metal and gadolinium zirconate engine configurations. Operational conditions: $1200 RPM, \dot{fuel} = 11.6 \frac{mg}{cycle}$

configurations are with 7^oC over the open cycle. As a result, charge heating (if any) would likely be minor.

A final qualitative note regarding the profiles plotted in Fig.6.12. Signal fidelity is much improved relative to the 'Psvii' location. This improvement strengthens the qualitative conclusions for the analysis associated with this location.

The high-fidelity signal further enhances solver closure at the sub-TBC temperature (Fig.6.12a) - where modeled/measured temperature traces are shown to agree within 0.01^oC (Fig.6.12b) . The sub-TBC convergence, and favorable signal characteristic enable relatively high qualitative consistency of the SFSM surface heat flux estimate (Fig.6.12c).

The heat flux reported in Fig.6.14a is again converted to an instantaneous heat flow rate (Fig.6.14b, left margin). Accordingly, this trace is integrated over the -90 to 90 CAD interval to evaluate total heat loss during late compression/combustion. The results for this particular probe location also suggest reduced heat loss for the TBC-treated engine.

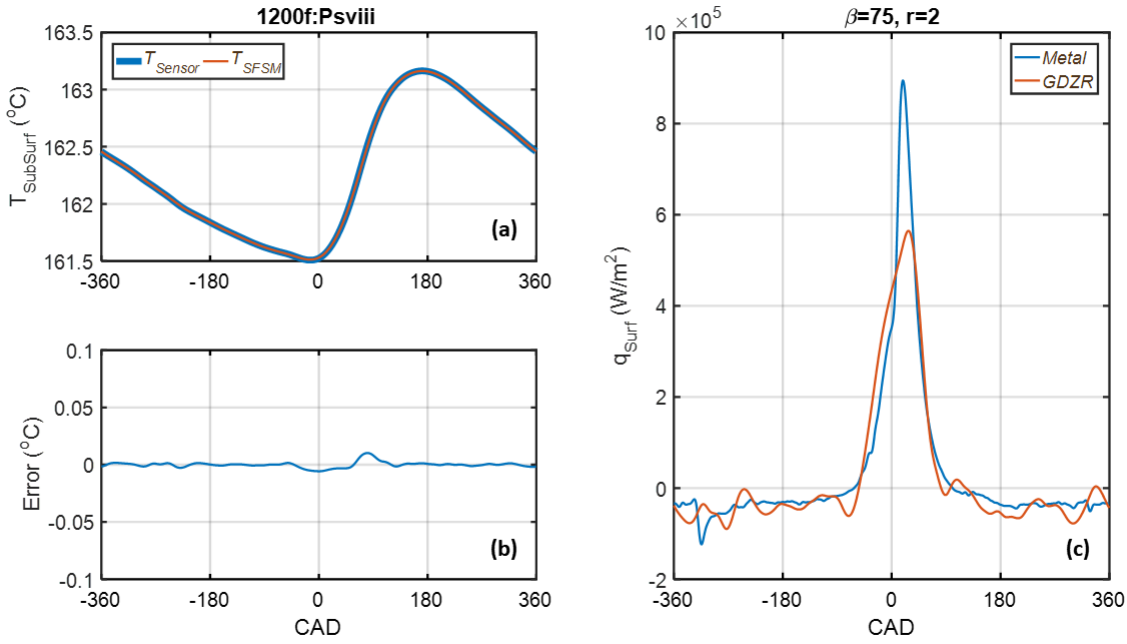

Figure 6.13: Summary of SFSM results, where: (a)Display's solver convergence at the node corresponding to the recorded subsurface temperature. (b)Displays difference (i.e., 'Error') between measured and modeled temps in (a). Lastly, (c) shows measured $q_{Surf,Metal}$ ('direct') and estimated $q_{Surf,GDZR}$ ('inverse').

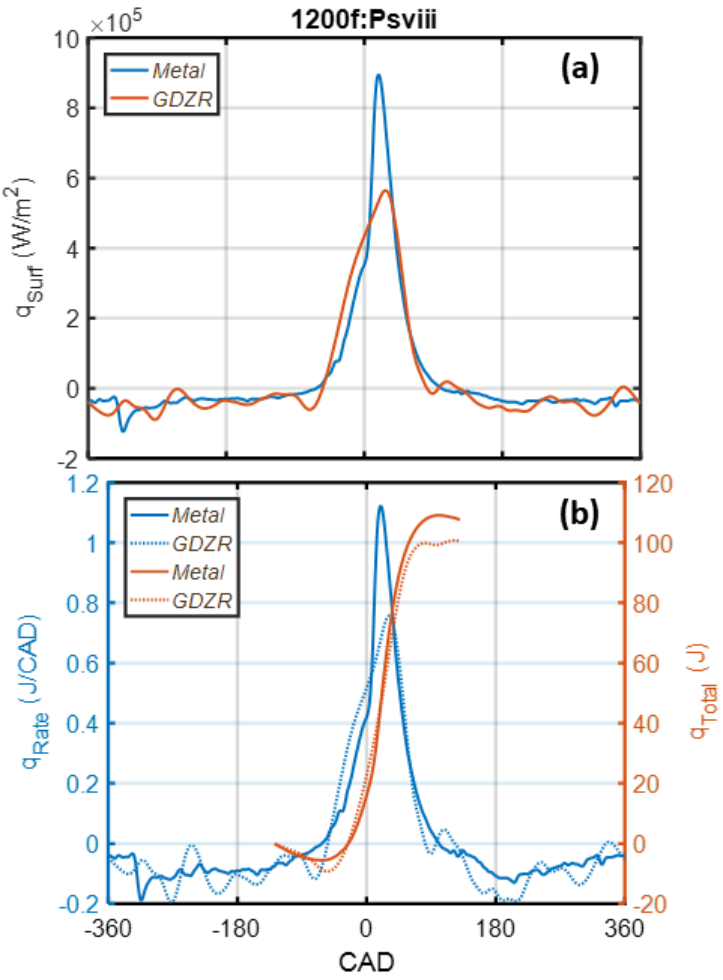

Figure 6.14: The instantaneous q_{Surf} profiles from 6.3 are replotted in (a). Instantaneous surface area is used to calculated the corresponding 'heat flow rate' ($\frac{J}{cad}$). This rate is then integrated over 'closed-cycle' crank angles to evaluate total heat loss at the wall (J) (b).

Head Location: 'HL'

The final shared in-cylinder sensor location corresponds to the 'HL' probe, which is mounted in the head. As a reminder, the heat flux probe at this location is coated to match the configuration of the corresponding piston. In this way, the metal engine utilizes an uncoated probe at this location while the GDZR-treated engine applies an identical TBC layer to the surface of the frontside junction.

A few critical details help distinguish measurements from this probe location from those described previously. First, the location itself is no longer confined to the piston region. Instead, the pulley-side, head location detailed in an earlier chapter is considered. The most immediate benefit of this location is its 'stationary' nature. That's to say, the 'HL' probe (and the fidelity of its signal) is not forced to withstand the extreme dynamic conditions of the piston-derived measurement. Second, the probe itself utilizes the IR-style design, where a stainless body (304 alloy) and laser welded platinum junction, is used in place of the MEDTERM probe type. In general, the IR probe results in heightened signal fidelity (i.e., higher magnitude temperature response given a fixed heat flux), and a more robust over-all design. This last point remains largely anecdotal, but none-the-less reflects observations and experimental outcomes obtained over 100 operational hours.

Data analysis for this probe location begins by reviewing the familiar sequence plotted in Fig.6.15. Here a temperature swing of 65^oC is estimated at the surface of the TBC. This magnitude remains consistent with the estimates obtained at other (piston) locations. As discussed, the stationary mounting at this location, combined with the enhanced 'IR' probe design/response results in a very 'clean' temperature signal. It is also important to note the TBC temperature profile at this location again 'mimics' metal-like values over the open cycle - providing further evidence of teh desired 'swing-like' behavior.

Figure 6.16a demonstrates the inverse solver's closure onto the measure sub-TBC temperatures at the 'HL' location. Error (Fig.6.16b) is well within acceptable limits. It should be noted that the 'largest' convergence error occurs during the rapid, combustion-driven transient. This behavior is consistent with the dynamic limitation(s) of the SFSM technique - where the 'recovery' of high frequency transients are somewhat limited by the stiffness introduced by regularization inherent to the methodology.

The final sequence of Fig.6.15 (i.e., 'c') displays the estimated surface heat flux at the 'HL' location. Notice the high quality character of the heat flux estimate, where the dynamic attributes of

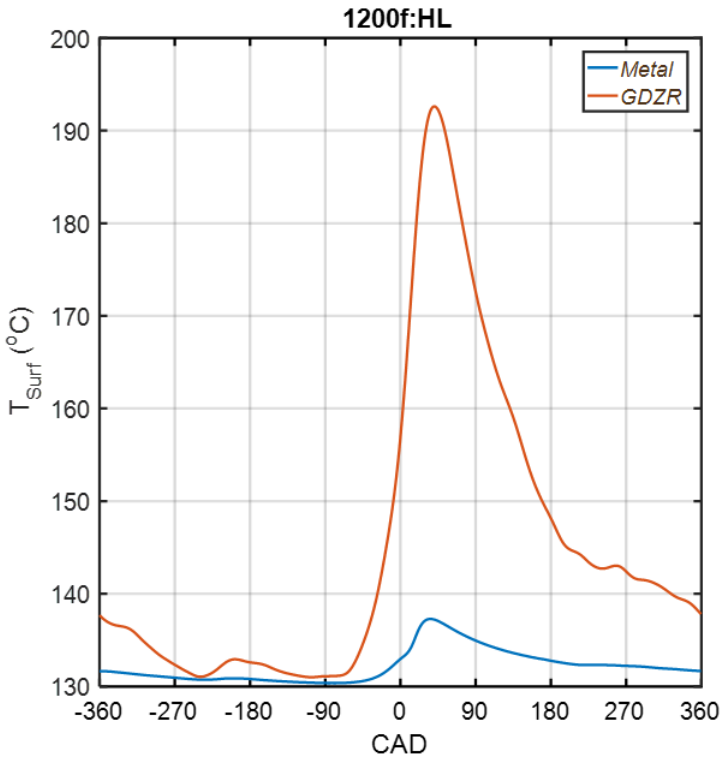

Figure 6.15: Measured ('direct') and estimated ('inverse') surface temperatures for the metal and gadolinium zirconate engine configurations. Operational conditions: $1200RPM, \dot{fuel} = 11.6\frac{mg}{cycle}$

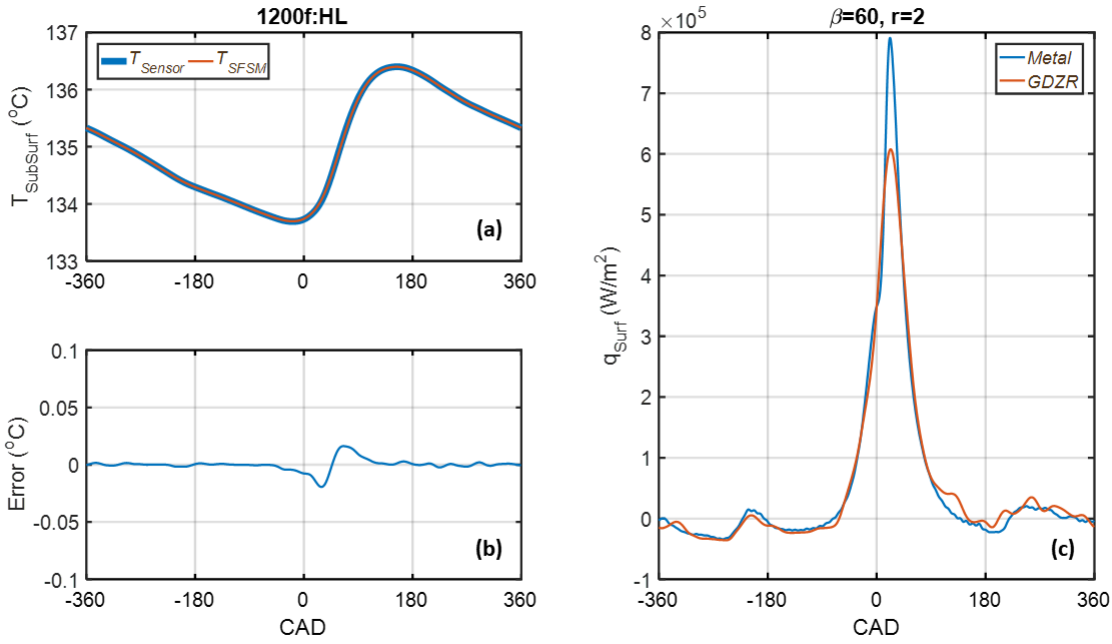

Figure 6.16: Summary of SFSM results, where: (a)Display's solver convergence at the node corresponding to the recorded subsurface temperature. (b)Displays difference (i.e., 'Error') between measured and modeled temps in (a). Lastly, (c) shows measured $q_{Surf,Metal}$ ('direct') and estimated $q_{Surf,GDZR}$ ('inverse').

secondary events (rebreath, gas exchange) are clearly visible. In general, this probe location exhibits the highest level of signal quality among the shared measurement array.

The crank-angle resolved surface heat flux of Fig.'s6.15c and 6.17a is again transformed into a representative heat flow rate using the surface area array. This result is shown in Fig.6.17b (left-hand axis). Due to the high signal fidelity present in the heat flux trace, the heat-flow rate profile exhibits a similar enhanced quality. Integrating over combustion relevant crank-angles results in the cumulative profile displayed in Fig.6.17b (right-hand axis). The cumulative profiles suggest an over-all decrease in Heat Loss for the GDZR engine. Qualitatively this result is consistent with the trends reported for the majority of the piston probe locations - lending further support to a 'global' decrease in heat loss within the TBC-treated engine.

Spatial Averaging and Global Heat Transfer

To better assess the net impact of the GDZR layer, a 'global' heat flux profile is constructed. This processes averages individual probe locations over the engine cycle - resulting in a spatially representative profile. Despite the limited instrumentation array, this approach has been shown to accurately close the energy balance associated with targetted 1^st Law analysis [19].

As with most averaging processes, random signal fluctuations associated with non-coherent noise are largely 'canceled' during the averaging process. Only the signal features which are shared among the probe locations 'survive' the averaging process. Thus, an additional benefit of the aforementioned 'spatial averaging' is the positive impact on signal noise.

Figure 6.18 plots the global results obtained using two separate averaging windows. This comparative effort is meant to demonstrate the influence of critical averaging decisions, including the impact of window size and the inclusion of individual low-quality traces. Figures 6.18a - 6.18b utilize the full measurement array (i.e., all shared probe locations). In contrast, the results shown in Figs.6.18c - 6.18d excluded the lowest quality measurement (i.e., signals from the 'Psvii' location). In addition to the piston locations highlighted in the embedded schematic, the 'HL' head-mounted probe is included in both averaging windows.

A general characteristic of the results presented in Fig.6.18 is the enhanced signal-to-noise ratio over open-cycle crank angles. As discussed above, most of the non-coherent contaminants have been removed by the averaging process. The increased signal fidelity enables a more direct comparison between the SFSM-derived results and those utilizing direct engine measurements.

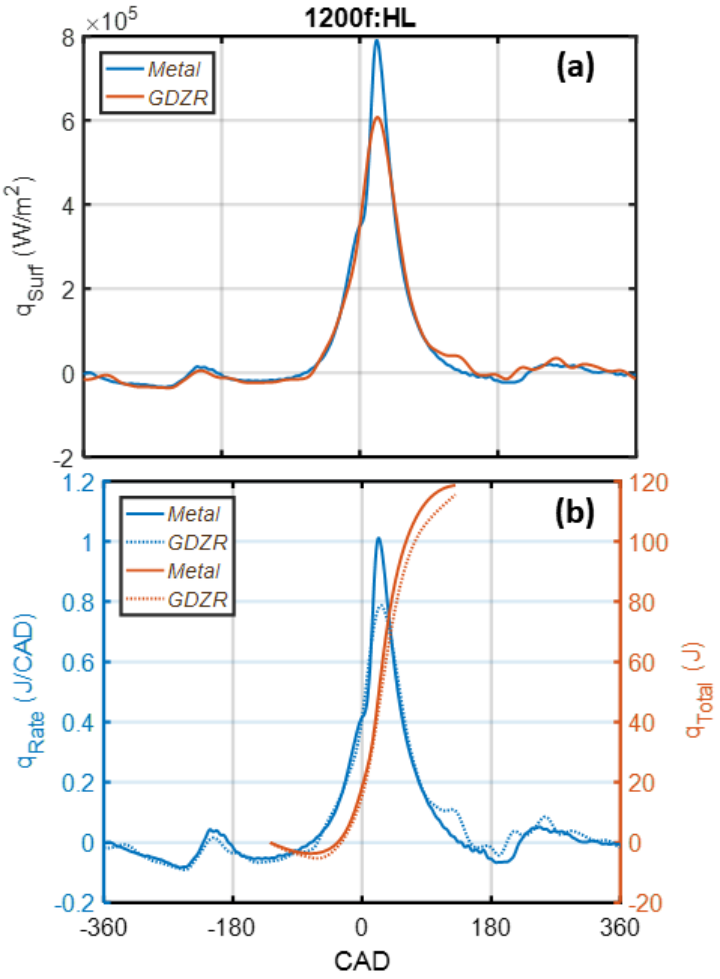

Figure 6.17: The instantaneous q_{Surf} profiles from 6.3 are replotted in (a). Instantaneous surface area is used to calculated the corresponding 'heat flow rate' ($\frac{J}{cad}$). This rate is then integrated over 'closed-cycle' crank angles to evaluate total heat loss at the wall (J) (b).

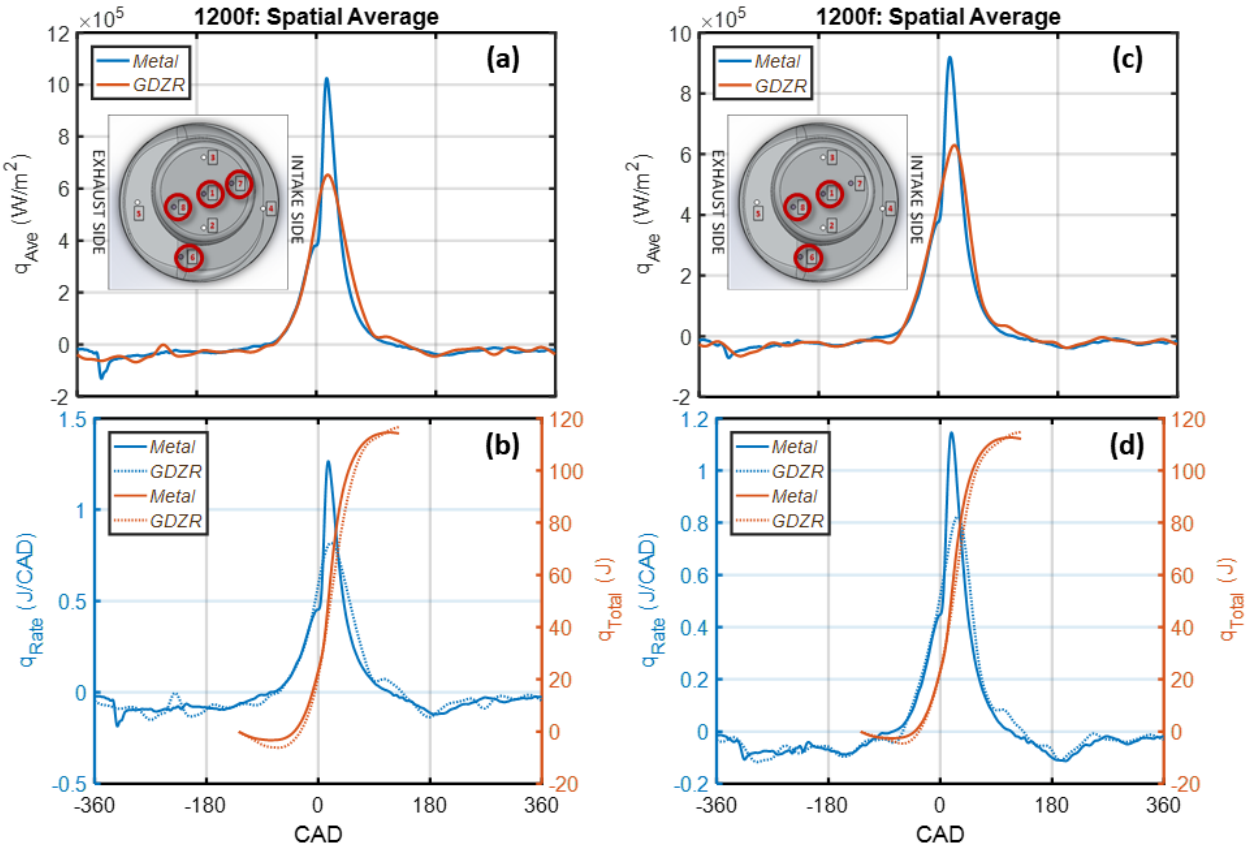

Figure 6.18: The instantaneous q_{Surf} profiles from 6.3 are re-plotted in (a). Instantaneous surface area is used to calculated the corresponding 'heat flow rate' ($\frac{J}{cad}$). This rate is then integrated over 'closed-cycle' crank angles to evaluate total heat loss at the wall (J) (b).

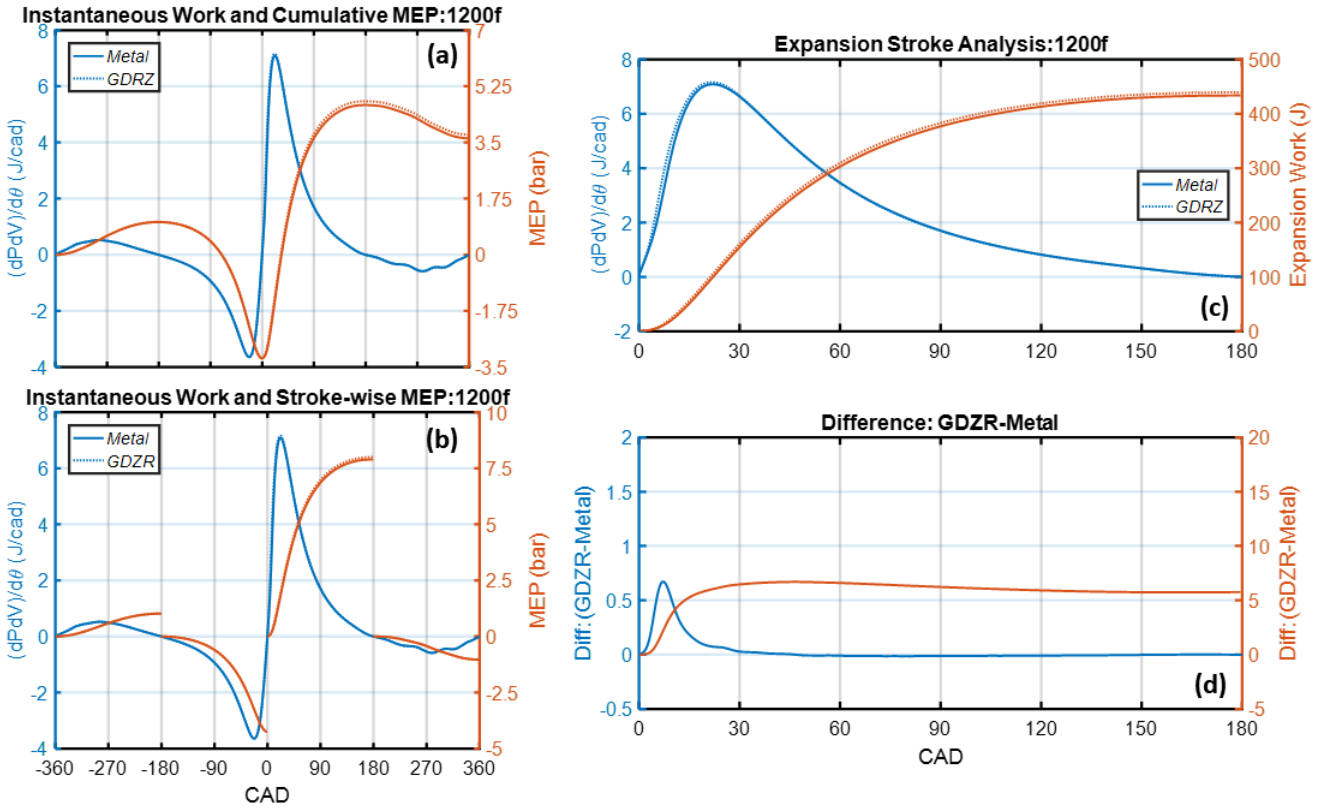

Figure 6.19: Instantaneous cycle work for the 1200 fuel match case. Continuous and stroke-wise work (a), and the associated IMEP values (b). To better determine the impact of the GDZR layer during combustion/expansion, a detailed view of the expansion stroke is shown in (c). The difference between the metal and GDZR trace is further highlighted in (d).

Global Heat Transfer/Instantaneous Work - 1200 Fuel Match

To better identify the impact(s) of the decreased heat loss reported in the preceding section, cycle work is evaluated. In this section, pressure-derived metrics (work, MEP, etc.) are used to explore the impact of TBC's without the aid of temperature measurements. This approach enables independent verification of the global trends reported in the preceding section. Of equal importance, is the ability to directly identify the gains (relative to instantaneous cycle work) resulting from reduced heat loss. These trends will be analyzed from both 'continuous' and 'stoke-wise' perspectives.

The profiles in Fig.6.19a provide visual representation of the integration pathway across the "P-V" curve. The left-hand axis considers an instantaneous work rate, where the 'localized' "P-V" integration is limited to a single time-step (i.e., .5 CADs). The rate-based expression can be integrated over the entire cycle to determine the net cycle work (indicated). This number is typically

normalized by the displaced volume, and reported as a Mean Effective Pressure (MEP) - which is shown on the rightmost axis of Fig.6.19a. As expected, the GDZR engine configuration exhibits higher MEP for the 1200 'Fuel Match' operational point.

To better understand the mechanism(s) driving the physical gains behind the increased cycle efficiency, the analysis of Fig.6.19a carried-out seperately for each stroke of the engine cycle. This effort is shown in Fig.6.19b. Rate-based estimates are again shown on the right, with cumulative results reported on the left. Inspection reveals essentially identical curves spanning the intake, compression, and exhaust profiles. The similarity is actually quite encouraging as it provides direct evidence that charge heating (and the associated increase in pumping work and/or decrease in peak compression work) is not a concern for this operational point. In contrast, the GDZR profile deviates from the metal trace during expansion. This is a critical observation and deserves additional discussion.

Returning to the conceptual temperature-swing model outlined in an earlier chapter, the reduced differential between bulk and surface temperature should reduce heat loss. As the TBC surface reaches it peak value shortly after TDC, the impact on heat transfer should be greatest. In the case of HCCI, decreased heat lost should help enhance both thermal and combustion efficiencies.

Indeed, this conceptual narrative is entirely consistent with the work-rate/MEP discrepancy shown in Fig.6.19b. Simply put, reduced heat loss during combustion/expansion in the GDZR engine manifests as additional cycle work. This trend is explored for the remaining operational points below.

6.1.3 Summary of Results Across Engine Operational Range

The analysis of the preceding section is extended to include a compete array of operational speeds. Additionally, in an effort to better isolate the impact(s) of heat transfer, engine measurements from both 'fuel match' and 'fuel/phase match' operational procedures are considered. Graphics summarizing these results follow. In general, the observations and trends detailed above remain consistent throughout the operational regime, further supporting the 'global' behavior and accompanying analysis. Finally, concise remarks summarizing high-level outcomes of this chapter are provided.

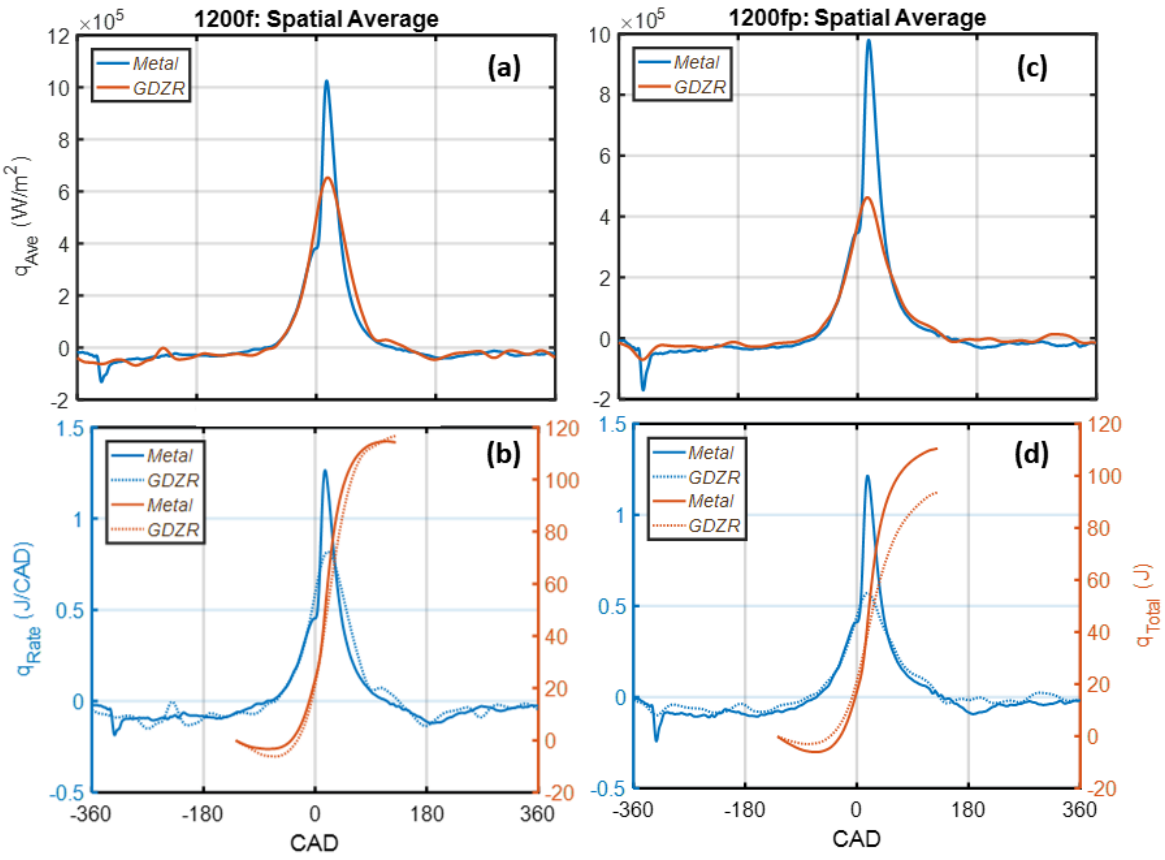

Figure 6.20: The spatially averaged q_{Surf} profiles are plotted in (a). Instantaneous surface area is used to calculated the corresponding 'heat flow rate' ($\frac{J}{cad}$). This rate is then integrated over 'closed-cycle' crank angles to evaluate total heat loss at the wall (J) (b).

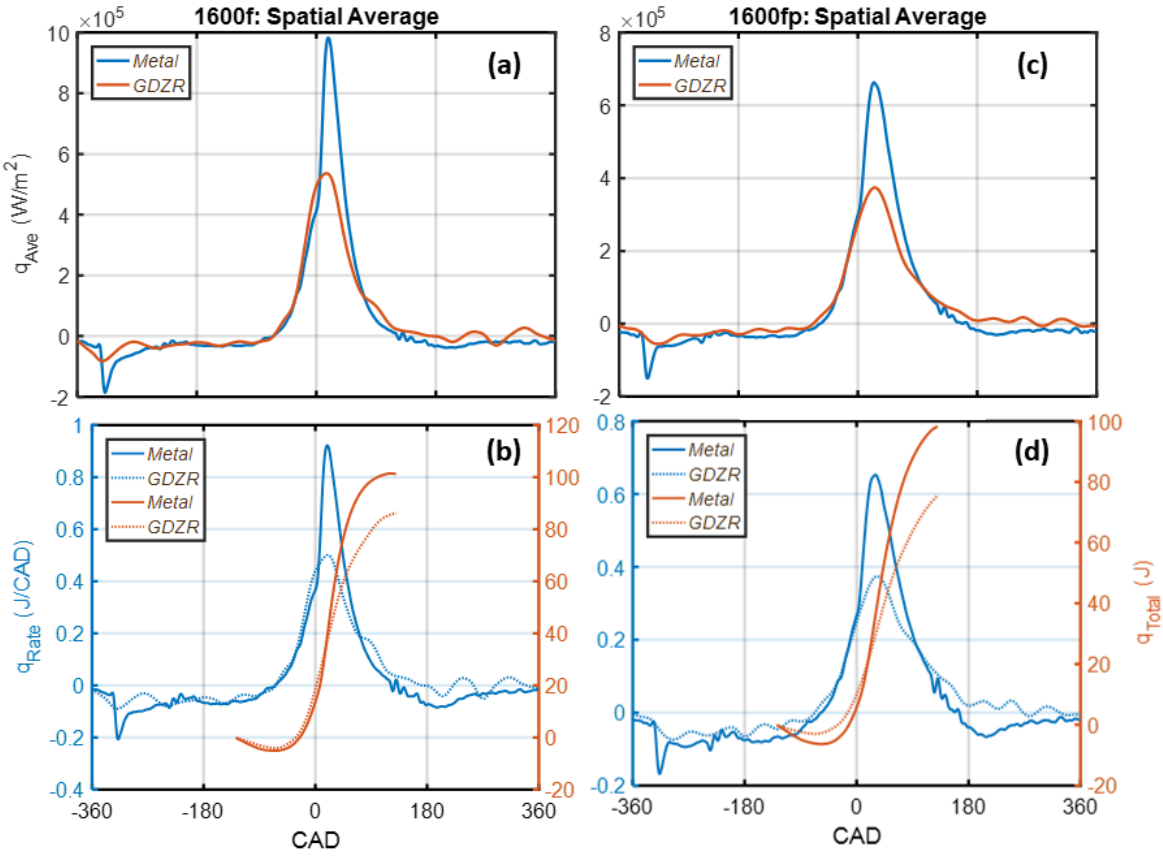

Figure 6.21: The spatially averaged q_{Surf} profiles are plotted in (a). Instantaneous surface area is used to calculated the corresponding 'heat flow rate' ($\frac{J}{cad}$). This rate is then integrated over 'closed-cycle' crank angles to evaluate total heat loss at the wall (J) (b).

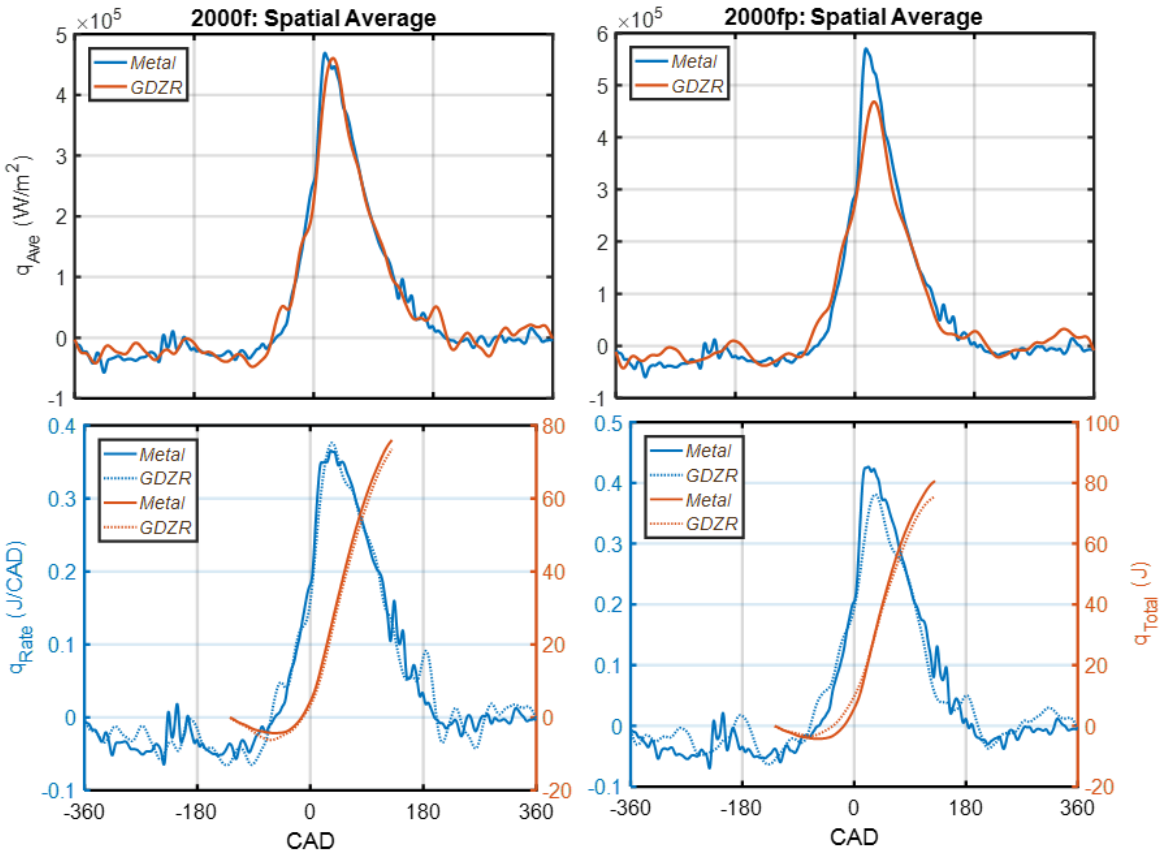

Figure 6.22: The spatially averaged q_{Surf} profiles are plotted in (a). Instantaneous surface area is used to calculated the corresponding 'heat flow rate' ($\frac{J}{cad}$). This rate is then integrated over 'closed-cycle' crank angles to evaluate total heat loss at the wall (J) (b).

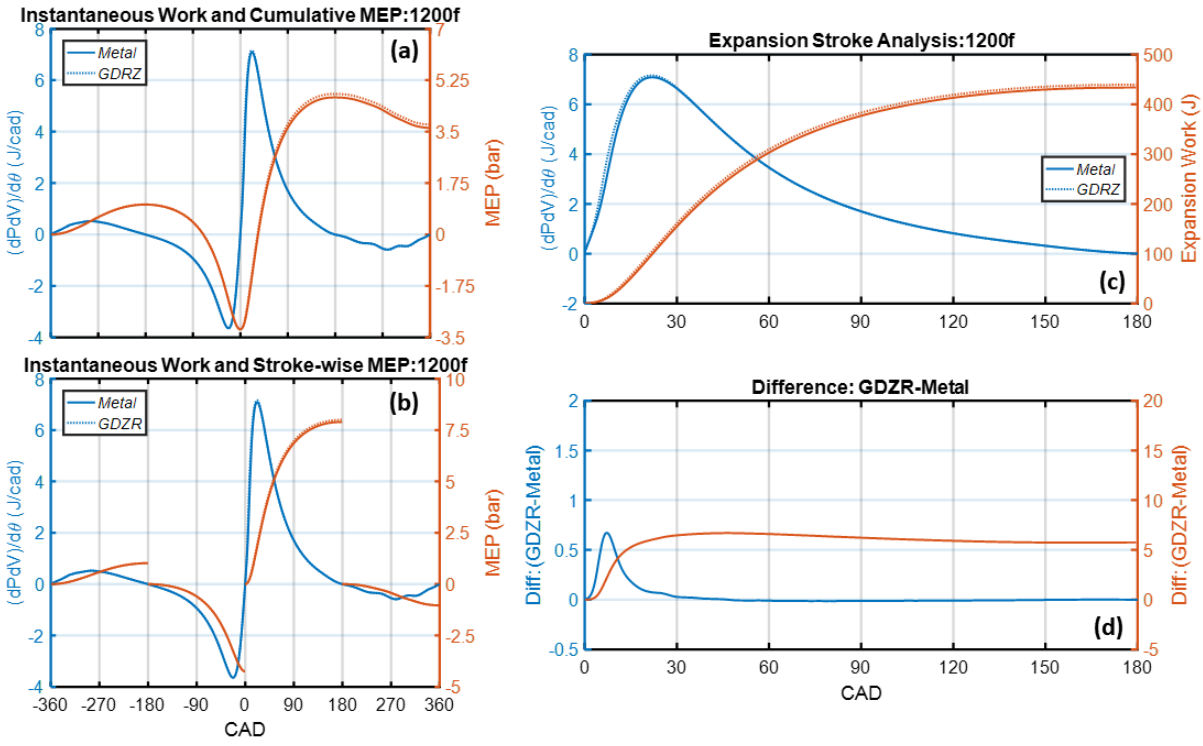

Figure 6.23: Instantaneous cycle work for the 1200 fuel match case. Continuous and stroke-wise work (a), and the associated IMEP values (b). To better determine the impact of the GDZR layer during combustion/expansion, a detailed view of the expansion stroke is shown in (c). The difference between the metal and GDZR trace is further highlighted in (d).

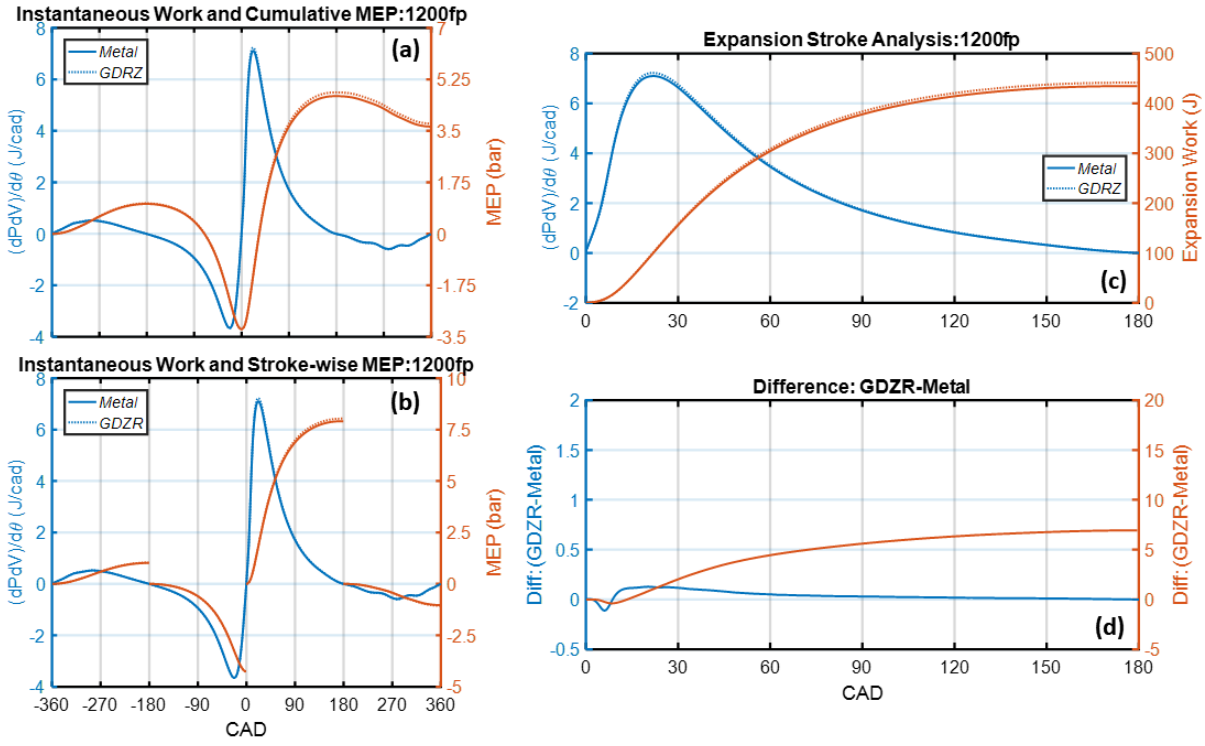

Figure 6.24: Instantaneous cycle work for the 1200 fuel/phase match case. Continuous and stroke-wise work (a), and the associated IMEP values (b). To better determine the impact of the GDZR layer during combustion/expansion, a detailed view of the expansion stroke is shown in (c). The difference between the metal and GDZR trace is further highlighted in (d).

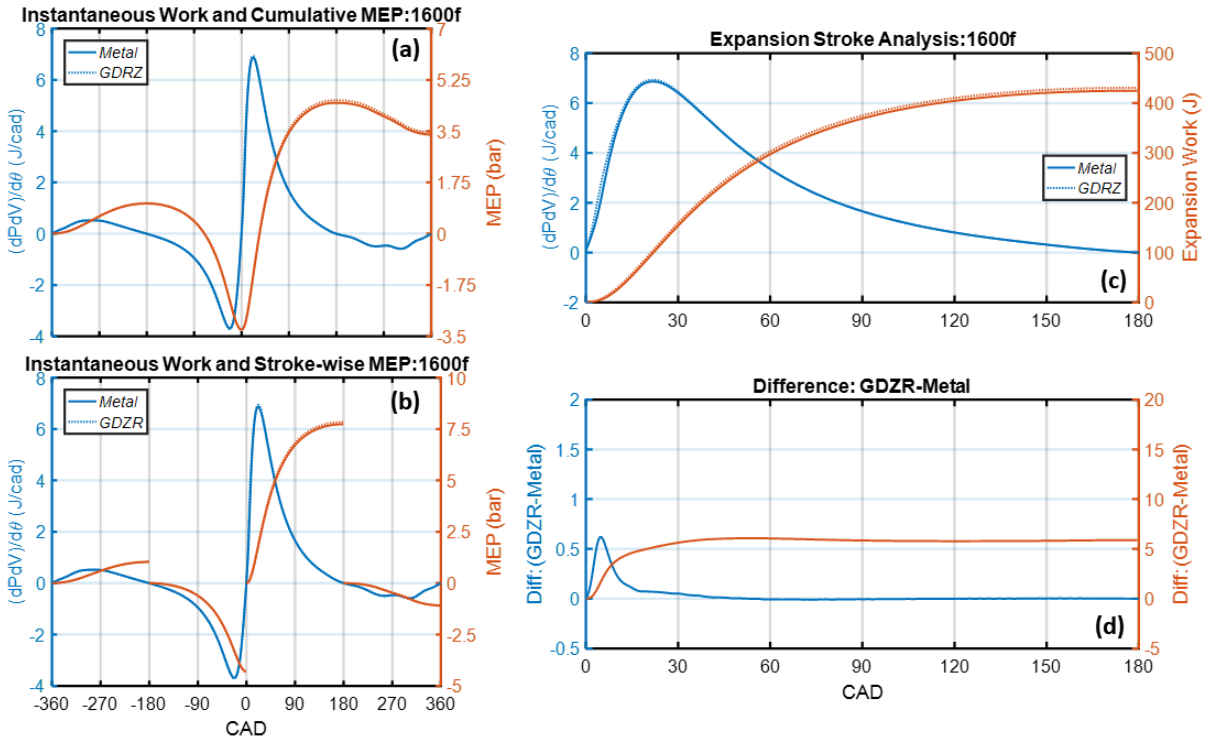

Figure 6.25: Instantaneous cycle work for the 1600 fuel match case. Continuous and stroke-wise work (a), and the associated IMEP values (b). To better determine the impact of the GDZR layer during combustion/expansion, a detailed view of the expansion stroke is shown in (c). The difference between the metal and GDZR trace is further highlighted in (d).

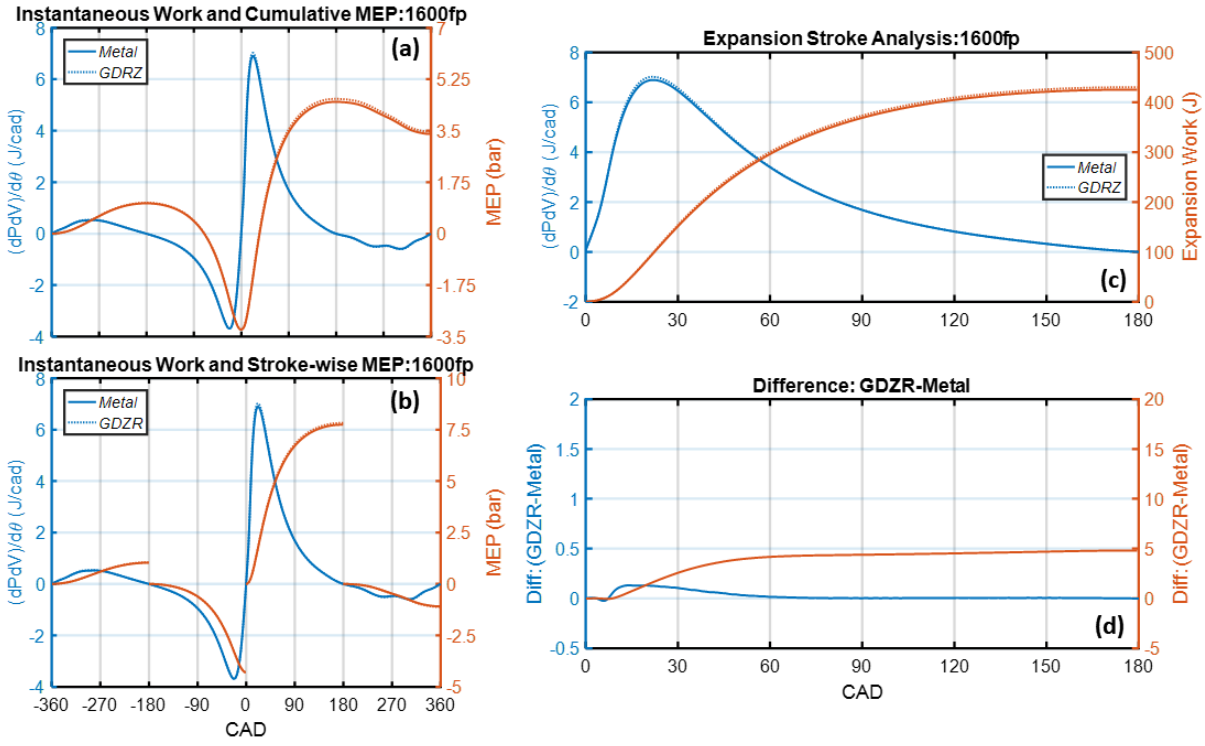

Figure 6.26: Instantaneous cycle work for the 1600 fuel/phase match case. Continuous and stroke-wise work (a), and the associated IMEP values (b). To better determine the impact of the GDZR layer during combustion/expansion, a detailed view of the expansion stroke is shown in (c). The difference between the metal and GDZR trace is further highlighted in (d).

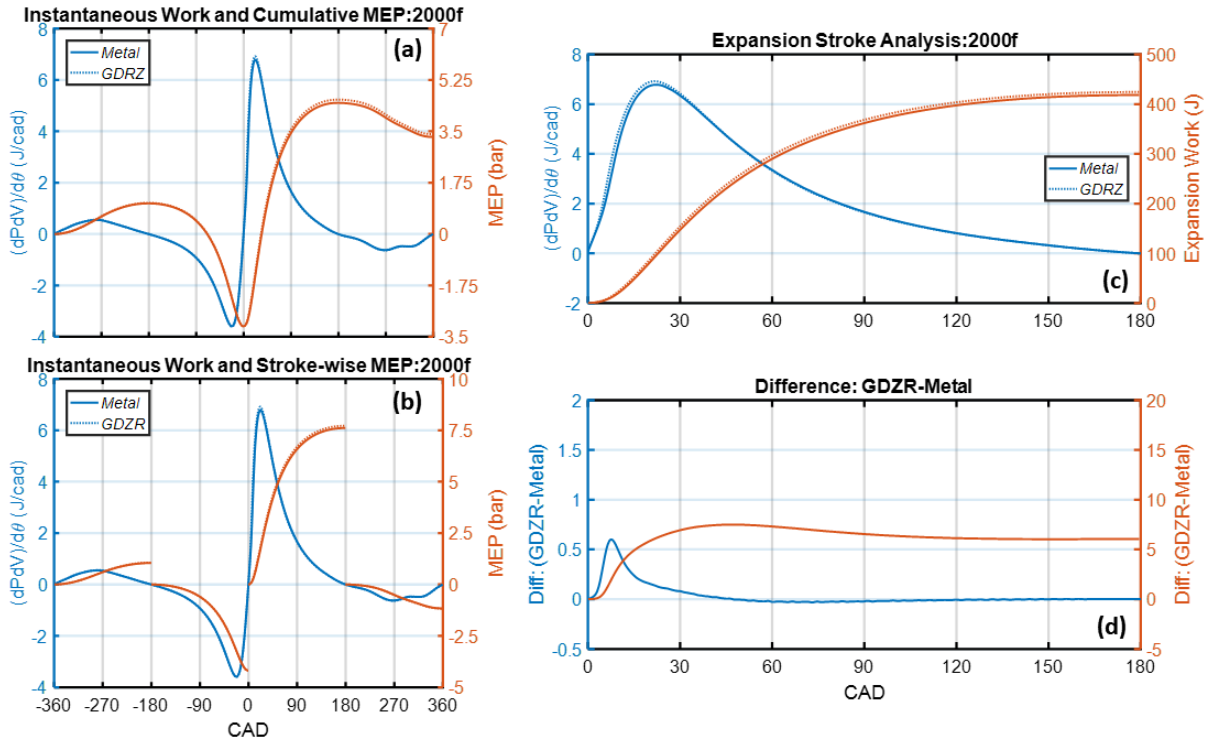

Figure 6.27: Instantaneous cycle work for the 2000 fuel match case. Continuous and stroke-wise work (a), and the associated IMEP values (b). To better determine the impact of the GDZR layer during combustion/expansion, a detailed view of the expansion stroke is shown in (c). The difference between the metal and GDZR trace is further highlighted in (d).

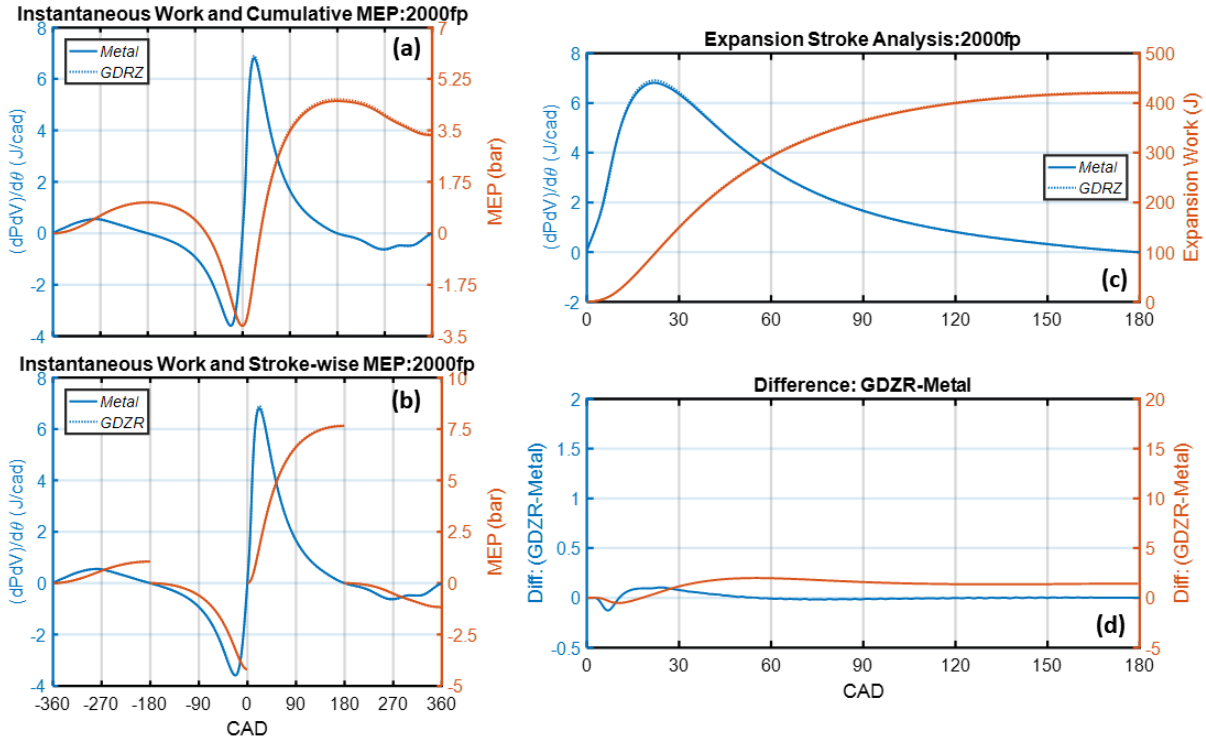

Figure 6.28: Instantaneous cycle work for the 2000 fuel/phase match case. Continuous and stroke-wise work (a), and the associated IMEP values (b). To better determine the impact of the GDZR layer during combustion/expansion, a detailed view of the expansion stroke is shown in (c). The difference between the metal and GDZR trace is further highlighted in (d).

6.1.4 Concluding Remarks

Analysis within this chapter has established an analytic benchmark with which surface temperature and heat transfer metrics are quantified. The gadolinium zirconate treated engine exhibits a substantial surface temperature "swing" in response to compression and combustion processes. The elevated closed-cycle surface temperature changes the conditions at the gas-wall interface, which in-turn has a quantifiable impact on heat transfer. Pressure-based analysis also reveals gains in cycle work as a result of decreased heat loss. Both instances show that the gains restricted to closed-cycle operation. Furthermore, charge heating (manifesting as increased pumping work during gas exchange) has not been observed. Together, these observations provide substantial experimental evidence of highly beneficial coating performance.

Chapter 7

Thermal Stratification Analysis

In this section, a post-processing technique known as Thermal Stratification Analysis (TSA) is used to quantify the impact of Thermal Barrier Coatings on the temperature distribution within the bulk gas of a gasoline-fueled Homogeneous Charge Compression Ignition (HCCI) engine. Using an empirically derived ignition delay correlation for HCCI-relevant air-to-fuel ratios, an autoignition integral is tracked across multiple temperature 'zones' within the cylinder. Mass is assigned to each zone using the Mass Fraction Burn (MFB) profile from the pressure-based heat release analysis. Estimates of charge temperature distributions across early-compression and combustion-relevant crank angles are calculated. Ultimately, this analysis provides a statistical description of in-cylinder thermal composition across a variety of TBC formulations.

7.1 Overview of TSA Methodology

A concise overview of Thermal Stratification Analysis is provided. Requisite theoretical background and other vital considerations are discussed. The content presented in this section (including motivating principles and background material) is largely derived from the pioneering work of [58] and [59]. The present effort contains a limited number of modifications/deviations with respect to the original formulation. These details are noted as are their implications.

The TSA constructs in-cylinder temperature distributions throughout the engine cycle from probability density functions constructed via the mass fraction burned behavior, which is derived from experimental pressure measurements. The cylinder contents are discretized into various zones,

which have no specific spatial orientation but contain a fixed portion of the total trapped mass. Interactions zones are limited to compression/expansion effects, with no inter-zonal diffusion or heat transfer. Autoignition of the charge within each temperature zone is tracked throughout the compression/combustion process. In this way, the zonal temperature histories are aligned with the experimental MFB.

A more detailed overview begins with a review of the interdependence between the thermo-kinetic processes underlying HCCI combustion and heat transfer losses at the cylinder wall.

7.1.1 Thermal Barriers and Thermo-Kinetic Combustion

The chemical kinetics governing gasoline compression ignition concepts are largely determined by the time-evolution of in-cylinder pressure and temperature. Simply put, for a uniform charge composition (i.e., spatial homogeneity in ϕ), autoignition chemistry is primarily a function of in-cylinder pressure and temperature. As a consequence, engines which operate in a fully-premixed, kinetically-driven, combustion mode (such as HCCI) are highly influenced by the in-cylinder temperature field.

In this way, HCCI combustion resembles a 'cascade' of separate autoignition events - with combustion progressing from the highest temperature zones towards those with lower temperature. Furthermore, excessively 'cool' charge temperatures will slow the reactions underlying oxidation, resulting in incomplete combustion. As will be shown, the 'cool tail' of the in-cylinder temperature distribution has a dramatic impact on combustion efficiency (η_{Comb}) and hydrocarbon emissions (UBHC).

Given the influence of charge temperature on HCCI combustion, efforts to actively influence the thermal conditions in the combustion chamber have been explored as a means to both control burn rates and extend operational limits - ([85] and [83]). Traditionally, this 'active' management of charge temperature has been limited to crank angle degrees (CAD) preceding intake valve closing (IVC). Such efforts include pre-heating/cooling of intake air and/or induction of similarly conditioned diluents. (The latter method impacts both the thermal and compositional make-up of the trapped charge).

More recent efforts, including those presented in this dissertation, extend their reach into the 'valve-closed' portion of the engine cycle. This is achieved primarily through the application of low conductivity materials to in-cylinder surfaces. As demonstrated, sufficiently 'thin' ($\approx\leq$150

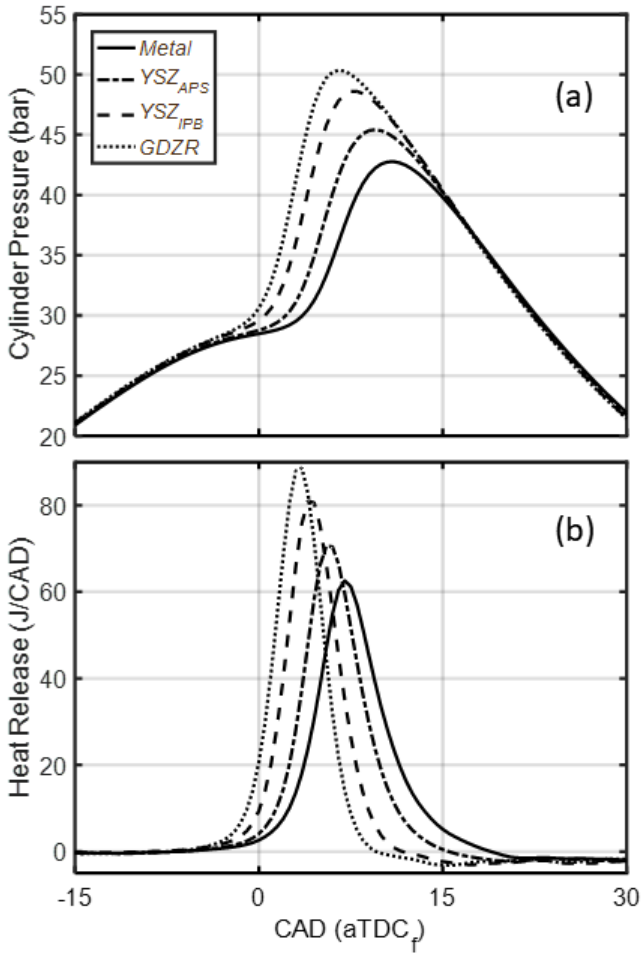

Figure 7.1: The impact of coatings on cylinder pressure and heat release rate. In general, combustion advances and burn duration decreases as TBC's with successively lower conductivities are considered.

μm), low-k coatings enable surface temperatures to closely mimic bulk gas behavior over the engine cycle - elevating surface temperatures during late compression/expansion while rapidly shedding heat to avoid charge heating during gas exchange. These elevated closed-cycle surface temperatures have a dramatic impact on heat transfer at the gas-wall boundary. This is particularly true for the gadolinium zirconate material, where surface temperature profiles are an order-of-magnitude larger than those measured for the metal engine configuration. Ultimately, the temperature at the gas-wall interface determines largely determines heat transfer across this boundary - and by extension the thermal composition of the interior charge.

An overriding goal of this work is to exploit the thermal sensitivity of HCCI through strategic elevation of combustion chamber surface temperature. To better evaluate progress towards meeting this goal, we will quantify the in-cylinder charge temperature distribution for a number of coating formulations.

7.1.2 Mass Fraction Burned Profiles: A Product of Heat Release Analysis

A critical component of the TSA methodology is the 'Mass Fraction Burned' (MFB) profile. The MFB considered in this work stems from heat release analysis (HRA) of the cylinder pressure. This section provides a concise overview of the theoretical framework supporting this analysis. Key assumptions are discussed, as are requisite sub-models.

Heat release calculations in the present analysis apply a single-zone control-volume to the combustion chamber in order to evaluate the energy balance of the system - i.e., $1^{st} Law$ approach. To simplify calculations, analysis is limited to closed-cycle operation where mass-flux due to gas exchange (and the associated enthalpy flow) is not present. Crevice losses and blow-by (i.e., additional mass loss) are also neglected in the current model. These pre-conditions enable the energy balance equation to be stated compactly:

$$dU = \partial Q - \partial W \tag{7.1}$$

Here, dU represents the sensible change in internal energy, ∂Q the energy associated with combustion (Q_C) and heat loss (Q_{HT}), and ∂W pressure-work on the piston. In the present work, heat release during combustion is adjusted to reflect combustion efficiency (η_{Comb}) such that:

$$Q_C = (m \cdot LHV)_{Fuel} \cdot \eta_{Comb} \tag{7.2}$$

Expanding the thermal energy term, and re-arranging Eq.7.1, the energy-balance may be re-expressed as:

$$\partial Q_F = dU + \partial W + \partial Q_{HT} \tag{7.3}$$

The total differential element dU (i.e., internal energy term) in the present analysis is modeled as a function of temperature, such that:

$$dU = mc_V(T) + u(T)dm \tag{7.4}$$

Where c_V is the specific heat of the air-fuel mixture at constant volume. Assuming Ideal Gas behavior over the closed-cycle, and making use of the thermodynamic identity $c_V/R = 1/(\gamma - 1)$, the energy balance equation is re-expressed in rate-based form:

$$\frac{dQ_F}{dt} = \frac{\gamma}{\gamma - 1} p \frac{dV}{dt} + \frac{1}{\gamma - 1} V \frac{dp}{dt} + \frac{dQ_{HT}}{dt} \tag{7.5}$$

This expression can be integrated over crank angles spanning combustion to produce the Cumulative Gross Heat Release (Q_F). This cumulative metric enables calculation of the Mass Fraction Burn Curve, where:

$$MFB(\theta) = \frac{Q_F(\theta)}{Q_F(\theta)_{Max}} \tag{7.6}$$

A more complete derivation of Eq.7.5, along with detailed discussion of individual terms (including the mass flux terms presently neglected) may be found in [43] and [31].

The integrity of the above model depends on the accuracy of the individual terms. As such, the ratio of specific heats (γ) and instantaneous heat-loss (Q_{HT}) are determined using empirical correlations derived specifically for gasoline-fueled HCCI. These procedures are detailed in the following section.

7.1.3 Heat Transfer, Ratio of Specific Heats, and their Empirical Correlations

Empirical correlations are employed to evaluate both γ and heat transfer (dQ_{HT}) terms within the energy-balance of Eq. 7.5. Woschni's well known heat transfer correlation [91] forms the foundation of the heat transfer model. In general, this approach assumes the following relation:

$$Nu = a \cdot Re^b \tag{7.7}$$

Where Nu and Re describe the respective 'Nusselt' and 'Reynolds' numbers. These expressions are typically defined for geometries approximating pipe flow. The a and b terms are 'tuning' parameters which may change depending on the specific application/dataset of interest. Re-arranging terms - see [91] for full details) - results in the following expression:

$$h(n) = \alpha \cdot L(n)^{b-1} \cdot \frac{k}{\mu^b} \cdot p(n)^b. \tag{7.8}$$

This original result has been further modified by Chang et al in [19] to reflect the HCCI combustion process. It should be noted that this modified correlation was derived using an identical engine platform to the current setup detailed above. Hence, its conclusions are directly applicable to the present experiments. The authors in [19] describe an instantaneous convection coefficient where:

$$h(n) = \alpha \cdot \left(\frac{4V(n)}{\pi B^2}\right)^{-0.2} \cdot p(n)^{0.8} \cdot T(n)^{-0.73} \cdot w(n)^{0.8} \tag{7.9}$$

Here, n is the generic time-step, α is a scaling coefficient used to reflect engine-specific characteristics, w is the instantaneous piston speed, k and μ reflect thermal conductivity and kinematic viscosity, p is the measured cylinder pressure, T is the associated bulk-charge temperature, and w describes a representative in-cylinder gas velocity. The reader should again refer to [91] and [19] for the specific form of these term. In general, gas velocity is expressed as a function of mean piston speed (during a motored cycle), with additional, combustion-mode-specific terms used to capture the combustion-induced component of gas velocity. This latter parameter represent a major difference between the referenced correlations.

A temperature-dependent expression for the ratio of specific heats 'γ' (also from [19]) is used Eq.7.5. Again, the interested reader is referred to the appropriate reference for full details.

Results are described using a 3^{rd} order polynomial, which appears below:

$$\gamma(T) = -9.967 \times 10^{-12} \cdot T^3 + 6.207 \times 10^{-8} \ldots \ldots \cdot T^2 - 1.436 \times 10^{-4} \cdot T + 1.396 \tag{7.10}$$

With the addition of the above expression Eq.7.5 can be evaluated across closed-cycle crank angles. This, and the methodology described in Eq. 7.6, enables calculation of the MFB profile at each of the engine operating conditions.

7.1.3.1 Autoignition Correlations and the Prediction of Ignition Delay'

A variety of HCCI-relevant ignition delay correlations are reported in the literature [40] [34]. In general, these expression are based on the experimental evaluation of ignition delay times using rapid compression machines and/or constant-volume combustion rigs. Critical parameters including effective pressure, temperature, equivalence ratio, and O_2 content are systematically varied across engine-relevant values. Results of this experimental matrix are often used to construct an Arrhenius power-law equation, with individual terms describing the relative contribution of the aforementioned parameters.

Figure 7.2 provides an example of a 'raw' experimental pressure time-history, derived from a rapid compression machine operating under HCCI-like conditions [40].

As an alternative to the direct measurement of ignition delay, autoignition time-scales may be examined using a numerical approach. Typically, a chemical mechanism (with $10^2 - 10^3$ individual species) is required to sufficiently model a representative fuel. (Isooctane, C_8H_{18}, is a commonly selected as a gasoline-like fuel). The system of equations governing oxidation chemistry are discretized, and solved across a range of thermo-kinetic parameters. In this way, the time interval corresponding to autoigntion can be evaluated. A considerable strength of this technique is the ability to track the contribution(s) of individual species and monitor intermediary reactions. However, the over-all fidelity of the method relies on the underlying fuel model. Furthermore, the complexity associated with 'real' fuel blends (including gasoline) are often beyond the practical limits of available computational resources. As a result, analysis is often limited to simplified (often single component) fuels such as iso-octane. A comprehensive study, comparing numerical results from a detailed chemical mechanism with the outcome of multiple experimental datasets can be found in [34].

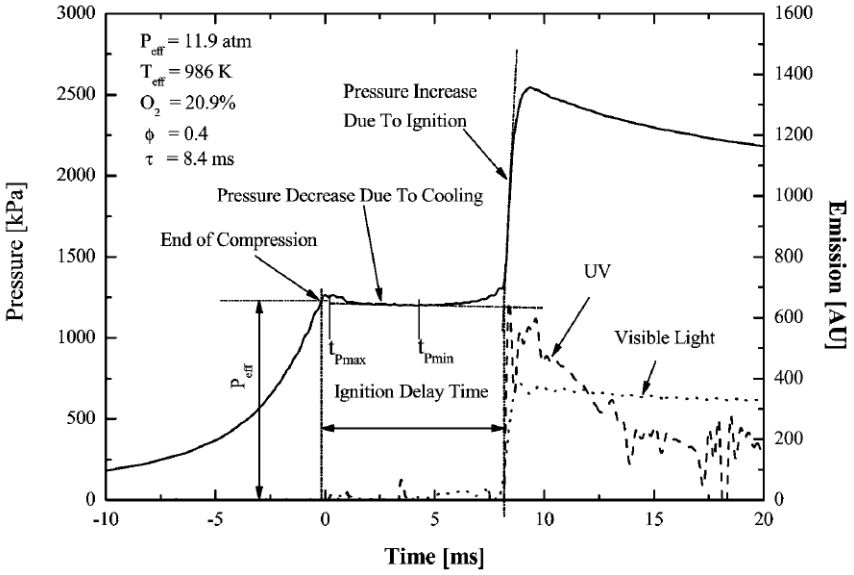

Figure 7.2: A lean air-fuel mixture is compressed ($-10ms \geq t < 0ms$) in a specialized (non-reciprocating) experimental rig. The compressed charge is maintained under quiescent, and quasi-static conditions. Peak compression pressure occurs at $t = 0ms$. The vessel pressure dips slightly - a result of heat loss - and is followed by a modest pressure rises at the onset of low-temperature reactions (i.e., 'cool flame' activity). These preliminary oxidation reactions are followed by a rapid increase in pressure at $t \approx 8ms$. This marks the onset of the primary combustion event. 'Ignition Delay' is thus defined as the time interval between 'End of Compression' and the recorded 'Ignition Pressure Increase'. Radiative emissions may also be used (UV and Visible light bands) to independently verify the onset of the primary combustion event. Reprinted from [40].

In the current work, thermal stratification analysis will utilize a modified form of the empirical correlation reported by He and co-authors in [40]. The original expression is described using an Arrhenius equation of the form:

$$\tau = 1.3 \cdot e^{-4} \cdot p^{-1.05} \cdot \phi^{-0.77} \cdot \chi_{O_2}^{-1.4} \cdot exp\frac{33700}{RT} \tag{7.11}$$

With the corresponding unit convention: $p(atm)$, $T(K)$, ϕ (iso-octane-to-O_2 molar ratio), $\chi O_2(O_2 molar)$, $\tau(ms)$, and $R = 1.98722 cal/mol \cdot K$.

To better reflect the multi-component gasoline, engine platform, and operational regime of the present analysis, a modified form of the above express is also considered [95].

$$\tau = 6.2 \cdot e^{-5} \cdot p^{-1.05} \cdot \chi_{O_2}^{-1.4} \cdot exp\frac{33700}{RT} \tag{7.12}$$

Following the methodology of Livengood and Wu [62], autoignition occurs when the cumulative delay time satisfies the following relation:

$$\int \frac{1}{\tau} \cdot dt = 1 \tag{7.13}$$

7.1.4 Constructing a Reduced Constituent Gasoline Surrogate

A number of thermo-chemical properties are required to fully evaluate the autoigniton correlations described in Eq.7.11 and Eq.7.12. Furthermore, the ratio of specific heats (γ) expressed in Eq.7.14 is (in reality) a multi-variate function of temperature, pressure, and charge composition. In order to more accurately account for the evolution of these parameters in the present analysis, it is necessary to construct a representative fuel surrogate based on more fundamental (and well-understood) constituents. For the analysis considered below, the research gasoline described in Table 3.2 will be modeled as a three-component blend of isooctane (C_8H_{18}), n-Pentane (nC_5H_{12}), and Benzene (C_6H_6). This effectively decomposes the research fuel into a much smaller subset of well-understood components. Teh reduced complexity of these constituents enables the use of empirical look-up tables. In other words, at each time-step, explicit values for critical parameters including γ, R, etc., can be determined using tabulated thermo-chemical archives.

In the present analysis, thermo-chemical properties of the three-component surrogate are derived from the NIST JANAF thermochemical database [86].

7.1.5 The 'Temperature Zone': A Definition

At this stage, it is necessary to define the so-called "Temperature Zone". This concept becomes critically important during the autoignition-to-MFB mapping procedure detailed at length in subsequent sections. In many ways, the temperature zone idea is at the heart of Thermal Stratification Analysis, and will be treated accordingly.

In order to construct 'Temperature Zones' which are compatible with the reduced dimensionality of the TSA methodology, a number of key simplifications/assumptions are required. Zonal interactions are limited to compression. There is no heat transfer or diffusion between the zones, but each zone is allowed to transfer heat to the cylinder walls. This assumption is congruous with the PLIF work of [24], subject to isentropic compression.

In dimensional form, zone evolution is entirely defined by the following equation:

$$T_{isen}(n) = T_{IVC} \cdot \frac{P(n)}{P_{IVC}}^{\left(\frac{\gamma-1}{\gamma}\right)} \tag{7.14}$$

As the above expression makes clear, the isentropic compression process if driven by the bulk cylinder pressure. In this way, temperature zones 'feel' both the motored and combustion-driven components of in-cylinder pressure. This is critical, as a substantial portion of the 'late' burn is in direct response to the post-TDC pressure rise. (Recall, in-cylinder pressure rise after $CAD = 0^o$ is the result of combustion, as the 'geometric' pressure peaks shortly before TDC.)

An example, detailing the evolution of unburned charge temperature profiles for T_{IVC} values, is provided in Fig. 7.3. Each of the individual temperature profiles correspond to a unique 'temperature zone'. This concept (and it's relationship to measured values) will be developed below.

The TSA method, as developed in [58] and [59], further defines the temperature zone concept in terms of a 'Normalized Zone Temperature' (NZT) - where charge temperature is referenced to both isentropic and combustion chamber surface temperature profiles. Mathematically, this translates to:

$$NZT = \frac{T_{Zone}(n) - T_{Surf}(n)}{T_{isen}(n) - T_{Surf}(n)} \tag{7.15}$$

For the special case where Normalized Zone Temperature equals unity, the dimensional zone temperature (T_{Zone}) mimics the isentropic temperature profile (T_{isen}) described by Eq. 7.14. In other words, $NZT = 1$ corresponds to the maximum temperature allowed given the underlying

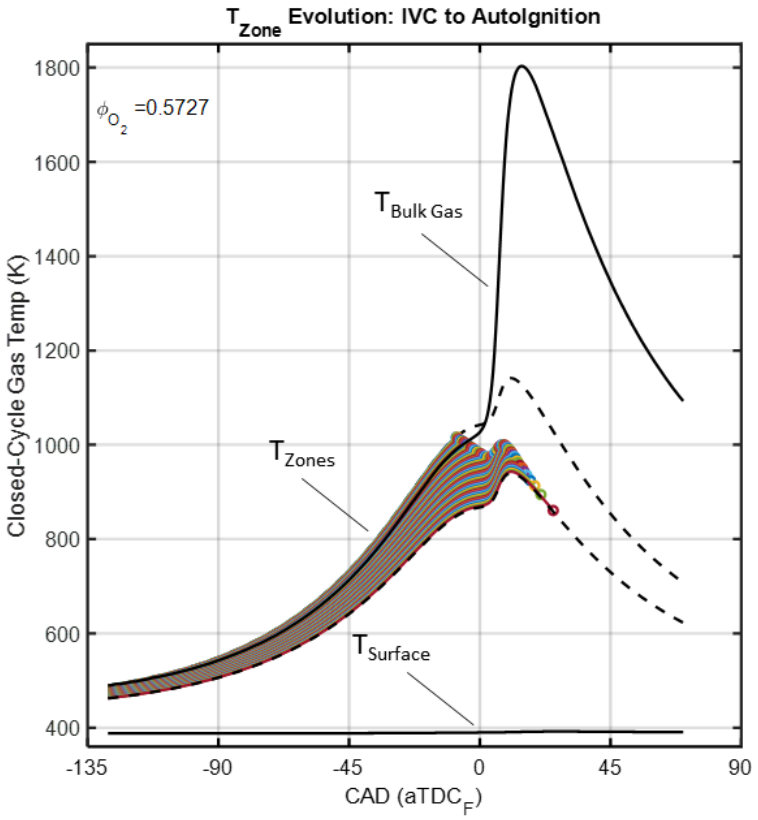

Figure 7.3: A comparison of closed-cycle temperature profiles. "Temperature Zone" profiles are plotted in color, beginning at the Intake Valve Closing event and terminating at their predicted autoignition time. For the data shown here, the ignition delay correlation of Eq.7.12 is used. As expected, the zone with the 'hottest' initial temperature is first to satisfy the autoignition requirements. Note how 'cooler' unburned temperature zones enjoy a secondary peak resulting from the combustion process. The dashed lines show the bounds of the allowable temperature range. It should be noted that the 'Bulk Temperature' is derived from the measured cylinder pressure - which is inherently subject to heat transfer losses. Hence the magnitude of T_{Bulk} dips below the hottest isentropic profiles during compression. For reference, the measured in-cylinder surface temperature is also plotted. Although difficult to detect at this scale, T_{Surf} of the metal engine increases slightly in response to compression/combustion heating.

theory and assumptions. Furthermore, the numeric value of NZT remains invariant across closed-cycle crank angles (denoted by n in Eq. 7.15.) This invariance simplifies calculation, at the cost of increased abstraction.

In order to regain some intuition, it is possible to re-express zone temperature in more familiar units. Solving Eq. 7.15 for the dimensional temperature (T_{Zone}), and re-arranging terms yields:

$$T_{Zone}(n) = (1 - NZT) \cdot T_{Surf}(n) + NZT \cdot T_{isen}(n) \tag{7.16}$$

A few comments regarding equation 7.16. First, this expression resembles a 'weighted average' between the maximum possible charge temperature (T_{isen}) and the minimum allowable temperature (T_{Surf}).

(In the optically-derived sequence reported in [24], the coolest gas structures extend from the 'near wall' region where heat flows from the trapped charge to the chamber surface. Given sufficient time and quiescent flow (however unlikely), the system will reach an equilibrium state when the gas temperature reaches that of the wall. Thus, T_{Surf} represents a reasonable 'lower bound' for charge temperature. This circumstance is synonymous with the $NZT = 0$ case.

In practice, Normalized Zone Temperature typically spans the $0.7 \leq NZT \leq 1$ range. The process used to determine the lower bound of Normalized Zone Temperatures for each engine configuration is developed in the following section.

7.1.6 Temperature-Zone-to-Charge-Mass 'Mapping'

This sections will overview the final (and perhaps most critical) component of the TSA method. Evidence in support of the chosen AI correlation will also be provided. This is followed by a detailed summary of the 'mapping' procedure where ignition-delay correlations, thermophysical properties, and MFB profiles collectively enable the 'mass weighting' of the temperature zones.

The mapping process begins by calculating ignition delay across multiple temperature zones. Independent autoignition integrals are then tracked across each zone until the conditions outlined in Eq. 7.13 are satisfied - i.e., cumulative "$1/\tau$" reaches unity. The crank angles spanning combustion are converted into 'equivalent time' (using RPM), and the ignition delay estimates are paired with their respective (temporal) location on the MFB profile. In this way, each temperature zone is 'mass

weighted' according to its 'position' on the mass fraction burned curve.

From a theoretical point of view, a 'perfectly calibrated' AI correlation should position the first autoignition event (i.e., AI for the 'hottest' zone) at $MFB \approx 1\%$. In other words, the predicted start of combustion (SOC) should align with experimental observation. As a consequence, the 'AI-to-MFB' mapping process can be used to assess the over-all quality of the ignition delay correlation.

For example, a mapping outcome in which the predicted SOI's fail to span the entirety of the MFB curve is most likely indicative of an AI-model/engine-experiment mismatch. Furthermore, unassigned charge mass - as a consequence of incomplete mapping - will not be included in the TSA-derived temperature distributions. Simply put, any error associated with ignition delay prediction will carry through the calculation sequence, contaminating the final product. Thus, selection of an appropriate ignition delay correlation is critical.

Examples of this 'mapping' process, using ignition delay predictions from four separate AI correlations, is provided in Fig.7.4. The sequence shown in Fig. (7.4) limits analysis to pressures/temperatures from the metal engine.

The various subplots of Fig.7.4 predict autoignition of the zonal temperatures utilizing four different ignition delay correlations. In general, Fig. 7.4b illustrate the best agreement between predicted autoignition and the actual SOC for hottest temperature zones. As a result, the aforementioned figures capture the highest amount of the charge mass - 98.9%relative to the experimental curves. Thus, the ignition delay correlation provided in Eq. 7.12 was chosen for this work.

The disparity between AI prediction quality is amplified when the aforementioned 'AI-to-MFB' mapping is performed on engine data from the gadolinium zirconate TBC configuration. Error within the autoignition correlation is essentially amplified in the presence of GDZR's more rapid burn. Results of this analysis is displayed in Fig. 7.5. Once again, the ignition delay correlation of Eq.7.12 best predicts the onset of combustion, capturing a higher percentage of the burned mass.

7.1.7 Putting It All Together: A Concise Overview of the TSA Process

The processes outlined in each of the preceding sections will now be brought together. Collectively, these components will enable a detailed description of the methodological approach underlying Thermal Stratification Analysis.

To begin, ignition delay time is calculated across multiple temperature zones for each of

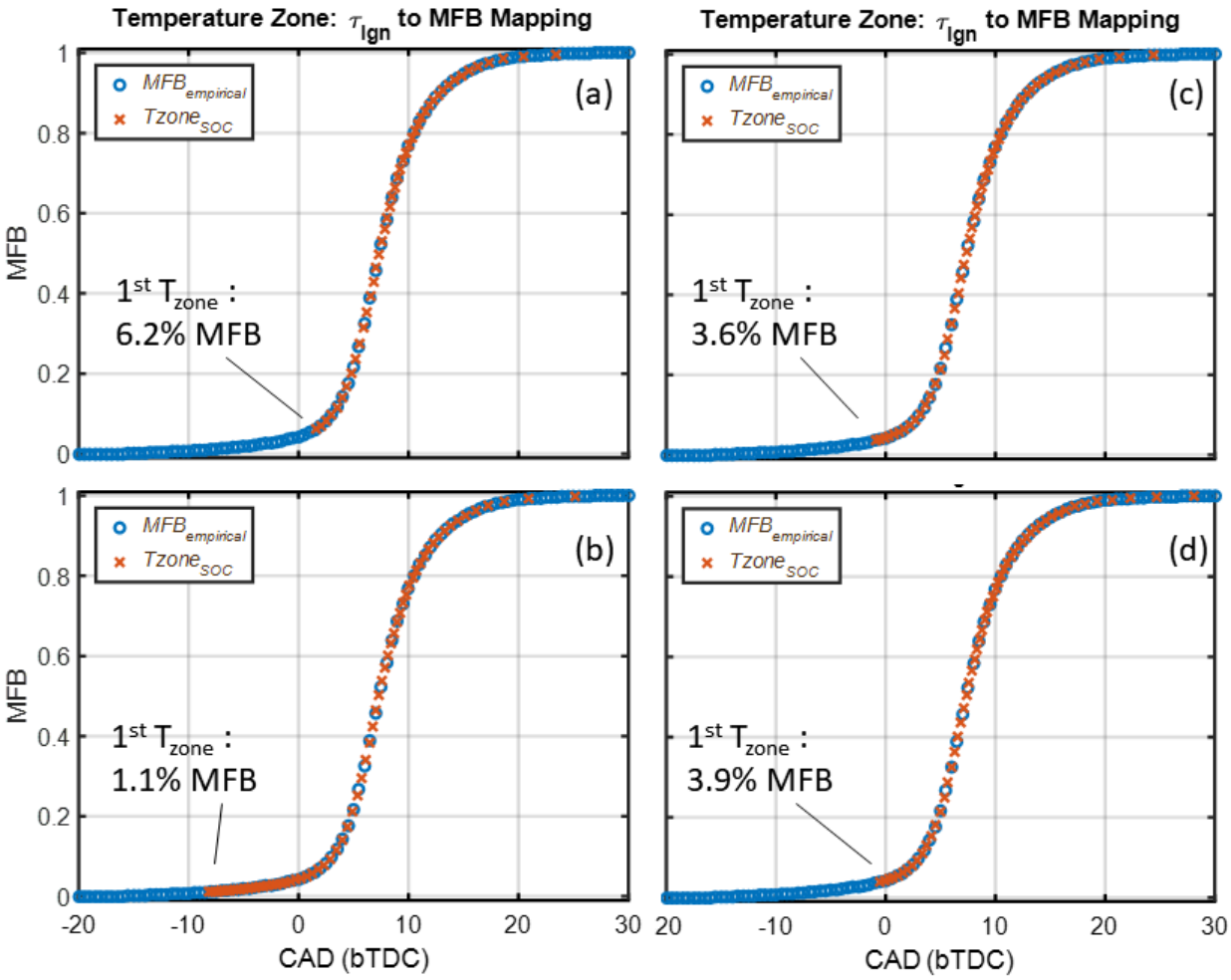

Figure 7.4: Mapping of the various Temperature Zone's autoignition time across a variety of correlations using measurements from the metal engine. These include: (a) τ_{Ign} of Eq. 7.11, (b) τ_{Ign} of Eq. 7.12, and (c) $\tau_{Ign,Exp}$ from [34], (d) $\tau_{Ign,Sim}$ from [34]. Operational conditions: $1200RPM$, $T_{Intake} = 90^oC$, and $11.6mg/cycle$ of fuel. The best over-all performance is demonstrated by the ignition delay correlation from Eq. 7.12 - where $\approx 98.9\%$ of the burned mass is accounted for.

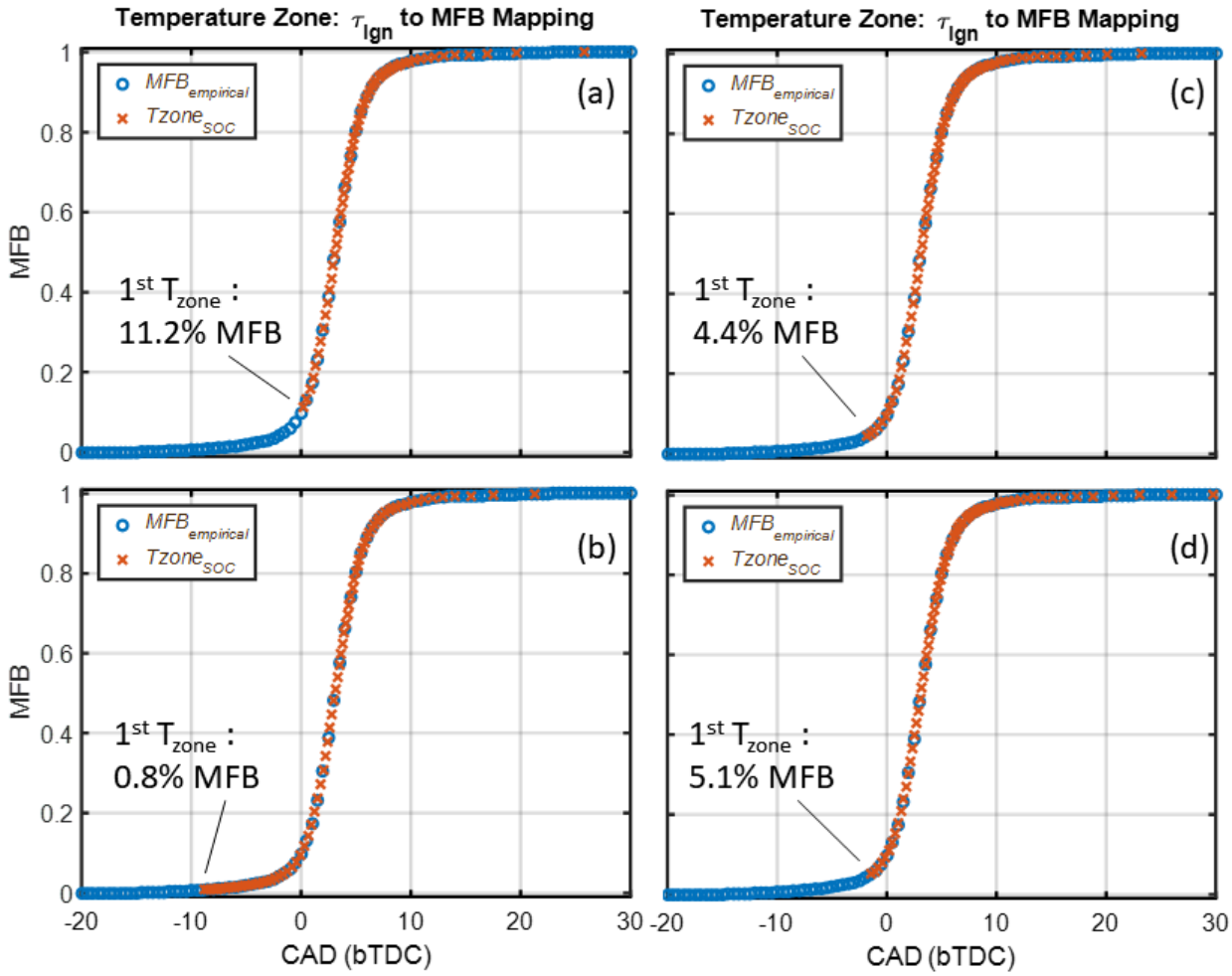

Figure 7.5: Mapping of the various Temperature Zones' autoignition time across a variety of correlations using measurements from the GDZR engine. These include: (a) τ_{Ign} of Eq. 7.11, (b) τ_{Ign} of Eq. 7.12, and (c) $\tau_{Ign,Exp}$ from [34], (d) $\tau_{Ign,Sim}$ from [34]. Operational conditions: $1200RPM$, $T_{Intake} = 90^oC$, and $11.6mg/cycle$ of Fuel. Again, the best over-all performance is demonstrated by Eq. 7.12 - where $\approx 99.2\%$ of the burned mass is accounted for. Note the contrast with results recorded in (a), where only 88.8% of burned mass is captured by the AI correlation of Eq. 7.11.

the engine configurations. The range of required T_{Zones} for each of the engine configurations is determined during the AI-to-MFB mapping procedure.

As a reminder, the initial temperature zone corresponds to the $NZT = 1$ case in Eq.7.16, and is analogous with a purely isentropic compression process. Subsequent 'normalized zone temperatures' are systematically lowered (i.e., $NZT \Longrightarrow .99, .98, .97, .96...$) until the temperature zones span the entirety of the MFB profile.

Note: Temperature zones which map to MFB values greater than unity are not allowed. This limitation is physically consistent with the actual combustion process, where unburned charge (and the possibility of combustion) does not extend beyond the upper bound of the mass fraction burn profile (i.e., $100\%MFB$). A sweep of allowable temperature profiles, along with the mapping of their non-dimensional counterparts are shown in Fig. 7.6a - Fig. 7.6b for the metal engine.

Next, the pairing of Normalized Temperature and Charge Mass (Fig. 7.6b) is used to establish the Cumulative Density Function (CDF) associated with the NZT's. Conceptually, it is helpful to interpret this process as a transpose in the T_{Zone}'s shown in Fig. 7.6b from the 'CAD/MFB plane' to its 'T_{Zone}/CDF' counterpart. The results of this effort are displayed on the right-hand axis of Fig. 7.6c.

With the Cumulative Density Function established, it is possible to derive the Probability Density Function (PDF) using the following relation:

$$PDF(T) = \frac{d\left(CDF(T)\right)}{dT} \tag{7.17}$$

In the present analysis, the PDF is calculated by evaluating the numerical derivative of the CDF profile. These results are shown in Fig. 7.6c.

An additional note regarding the PDF profiles. In order to verify the integrity of these numerically-derived distributions, an additional effort is made to construct a theoretically-sound T_{zone} distribution. This secondary effort utilizes the "fitdist" function available in the MATLAB computational environment [66]. A 'kernel' distribution is selected, and the MFB-derived cumulative density function is specified as the input object. From the documentation in [66],

> A kernel distribution produces a non-parametric probability density estimate that adapts itself to the data, rather than selecting a density with a particular parametric form and estimating the parameters. This distribution is defined by a kernel density

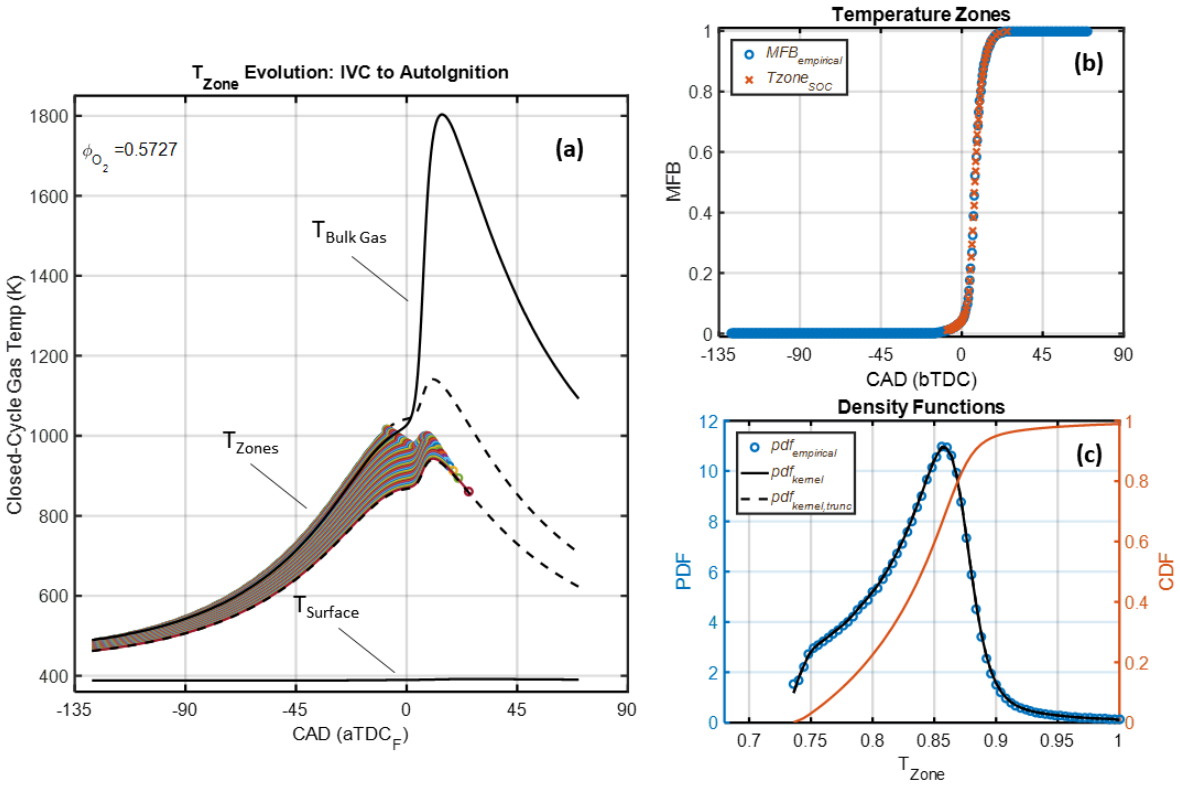

Figure 7.6: An overview of the main processing sequence of Thermal Stratification Analysis. In (a), the isentropic temperature of the unburned charge is calculated by evaluating Eq.7.14 across multiple 'zones'. These temperatures (along with empirically derived pressure and O_2 fraction) are used to evaluate the ignition delay (Eq. 7.12) and the corresponding autoigntion integral (Eq. 7.13). A circular marker 'o' indicates the predicted autoignition time for each of the temperature profiles. Figure (b) maps individual temperature zones (T_{Zone}) onto the MFB profile using the results of (a). Finally, Fig. (c) plots the cumulative density function and the associated PDF of the temperature distribution at 20^o bTDC.

estimator, a smoothing function that determines the shape of the curve used to generate the PDF, and a bandwidth value that controls the smoothness of the resulting density curve."

Simply stated, the kernel distribution does not impose a specific form (Gaussian, Binomial, etc.) Rather, the input data alone drives the shape of the distribution - avoiding the various assumptions and preconditions associated with parametric density functions. Additionally, the MATLAB-derived distribution satisfies the following property:

$$\int PDF(T)dT = 1 \tag{7.18}$$

The above condition is a fundamental property of all mathematically sound probability density functions. However, such rigid 'completeness' is not guaranteed when the PDF calculation 'pathway' involves the numerically differentiating an empirically-derived CDF.

As discussed, error in the predicted autoignition time translates into 'incomplete' mapping of the MFB profile - which in the present analysis has an immediate impact on the PDF estimate. Fig. 7.5a provides a dramatic example of such a breakdown. Furthermore, this error typically manifests during the earliest portion of the burn - about the first 11% of total mass in the aforementioned case. From the perspective of fully-premixed autoignition (i.e., HCCI), this early burn is driven by the behavior of the 'hottest' temperature zones. If the ignition delay correlation fails to map the early burn period, the mass occupying these zones is left unassigned - which in-effect biases the temperature distribution in the direction of 'cooler' T_{Zone}'s.

Thus, it is possible to evaluate the integrity of the empirically derived PDF (Eq. 7.17) by comparing against the analogous kernel density estimate. If the two profiles do not 'overlay' one another, then the Autoignition-to-MFB mapping has failed to sufficiently capture the full range of trapped mass. This point is visualized in Fig. 7.6c.

7.2 Closed-Cycle Charge Temperature Distribution

The theoretical framework and analytic methodology reviewed in the preceding sections provide the foundation of Thermal Stratification Analysis. Having detailed the integration of these components, the method is ready to be deployed. Accordingly, the distribution of temperature zones

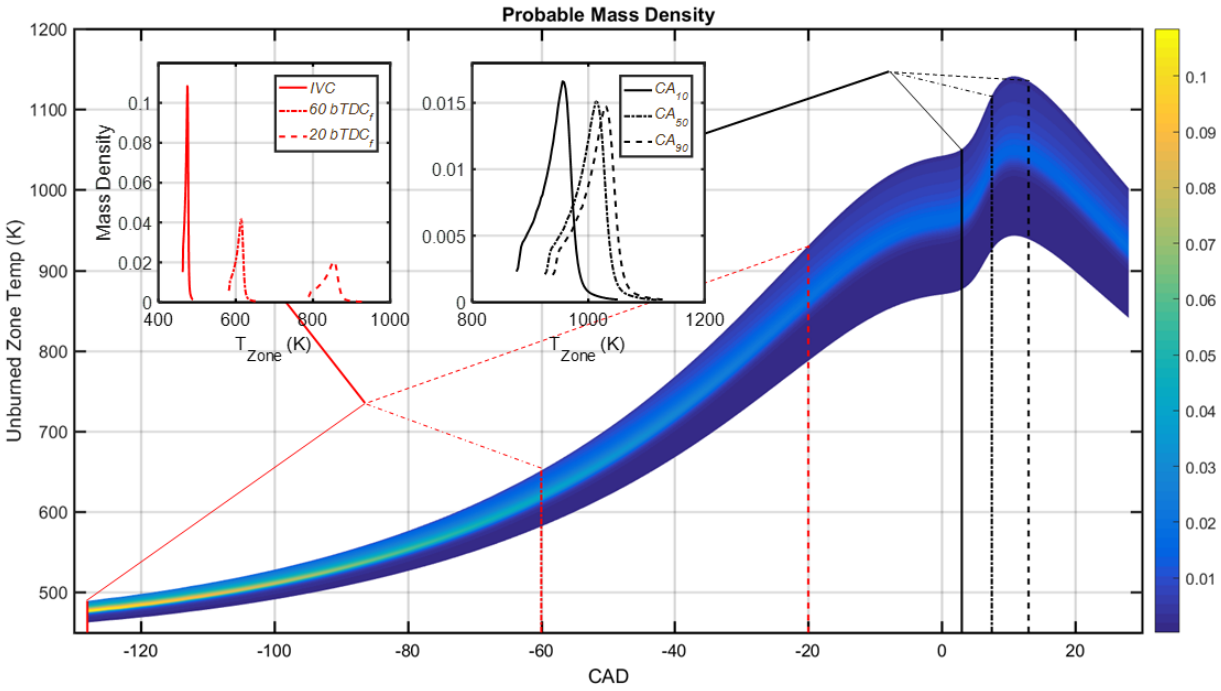

Figure 7.7: TSA results for the metal engine configuration operating at $1200RPM$, $T_{Intake} = 90^oC$, and $11.6mg/cycle$ of Fuel. The zone temperature is plotted as a continuous surface starting across the range of interest. Analysis begins at IVC and terminates at the CA90 location. The continuous distribution is 'sliced' at critical locations during the compression and combustion processes. These results are plotted on the embedded figures in the upper-half of the main figure.

will be estimated across a variety of engine configurations. Analysis will focus on the 1200 rpm 'fuel match' operational point to ensure consistency between the data sets. Furthermore, the relatively low rotational speed of this operating point offers the largest time-scale (in an absolute sense) for heat transfer. The results of this analysis, both stand-alone and comparative, are presented below.

7.2.1 TSA Results: Metal Engine Configuration

Figure 7.7 offers an expanded view of the results originally summarized in Fig. 7.6. A few important details must be discussed. First the temperature zones are reported in dimensionalized form. This requires Eq. 7.16 to be evaluated across the majority closed-cycle crank angles. In fact, TSA analysis begins at IVC (which remains the same for each engine configuration) and ends when the last (and 'coolest') T_{Zone} ignites. As a result, the crank-angle range covered by the T_{Zone} PDF varies slightly between engine configuration.

The general evolution of the density function in Fig.7.7 is captured by the surface plot, where the relative color intensity indicates mass density across the temperature zones. (See legend beyond the right axis.) Some general characteristics of the density function include: i) the stretching of 'thermal width' as the mixture is compressed and ii) the associated re-distribution of mass-density into zones at the periphery (namely, towards the direction of 'cooler' temperatures). Upon initial inspection, this trend remains consistent with both the qualitative behavior reported in [24] and physical intuition. Namely, charge exhibiting very little temperature variation is trapped in-cylinder at IVC. As the piston proceeds toward TDC, and the charge compresses, the range of T_{Zone} extends into lower temperatures, where a 'growing' portion of the overall mass is re-assigned to cooler temperature zones due to heat transfer at the cylinder wall. Remarkably, this predicted behavior is consistent with the highly complex turbulent mixing process driving heat transfer. Recall the results of Dronniou, et al [24], where the complex in-cylinder flow-field transports cold, wall-derived, gas structures into the hotter core region - extending the range of in-cylinder temperatures as charge is compressed. The thermal width of the evolving PDF appears to peak in the proximity of TDC, at which point the effects of combustion-driven compression can be seen.

To provide a more detailed perspective, the continuous PDF surface is 'sliced' at strategic locations across the closed-cycle. This 'slicing' process targets two distinct in-cylinder processes: i) the motor-driven compression of the air-fuel mixture, and ii) the evolution of the 'burn' throughout key combustion markers. The cross-sections for each of these processes are projected into the upper left corner of the main figure. The 'widening' of zone temperatures is again displayed in the plots of individual 'compression slices' (red). The compression curve is sampled at 60^o, 40^o, and 20^o $bTDC_f$ - again showing T_{Zone} mass density moving in the direction of lower temperatures. The second collection of PDF 'slices' occur over the crank-angles spanning combustion, and correspond to CA10, CA50, and CA90. These profiles are plotted in black in the right-most embedded plot. In contrast to the monotonic increase in thermal width witnessed during compression, PDF profiles maintain a relatively constant amplitude and span during the combustion process. Combustion-driven compression heating effectively shifts the temperature distribution associated with the early burn period (CA10) into higher temperatures without dramatic change to the general shape and magnitude of the profile.

Having established a general familiarity with the T_{Zone} distribution of the metal engine configuration, analogous plots are generated for a variety of coating formulations.

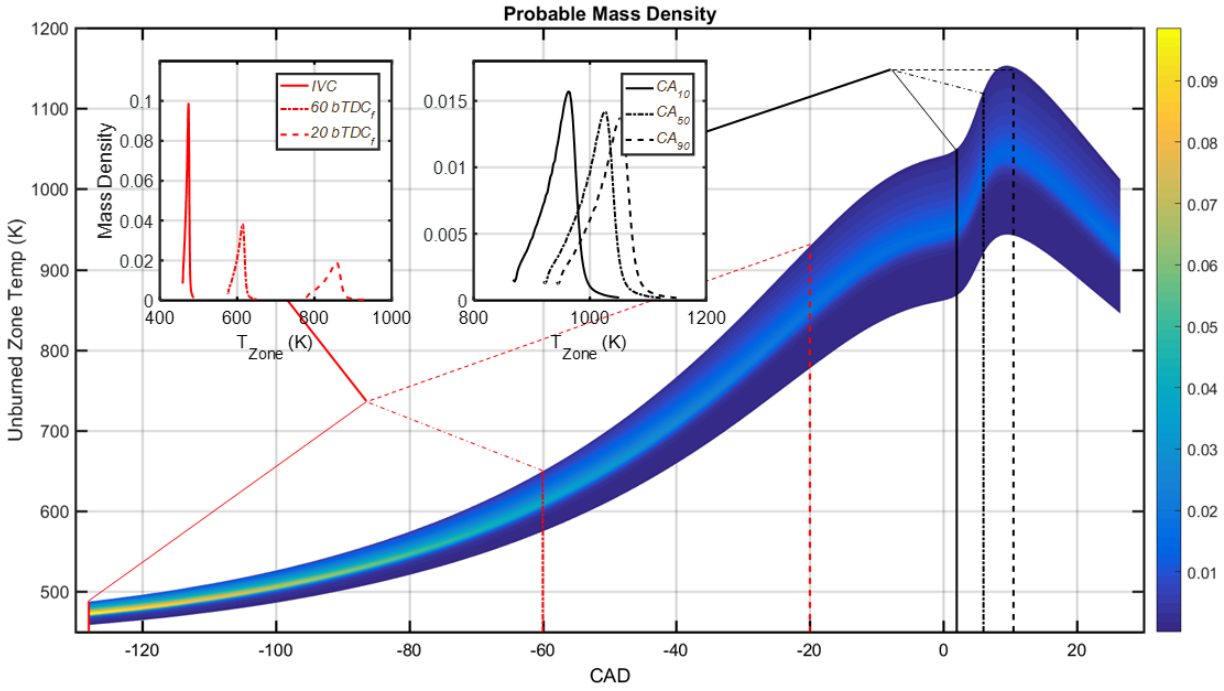

Figure 7.8: TSA results for the APS YSZ engine configuration operating at $1200RPM$, $T_{Intake} = 90^oC$, and $11.6mg/cycle$ of Fuel. The zone temperature is plotted as a continuous surface starting across the range of interest. Analysis begins at IVC and terminates at the CA90 location. To continuous distribution is 'sliced' at critical locations during the compression and combustion processes. These results are plotted on the embedded figures in the upper-half of the main figure.

7.2.2 TSA Results: APS YSZ Engine Configuration

Figure 7.8 displays TSA results for the air plasma sprayed yittria stabilized zirconia (APS-YSZ) TBC. This material represents a dramatic decrease in both thermal conductivity and heat capacity relative to the aluminum piston. The reader is reminded of the outcomes summarized in insert appropriate reference here - where SFSM analysis revealed a dramatic surface temperature swing for the APS-YSZ material during late-compression/combustion. This elevated closed-cycle surface temperature was shown to have a discernible impact on heat transfer, where heat loss over combustion-relevant crank-angles decreased for the APS configuration.

The general character of the APS engine's temperature PDF remains consistent with the results discussed in Sec. 7.2.1. For example, the distribution exhibits a 'widening' behavior as the charge is compressed towards TDC. Furthermore, the thermal width of the distributions remains relatively constant over the duration of the burn. Again, T_{Zones} are 'pushed' into higher temper-

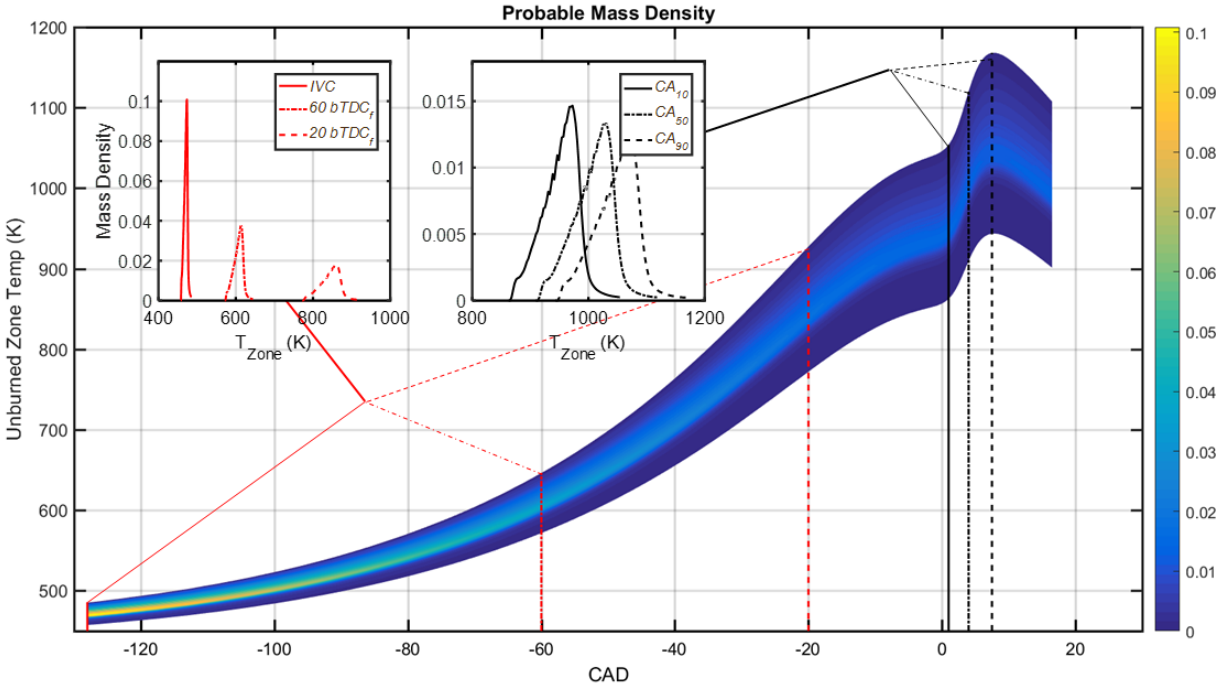

Figure 7.9: TSA results for the IPBiii engine configuration operating at $1200RPM$, $T_{Intake} = 90^oC$, and $11.6mg/cycle$ of Fuel. The zone temperature is plotted as a continuous surface starting across the range of interest. Analysis begins at IVC and terminates at the CA90 location. To continuous distribution is 'sliced' at critical locations during the compression and combustion processes. These results are plotted on the embedded figures in the upper-half of the main figure.

atures in response to combustion-driven compression. A more complete comparison is reserved for Section 7.2.5, where the results from individual engine configurations are collectively examined.

7.2.3 TSA Results: IPBiii Engine Configuration

The IPBiii material is considered next. Figure 7.9 displays the familiar collection of temperature zone distributions. Again, two distinct behaviors divide the motor-driven and combustion-driven compression regimes. It should be noted that the distribution sequence terminates at an earlier crank angle than the prior two case. This remains consistent with the advanced combustion phasing and shorter burn duration accompanying the IPPBiii engine build.

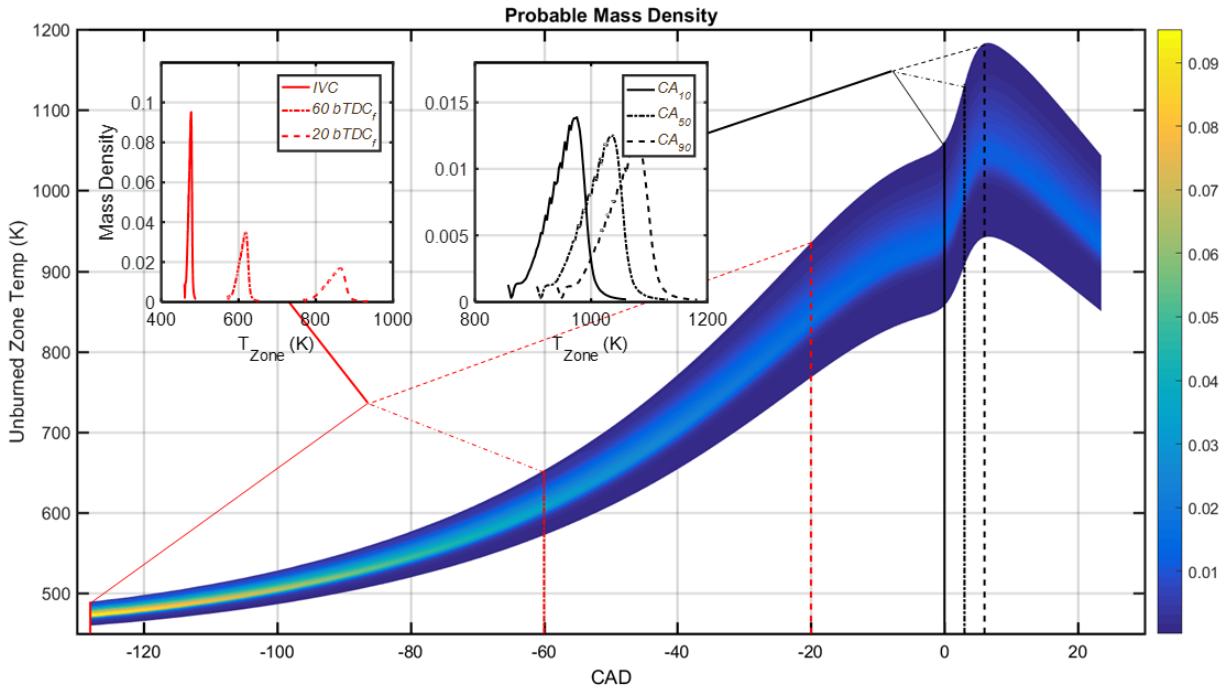

Figure 7.10: TSA results for the GDZR engine configuration operating at $1200RPM$, $T_{Intake} = 90^oC$, and $11.6mg/cycle$ of Fuel. The zone temperature is plotted as a continuous surface starting across the range of interest. Analysis begins at IVC and terminates at the CA90 location. To continuous distribution is 'sliced' at critical locations during the compression and combustion processes. These results are plotted on the embedded figures in the upper-half of the main figure.

7.2.4 TSA Results: GDZR Engine Configuration

A final iteration of TSA processing targets the gadolinium zirconate engine. As a reminder, the GDZR material realizes the lowest thermal-conductivity/heat capacity among the TBCs considered in this study. As a result of these inherently attractive thermal properties, this engine configuration exhibits the largest impact on heat-transfer - recall the analysis of Sec. insert appropriate reference here. As will be fully explored in Sec. 7.2.5, additional heat retained in-cylinder (as a result of the GDZR material) has a dramatic impact on the T_{Zone} distributions - particularly over the crank angles spanning combustion.

It should be noted that the GDZR distribution extends across a larger crank angle range than any of the other profiles. Physically, the temperature zones with the 'coolest' over-all time histories autoignite last - positioning their respective distributions across these later crank angles. The elongation of GDZR's T_{Zone} progression, exists somewhat in opposition to the more rapid burn

of this engine configuration (i.e., decreased CA10-CA90 interval).

Although speculative, it is most likely error associated with the latest portion of the burn - specifically the predicted autoignition of charge mass after the 90% burn fraction marker - which is responsible for artificially extending the distribution into later crank angles. Supporting this conjecture is the fact that $CA90$ for the GDZR engine remains advanced of all other configures. This implies that despite exhibiting a marked reduction in $CA10$ to $CA90$ duration, the GDZR engine configuration also has the 'longest' $CA90$ to $CA100$ duration. In summary, the result for this latest region should be taken with a proverbial 'grain of salt'.

The extend to which the more general characteristics of this distribution deviate from the behavior of the YSZ-based formulations will be examined more closely in subsequent analysis.

7.2.5 TSA Results: A Comparison of Engine Configurations

The continuous PDF for each engine configuration is 'sliced' at fixed crank angles corresponding to specific compression (IVC, $60^{o}bTDC_{f}$, $20^{o}bTDC_{f}$) and combustion (CA10, CA50, CA90) markers. In an effort to identify systematic trends, analysis is expanded to include temperature distributions from each engine configuration. As will be demonstrated, these profiles provide a more direct comparison than the 'single-case' sequential plots shown in Fig.7.7. Analysis in the present section will enable targeted 'bench-marking' between individual coating formulations.

7.2.6 Evolution of Charge Temperature Distribution During Compression

Figure 7.11 displays the the temperature zone distributions associated with the compression (upper row) and combustion processes (lower row) for each engine configurations. Focusing first on the motor-driven compression profiles, the extension of the T_{zones} tail into lower temperatures (as the charge compresses toward TDC) is observed for all of the configurations. As discussed above, this trend remains consistent with the turbulent entrainment of 'cool', wall-derived, zones into the interior of the bulk charge. This is largely a consequence of the increasing temperature differential (between in-cylinder gas and surface conditions) and the complex flow and adverse pressure gradient at the wall.

A slightly different, but still complimentary, interpretation position temperature zones with

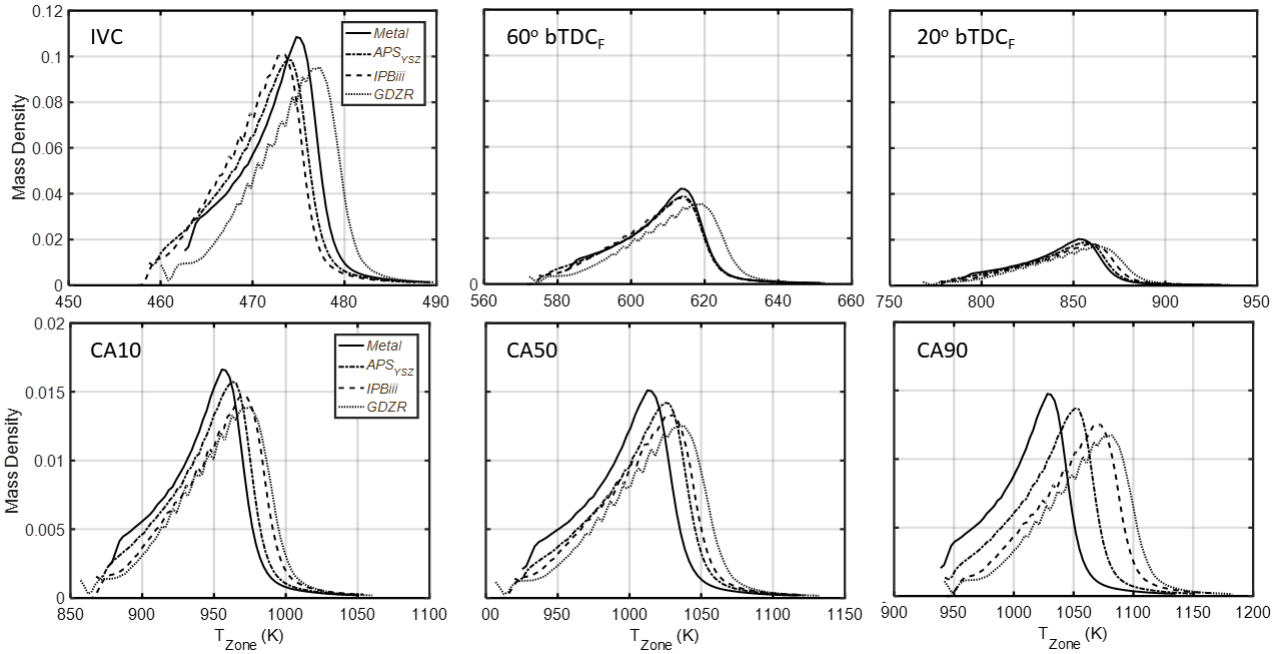

Figure 7.11: Temperature zone evolution during compression (upper row) and combustion (lower row) processes. Specific location (e.g., 'IVC', 'CA10', etc.) is noted in the upper left corner of each plot. The legends is included in the leftmost plot, and remains consistent across all locations.

the most 'isentropic-like' behavior at the high-temperature tail of the temperature distribution. In contrast, charge mass most affected by heat transfer is pushed into zones occupying the lowest temperatures. Within this interpretive framework, one should reasonably expect charge temperature of the TBC-treated engines to 'shift' towards higher values - which is indeed the observed behavior.

A clear separation can be seen between the results reported for the gadolinium zirconate material when compared the remaining engine configurations. That's to say, the GDZR profiles appear to experience a larger shift into higher temperatures vs. other engine configurations while maintaining similar over-all form and magnitude. This dramatic characteristic difference deserves a few additional comments.

Autoignition in this engine is supported by a "re-induction" event - where $\approx 45\%$ of residual gas is re-induced during the valve overlap period. The re-entry of hot residual has a modest (but measurable) impact on surface temperature(s) as seen in the re-breath 'humps' displayed in [36] and [72]. This heating event elevates in-cylinder surface temperature in a manner consistent with the main 'T_{Swing}' phenomena discussed at length in [56] [30] [71] [72], where elevated surface temperatures help preserve heat in-cylinder.

Following this reasoning to its logical conclusion yields the following outcomes: i) Retained thermal energy at IVC 'pushes' the T_{zone} distribution into higher temperatures, and ii) higher zone temperatures would help facilitate the advanced combustion phasing and reduced burn duration experienced by the GDZR engine configuration.

7.2.7 Evolution of Charge Temperature Distribution During Combustion

Returning to Fig.7.11, focus is shifted to the temperature zones plotted in the lower row. This sequence tracks the evolution of the temperature distribution across the familiar combustion locations: CA10, CA50, CA90.

A cautionary note: 'Slicing' the PDF surface relative to combustion markers (instead of specific crank locations) prevents direct temporal comparison between engine builds. Recall, combustion phasing and duration vary with engine configuration - as shown in Fig. 7.1. This is a subtle, but noteworthy distinction. That said, linking PDF's to the combustion event will ensure a more consistent analysis of the respective TBC formulations across the combustion process.

At the onset of combustion (i.e., CA10), the temperature distributions shown in Fig.7.11 remain consistent with the late compression-period distribution (i.e., $20^{o}bTDC_{f}$). The $metal$, YSZ,

and YSZ_{SP} results are tightly grouped. The unburned charge mass in the gadolinium zirconate engine is again 'pushed' into slightly higher temperatures, while the qualitative shape of the distributions remain consistent.

As the burn progresses towards CA50, the TBC-affected temperature distributions begin to 'advance' towards higher temperatures. A few physical mechanisms are likely supporting this behavior. First, the combustion-driven pressure-rise elevates unburned zone temperature in a manner consistent with Eq.7.14. As a consequence, engine configurations with advanced phasing - and by default less available volume - will realize higher in-cylinder temperatures. Second, as TBC surface temperature begins to rise in response to the initial burn, heat loss decreases, preserving higher temperatures.

The above trends accelerate as combustion nears the CA90 marker. Cylinder pressure continues to rise as remaining unburned charge ignites. Available volume remains small, largely due to HCCI's rapid burn. These trends, combined with the continued upward 'swing' of the TBC surface temperatures, transfer considerably more charge mass into higher temperature zones. Reduced heat loss also facilitates higher combustion efficiency which releases more heat (via HC oxidation) in-cylinder, further elevating charge temperature.

It is worthwhile considering the enhanced η_{Comb} from a slightly different perspective. The elevated pressures associated with the TBC-treated engines enable cooler zones to ignite. This effectively extends the thermal width of their respective distributions. In comparison, the charge mass which occupies similarly 'cool' temperature zones in the metal engine would fail to fully oxidize. This is not only consistent with the increase in combustion efficiency experienced in TBC-coated engines [80] [71], but provides a logical link between increased T_{zone} width and reduced hydrocarbons in the exhaust stream.

7.3 Conclusions

Insight from the preceding section provides an analytic pathway between TBC's thermophysical properties and associated cycle-level observations. The evolution of unburned zone temperatures is, in reality, largely influenced by heat loss at the gas-wall interface. Thermal barrier coatings, with their inherently low thermal conductivity, exhibit elevated surface temperatures over combustion-relevant crank angles [56] [30] [72] [71]. The magnitude and time-scale of this "temper-

ature swing" is primarily determined by the thermophysical properties of the underlying material, with low-conductivity/low-heat capacity formulations exhibiting the highest closed-cycle surface temperatures. The TSA method correlates these fundamental material characteristics with the thermal stratification of the trapped charge. In the context of HCCI, charge temperature largely determines the onset of autoigniton. Excessively cool temperature zones, which fails to ignite, contributes directly to increased UBHC and CO emissions - a result of reduced combustion efficiency. Unburned charge also lowers peak cylinder pressure, which limits expansion work, decreasing the thermal effeciency of the cycle. Such trends are reported in [80] and [71].

In general, the temperature zone distributions associated with TBC engine configurations 'preserve' a higher percentage of charge mass in the 'hottest' possible temperature zones. This is particularly true over crank angles spanning the combustion process. Furthermore, the general trend is exaggerated for the TBC's with the most attractive thermal properties (lowest conductivity, lowest heat capacity). As a result, the gadolinium zirconate material preserves the highest relative percentage of charge mass towards the isentropic limit. The relative width of the temperature distribution has also been linked with the observed combustion efficiency trends.

Finally, it is import to re-call the methodological foundation underlying Thermal Stratification Analysis. The results discussed above are derived (almost exclusively) from cylinder pressure measurements. Much of the conceptual 'motivation' behind the interest in 'thin' thermal barrier applications is focused on the interplay between surface temperature 'swing' and heat loss at the wall. The pressure-based analysis of the present work has quantified TBC's impact on heat transfer with minimal reliance on measured/estimated surface temperatures. This serves as an important (and essentially independent) 'check' on the results of more conventional temperature-based analysis.

Chapter 8

Conclusions and Contributions

This concluding chapter will provide a concise review of the main outcomes of the preceding chapters. Contributions within the current document which represent original work are also highlighted.

8.1 Summary of Conclusions

8.1.1 A Conceptual Exploration of Thermal Barrier Coating Design Space

- Temperature 'swing' behavior is defined in the context of engine operation. Here, surface temperature profiles of idealized TBCs respond quickly to the compression and combustion heating events, reducing the wall-gas temperature differential.
- Employing a reduced dimensional model to explore the relevant TBC 'design space', a number of critical outcomes have been identified. These include the relative impact (and importance) of key TBC parameters including: thickness, heat capacity, and thermal conductivity.
- Furthermore, the influence of engine speed (relative to absolute heat transfer timescale) is also considered. The modeling outcomes suggests a coating selection which minimizes conductivity, volumetric heat capacity, and thickness represents a preferred pathway.
- Finally, parametric optimization (via modeling) helps to define the range of time-scales (and thus, rpm) over which coating formulations exhibits favorable behavior relative to the metal engine configuration.

8.1.2 Inverse Heat Conduction and the Sequential Function Specification Method

- This section modifies the SFSM via inclusion of a diffusive time scale. Efforts are made to quantify the time-lag between a specific surface temperature 'event' and its subsequent response at subsurface temperature probe. A review of parabolic heat diffusion is provided, followed by suggested methodology for estimation and eventual measurement of the surface-to-sensor time lag.

- Utilizing the ex-situ experimental apparatus (i.e., 'Radiation Chamber'), two heat flux probes are simultaneously subjected to the same heat square flux pulse. One sensor remains uncoated and, while the second probe has a low conductivity TBC applied to it's surface measurement junction. This configuration enables direct comparison between direct and inverse solution methodology.

- Having been validated ex situ, the modified solver is applied to engine data where the temperature swing is quantified under firing conditions.

- Given the dominance of convection within the engine environment, differences in thermal conditions at the gas-wall boundary (including elevated surface temperatures) are shown to reduce heat loss at the sensor location.

8.1.3 Quantifying the Impact of Thermal Barrier Coatings on Heat Transfer

- Using the inverse solver developed in the preceding chapter, along with direct measurements from the metal engine, surface temperatures and heat flux profiles were quantified for metal and GDZR-treated engine configurations.

- Analysis also considered key cycle metrics, including instantaneous work-rate and combustion efficiency in an effort to better understand the mechanism(s) underlying performance and efficiency gains.

- Instrumentation is expanded to include both head mounted heat flux probes and instrumented pistons.

- The four shared piston locations (plus head probes) were used to derive a spatially 'global' heat flux profile which revealed reduced heat loss during closed-cycle operation for the GDZR engine.

- Furthermore, instantaneous work-rate profiles (derived from in-cylinder pressure measurements) further support the outcomes of the temperature-based analysis. Here, decreased heat loss translates to increased work (and enhanced cycle efficiency).

8.1.4 Thermal Stratification Analysis

- In this section, a post-processing technique known as Thermal Stratification Analysis (TSA) is used to quantify the impact of Thermal Barrier Coatings on the temperature distribution within the engine.

- Some general characteristics of the density function include: i) the stretching of 'thermal width' as the mixture is compressed and ii) the associated re-distribution of mass-density into zones at the periphery (namely, towards the direction of 'cooler' temperatures).

- These trend remains consistent with both the qualitative behavior reported in [24] and physical intuition. Namely, charge exhibiting very little temperature variation is trapped in-cylinder at IVC. As the piston proceeds toward TDC, and the charge compresses, the range of T_{Zone} extends into lower temperatures, where a 'growing' portion of the overall mass is re-assigned to cooler temperature zones due to heat transfer at the cylinder wall.

- The thermal width of the evolving PDF appears to peak in the proximity of TDC, at which point the effects of combustion-driven compression can be seen.

- Temperature zone distributions associated with TBC engine configurations 'preserve' a higher percentage of charge mass in the 'hottest' possible temperature zones. This is particularly true over crank angles spanning the combustion process.

- This trend is exaggerated for the TBC's with the most attractive thermal properties (lowest conductivity, lowest heat capacity).

- As a result, the temperature distribution associated with gadolinium zirconate preserves the highest relative percentage of charge mass towards the isentropic limit.

- The width of the temperature distribution has also been linked with the observed combustion efficiency trends.
- The elevated pressures associated with the TBC-treated engine, (a result of the advanced combustion phasing), helps support autoigniton within the cooler zones. In effect, the increased pressure compensates for lower temperatures.
- In comparison, the charge mass which occupies similarly 'cool' temperature zones in the metal engine fails to fully oxidize.
- This is consistent with the increase in combustion efficiency experienced in TBC-coated engines and provides a logical link between increased T_{zone} width and reduced hydrocarbons in the exhaust stream.

8.2 Overview of Original Contributions

- **Modification of the Sequential Function Specification Methodology to include the diffusive time scale.** This work was critical to ensure the success of the inverse solver. The engine environment is inherently requires targeted regularization to ensure stability of the solver while preserving fidelity of the surface temperature and heat flux estimates.
- **Application of modified SFSM to an engine-specific inverse heat transfer configuration.** The inverse heat transfer configuration resulting from the TBC-treated heat flux probes and piston provided a fitting platform to apply the methodology detailed above. Prior efforts to evaluate thermal conditions of in-cylinder surfaces required direct measurements.
- **Expanded instrumentation, including the GDZR-treated telemetry linkage system.** Considerable effort was invested into coating, constructing, and processing the sub-TBC temperature measurements from the GDZR-treated piston.
- **Evaluation of global heat loss between metal and TBC-treated engine platforms.** The present work represents the first systematic (and thorough) evaluation of heat transfer between metal and TBC-treated engine variants.
- **Related analysis of charge temperature stratification (as a result of heat transfer) between metal and TBC engines.** Temperature based analysis is extended to consider

pressure-derived metrics using Thermal Stratification Analysis. This effort provides considerable insight into the physical mechanisms underlying the advanced combustion phasing and enhanced combustion efficiency of the TDC-treated engine.

Work Cited

[1] Salvador M Aceves, Daniel L Flowers, Charles K Westbrook, J Ray Smith, William Pitz, Robert Dibble, Magnus Christensen, and Bengt Johansson. A multi-zone model for prediction of hcci combustion and emissions. Technical report, SAE Technical paper, 2000.

[2] Ali Y Alharbi and Volker Sick. Investigation of boundary layers in internal combustion engines using a hybrid algorithm of high speed micro-piv and ptv. *Experiments in fluids*, 49(4):949–959, 2010.

[3] OM Alifanov and Eo A Artyukhin. Regularized numerical solution of nonlinear inverse heat-conduction problem. *Journal of Engineering Physics*, 29(1):934–938, 1975.

[4] AC Alkidas. Heat transfer characteristics of a spark-ignition engine. *Journal of Heat Transfer*, 102(2):189–193, 1980.

[5] Dennis N Assanis and Edward Badillo. Transient heat conduction in low-heat-rejection engine combustion chambers. Technical report, SAE Technical Paper, 1987.

[6] DN Assanis. The effect of thin ceramic coatings on petrol engine performance and emissions. *International Journal of Vehicle Design*, 13(4):378–387, 1992.

[7] James V Beck, Ben Blackwell, and Charles R St Clair Jr. *Inverse heat conduction: Ill-posed problems*. James Beck, 1985.

[8] James Vere Beck and Herbert Wolf. Nonlinear inverse heat conduction problem. In *MECHANICAL ENGINEERING*, volume 87, page 77. ASME-AMER SOC MECHANICAL ENG 345 E 47TH ST, NEW YORK, NY 10017, 1965.

[9] JV Beck. Calculation of surface heat flux from an internal temperature history. *ASME paper*, 62, 1962.

[10] John B Bell and Andrew B Wardlaw Jr. Numerical solution of an ill-posed problem arising in wind tunnel heat transfer data reduction. Technical report, DTIC Document, 1981.

[11] Peter Bradshaw and George P Huang. The law of the wall in turbulent flow. In *Proceedings of the Royal Society of London A: Mathematical, Physical and Engineering Sciences*, volume 451, pages 165–188. The Royal Society, 1995.

[12] Rudiger Brandt, L Pawlowski, G Neuer, and P Fauchais. Specific heat and thermal conductivity of plasma sprayed yttria-stabilized zirconia and nial, nicr, nicral, nicraly, nicocraly coatings. *High Temp.–High Press.*, 18(1):65–77, 1986.

[13] Walter Bryzik and Roy Kamo. Tacom/cummins adiabatic engine program. Technical report, SAE Technical Paper, 1983.

[14] Jerald A Caton. Comparisons of global heat transfer correlations for conventional and high efficiency reciprocating engines. In *ASME 2011 Internal Combustion Engine Division Fall Technical Conference*, pages 327–337. American Society of Mechanical Engineers, 2011.

[15] Jerald A Caton. The thermodynamic characteristics of high efficiency, internal-combustion engines. *Energy Conversion and Management*, 58:84–93, 2012.

[16] Jerald A Caton. On the importance of specific heats as regards efficiency increases for highly dilute ic engines. *Energy Conversion and Management*, 79:146–160, 2014.

[17] Jerald A Caton. Thermodynamic considerations for advanced, high efficiency ic engines. *Journal of Engineering for Gas Turbines and Power*, 136(10):101512, 2014.

[18] J Chang, Z Filipi, D Assanis, TW Kuo, P Najt, and R Rask. Characterizing the thermal sensitivity of a gasoline homogeneous charge compression ignition engine with measurements of instantaneous wall temperature and heat flux. *International Journal of Engine Research*, 6(4):289–310, 2005.

[19] Junseok Chang, Orgun Güralp, Zoran Filipi, Dennis Assanis, Tang-Wei Kuo, Paul Najt, and Rod Rask. New heat transfer correlation for an hcci engine derived from measurements of instantaneous surface heat flux. *SAE paper*, (2004-01):2996, 2004.

[20] Kevin D Cole, James V Beck, A Haji-Sheikh, and Bahman Litkouhi. *Heat conduction using Greens functions*. Taylor & Francis, 2010.

[21] Kistler Corp. *Kistler 6125a Pressure Transducer*. Documentation Available: www.kistler.com.

[22] Medtherm Corporation. Medtherm Bulletin 500. Huntsville, Alabama.

[23] Jeremie Dernotte, John E Dec, and Chunsheng Ji. Energy distribution analysis in boosted hcci-like/ltgc engines-understanding the trade-offs to maximize the thermal efficiency. *SAE International Journal of Engines*, 8(3):956–980, 2015.

[24] Nicolas Dronniou and John Dec. Investigating the development of thermal stratification from the near-wall regions to the bulk-gas in an hcci engine with planar imaging thermometry. *SAE International Journal of Engines*, 5(3):1046–1074, 2012.

[25] Alireza Ebadi, Faraz Mehdi, and Christopher M White. An exact integral method to evaluate wall heat flux in spatially developing two-dimensional wall-bounded flows. *International Journal of Heat and Mass Transfer*, 84:856–861, 2015.

[26] Alireza Ebadi, Christopher White, Ian Pond, and Yves Dubief. An integral method to evaluate wall heat flux in oscillatory wall-bounded flow. *Bulletin of the American Physical Society*, 59, 2014.

[27] Yoshiteru ENOMOTO and Shoichi FURUHAMA. Heat transfer to wall of ceramic combustion chamber of internal combustion engine. *Bulletin of JSME*, 29(250):1211–1217, 1986.

[28] David E Foster. Guest forum - horriba.

[29] CC French. Ceramics in reciprocating internal combustion engines. Technical report, Society of Automotive Engineers, Inc., Warrendale, PA, 1984.

[30] Kenji Fukui, Yoshifumi Wakisaka, Kazuaki Nishikawa, Yoshiaki Hattori, Hidemasa Kosaka, and Akio Kawaguchi. Development of instantaneous temperature measurement technique for combustion chamber surface and verification of temperature swing concept. Technical report, SAE Technical Paper, 2016.

[31] JA Gatowski, En N Balles, KM Chun, FE Nelson, JA Ekchian, and John B Heywood. Heat release analysis of engine pressure data. Technical report, SAE Technical paper, 1984.

[32] William K George. Is there a universal log law for turbulent wall-bounded flows? *Philosophical Transactions of the Royal Society of London A: Mathematical, Physical and Engineering Sciences*, 365(1852):789–806, 2007.

[33] William K George and Luciano Castillo. Zero-pressure-gradient turbulent boundary layer. *Applied Mechanics Reviews*, 50(12):689–729, 1997.

[34] S Scott Goldsborough. A chemical kinetically based ignition delay correlation for iso-octane covering a wide range of conditions including the ntc region. *Combustion and Flame*, 156(6):1248–1262, 2009.

[35] O Guralp, Z Filipi, T Kuo, P Najt, and R Rask. Characterizing the effect of combustion chamber deposits on a gasoline hcci engine. *SAE paper*, (2006-01):3277, 2006.

[36] OA Güralp. *Development and Application of a Telemetry System for Piston Surface Temperature Measurements in a Homogeneous Charge Compression Ignition Engine*. PhD thesis, MS Thesis, University of Michigan, Ann Arbor, 2004.

[37] Orgun Güralp, Mark A Hoffman, Dennis Assanis, Zoran Filipi, Tang Wei Kuo, Paul Najt, and Rod Rask. Thermal characterization of combustion chamber deposits on the hcci engine piston and cylinder head using instantaneous temperature measurements. 2009.

[38] Orgun Güralp, Paul Najt, and Zoran S Filipi. Method for determining instantaneous temperature at the surface of combustion chamber deposits in an hcci engine. *Journal of Engineering for Gas Turbines and Power*, 135(8):081501, 2013.

[39] Patrick Haenel, Henning Kleeberg, Dean Tomazic, and Shawn Dolan. Investigation regarding the influence of a catalytic combustion chamber coating on gasoline combustion characteristics, emission formation and engine efficiency. Technical report, SAE Technical Paper, 2012.

[40] X He, MT Donovan, BT Zigler, TR Palmer, SM Walton, MS Wooldridge, and A Atreya. An experimental and modeling study of iso-octane ignition delay times under homogeneous charge compression ignition conditions. *Combustion and Flame*, 142(3):266–275, 2005.

[41] Terry Hendricks and Jaal Ghandhi. Estimation of surface heat flux in ic engines using temperature measurements: processing code effects. *SAE International Journal of Engines*, 5(3):1268–1285, 2012.

[42] Carl-Anders Hergart, Abdelilah Louki, and Norbert Peters. On the potential of low heat rejection dl diesel engines to reduce tail-pipe emissions. *SAE transactions*, 114(3):790–802, 2005.

[43] John B Heywood et al. *Internal combustion engine fundamentals*, volume 930. Mcgraw-hill New York, 1988.

[44] Mark A Hoffman, Benjamin J Lawler, Zoran S Filipi, Orgun A Güralp, and Paul M Najt. Development of a device for the nondestructive thermal diffusivity determination of combustion chamber deposits and thin coatings. *Journal of Heat Transfer*, 136(7):071601, 2014.

[45] Klaus A Hoffmann and Steve T Chiang. {*Computational fluid dynamics, Vol. 1*}. 2000.

[46] A. Hultqvist. *Characterization of the Homogeneous Charge Compression Ignition Combustion Process*. PhD thesis, 202.

[47] Anders Hultqvist, Magnus Christensen, Bengt Johansson, Mattias Richter, Jenny Nygren, Johan Hult, and Marcus AldJn. The hcci combustion process in a single cycle-speed fuel tracer lif and chemiluminescence imaging. Technical report, SAE Technical Paper, 2002.

[48] Amol D Jadhav, Nitin P Padture, Eric H Jordan, Maurice Gell, Pilar Miranzo, and Edwin R Fuller. Low-thermal-conductivity plasma-sprayed thermal barrier coatings with engineered microstructures. *Acta Materialia*, 54(12):3343–3349, 2006.

[49] S Jaichandar and P Tamilporai. The status of experimental investigations on low heat rejection engines. Technical report, SAE Technical Paper, 2004.

[50] Christopher Jainski, Louise Lu, Andreas Dreizler, and Volker Sick. High-speed micro particle image velocimetry studies of boundary-layer flows in a direct-injection engine. *International Journal of Engine Research*, 14(3):247–259, 2013.

[51] Eric H Jordan, L Xie, M Gell, NP Padture, B Cetegen, A Ozturk, X Ma, J Roth, TD Xiao, and PEC Bryant. Superior thermal barrier coatings using solution precursor plasma spray. *Journal of Thermal Spray Technology*, 13(1):57–65, 2004.

[52] Takeyuki Kamimoto and Myurng-hoan Bae. High combustion temperature for the reduction of particulate in diesel engines. Technical report, SAE Technical Paper, 1988.

[53] R Kamo and Walter Bryzik. Adiabatic turbocompound engine performance prediction. Technical report, Society of Automotive Engineers, Inc., Warrendale, PA, 1978.

[54] Hideo Kawamura. Development status of isuzu ceramic engine. Technical report, SAE Technical Paper, 1988.

[55] Russell G Keanini, Xianwu Ling, and Harischandra P Cherukuri. A modified sequential function specification finite element-based method for parabolic inverse heat conduction problems. *Computational Mechanics*, 36(2):117–128, 2005.

[56] Hidemasa Kosaka, Yoshifumi Wakisaka, Yoshihiro Nomura, Yoshihiro Hotta, Makoto Koike, Kiyomi Nakakita, and Akio Kawaguchi. Concept of temperature swing heat insulation in combustion chamber walls, and appropriate thermo-physical properties for heat insulation coat. *SAE International Journal of Engines*, 6(2013-01-0274):142–149, 2013.

[57] L Lave, M Savitz, R Berry, M Brown, L Cohen, M Craford, P Decotis, J Degraffenreidt, H Geller, D Goldstein, et al. Real prospects for energy efficiency in the united states, 2009.

[58] Benjamin Lawler, Mark Hoffman, Zoran Filipi, Orgun Güralp, and Paul Najt. Development of a postprocessing methodology for studying thermal stratification in an hcci engine. *Journal of Engineering for Gas Turbines and Power*, 134(10):102801, 2012.

[59] Benjamin Lawler, Joshua Lacey, Nicolas Dronniou, Jeremie Dernotte, John E Dec, Orgun Guralp, Paul Najt, and Zoran Filipi. Refinement and validation of the thermal stratification analysis: A post-processing methodology for determining temperature distributions in an experimental hcci engine. Technical report, SAE Technical Paper, 2014.

[60] Benjamin Lawler, Elliott Ortiz-Soto, Rohit Gupta, Huei Peng, and Zoran Filipi. Hybrid electric vehicle powertrain and control strategy optimization to maximize the synergy with a gasoline hcci engine. *SAE International Journal of Engines*, 4(2011-01-0888):1115–1126, 2011.

[61] Henry Lehmann, Dieter Pitzer, Gerhard Pracht, Robert Vassen, and Detlef Stöver. Thermal conductivity and thermal expansion coefficients of the lanthanum rare-earth-element zirconate system. *Journal of the American Ceramic Society*, 86(8):1338–1344, 2003.

[62] JC Livengood and PC Wu. Correlation of autoignition phenomena in internal combustion engines and rapid compression machines. In *Symposium (international) on combustion*, volume 5, pages 347–356. Elsevier, 1955.

[63] Robert P Lucht, Derek Dunn-Rankin, Thomas Walter, Thomas Dreier, and Stefan C Bopp. Heat transfer in engines: Comparison of cars thermal boundary layer measurements and heat flux measurements. Technical report, SAE Technical Paper, 1991.

[64] Xi Luo, Xin Yu, and Marcis Jansons. Simultaneous in-cylinder surface temperature measurements with thermocouple, laser-induced phosphorescence, and dual wavelength infrared diagnostic techniques in an optical engine. Technical report, SAE Technical Paper, 2015.

[65] Satyapal Mahade, Nicholas Curry, Stefan Björklund, Nicolaie Markocsan, and Per Nylén. Thermal conductivity and thermal cyclic fatigue of multilayered gd2zr2o7/ysz thermal barrier coatings processed by suspension plasma spray. *Surface and Coatings Technology*, 283:329–336, 2015.

[66] MathWorks. *MathWorks 'fitdist' Documentation*. For complete details: https://www.mathworks.com/help/stats/fitdist.html.

[67] Glen E Myers. Analytical methods in conduction heat transfer. 1971.

[68] Paul M Najt and David E Foster. Compression-ignited homogeneous charge combustion. Technical report, SAE Technical paper, 1983.

[69] DJ Oude Nijeweme, JBW Kok, CR Stone, and L Wyszynski. Unsteady in-cylinder heat transfer in a spark ignition engine: experiments and modelling. *Proceedings of the Institution of Mechanical Engineers, Part D: Journal of Automobile Engineering*, 215(6):747–760, 2001.

[70] Masaaki Noguchi, Yukiyasu Tanaka, Taro Tanaka, and Yukihisa Takeuchi. A study on gasoline engine combustion by observation of intermediate reactive products during combustion. Technical report, SAE Technical Paper, 1979.

[71] Ryan O'Donnell, Tommy Powell, Mark Hoffman, Eric Jordan, and Zoran Filipi. Inverse analysis of in-cylinder gas-wall boundary conditions: Investigation of a yttria-stabilized zirconia thermal barrier coating for homogeneous charge compression ignition. *Journal of Engineering for Gas Turbines and Power*, 139(10):102808, 2017.

[72] Ryan N O'Donnell, Thomas R Powell, Zoran S Filipi, and Mark A Hoffman. Estimation of thermal barrier coating surface temperature and heat flux profiles in a low temperature combustion engine using a modified sequential function specification approach. *Journal of Heat Transfer*, 139(4):041201, 2017.

[73] The Ceramic Society of Japan and Nihon Seramikkusu Kyōkai. *Advanced Ceramic Technologies & Products*. Springer Science & Business Media, 2012.

[74] Shigeru Onishi, Souk Hong Jo, Katsuji Shoda, Pan Do Jo, and Satoshi Kato. Active thermoatmosphere combustion (atac)-a new combustion process for internal combustion engines. Technical report, SAE Technical paper, 1979.

[75] Alan V Oppenheim. *Discrete-time signal processing*. Pearson Education, 1999.

[76] M Necat Ozisik. *Inverse heat transfer: fundamentals and applications*. CRC Press, 2000.

[77] M Necati Ozisik. *Heat conduction*. John Wiley & Sons, 1993.

[78] Necati Ozisik. *Finite difference methods in heat transfer*. CRC press, 1994.

[79] Tommy Powell, Nick Killingsworth, Mark Hoffman, Ryan O'Donnell, Robert Prucka, and Zoran Filipi. Predicting the gas-wall boundary conditions in a thermal barrier coated low temperature combustion engine using sub-coating temperature measurements. *International Journal of Powertrains*, 6(2):125–150, 2017.

[80] Tommy Powell, Ryan O'Donnell, Mark Hoffman, and Zoran Filipi. Impact of a yttria-stabilized zirconia thermal barrier coating on hcci engine combustion, emissions, and efficiency. *Journal of Engineering for Gas Turbines and Power*, 139(11):111504, 2017.

[81] William H Press. *Numerical recipes 3rd edition: The art of scientific computing*. Cambridge university press, 2007.

[82] CD Rakopoulos, GM Kosmadakis, and EG Pariotis. Critical evaluation of current heat transfer models used in cfd in-cylinder engine simulations and establishment of a comprehensive wall-function formulation. *Applied Energy*, 87(5):1612–1630, 2010.

[83] Magnus Sjöberg and John E Dec. Smoothing hcci heat-release rates using partial fuel stratification with two-stage ignition fuels. Technical report, SAE Technical Paper, 2006.

[84] Magnus Sjöberg, John E Dec, Aristotelis Babajimopoulos, and Dennis N Assanis. Comparing enhanced natural thermal stratification against retarded combustion phasing for smoothing of hcci heat-release rates. Technical report, SAE Technical Paper, 2004.

[85] Magnus Sjöberg, John E Dec, and Nicholas P Cernansky. Potential of thermal stratification and combustion retard for reducing pressure-rise rates in hcci engines, based on multi-zone modeling and experiments. *SAE transactions*, 114(3):236–251, 2005.

[86] Daniel Richard Stull and Harold Prophet. Janaf thermochemical tables. Technical report, National Standard Reference Data System, 1971.

[87] Takashi Suzuki, IC Engine, NA Otto, H Engine, S Carnot, E Life, E Compartments, R Royce, and DBD Engine. The romance of engines. *Training*, 2010:03–15, 1997.

[88] Rodney J Tabaczynski, Colin R Ferguson, and Krisna Radhakrishnan. Turbulent entrainment model for spark-ignition engine combustion. Technical report, Society of Automotive Engineers, Inc., Warrendale, PA, 1977.

[89] Andreĭ Nikolaevich Tikhonov and Vasiliĭ IAkovlevich Arsenin. *Solutions of ill-posed problems*. Vh Winston, 1977.

[90] Keith A Woodbury. *Inverse engineering handbook*. Crc press, 2002.

[91] Gerhard Woschni. A universally applicable equation for the instantaneous heat transfer coefficient in the internal combustion engine. Technical report, SAE Technical paper, 1967.

[92] Gerhard Woschni, Walter Spindler, and Konrad Kolesa. Heat insulation of combustion chamber walls-a measure to decrease the fuel consumption of ic engines. Technical report, Technische Universitat, Munchen, 1987.

[93] Martin Wosnik. reconciling the zagarola/smits scaling with the george/castillo theory for the zero pressure gradient turbulent boundary layer. *38th AIAA Ann. Atg. Reno, NV, Jan*, pages 10–13, 2000.

[94] Jie Wu, Xuezheng Wei, Nitin P Padture, Paul G Klemens, Maurice Gell, Eugenio García, Pilar Miranzo, and Maria I Osendi. Low-thermal-conductivity rare-earth zirconates for potential thermal-barrier-coating applications. *Journal of the American Ceramic Society*, 85(12):3031–3035, 2002.

[95] Hanho Yun, Orgun Guralp, Ronald O Grover Jr, and Paul M Najt. The effect of temperature and oxygen concentration on auto-ignition at low-load operating conditions in a gasoline homogeneous charge compression ignition engine. *International Journal of Engine Research*, 14(5):512–524, 2013.

[96] James Zucchetto, Phillip Myers, John Johnson, and Dennis Miller. An assessment of the performance and requirements for'adiabatic' engines. *Science*, 240(5):1157–62, 1988.